Searching for Heavy Particles Coupled to Top Quarks with CMS

Dissertation
zur Erlangung des Doktorgrades
an der Fakultät für Mathematik, Informatik und Naturwissenschaften
Fachbereich Physik
der Universität Hamburg

vorgelegt von

Arne Christoph Reimers

Hamburg
2019

Gutachter/innen der Dissertation:	Prof. Dr. Johannes Haller
	Prof. Dr. Elisabetta Gallo
Zusammensetzung der Prüfungskommission:	Prof. Dr. Johannes Haller
	Prof. Dr. Elisabetta Gallo
	Prof. Dr. Günter Sigl
	Prof. Dr. Christian Schwanenberger
	Prof. Dr. Peter Schleper
Vorsitzender der Prüfungskommission:	Prof. Dr. Günter Sigl
Datum der Disputation:	26.06.2020
Vorsitzender des Fach-Promotionsausschusses Physik:	Prof. Dr. Günter Sigl
Leiter des Fachbereichs Physik:	Prof. Dr. Wolfgang Hansen
Dekan der Fakultät MIN:	Prof. Dr. Heinrich Graener

Abstract

In this thesis, two searches for new heavy particles with top quarks in the final state are presented. They are based on data recorded by the CMS detector in the years 2016 and 2017, respectively.

In the first part of this thesis, the first search for pair-produced leptoquarks (LQs) decaying to top quarks and muons is presented. Lately, this decay mode has attracted attention because it could contribute to an explanation of the anomalies recently observed in the decay of B mesons and of the anomalous magnetic moment of the muon. The search is based on proton-proton collision data recorded by the CMS experiment in the year 2016 corresponding to an integrated luminosity of $35.9\,\mathrm{fb}^{-1}$. The search is performed in the final state with at least two muons and jets. Events are categorized based on the presence of an additional electron or muon. No excess over the standard model expectation is observed and upper limits on the LQ pair production cross section are derived. Assuming unit branching fraction for the decay $\mathrm{LQ} \to \mathrm{t}\mu$, LQs are excluded below masses of 1420 GeV. In combination with results in the $\mathrm{LQ} \to \mathrm{t}\tau$ and $\mathrm{LQ} \to \mathrm{b}\nu$ decay channels, LQs with masses below 900 GeV are excluded for all possible branching fractions of decays to $\mathrm{t}\mu$ and $\mathrm{t}\tau$ or $\mathrm{b}\nu$. At the High-Luminosity LHC, LQs decaying to $\mathrm{t}\mu$ or $\mathrm{t}\tau$ are expected to be in reach for a discovery at the 5σ level or to be excluded up to masses of 1200 or 1400 GeV, respectively, for all values of the branching fraction.

In the second part of this thesis, simulation-based studies aiming at improving the sensitivity of existing searches of resonant top quark pair production with a novel analysis strategy are presented. The analysis is performed in the final state with exactly one muon and jets for an integrated luminosity of $45.1\,\mathrm{fb}^{-1}$, which corresponds to the dataset recorded by the CMS experiment in the year 2017. A deep-neural-network-based multi-class event classifier is developed. The classification performance and expected sensitivity are compared between a signal-agnostic and signal-specific training of the classifier. The former approach enables reinterpretability of the results and improves the sensitivity especially for low resonance masses. With the latter approach, the expected upper limit on the Kaluza-Klein gluon production cross section is improved by about 50% or more over the whole mass range compared to the 2016 analysis. Such particles are expected to be excluded below masses of 4.30 TeV under the assumption of exclusive decays to $\mathrm{t\bar{t}}$.

Zusammenfassung

In der vorgelegten Arbeit werden zwei Suchen nach neuen schweren Teilchen mit Top Quarks im Endzustand ihres Zerfalls präsentiert. Die Analysen basieren auf Daten, die vom CMS Detektor in den Jahren 2016 beziehungsweise 2017 aufgenommen wurden.

Im ersten Teil dieser Arbeit wird die erste Suche nach paar-produzierten Leptoquarks (LQs), die in Top Quarks und Myonen zerfallen, präsentiert. Dieser Zerfallskanal hat jüngst Aufmerksamkeit auf sich gezogen, weil er zu einer Erklärung der Anomalien, die in Zerfällen von B Mesonen gemessen wurden, und des anomalen magnetischen Moments des Myons beitragen könnte. Der für diese Analyse verwendete Datensatz wurde vom CMS Detektor in Proton-Proton Kollisionen bei einer Schwerpunktsenergie von 13 TeV im Jahr 2016 aufgenommen und entspricht einer integrierten Luminosität von $35.9\,\mathrm{fb}^{-1}$. Ereignisse mit mindestens zwei Myonen und Jets werden analysiert und basierend auf der Präsenz eines zusätzlichen Elektrons oder Myons kategorisiert. Keine Abweichung von der Vorhersage des Standardmodells wird festgestellt und obere Grenzen auf den LQ-Paarproduktionswirkungsquerschnitt werden bestimmt. Unter der Annahme eines Verzweigungsverhältnisses von 1 für den Zerfall $\mathrm{LQ} \to \mathrm{t}\mu$ werden LQs unterhalb einer Masse von 1420 GeV ausgeschlossen. In Kombination mit Ergebnissen in den $\mathrm{LQ} \to \mathrm{t}\tau$ und $\mathrm{LQ} \to \mathrm{b}\nu$ Zerfallskanälen werden LQs mit Massen von weniger als 900 GeV für jede Kombination von Verzweigungsverhältnissen für Zerfälle in $\mathrm{t}\mu$ und $\mathrm{t}\tau$ oder $\mathrm{b}\nu$ ausgeschlossen. Für den High-Luminosity LHC wird erwartet, dass LQs, die in $\mathrm{t}\mu$ oder $\mathrm{t}\tau$ zerfallen, für Massen unterhalb von 1400 oder 1200 GeV ausgeschlossen oder mit einer Signifikanz von 5σ entdeckt werden können.

Im zweiten Teil dieser Arbeit werden simulationsbasierte Studien für die Verbesserung der Sensitivität existierender Suchen nach resonanter Top-Quark Paarproduktion mit einer neuartigen Analysemethode präsentiert. Die Analyse wird im Endzustand mit genau einem Myon und Jets für eine integrierte Luminosität von $41.5\,\mathrm{fb}^{-1}$ durchgeführt, was dem Datensatz, der vom CMS Experiment im Jahr 2017 aufgenommen wurde, entspricht. Klassifikationsalgorithmen, die auf tiefen neuronalen Netzen basieren, werden entwickelt. Deren Leistungsfähigkeit und die erwartete Sensitivität werden für Algorithmen, die mit oder ohne Signalereignisse trainiert wurden, verglichen. Während der erste Ansatz eine Reinterpretation der Ergebisse ermöglicht und die Sensitivität insbesondere für niedrige Massen verbessert, werden die oberen Grenzen auf den Produktionswirkungsquerschnitt von Kaluza-Klein Gluonen um etwa 50% oder mehr im Vergleich zur Analyse des Datensatzes aus 2016 verbessert. Unter der Annahme von Zerfällen in $\mathrm{t}\bar{\mathrm{t}}$ werden solche Teilchen voraussichtlich bis zu Massen von 4.30 TeV ausgeschlossen.

Contents

Chapter 1

Introduction

The standard model (SM) of particle physics is a theory describing all known elementary particles and three of the four fundamental interactions between them. Having been tested to high precision, it is one of the most successful theories to date.

However, the SM is known to be an incomplete theory. For example, the experimental evidence for the existence of dark matter cannot be explained by the SM particle content. Furthermore, the gravitational interaction has not yet been successfully formulated as a quantum field theory (QFT) and is not described by the SM. In addition, there are open questions the SM is unable to explain, for example the remarkable symmetry between the quark and lepton sectors. A plethora of theories has been proposed that extend the SM with the aim of resolving its shortcomings. While deviations from the SM prediction in precision measurements could reveal effects of physics beyond the SM (BSM), it is crucial to probe the validity of such theories in direct searches for new particles.

Hints for the violation of lepton flavor universality, recently measured in the decays of b-flavored mesons, could be explained by the existence of leptoquarks (LQs). LQs are hypothetical new scalar or vector bosons coupling to a quark and a lepton and are predicted by many BSM theories. LQs predicted to exhibit dominant couplings to third-generation quarks and to have masses at the TeV scale could contribute to specific low-energy processes while avoiding flavor-constraints imposed from precision measurements.

Furthermore, many BSM theories predict the existence of new, heavy particles coupled predominantly to third-generation fermions. Such new color-singlet and -octet gauge bosons also appear in models predicting vector LQs. It is the aim of this thesis to search for hints of these particles. Two major contributions are presented in this work.

At the Large Hadron Collider (LHC), the world's most powerful and luminous proton-proton (pp) and heavy-ion collider, searches for LQs have been performed in various final states. No evidence has been found for the existence of LQs coupled exclusively to first-, second-, or third-generation quarks and leptons. However, many BSM models addressing the b-flavor anomalies predict the existence of LQs with large couplings to third-generation quarks and second-generation leptons. Previous searches have not set lower limits on the mass of LQs coupled to top quarks and muons, which could contribute to an explanation of the b-flavor data.

In this thesis, the first search for pair production of LQs decaying to top quarks and muons is presented. Data recorded by the CMS Collaboration in pp collisions at a center-of-mass energy of 13 TeV in the year 2016, corresponding to an integrated luminosity of $35.9\,\mathrm{fb}^{-1}$, are analyzed. The search is carried out in the final state with at least two muons and jets. All possible decay modes of the top quark pair are considered in the event selection. Events are categorized based on the presence of at least one additional electron or muon from the top quark decays. The results of this analysis are combined with those of searches for LQs decaying to top quarks and τ leptons or bottom quarks and neutrinos, respectively. Prospects for the High-Luminosity LHC (HL-LHC) are presented afterwards.

Furthermore, a simulation-based study for the search for new heavy resonances decaying to a pair of top quarks in the final state with one muon and jets is presented. The study is performed for an integrated luminosity of $41.5\,\mathrm{fb}^{-1}$, which corresponds to the dataset recorded by the CMS Collaboration in the year 2017. Improvements to the strategy of the published CMS result based on 2016 data, employing multi-class deep neural network (DNN) event classifiers, are presented.

This thesis is organized as follows: In chapter 2, relevant aspects of the SM in general and pp collisions in particular are discussed. In chapter 3, measurements hinting at the existence of physics beyond the SM are presented and connected to LQs, whose phenomenology is also introduced. Chapter 4 gives an overview over the experimental setup, the LHC and the CMS detector, while in chapter 5, the reconstruction of physics objects in CMS is detailed. The measurement of relative residual jet energy scale corrections is presented in chapter 6. Afterwards, the search for pair-produced LQs coupling to top quarks and muons is discussed in detail in chapter 7. Expected improvements using DNN-based event classification in the context of a search for resonant production of top quark pairs are presented in chapter 8. This thesis ends with a conclusion in chapter 9.

Chapter 2

Physics of the Standard Model

All elementary particles discovered to date, along with three of the four known interactions between them, can be described by the *standard model* of particle physics. It is formulated as a quantum field theory and has been outstandingly successful in making numerous predictions, all of which were later confirmed by experimental data. In this chapter, the basic concept of the SM and its implications for physics at proton-proton colliders is discussed briefly. This chapter is based on information from Refs. [1–3] unless stated otherwise.

2.1 Particles and Forces in the Standard Model

The particles contained in the SM are divided into two groups, *fermions* that have spin 1/2 and *bosons* with integer spin. Fermions are the fundamental constituents of matter, while the bosons are responsible for mediating the interactions between all SM particles. The three forces described in the SM are the strong force, the electromagnetic (EM) force, and the weak force. Gravity, the fourth and last known force, has not yet successfully been expressed as a QFT and is therefore not included in the SM.

Depending on the charges of the fermions, they are further categorized into six *quarks*, which are susceptible to all of the forces mentioned above, and six *leptons*, which do not participate in the strong interaction. While all quarks are electrically charged, leptons can be either charged or neutral. The neutral leptons, *neutrinos*, therefore only interact via the weak force. Additionally, for each fermion in the SM, there is also a corresponding antiparticle with the same quantum numbers except for an opposite-sign electric charge.

The SM bosons have a spin of either 1 (vector boson) or 0 (scalar boson). In contrast to the fermions, vector bosons naturally arise from the theory by postulating invariance

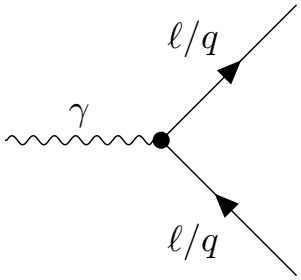

Figure 2.1: Elementary vertex of the EM interaction. The symbol ℓ denotes charged leptons.

of the SM Lagrangian density under local gauge transformations of certain symmetry groups. For each force, such a symmetry group and a corresponding conserved charge can be identified. In the following, the three SM interactions are introduced briefly, followed by a short discussion of the mechanism of electroweak symmetry breaking.

2.1.1 Quantum Electrodynamics

The theory of the electromagnetic interaction is described by Quantum Electrodynamics (QED), which is based on local gauge transformations of the U(1) symmetry group. The charge conserved under such transformations is the electric charge, which, however, will be replaced by the so-called *hypercharge* in the context of electroweak unification (see section 2.1.4). The U(1) group is an Abelian symmetry group that invokes scalar, real phase shifts. The requirement of invariance under U(1) transformations necessitates the insertion of a new vector field A^μ and its interactions with electrically charged particles into the SM Lagrangian density. The gauge field is identified with the photon field mediating the EM interaction. Since scalar phase shifts are commutative, the photon field itself is electrically neutral and does not couple to itself. The elementary QED vertex is shown in figure 2.1.

Given that only fermions can contribute to loop corrections of the photon propagator that affect the EM coupling $\alpha = e^2/4\pi$, with e the electric charge of the electron, the strength of the EM interaction decreases in processes with smaller momentum transfer. Qualitatively, this can be interpreted as the polarized vacuum effectively (partially) shielding the electric charge at high distances. In the limit of vanishing transferred momentum, the EM coupling has a value of $\alpha(q^2 \to 0) \simeq 1/137$ [4]. Consequently, perturbative expansion series in QED converge quickly and yield very precise results already at low orders.

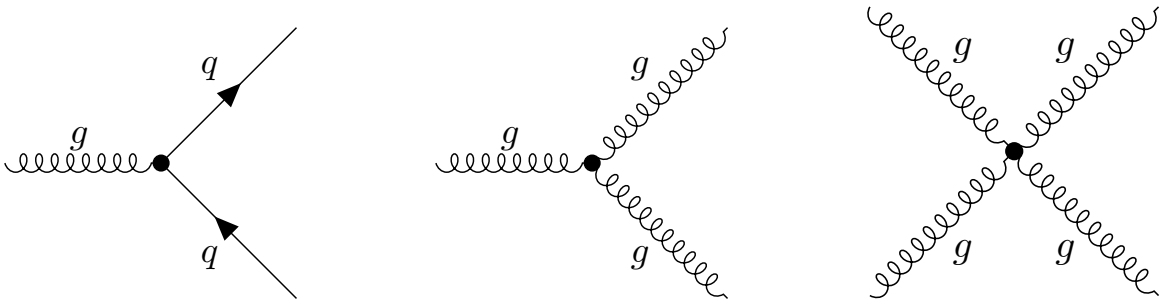

Figure 2.2: Elementary vertices of the strong interaction.

2.1.2 Quantum Chromodynamics

Quantum Chromodynamics (QCD) is the theory of the strong interaction in the SM. Similarly to the approach in QED, invariance of the SM Lagrangian under $\mathrm{SU}(3)_\mathrm{C}$ local gauge transformations is postulated. Here, the subscript C denotes the *color* charge conserved in such interactions. Since $SU(N)$ groups have N^2-1 linearly independent generators, eight generators are needed for SU(3) transformations, represented by non-commutative, Hermitian 3×3 matrices. The number of generators is related to the number of vector bosons mediating the strong interaction, which are eight massless gluons. From the dimension of the generators, it becomes clear that quarks must possess three additional degrees of freedom, which correspond to the three possible color charges.

The Lagrangian density of a free quark is not invariant under local SU(3) transformations. Hence, in order to preserve gauge invariance, new terms must be added to the Lagrangian density. These represent interactions between the quarks and the gluon fields. As a consequence of SU(3) being non-Abelian, self-interactions of the gluon fields are also possible, which leads to the conclusion that gluons themselves are colored particles. The elementary vertices predicted by QCD are shown in figure 2.2. The self-coupling of gluons has important implications for the phenomenology of the strong interaction.

In general, the coupling of any SM interaction depends on the scale (i.e. the transferred momentum q^2) of the process. The value of a coupling therefore depends on the energy scale considered. For the strong interaction, $\alpha_s(M_\mathrm{Z}\simeq 91.2\,\mathrm{GeV}) = 0.1181\pm0.0011$ [4]. Because both spin-1/2 quarks and spin-1 gluons contribute to the vacuum polarization via loop corrections of the gluon propagator, the coupling strength α_s of the strong force increases at large distances or, equivalently, low momentum transfer q^2. Consequently, the potential of the gluon field between two colored particles increases with the distance between the particles due to the self-interaction

of the gluons. If the distance becomes sufficiently large, a new quark-antiquark pair is formed. Ultimately, quarks will always form color-neutral bound states of either a quark-antiquark pair (mesons) or three quarks (baryons) called *hadrons*, and cannot be observed freely. This property is referred to as *color confinement*. As a consequence of color confinement, quarks and gluons produced in highly energetic particle collisions are not measured directly but form collimated sprays of particles, referred to as *jets* (cf. section 5.5).

At scales of $|q| \simeq 1\,\text{GeV}$, α_s becomes too large to perform calculations in perturbation theory, as higher-order terms no longer represent small perturbations. Hence, low-energy processes like the hadronization cannot be calculated analytically but must be modelled phenomenologically. Moreover, the higher-order corrections in QCD typically have a considerable impact and must be taken into account to provide precise predictions.

At high q^2, on the other hand, α_s decreases and enables a perturbative treatment of the strong interaction. The fact that colored particles behave like quasi-free particles at small distances from each other (*asymptotic freedom*) allows to calculate interaction cross sections at hadron colliders to higher orders of perturbation theory.

2.1.3 The Weak Interaction

The third and last interaction described by the SM is the weak interaction, which is based on $\text{SU}(2)_\text{L}$ gauge transformations in a similar way as QCD and QED. This theory can be unified with the EM interaction, which is then called *electroweak unification* (cf. section 2.1.4). The subscript L indicates the fact that the weak charged current (CC) only couples to left-handed particles (and right-handed antiparticles). The corresponding charge for the weak interaction is the *weak isospin*, which is discussed below.

The generators of the non-abelian SU(2) gauge group are three non-commutative, linearly independent Hermitian 2×2 matrices. Similar to the reasoning in section 2.1.2, it can be argued that the fermions participating in the weak interaction must be arranged in isospin doublets. Therefore, the weak isospin T of particles in such a doublet is $T = 1/2$ and its third component is $T_3 = \pm 1/2$.

The famous experiment by C. S. Wu et al. [5] showed that the CC weak interaction violates parity. Formally, this can be explained with the CC weak interaction only coupling to left-handed particles or right-handed antiparticles. Therefore, all of these aforementioned particles are arranged in isospin doublets, while (anti)particles with opposite chirality have $T = 0$ and hence do not participate in the CC weak interaction.

The property of the weak CC only coupling to fermions that are left-handed and arranged in isospin doublets gives rise to the categorization of left-handed quarks and leptons into three isospin doublets, so-called *generations*, containing two particles each. They are grouped as follows:

$$\begin{pmatrix} u \\ d \end{pmatrix}_{\mathrm{L}}, \begin{pmatrix} c \\ s \end{pmatrix}_{\mathrm{L}}, \begin{pmatrix} t \\ b \end{pmatrix}_{\mathrm{L}}, \tag{2.1}$$

$$\begin{pmatrix} \nu_e \\ e \end{pmatrix}_{\mathrm{L}}, \begin{pmatrix} \nu_\mu \\ \mu \end{pmatrix}_{\mathrm{L}}, \begin{pmatrix} \nu_\tau \\ \tau \end{pmatrix}_{\mathrm{L}}. \tag{2.2}$$

The up-type quarks in the upper row of (2.1) are the *up*, *charm*, and *top* quark, carrying an electric charge of $Q = +2/3e$. The down-type quarks in the lower row are the *down*, *strange*, and *bottom* quark with $Q = -1/3e$. Up-type quarks have a weak isospin of $T_3 = +1/2$ while their down-type partners have $T_3 = -1/2$. The leptons in (2.2) are arranged in a similar way. The *electron*-, *muon*-, and *tau*-neutrinos in the upper row are electrically neutral and carry a weak isospin of $T_3 = +1/2$ while the charged leptons (denoted ℓ in the following) in the lower row, the *electron*, *muon*, and *tau*-lepton, have $Q = -e$ and $T_3 = -1/2$.

Requiring invariance of the SM Langrangian under transformations of the $\mathrm{SU(2)_L}$ gauge group leads to the existence of three new spin-1 gauge fields, $\mathrm{W}^\mu_{1,2,3}$, which mediate the weak interaction. The coupling of this interaction is denoted α_W. Two of the three new fields always couple states of different T_3, while the third one mediates interactions only between two particles with identical T_3.

By comparing with experiment, the physical $\mathrm{W}^\pm$ bosons can be identified with linear combinations of $\mathrm{W}^\mu_{1,2}$, such that the $\mathrm{W}^\pm$ bosons mediate transitions from states with $T_3 = +1/2$ to $T_3 = -1/2$ and vice versa. From the charges of the particles in (2.1) and (2.2) it is obvious that these bosons must indeed have an electric charge of $Q = \pm e$. Due to the mixture of vector and axial-vector couplings in their interaction, the weak CC maximally violates parity in the sense that it only couples to isospin doublets and not to singlets. The remaining W^μ_3 field represents the weak neutral current. It is important to note that also the neutral weak current only couples to isospin doublets. The experimentally measured Z boson, however, also couples to isospin singlets. It is obtained from the theory when unifying the weak and the EM interaction (see section 2.1.4).

Measurements of the weak interaction of quarks have shown that the mass eigen-

states given in (2.1) are not simultaneous eigenstates of the weak interaction. The Cabibbo-Kobayashi-Maskawa (CKM) matrix is a unitary matrix relating both eigenstates, where the primed quarks now denote eigenstates of the weak interaction:

$$\begin{pmatrix} d' \\ s' \\ b' \end{pmatrix} = \begin{pmatrix} V_{ud} & V_{us} & V_{ub} \\ V_{cd} & V_{cs} & V_{cb} \\ V_{td} & V_{ts} & V_{tb} \end{pmatrix} \begin{pmatrix} d \\ s \\ b \end{pmatrix}. \tag{2.3}$$

The CKM matrix has four free parameters, three rotation angles and one complex phase, which is responsible for the CP violation in the SM. The values of V_{ij} can be obtained from a global fit to the available measurements of each matrix element while imposing unitarity in all three generations. Their magnitudes were found to be [4]:

$$\begin{pmatrix} V_{ud} & V_{us} & V_{ub} \\ V_{cd} & V_{cs} & V_{cb} \\ V_{td} & V_{ts} & V_{tb} \end{pmatrix} \simeq \begin{pmatrix} 0.974 & 0.225 & 0.004 \\ 0.224 & 0.974 & 0.042 \\ 0.009 & 0.041 & 0.999 \end{pmatrix}. \tag{2.4}$$

Equation (2.4) implies that the probability $|V_{ij}|^2$ for transitions between up- and down-type quarks is highest for transitions within one generation. However, for the first and second generation, there is a non-negligible probability of cross-generational couplings, which is practically negligible in processes involving third-generation quarks.

2.1.4 Electroweak Unification

The unified description of the EM and the weak interactions is based on local transformations of the direct product of gauge groups $\mathrm{SU(2)_L} \times \mathrm{U(1)_Y}$ [6–8]. Here, the subscript Y indicates that the hypercharge (cf. section 2.1.1) is conserved in electroweak interactions.

In analogy to the procedure outlined in section 2.1.1, imposing gauge invariance under $\mathrm{U(1)_Y}$ transformations requires one additional field, called B^μ, which couples to particles with hypercharge. Here, the hypercharge Y and the electric charge Q are not identical, therefore B^μ is not the photon field introduced earlier. To obtain the physically measured photon field A^μ (which couples to the electric charge and is massless) and the Z^μ field , it is necessary to express these two in the basis of W_3^μ and B^μ. They emerge from these fields via a rotation by the weak mixing angle θ_W:

$$\begin{pmatrix} W_3^\mu \\ B^\mu \end{pmatrix} = \begin{pmatrix} \cos\theta_\mathrm{W} & \sin\theta_\mathrm{W} \\ -\sin\theta_\mathrm{W} & \cos\theta_\mathrm{W} \end{pmatrix} \begin{pmatrix} A^\mu \\ Z^\mu \end{pmatrix}. \tag{2.5}$$

The photon field A^μ couples to the electric charge instead of the hypercharge, while the Z boson couples to both isospin doublets and singlets (although with different coupling strengths). The hypercharge can be identified as

$$Y = 2(Q - T_3) \tag{2.6}$$

and the relation between the EM and the weak coupling constants (α and α_W, respectively) is given by

$$\frac{\alpha}{\alpha_\mathrm{W}} = \frac{e^2}{g_\mathrm{W}^2} = \sin^2\theta_\mathrm{W}, \tag{2.7}$$

where g_W denotes the coupling of the $\mathrm{SU(2)_L}$ gauge interaction.

Since the $\mathrm{W}^\pm$ bosons are superpositions only of fields of the $\mathrm{SU(2)_L}$ symmetry, the coupling of the charged weak gauge bosons is identical to α_W. On the other hand, the Z boson is obtained from the transformation in equation (2.5) and contains contributions from both the $\mathrm{U(1)_Y}$ and the $\mathrm{SU(2)_L}$ interaction. Consequently, it couples differently to left- and right-handed particles, which is in agreement with experimental measurements. The coupling of the Z boson is given by

$$g_\mathrm{Z} = \frac{g_\mathrm{W}}{\cos\theta_\mathrm{W}}, \tag{2.8}$$

which is modified differently for fermions of a given chirality, i.e.

$$g_\mathrm{Z}^\mathrm{L,R} = \frac{g_\mathrm{W}}{\cos\theta_\mathrm{W}} \cdot c_\mathrm{L,R}, \tag{2.9}$$

where $c_\mathrm{L} = T_3 - Q \cdot \sin^2\theta_\mathrm{W}$ and $c_\mathrm{R} = -Q \cdot \sin^2\theta_\mathrm{W}$.

From equations (2.7) and (2.8) it becomes apparent that the pure coupling of the weak interaction is larger than the EM coupling. However, weak processes are suppressed with respect to EM ones due to the high masses of the weak gauge bosons of $M_\mathrm{W} = 80.379 \pm 0.012\,\mathrm{GeV}$ and $M_\mathrm{Z} = 91.1976 \pm 0.0021\,\mathrm{GeV}$ [4].

Since the $\mathrm{SU(2)_L}$ group is non-abelian, the weak gauge bosons couple to themselves, allowing interaction vertices involving two, three, and four massive gauge bosons. The fundamental vertices involving massive gauge bosons are shown in figure 2.3. The weak coupling depends on the energy scale considered in a similar way as the strong

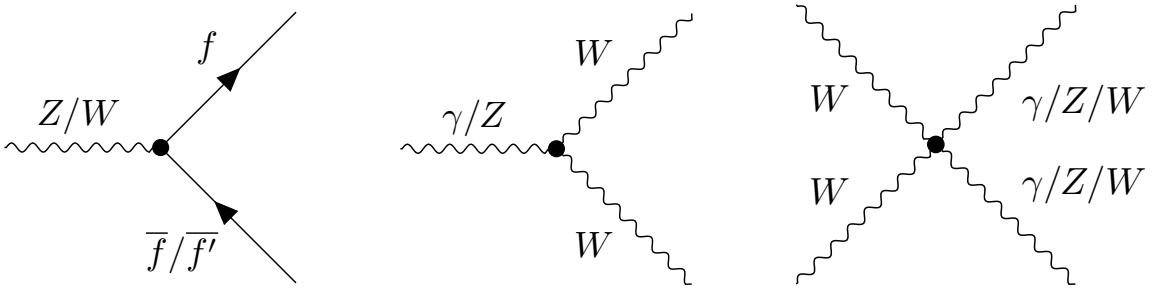

Figure 2.3: Elementary vertices of the electroweak interaction involving massive gauge bosons. The symbol f ($\overline{f}$) represents any (anti)fermion.

coupling in QCD, which is also a non-abelian theory. Both couplings decrease with increasing q^2. This fact is reflected in equation (2.7) by both α and θ_{W} being energy scale dependent.

2.1.5 Electroweak Symmetry Breaking

The previous sections related the interactions in the SM to the requirement of local gauge invariance under the $\mathrm{SU(3)_C \times SU(2)_L \times U(1)_Y}$ symmetry groups. While this provides a sound theoretical basis for describing three of the four known forces, another profound property of particles is in apparent contradiction with this local gauge principle: since explicit mass terms in the SM Lagrangian density would break gauge invariance under any of the SM symmetry groups, all particles would have to be massless. This would be in clear contradiction to experimental data. The mechanism of electroweak symmetry breaking provides a way to incorporate mass terms in the SM Lagrangian density, and is discussed briefly in the following.

In 1964, Brout, Englert, and Higgs postulated the existence of a new complex, scalar field ϕ [9–11] embedded in the electroweak sector of the SM as an $\mathrm{SU(2)_L}$ doublet with hypercharge $Y = 1$,

$$\phi = \begin{pmatrix} \phi^+ \\ \phi^0 \end{pmatrix} = \begin{pmatrix} \phi_1 + i\phi_2 \\ \phi_3 + i\phi_4 \end{pmatrix}, \tag{2.10}$$

and its potential

$$V(\phi) = \mu^2 \phi^\dagger \phi + \lambda (\phi^\dagger \phi)^2, \tag{2.11}$$

where μ and λ are coefficients satisfying $\mu^2 < 0$ and $\lambda > 0$. With this choice of coefficients, the potential has a set of minima at $\phi^\dagger \phi \equiv v^2/2 = -\frac{\mu^2}{2\lambda}$. The parameter v is also

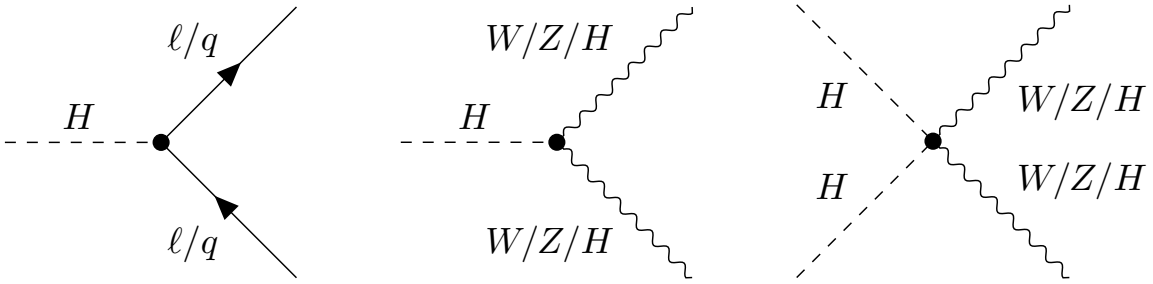

Figure 2.4: Elementary SM vertices involving the Higgs boson.

referred to as *vacuum expectation value*. Because $v \neq 0$, this potential spontaneously breaks the $\mathrm{SU(2)_L \times U(1)_Y}$ symmetry when inserted into the corresponding Lagrangian density.

Since the vacuum is neutral, the ground state ϕ_v in the appropriate gauge taken in this potential can be non-zero only in the neutral component of ϕ. Expanding ϕ around this minimum yields excitations $h(x)$, which are interpreted as the real, massive Higgs boson:

$$\phi(x) = \frac{1}{\sqrt{2}} \begin{pmatrix} 0 \\ v + h(x) \end{pmatrix}. \tag{2.12}$$

The insertion of the potential of this field into the SM Lagrangian density results in a mass term of the Higgs boson, $M_h = \sqrt{-2\mu^2}$, Higgs self-interactions, and interactions of it with the electroweak gauge bosons. The SM vertices involving the Higgs field are presented in figure 2.4. In this way, it is possible to identify mass terms for the electroweak bosons that do not break the gauge symmetry. Instead, their masses are now predicted by the theory to be

$$M_\mathrm{W} = \frac{1}{2} v g_\mathrm{W}, \qquad\qquad M_\mathrm{Z} = \frac{1}{2} v \sqrt{g_\mathrm{W}^2 + g'^2}, \tag{2.13}$$

with $g' = e/\cos\theta_\mathrm{W}$ the coupling of the $\mathrm{U(1)_Y}$ gauge interaction, and are no free parameters any longer. The photon remains massless since the charged component of the Higgs doublet vanishes after spontaneous symmetry breaking. From equation (2.13), v is related to the reduced Fermi coupling constant G_F^0 via

$$v = \frac{\sqrt{2} \cdot M_\mathrm{W}^2}{8 \cdot g_\mathrm{W}^2} = \frac{1}{\sqrt{\sqrt{2} G_\mathrm{F}^0}} \simeq 246\,\mathrm{GeV}. \tag{2.14}$$

Mass terms for fermions can also be inserted into the Lagrangian density using the Higgs mechanism. Similar to the case with gauge bosons, fermions also acquire mass via coupling to the Higgs field. Here, the fermion mass is given by

$$M_{\mathrm{f}_i} = \frac{1}{\sqrt{2}} v y_i, \tag{2.15}$$

where y_i is the Yukawa coupling strength of the Higgs field to a given fermion f_i. These couplings, and therefore also the fermion masses, are not predicted by the theory and remain free parameters of the SM.

2.2 Physics of Proton-Proton Collisions

In order to probe the SM and validate or falsify its predictions, high-energy physics collider experiments have a long history and have provided precise measurements of many of the SM parameters. The most recent collider is the Large Hadron Collider [12], a pp collider at the European Organization for Nuclear Research (CERN). A detailed understanding of the physics of proton-proton collisions is therefore needed to derive predictions from the SM and compare them to the experimental data from the LHC. This section introduces a number of important aspects of pp collisions, and connects the SM predictions to measurements conducted at pp machines.

2.2.1 Proton Structure

Because the proton is not an elementary particle but composed of quarks and gluons, a detailed understanding of its structure is necessary for the understanding of pp collider physics. The proton's primary constituents, so-called *valence quarks*, are two up quarks and one down quark. They are constantly interacting with each other through the exchange of gluons, which themselves also interact with each other. There is a *sea* of other quarks and antiquarks, which are spontaneously created and annihilated in vacuum fluctuations. As a consequence, the momentum of a proton is distributed among its constituents, generally referred to as *partons*. The fraction of the proton momentum carried by a given parton is referred to as Bjorken-x.

Each of the partons has a distinct parton distribution function (PDF), which is the probability density function to find a given parton with momentum fraction x at a given q^2. Since the PDFs depend on q^2 of the process and the value of x, the PDFs can be measured in a multitude of ways, for example in fixed-target experiments, deep inelastic

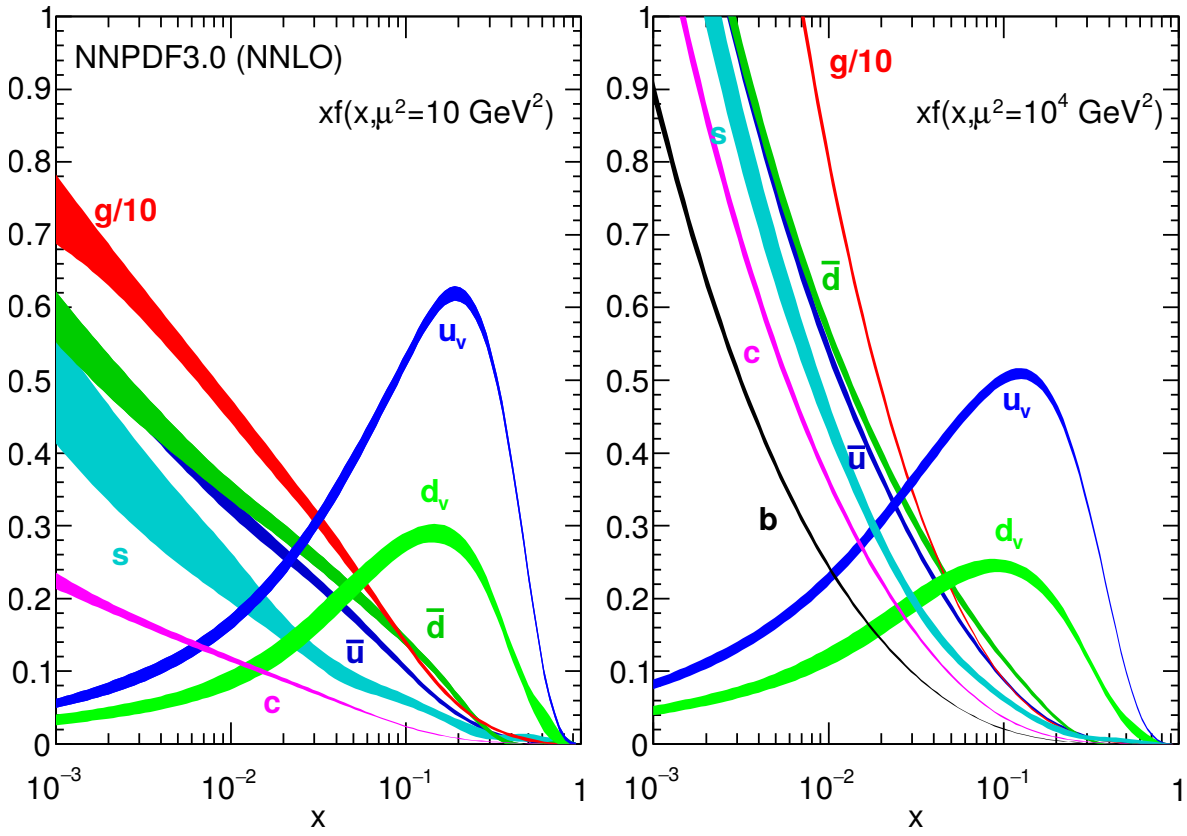

Figure 2.5: Parton distribution functions at NNLO as obtained by the NNPDF Collaboration [16] for $q^2 = 10\,\mathrm{GeV}^2$ (left) and $q^2 = 1000\,\mathrm{GeV}^2$ (right) as a function of x. Taken from Ref. [4].

proton-lepton scattering, and also proton-(anti)proton collisions. Those processes are sensitive to different regions of q^2 and x and provide complementary measurements over a large range of the phase space. Depending on the initial and final state of the interaction, different PDFs can be probed. Parameterizing the dependence of the PDFs on x at a reference scale q_0^2, their scale dependence can be calculated with the DGLAP equations [13–15] to a given order for higher scales $q^2 > q_0^2$, where they can be compared to data. Figure 2.5 shows the PDFs as obtained by the NNPDF Collaboration [16] from a global fit to available measurements at next-to-next-to-leading order (NNLO) for $q^2 = 10\,\mathrm{GeV}^2$ (left) and $q^2 = 1000\,\mathrm{GeV}^2$ (right). At low values of x, processes are mostly induced by gluons and sea quarks, while at high x the proton's valence quarks dominate.

As a consequence of the composite structure of the proton, in pp collisions the center-of-mass system of the colliding partons is Lorentz-boosted in z-direction with respect to the laboratory system. Therefore, the longitudinal component of the momentum is unknown in the initial and in the final state of the pp collision. However,

because the transverse component of the initial state momentum vanishes in good approximation, all transverse momenta measured for the final state particles must originate from the reaction itself and not from a momentum imbalance in the initial state. The transverse momentum (p_{T}) is therefore used frequently in the description of pp collisions.

2.2.2 Cross sections in proton-proton collisions

With the detailed knowledge about the PDFs, and using the theoretical framework of the SM to calculate transition matrix elements, it is possible to predict the cross section for a large number of processes in inelastic pp collisions. According to the factorization theorem [17, 18], it is a convolution of the PDFs f_i and f_j of the two interacting partons, where i and j denote the initial state parton flavors, and the cross section $\hat{\sigma}_{ij}(x_1, x_2, q^2)$ of the hard subprocess, with x_1 and x_2 being the momentum fractions the two partons carry. Integrating over $x_{1,2}$ and summing over the possible parton flavors of a given process yields the expression for the total cross section in pp collisions σ_{pp}:

$$\sigma_{\mathrm{pp}} = \sum_{i,j} \iint dx_1 dx_2 f_i(x_1, q^2) f_j(x_2, q^2) \hat{\sigma}_{ij}(x_1, x_2, q^2). \tag{2.16}$$

The cross section $\sigma_{\mathrm{pp}\to\mathrm{X}}$ for a process $\mathrm{pp} \to \mathrm{X}$ is given by

$$\sigma_{\mathrm{pp}\to\mathrm{X}} = \sum_{i,j} \iint dx_1 dx_2 f_i(x_1, q^2) f_j(x_2, q^2) \hat{\sigma}_{ij\to\mathrm{X}}(x_1, x_2, q^2), \tag{2.17}$$

where $\hat{\sigma}_{ij\to\mathrm{X}}$ denotes the cross section for the hard subprocess $ij \to \mathrm{X}$ and the sum runs over all parton flavors i and j that can participate in a given process.

It is a key task in experimental high-energy physics to probe the SM in as many ways as possible by comparing its predictions to various measurements; any deviation or, even more so, a coherent set of deviations, would hint at BSM physics. Long before they were discovered experimentally, the existence of several particles has been predicted by the SM, such as the electroweak gauge bosons, the top quark, and the Higgs boson. Their later discoveries [19–26] are an outstanding achievement for both experiment and the theory.

Not only has the existence of all particles as predicted by the SM been confirmed experimentally, but also the predicted cross section of various processes in the SM is in agreement with their measurements. Figure 2.6 shows the predicted total production

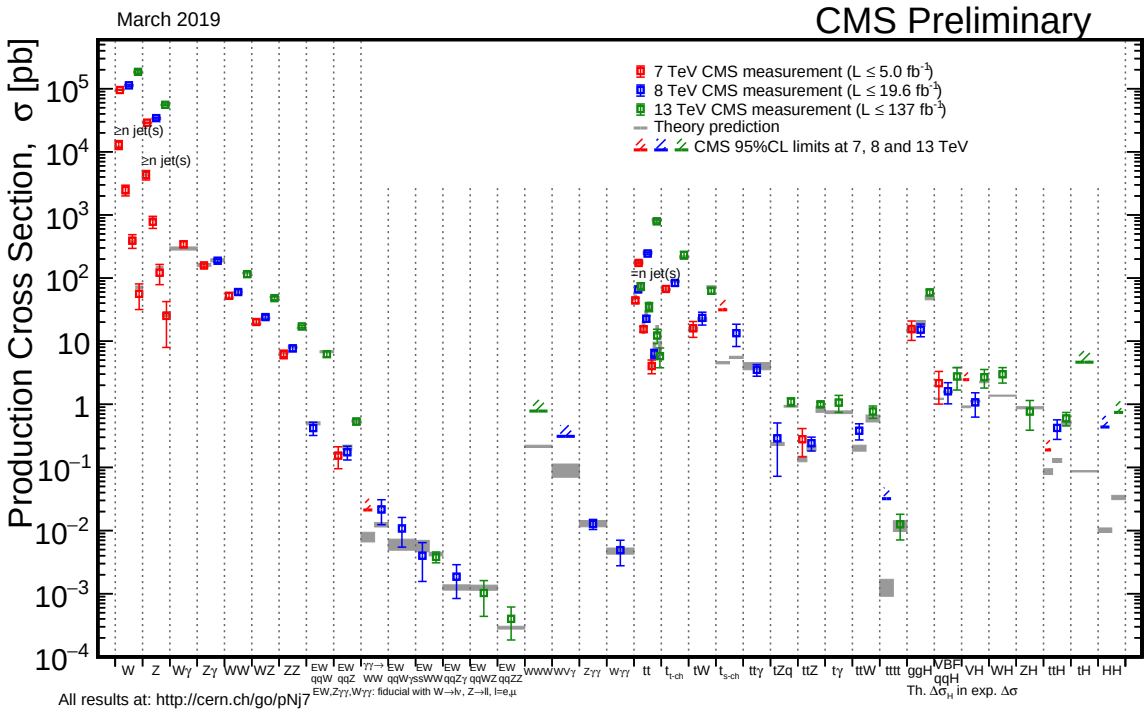

Figure 2.6: Predicted and measured cross sections for a variety of SM processes in pp collisions at center-of-mass energies of $\sqrt{s} = 7$, 8, and 13 TeV. Taken from Ref. [27]

cross sections for a number of SM processes in pp collisions and the corresponding values measured by the CMS Collaboration [27]. Strikingly, the SM has been confirmed by experimental results over nine orders of magnitude in the cross section with various final states.

2.3 Event Simulation

The SM prediction needed for comparison with the experimental data is obtained from simulating events with Monte-Carlo (MC) event generators. These programs sample randomly from given probability densities to generate events according to the SM expectation. The simulation of events is performed in a chain of subsequent steps, which are briefly introduced in the following.

First, the hard interaction of the primary partons is simulated, effectively randomly sampling from the probability densities part of equations (2.16) or (2.17). This includes the choice of the initial-state partons, the evaluation of the respective PDFs, and the generation of the final-state particles according to the partonic interaction cross section. The hard interaction can be simulated by all generators used in the analyses

presented, i.e. POWHEG [28–30], MADGRAPH5_AMC@NLO [31], HERWIG++ [32], and PYTHIA 8 [33, 34].

The probabilistic modelling of showers initiated by the particles in the final state is the second step. Here, they are subject to the emission of further partons, e.g. gluons or photons, from very high energy scales similar to that of the hard interaction down to energies of $\mathcal{O}(1\,\text{GeV})$. At such low scales, colored partons start to hadronize, i.e. form color-neutral states. As detailed in section 2.1.2, processes at those scales must be modelled phenomenologically. In this thesis, the showering and hadronization are simulated with HERWIG++ or PYTHIA 8. If the hard interaction was generated with a different program, the final state particles of the hard process are matched to the parton showers with the FxFx [35] or MLM [36] algorithm in this thesis.

In the third step, activity additional to the hard interaction is modelled. On the one hand, this can be caused by additional parton interactions between the colliding protons that do not contribute to the hard scattering, which is referred to as *underlying event (UE)*. On the other hand, also additional interactions between protons in the same or adjacent bunch crossings, referred to as *pileup (PU)* interactions are simulated. The UE is modelled phenomenologically by measuring UE-sensitive variables in data and tuning a set of parameters such that the prediction agrees with the measured distributions. Such a set of tuned parameters is referred to as *tune*. Both UE and PU are simulated either with HERWIG++ or PYTHIA in this thesis.

Last, all particles produced in the previous steps are passed through a simulation of the Compact Muon Solenoid (CMS) detector in order to predict their interactions with the detector material and the expected electronic signals. The GEANT4 toolkit [37, 38] is used for this purpose in CMS.

Chapter 3

Beyond the Standard Model

Despite the success of the SM describing a multitude of phenomena, there are a number of indicators that the SM is incomplete. These include theoretically motivated arguments concerning certain properties of the SM, as well as experimental evidence for which the SM is unable to provide an explanation. Some examples are briefly introduced in section 3.1. Theories extending the SM are discussed in section 3.2 and leptoquarks are presented in detail in section 3.3.

3.1 Shortcomings of the Standard Model

First of all, the fact that gravity can not be explained by the SM clearly shows that the SM is not a complete theory yet. Related to gravity and its weakness relative to the other three fundamental interactions is the difference between the measured Higgs boson mass and its corrections at different energy scales Λ. While at the electroweak scale the measured Higgs boson mass is approximately 125 GeV, the loop corrections it obtains depend quadratically on the value of Λ considered. If the SM is assumed to be valid up to the Planck scale, $\Lambda_{\text{Planck}} \sim 10^{19}\,\text{GeV}$, where the gravitational interaction is not negligible anymore, the corrections to the Higgs boson mass exceed its measured mass by many orders of magnitude. This behavior is referred to as *hierarchy problem*. In order to keep the measured mass independent of the scale, the individual contributions of the loop corrections need to cancel each other almost exactly, which is considered theoretically unnatural.

Another intriguing property of the SM is the apparent similarity between the quark and lepton sectors. Each contains three generations of left-handed SU(2) doublets that are ordered in mass. Also, the charge of quarks and leptons being multiples of $1/3e$, ultimately making atoms electrically neutral and the universe transparent, is not

predicted by theory but only a fact established experimentally. A similar argument for an underlying connection between the lepton and quark sectors is given by the cancellation of chiral anomalies in the SM, which hints at a relation between the number of color charges and the electric charge of leptons and quarks as well as the number of generations of quarks and leptons.

It is not only the aforementioned arguments, but also various experimental measurements, that indicate that the SM is still an incomplete theory. For example, measurements of the rotational velocity of galaxies point at the existence of dark matter. Candidate particles for dark matter must be massive in order to explain the measurements via their gravitational interaction, and otherwise have only weak interactions with known particles. Neither gravitation nor a suitable dark matter candidate are included in the SM. Furthermore, the SM cannot explain the imbalance between matter and antimatter observed the universe as the CP-violation introduced via the CKM matrix is not sufficiently large. Apart from such missing pieces, experimental data also suggest that certain predictions of the SM might be violated, hinting at the existence of BSM physics.

For example, the measurement of the anomalous magnetic moment of the muon a_μ, one of the most precisely measured quantities in particle physics, is at odds with the SM prediction at a level of about 3.5 standard deviations [39, 40]. It is also an experimentally established fact that the coupling of the weak CC to leptons is equal for all three lepton generations, as opposed to the CKM mixing in the quark sector. Although those couplings are free parameters of the theory, measurements confirmed the lepton flavor universality (LFU) of the weak interaction, for example in measurements of the branching fractions of the τ lepton decay. However, recent measurements in the b-flavor sector show hints for violation of LFU. In section 3.3.4, such measurements and their possible implications are discussed in detail.

3.2 Theories Beyond the Standard Model

In order to resolve the shortcomings discussed above, various extensions to the SM have been proposed. Among them are supersymmetry (SUSY) and Grand Unified Theories (GUTs), as well as compositeness models, all of which will be discussed briefly in the following. However, many more theories of BSM models have been proposed in the literature.

Supersymmetric models [41] introduce a new symmetry between fermions and bosons. A transformation under this symmetry converts fermions into bosons and

vice-versa, leading to the postulation of *superpartners* to the SM particles with the same quantum numbers but a spin differing by 1/2. As no SUSY particles have yet been observed, this symmetry must be broken in order to explain the differences in mass between SUSY and SM particles. The additional corrections of SUSY particles to the Higgs boson mass cancel out the SM contributions and stabilize it at the measured value. To protect baryon and lepton number conservation, many models introduce a multiplicative, conserved, quantum number $R = (-1)^{3(B-L)+2S}$, which is $+1$ for SM particles and -1 for the SUSY partners. In R-parity conserving theories, the lightest supersymmetric particle is stable, making it a potential dark matter candidate.

In compositeness models [42–44] it is assumed that the SM particles are not elementary but instead composed of common elementary constituents. Potential compositeness could manifest itself in excited fermionic states or facilitate transitions between leptons and quarks, therefore directly connecting the lepton and quark sectors. Should the Higgs boson be a composite particle [45–48], its mass would only receive corrections below the scale on which its fundamental constituents are confined, potentially resolving the hierarchy problem.

Furthermore, GUTs [49–51] aim at unifying all three interactions in the SM, similar to the electroweak unification discussed in the previous chapter. In this context, the SM gauge groups are embedded in a higher symmetry group, which is broken below the *GUT scale*, and hence yields the three known interactions at low energies. In such theories, leptons and quarks appear in common multiplets, necessarily relating their electric charges and naturally explaining the apparent symmetry between quarks and leptons in the SM. In higher symmetry groups, a number of new particles is always predicted, like LQs or heavy color-singlet or -octet gauge bosons. Some of the gauge bosons proposed can mediate transitions between states in a multiplet, while others can appear as heavier partners of the SM gauge bosons or fermions. The masses of the new particles are mostly expected to be of a similar order as the GUT scale, but there are models also predicting low-mass manifestations of the additional symmetry at the TeV scale. The first attempts to accomodate the SM in an SU(4) or SU(5) group were made by Pati and Salam [49] and Georgi and Glashow [50], respectively. Although such minimal GUTs have already been excluded by measurements of, for example, the proton lifetime, extensions of these models or even higher symmetry groups are still viable options to be realized in nature.

In figure 3.1, a summary of the results of CMS searches for such new particles with large couplings to heavy SM bosons or third-generation quarks is shown. No evidence for the presence of new particles has been found to date. Among the par-

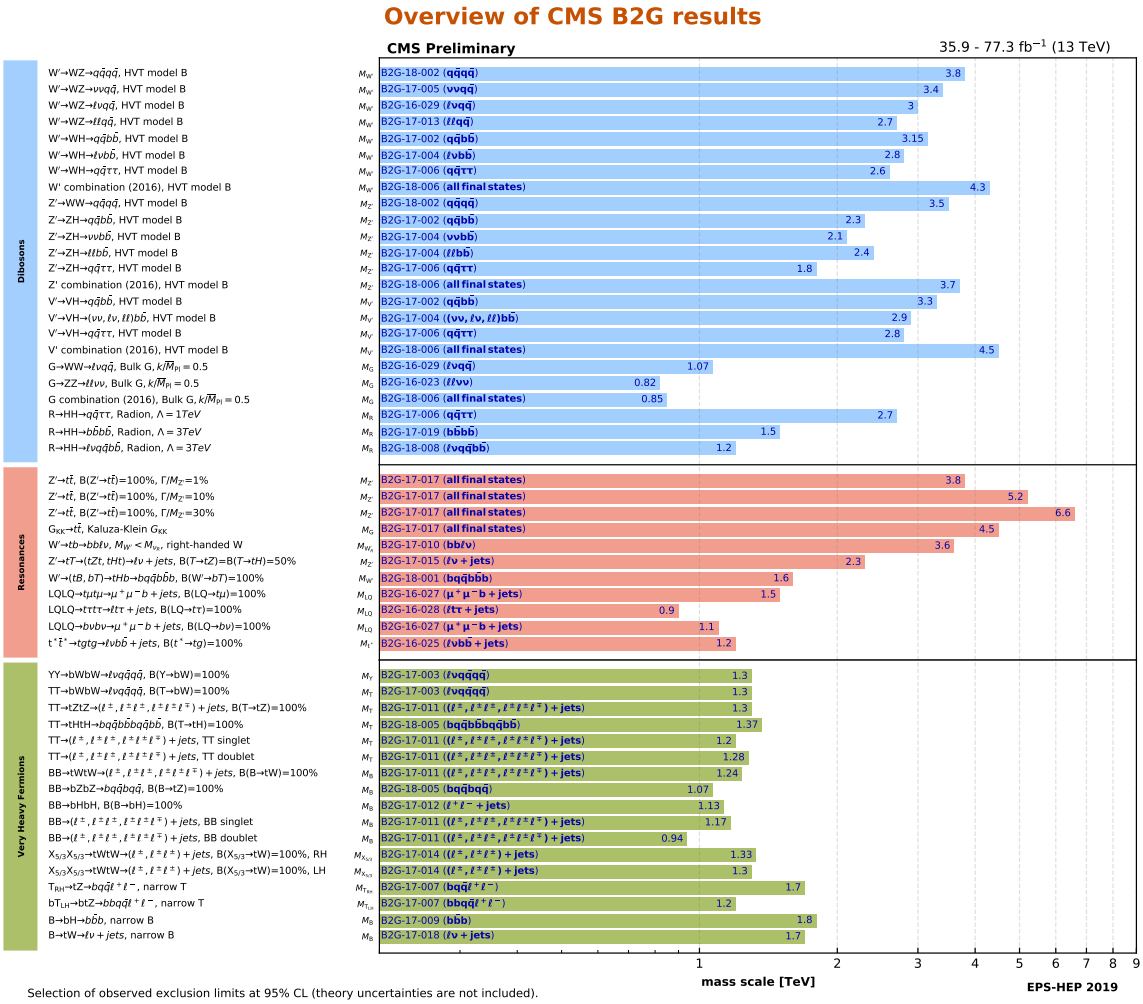

Figure 3.1: Summary of mass exclusion limits placed by various CMS searches for new particles with large couplings to heavy SM bosons or third-generation quarks. Taken from Ref. [52].

ticles predicted are new heavy resonances and leptoquarks, which could decay to SM particles. Resonances with dominant decays to a pair of top quarks are, for instance, predicted by theories that contain pseudoscalar Higgs bosons coupled predominantly to top quarks [53], axigluons [54–56], color-singlet Z′ bosons [57–59], or heavy color-octets [60–63]. Moreover, extensions of the Randall-Sundrum model [64, 65] predict Kaluza-Klein (KK) excitations of the gluon (g_{KK}) [66], which can decay to a top quark pair with a high branching fraction. In this thesis, a search for such a resonance decaying to a pair of top quarks is presented in chapter 8. New, heavy resonances also necessarily appear in BSM models predicting *vector leptoquarks*. Like the LQs, the resonances can arise from higher gauge symmetry groups and have dominant couplings to third-generation fermions [67]. As a search for LQs decaying to top quarks and muons is presented in this thesis (cf. chapter 7), LQs are introduced in detail in the following section.

3.3 Leptoquarks

Leptoquarks are new, hypothetical bosons decaying into a quark and a lepton. They can be either scalar (spin-0) or vector (spin-1) particles carrying both baryon and lepton number, and an electric charge in multiples of $1/3\,e$. Under the assumption that their couplings are dimensionless and invariant under the SM gauge group, the possible quantum numbers of LQs are restricted to those given in the Buchmüller-Rückl-Wyler model [68]. Table 3.1 lists all LQ states in this model together with their quantum numbers and couplings.

In general, LQs arise in many different types of BSM theories, such as GUTs or compositeness models. In the former, they can be identified with the bosons mediating transitions between elements of the fermionic multiplets mentioned before. In the latter, LQs and also the SM fermions appear as composite states of the new, elementary particles and hence naturally could decay to a quark and a lepton. Also in SUSY models that do not conserve R-parity, new particles with simultaneous couplings to quarks and leptons can occur. It is important to note that in all of the above cases, especially in the case of vector LQs, LQs are usually accompanied by other new particles as a consequence of the structure of the theory [67], such as new neutral and charged gauge bosons, heavy quark partners with vector-couplings in the weak interaction, or additional supersymmetric partners of the SM particles.

LQ state	S	$3B+L$	$\mathrm{SU(3)_C}$	$\mathrm{SU(2)_W}$	$\mathrm{U(1)_Y}$	Couplings
$\mathrm{S_1}$	0	-2	$\overline{3}$	1	1/3	$\bar{\mathrm{q}}^{\mathrm{c}}_{\mathrm{L}}\ell_{\mathrm{L}}$ or $\bar{\mathrm{u}}^{\mathrm{c}}_{\mathrm{R}}\mathrm{e}_{\mathrm{R}}$
$\tilde{\mathrm{S}}_1$	0	-2	$\overline{3}$	1	4/3	$\bar{\mathrm{d}}^{\mathrm{c}}_{\mathrm{R}}\mathrm{e}_{\mathrm{R}}$
$\mathrm{S_3}$	0	-2	$\overline{3}$	3	1/3	$\bar{\mathrm{q}}^{\mathrm{c}}_{\mathrm{L}}\ell_{\mathrm{L}}$
$\mathrm{R_2}$	0	0	3	2	7/6	$\bar{\mathrm{q}}_{\mathrm{L}}\mathrm{e}_{\mathrm{R}}$ or $\bar{\mathrm{u}}_{\mathrm{R}}\ell_{\mathrm{L}}$
$\tilde{\mathrm{R}}_2$	0	0	3	2	1/6	$\bar{\mathrm{d}}_{\mathrm{R}}\ell_{\mathrm{L}}$
$\mathrm{V_2}$	1	-2	$\overline{3}$	2	5/6	$\bar{\mathrm{q}}^{\mathrm{c}}_{\mathrm{L}}\gamma^{\mu}\mathrm{e}_{\mathrm{R}}$ or $\bar{\mathrm{d}}^{\mathrm{c}}_{\mathrm{R}}\gamma^{\mu}\ell_{\mathrm{L}}$
$\tilde{\mathrm{V}}_2$	1	-2	$\overline{3}$	2	$-1/6$	$\bar{\mathrm{u}}^{\mathrm{c}}_{\mathrm{R}}\gamma^{\mu}\ell_{\mathrm{L}}$
$\mathrm{U_1}$	1	0	3	1	2/3	$\bar{\mathrm{q}}_{\mathrm{L}}\gamma^{\mu}\ell_{\mathrm{L}}$ or $\bar{\mathrm{d}}_{\mathrm{R}}\gamma^{\mu}\mathrm{e}_{\mathrm{R}}$
$\tilde{\mathrm{U}}_1$	1	0	3	1	5/3	$\bar{\mathrm{u}}_{\mathrm{R}}\gamma^{\mu}\mathrm{e}_{\mathrm{R}}$
$\mathrm{U_3}$	1	0	3	3	2/3	$\bar{\mathrm{q}}_{\mathrm{L}}\gamma^{\mu}\ell_{\mathrm{L}}$

Table 3.1: Possible leptoquark states, their quantum numbers and allowed couplings as given in the Buchmüller-Rückl-Wyler model [68]. The LQ state is named in the first column and the spin and the fermion number given in the second and third column, respectively. The LQ's representation under the SM gauge groups are listed in the fourth to sixth column. The last column shows the allowed couplings. Adapted from Refs. [4, 68].

3.3.1 Constraints on Leptoquarks

Depending on their charge and coupling structure, LQs could in principle decay to any combination of SM fermions, potentially coupling quarks and leptons of different generations. Such couplings could invoke processes that are constrained by precision measurements and hence face indirect bounds. For example, measurements of atomic parity violation or the proton lifetime can constrain LQ couplings to first-generation fermions. A review of indirect constraints on LQs can be found in Ref. [69]. Should LQs couple to more than a single generation of quarks and a (potentially different) single generation of leptons, their interactions generate flavor-changing neutral currents (FCNCs). Since FCNCs are suppressed in the SM, the presence of LQs could be detected in precision measurements, or, conversely, such measurements can hint at LQs if in tension with the SM prediction.

Not only FCNCs but also lepton flavor violation would be invoked by LQs coupling to more than one generation of leptons. For example, $\ell \to \ell'\gamma$ or $\ell \to 3\ell'$ decays would become possible, as shown in figure 3.2. These signatures could also be observable in low-energy precision measurements. To date, no evidence for such lepton flavor violating decays has been observed, setting upper bounds on their branching fraction. The MEG Collaboration has excluded the decay $\mu \to \mathrm{e}\gamma$ for a branching fraction of $\mathcal{B} > 4.2 \times 10^{-13}$ [70], while the τ lepton decays violating lepton flavor are much less constrained [71]. The upper limit on the branching fraction of the $\mu \to 3\mathrm{e}$ transition is

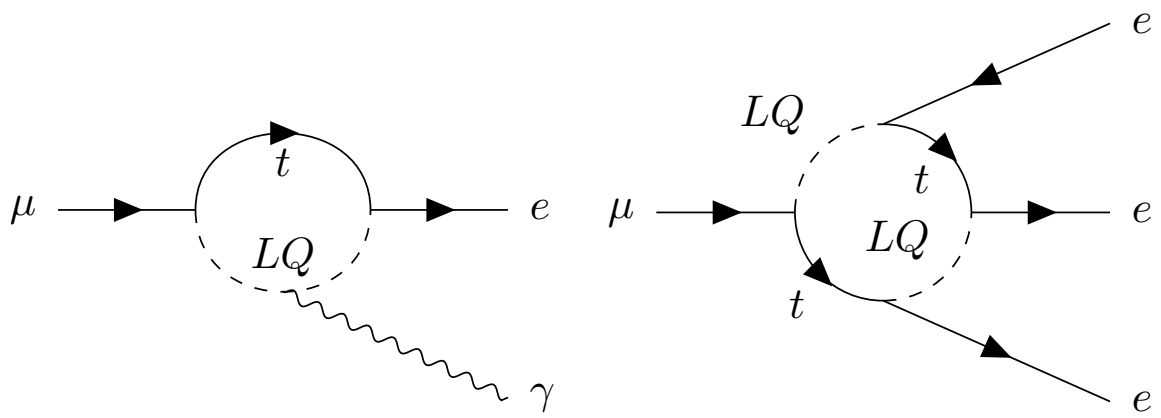

Figure 3.2: Feynman diagrams for the decays $\mu \to e\gamma$ (left) and $\mu \to 3e$ (right) mediated by an LQ coupling to top quarks and muons and electrons.

$\mathcal{B} = 1.0 \times 10^{-12}$ [72]. Again, τ lepton decays have much weaker constraints [4]. Those measurements impose strong constraints on the magnitude and structure of allowed LQ couplings, especially if a given LQ could decay into muons and electrons. Since limits in the τ lepton sector are weaker by several orders of magnitude, an LQ coupling to τ leptons and electrons or muons faces less severe restrictions [73–75].

Direct searches for LQs have been performed by various experiments. A comprehensive overview is given in Ref. [69]. At the HERA electron-proton collider, LQs coupled to first-generation fermions could have been produced in the s-channel, resulting in the most stringent constraints on LQs for $M_{\mathrm{LQ}} < \sqrt{s} \simeq 320\,\mathrm{GeV}$. Couplings to different generations of fermions have been studied as well. At the Tevatron, LQs coupled to all three generations of SM fermions have been sought for. In Ref. [76], a summary of the results of searches for LQs at the HERA and Tevatron colliders is given. No evidence for their existence has been observed and lower limits on their mass have been placed. Also at the LEP e^+e^- collider, searches for LQs have been performed, placing upper limits on the LQ mass of $\mathcal{O}(100 - 200\,\mathrm{GeV})$ in the absence of a deviation from the SM prediction [69].

3.3.2 Leptoquarks at the LHC

In pp collisions at the LHC, LQs can be produced singly or in pairs at the tree-level. Depending on the assumed properties of the leptoquark, one mechanism may be dominant. As in this thesis a search for LQs coupled to top quarks and muons is presented, the discussion in this section is focused on such LQs. For this coupling, pair production is the dominant mechanism in pp collisions. In this thesis, it is assumed that the LQ Yukawa coupling to quarks and leptons is sufficiently large to cause prompt

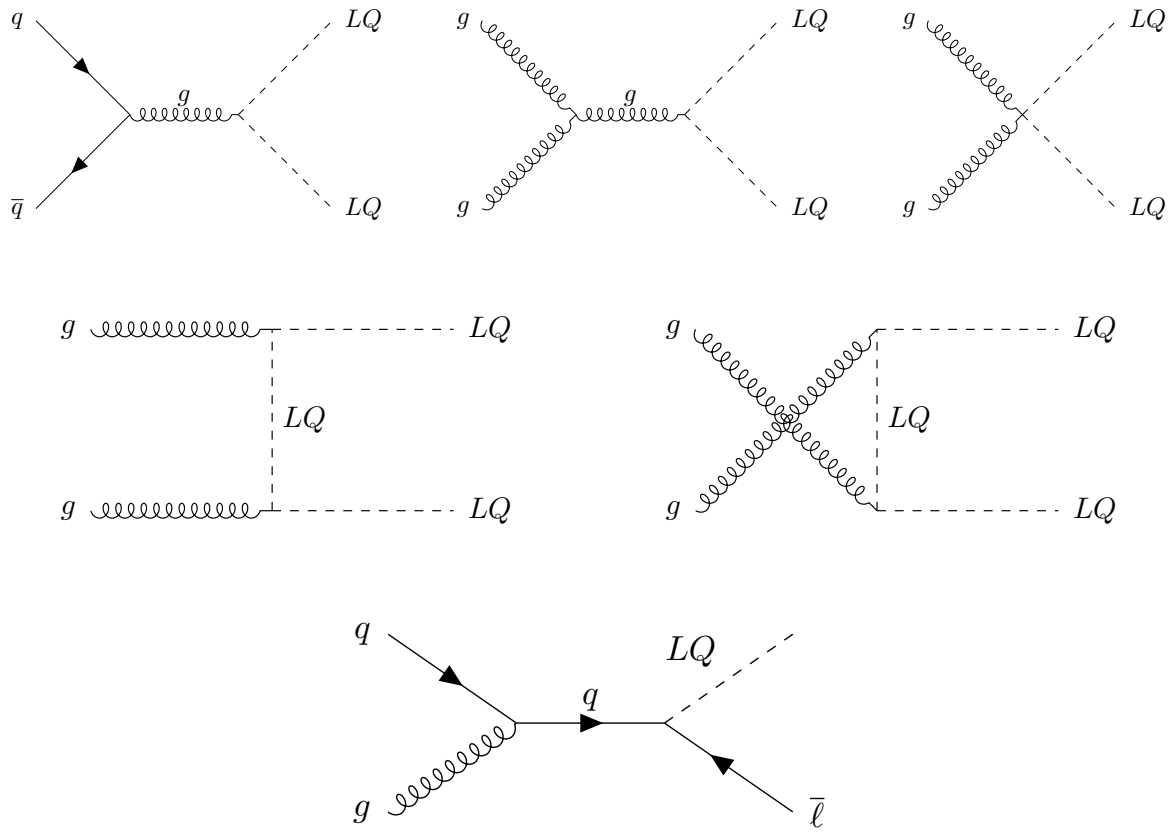

Figure 3.3: Upper and middle row: Leading-order Feynman diagrams of strong LQ pair production. Lower row: Example Feynman diagram of single LQ production at the LHC.

decays of the LQs and avoid bound LQ states.

Pairs of the LQs under consideration here are predominantly produced via gluon-gluon fusion and quark-antiquark annihilation in pp collisions, where the former has the largest contribution at small LQ masses, while the latter is dominant at high masses. The pair production cross section to a good approximation only depends on the LQ mass M_{LQ}, since both processes can be calculated in QCD and do not involve model-specific parameters [77, 78]. The leading-order Feynman diagrams for strong LQ pair production are given in figure 3.3 (upper and middle row). The pair production cross section for scalar LQs is known at next-to-leading order (NLO) precision [77]. The vector LQ pair production cross section is known at leading order (LO) [78] and is a function of one additional, dimensionless parameter κ, which is 1 in the Yang-Mills case and 0 in the minimal coupling case. Figure 3.4 shows the cross section for LQ pair production at a center-of-mass energy $\sqrt{s} = 13\,\mathrm{TeV}$ for scalar and vector LQs, as a function of the LQ mass.

An example Feynman diagram for single LQ production at the LHC is shown in

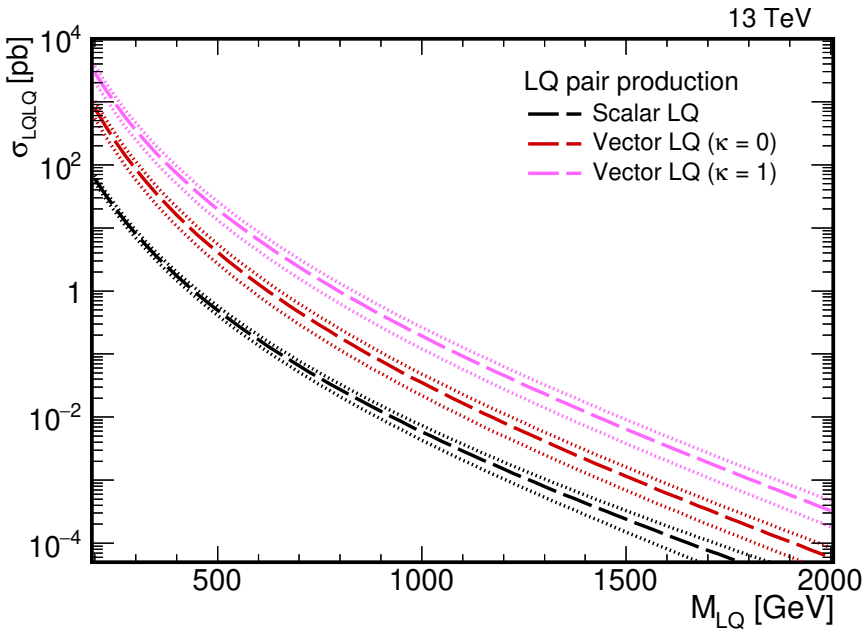

Figure 3.4: Leptoquark pair production cross section in pp collisions of $\sqrt{s} = 13\,\text{TeV}$ of scalar LQs [77] (black) and vector LQs [78] for $\kappa = 0$ (red) and $\kappa = 1$ (magenta) with uncertainties from PDF and scale variations as a function of the LQ mass.

figure 3.3 (lower). Single production of LQs coupled to top quarks and muons is suppressed in pp collisions because this process would require a top quark in the initial state. However, for different LQ couplings, this single production cross section could be sizeable. It depends on the LQ mass and the LQ-quark-lepton coupling λ. Especially for very high M_{LQ}, this process might become enhanced over the pair production cross section at a given center-of-mass energy [78]. The single production channel also provides the opportunity to probe the coupling λ, which is not possible when analyzing LQ pairs.

3.3.3 Status of LHC searches for Leptoquarks

Searches for LQs have been performed in pp collisions at the LHC in multiple final states, targeting a multitude of decay modes. To date, no evidence for the existence of any LQ has been found, and the most stringent direct lower limits on the LQ mass have been set. In table 3.2, the currently highest excluded values of M_{LQ} at the 95% confidence level (CL) for the respective decay channels are presented. Those values have been obtained for scalar LQs, and are higher in the case of vector LQs (cf. section 3.3.2) due to the larger production cross section.

Notably, a large number of potential LQ couplings is covered by experimental

Decay modes	$\mathcal{B}(\mathrm{LQ} \to q\ell)$	Experiment	Lower mass limit [GeV]
qe	1.0	ATLAS [79], CMS [80]	1400, 1435
qe, qν	0.5	ATLAS [79], CMS [80]	1290, 1270
qμ	1.0	ATLAS [79], CMS [81]	1560, 1530
qμ, qν	0.5	ATLAS [79], CMS [81]	1230, 1285
qν	0.0	CMS [82]	980
tμ	1.0	CMS [83]	1420
tτ	1.0	ATLAS [84], CMS [85]	930, 900
tτ, bν	0.5	ATLAS [84], CMS [85]	800, 810
bν	0.0	ATLAS [84], CMS [82]	970, 1100
bτ	1.0	ATLAS [84], CMS [86]	1030, 1020
bτ, tν	0.5	ATLAS [84]	780
tν	0.0	ATLAS [84], CMS [82]	1000, 1020

Table 3.2: Summary of searches for pair-produced scalar LQs at the LHC. The first column denotes the possible LQ decay modes considered in each search, the second line gives the branching fraction $\mathcal{B}(\mathrm{LQ} \to \mathrm{q}\ell) = 1 - \mathcal{B}(\mathrm{LQ} \to \mathrm{q}\nu)$ assumed in each analysis. The third column names the experiment(s) having conducted a search in the respective decay channel, and the last column gives the lower limit(s) on the scalar LQ mass at the 95% CL assuming the branching fraction given in the second column.

searches. This offers the possibility of extending the physical conclusions drawn beyond the case of a single allowed coupling and towards setting constraints on a fully variable composition of branching fractions. Throughout this work, the branching fraction of LQ decays is defined as the probability of an LQ to decay to a quark and a charged lepton, $\mathcal{B} \equiv \mathcal{B}(\mathrm{LQ} \to \mathrm{q}\ell)$ (as opposed to the decay to a quark and a neutrino). Although all limits given in table 3.2 have been obtained in searches for pair-produced LQs, it is worth mentioning the only search for singly-produced LQs at the LHC, which is presented in Ref. [87]. It offers the possibility to constrain the LQ-quark-lepton Yukawa coupling in addition to the LQ mass.

3.3.4 Hints for Lepton Flavor Universality Violation

In the SM, the weak CC couples equally strongly to leptons of all three generations, which is referred to as LFU. Probing the realization of LFU in nature is crucial, since any measured deviation would be a sign of BSM physics. In principle, there are many processes in which LFU violation could be detected. In this section, the results of measurements of branching fraction ratios in decays of B mesons to lighter mesons and leptons are discussed, as measured deviations from the SM prediction hint at the presence of new physics effects, which could be explained by the realization of LQs in

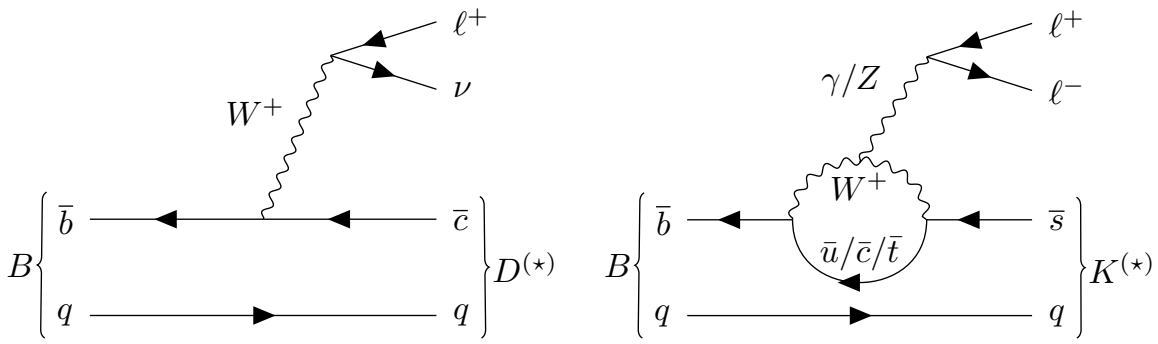

Figure 3.5: Examples of Feynman diagrams for the decay of a B meson to a $\mathrm{D}^{(\star)}$ (left) or $\mathrm{K}^{(\star)}$ (right) meson via a $\mathrm{b} \to \mathrm{c}\ell\nu$ or $\mathrm{b} \to \mathrm{s}\ell\ell$ transition, respectively.

nature.

An observable sensitive to potential LFU violation can, for example, be constructed from the branching fractions $\mathcal{B}$ of B mesons decaying to $\mathrm{D}^{(\star)}$ mesons, a charged lepton, and a neutrino. The B meson decay to a $\mathrm{K}^{(\star)}$ meson and two oppositely-charged leptons is also used for that purpose. The former decay happens via a $\mathrm{b} \to \mathrm{c}\ell\nu$ transition, while in the latter a $\mathrm{b} \to \mathrm{s}\ell\ell$ decay takes place. Example Feynman diagrams of both decays in the SM are shown in figure 3.5. In particular, the ratios $R_{\mathrm{D}^{(\star)}}$ and $R_{\mathrm{K}^{(\star)}}$ of branching fractions, defined as

$$R_{\mathrm{D}^{(\star)}} = \frac{\mathcal{B}(\mathrm{B} \to \mathrm{D}^{(\star)} + \tau + \nu)}{\mathcal{B}(\mathrm{B} \to \mathrm{D}^{(\star)} + \mathrm{e}/\mu + \nu)} \quad \text{and} \quad R_{\mathrm{K}^{(\star)}} = \frac{\mathcal{B}(\mathrm{B} \to \mathrm{K}^{(\star)} + \mu\mu)}{\mathcal{B}(\mathrm{B} \to \mathrm{K}^{(\star)} + \mathrm{ee})}, \tag{3.1}$$

offer the possibility to test the SM predictions with largely cancelled-out hadronic uncertainties, such as form factors, or QCD corrections due to the decay of the $\mathrm{D}^{(\star)}$ meson.

The weak decay of B mesons via $\mathrm{b} \to \mathrm{s}\ell\ell$ transitions happens via FCNCs, which are suppressed in the SM. Because the cross section for such processes is very small, these decays are especially sensitive to contributions from hypothetical new particles predicted in BSM theories. The value of $R_{\mathrm{D}^{(\star)}}$ has been measured by the BaBar [89, 90], Belle [91–94], and LHCb Collaborations [95–97]. Considering the measurements in Refs. [89–93, 95, 96], the combined statistical significance of the deviation from the SM prediction amounts to 4.1 standard deviations [4, 98]. However, taking into account the most recent measurements presented in Ref. [97] by the LHCb Collaboration and Ref. [94] by the Belle Collaboration, the statistical significance is reduced to about 3.1 standard deviations [88]. The combined measurements as well as the SM prediction for $R_{\mathrm{D}^{(\star)}}$ are shown in figure 3.6.

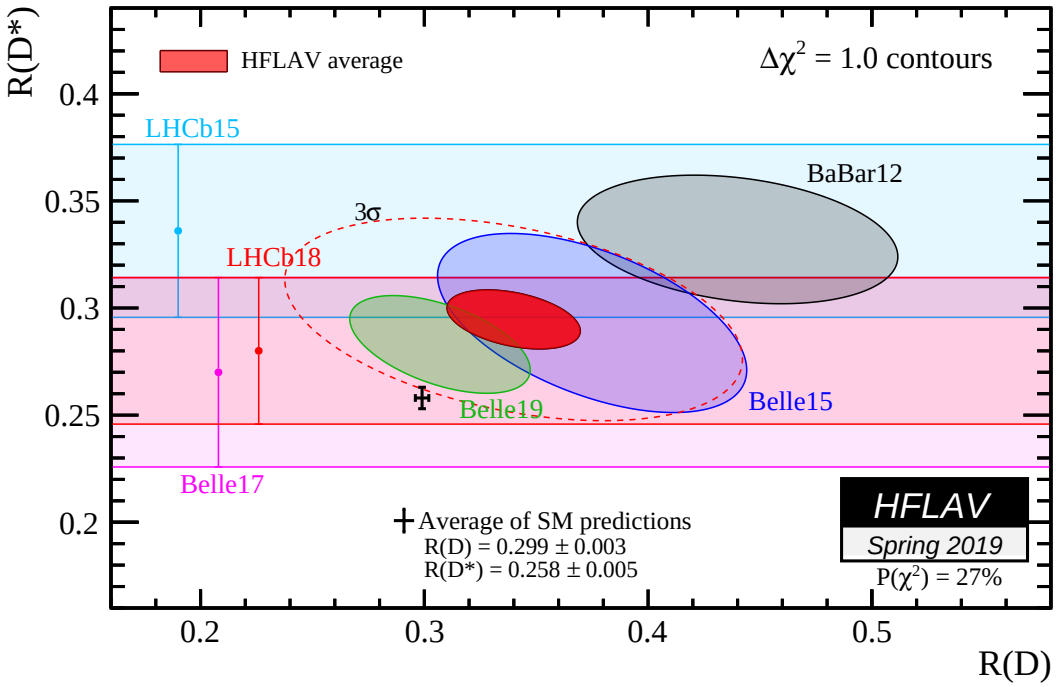

Figure 3.6: Measurements of $R_{D^{(\star)}}$ by the BaBar, Belle, and LHCb Collaborations and their average together with the SM prediction. Taken from Ref. [88].

Furthermore, a measurement of the $R_{K^{(\star)}}$ variable probes the validity of LFU, in particular because the SM prediction, $R_{K^{(\star)}} = 1.00 \pm \mathcal{O}(10^{-2})$ [99], when considering values of q^2 sufficiently greater than zero (i.e., in a regime to mediate the $b \to s\mu\mu$ transition well above its kinematic threshold), has very small uncertainties that arise from the different masses of electrons and muons, as well as from QED higher-order corrections [99]. The most recent measurements of $R_{K^{(\star)}}$ have been performed by the LHCb [100, 101] and Belle [102, 103] Collaborations. The LHCb results show a departure from the SM prediction by 2.1–2.5 standard deviations, depending on the decay mode and value of q^2 considered; however, the Belle measurements in the respective bins of q^2 are compatible with both, the SM expectation and the values measured by LHCb.

Considered together, the results presented above hint at LFU violation potentially being realized in nature. Once investigated further, they offer a possibility to probe the SM and potentially find conclusive evidence for physics beyond the SM. It would be appealing from a theoretical point of view if all of those anomalies could be simultaneously explained by a single BSM theory. Indeed, many models focus on explaining the experimental data by postulating the existence of LQs [74, 104–122], which are

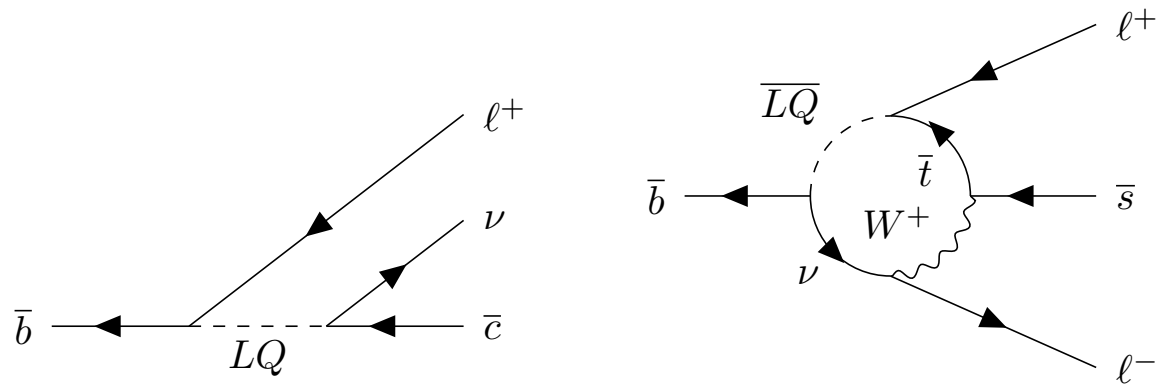

Figure 3.7: Hypothetical LQ contributions to $b \to c\ell\nu$ (left) or $b \to s\ell\ell$ (right) transitions.

excellent candidate particles due to their simultaneous couplings to quarks and leptons, and whose contribution to the decay of B mesons could explain the measured data. Owing to the nature of the anomalies, LQs with masses at the TeV scale and enhanced couplings to third-generation quarks are preferred by those models. LQs with such couplings are generally able to comply with the indirect bounds discussed in section 3.3.1. A combined explanation of the deviations measured in $R_{D^{(\star)}}$ and $R_{K^{(\star)}}$ is possible by postulating at least a single vector LQ or at least two scalar LQs [123] at the TeV scale.

The Feynman diagrams in figure 3.7 show possible LQ contributions to the $b \to c\ell\nu$ and $b \to s\ell\ell$ transitions. In this thesis, a search for LQs decaying to top quarks and muons is presented. Such LQs would be an appealing explanation for the tension in the $R_{K^{(\star)}}$ variable and/or the muon's anomalous magnetic moment [74, 110–115]. LQs with simultaneous couplings to top quarks and muons as well as bottom quarks and neutrinos could, for example, invoke the decay modes shown in figure 3.7 (right).

In order to gain sensitivity to LQ models focusing on $R_{D^{(\star)}}$ and provide results in a larger area of LQ coupling space, this search will be combined with results of LQ searches in the $t\tau$ and $b\nu$ decay channels. Since most models predict a number of different possible decays, simultaneous sensitivity to such decay modes of an LQ with a charge of $-1/3e$ involving third-generation quarks is obtained, where such couplings are particularly important to explain $R_{D^{(\star)}}$, $R_{K^{(\star)}}$, and the anomalous magnetic moment of the muon. While this analysis is also sensitive to LQs with other electric charges, the results will only be interpreted in this context. Closing the important gap of the $t\mu$ decay mode allows to constrain dedicated models in many of their predicted final states, and enables re-interpretation with varied predicted branching fractions.

Chapter 4

Experimental Setup

The work presented in this thesis is based on pp collision data recorded with the CMS detector at the LHC in the years 2016 and 2017. This chapter summarizes the experimental setup by introducing the LHC in the first section and giving an overview over the CMS detector afterwards.

4.1 The Large Hadron Collider

The LHC [12, 124] is the worlds most powerful particle collider situated at CERN in Switzerland. It is located in an underground tunnel that previously hosted the Large Electron-Positron (LEP) Collider with a circumference of 26.7 km. The LHC machine is designed to collide protons and also heavy lead ions. In the following, the pp operational mode is detailed.

The protons used for the LHC operation are obtained from ionizing hydrogen molecules. Before being injected into the LHC, they are accelerated in a chain of pre-accelerators available at the CERN site, which is shown schematically in figure 4.1. First, protons pass several linear accelerators and the Proton Synchrotron Booster. Afterwards, they enter the Proton Synchrotron and finally, in the Super Proton Synchrotron, they are accelerated to an energy of 450 GeV, with which they are injected into the LHC in two counterrotating beams. The LHC is designed to accelerate protons up to energies of 7 TeV, leading to a maximum center-of-mass energy of $\sqrt{s} = 14\,\text{TeV}$. To date, the LHC delivered pp collisions of three different center-of-mass energies. In 2010-2011, 2012, and 2015-2018 values of $\sqrt{s}$ of 7, 8, and 13 TeV were achieved. In the future, also the nominal value of $\sqrt{s} = 14\,\text{TeV}$ is targeted.

The two proton beams are brought to collision in four nominal interaction points, at each of which one detector is placed to record the particles produced. The main LHC

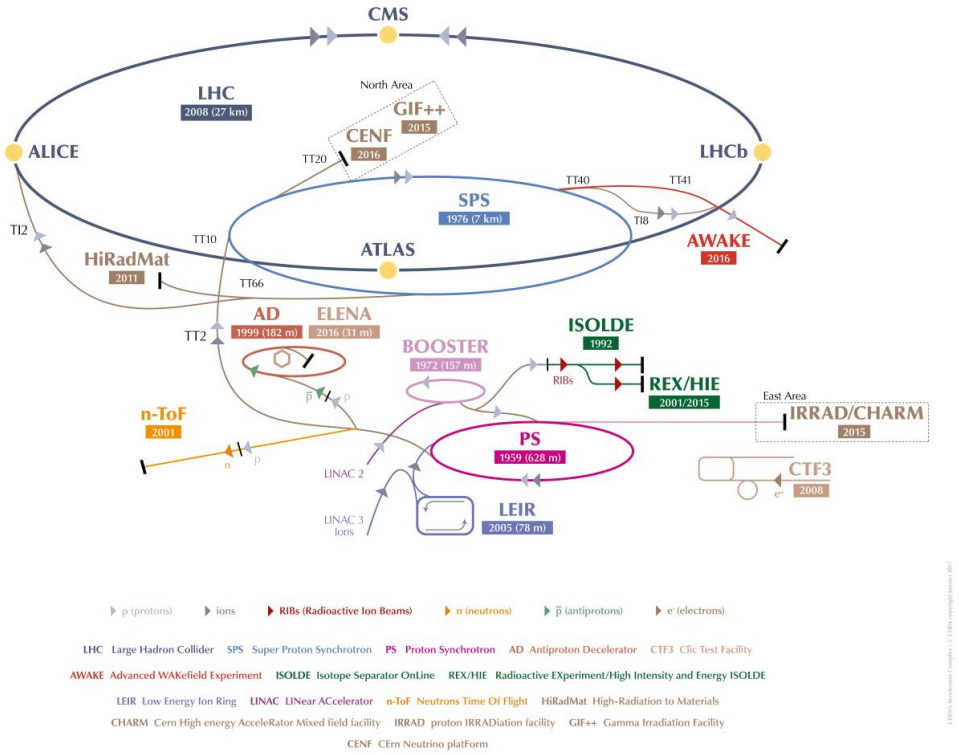

Figure 4.1: Schematic view of the CERN accelerator complex. Taken from Ref. [125].

experiments are ATLAS (A Toroidal LHC Apparatus), CMS, LHCb (Large Hadron Collider beauty), and ALICE (A Large Ion Collider Experiment). The former two use multipurpose detectors for a broad spectrum of physics analyses including precision measurements of SM processes, the discovery of the Higgs boson and subsequent analysis of its properties, and searches for BSM physics. The LHCb experiment focuses on measurements of B meson physics (see section 3.3.4), and the ALICE experiment is devoted to studying the quark-gluon-plasma created when colliding heavy ions.

Not only the high achievable collision energy but also the large instantaneous luminosity $\mathcal{L}$ is a key advantage of hadron colliders over their pendants colliding electrons. It is a measure of the number of pp interactions per time and unit cross section and defined as

$$\mathcal{L} = N_\mathrm{b} f_\mathrm{rev} \frac{n_1 n_2}{4\pi\sigma_x\sigma_y}, \tag{4.1}$$

where N_b is the number of colliding bunches in each proton beam, f_rev the proton revolution frequency, n_i the number of protons in a bunch, and $\sigma_{x,y}$ the effective beam widths transverse to the direction of flight. The LHC is designed to operate at an

instantaneous luminosity of $\mathcal{L} = 10^{34}\,\mathrm{s}^{-1}\mathrm{cm}^{-2}$, which requires the machine parameters in equation (4.1) to be $N_\mathrm{b} = 2080$, $f_\mathrm{rev} = 11.25\,\mathrm{kHz}$, and $n_1 = n_2 = 1.15 \cdot 10^{11}$. The luminosity can be varied by changing the denominator of equation (4.1) via adjusting the beam width and the angle under which the protons are collided. The highest value of $\mathcal{L}$ the LHC achieved so far, $\mathcal{L}_\mathrm{max} = 2.14 \cdot 10^{34}\,\mathrm{s}^{-1}\mathrm{cm}^{-2}$, was reached in the year 2018 and exceeded the design value by more than a factor of 2.

According to the definition of $\mathcal{L}$, a measure for the number of pp collisions collected in a given time interval is given by the *integrated luminosity* L, which is defined as the time integral over the instantaneous luminosity,

$$L = \int \mathcal{L}\,\mathrm{d}t. \tag{4.2}$$

The integrated luminosity delivered by the LHC at the CMS interaction point in the years 2010 – 2018 is shown in figure 4.2. The number of events N of a process with a given cross-section σ expected to have taken place is related to the integrated luminosity of a dataset via the expression

$$N = \sigma \cdot L. \tag{4.3}$$

4.2 The Compact Muon Solenoid Detector

The CMS detector is one of the two multipurpose detectors at the LHC. It is 21.6 m long and has a diameter of 14.6 m. The layout of the CMS detector is shown schematically in figure 4.3. It is symmetric around the beam pipe and consists of a *barrel* and two *endcaps*, respectively covering the central and the forward and backward regions. In total, coverage of almost the full solid angle is achieved.

In order to identify all particles produced in pp and lead-lead collisions and measure their trajectories, charge, momentum, and energy with excellent precision, the CMS detector consists of several sub-systems, each serving a distinct purpose. Combining information from all of those systems allows to achieve the best performance. The core of the CMS detector is a superconducting solenoid magnet providing a homogeneous magnetic field of up to 4 T along the beam axis. Inside the solenoid, closest to the nominal interaction point, the tracking system followed by the calorimeters is located, while the muon chambers are placed outside.

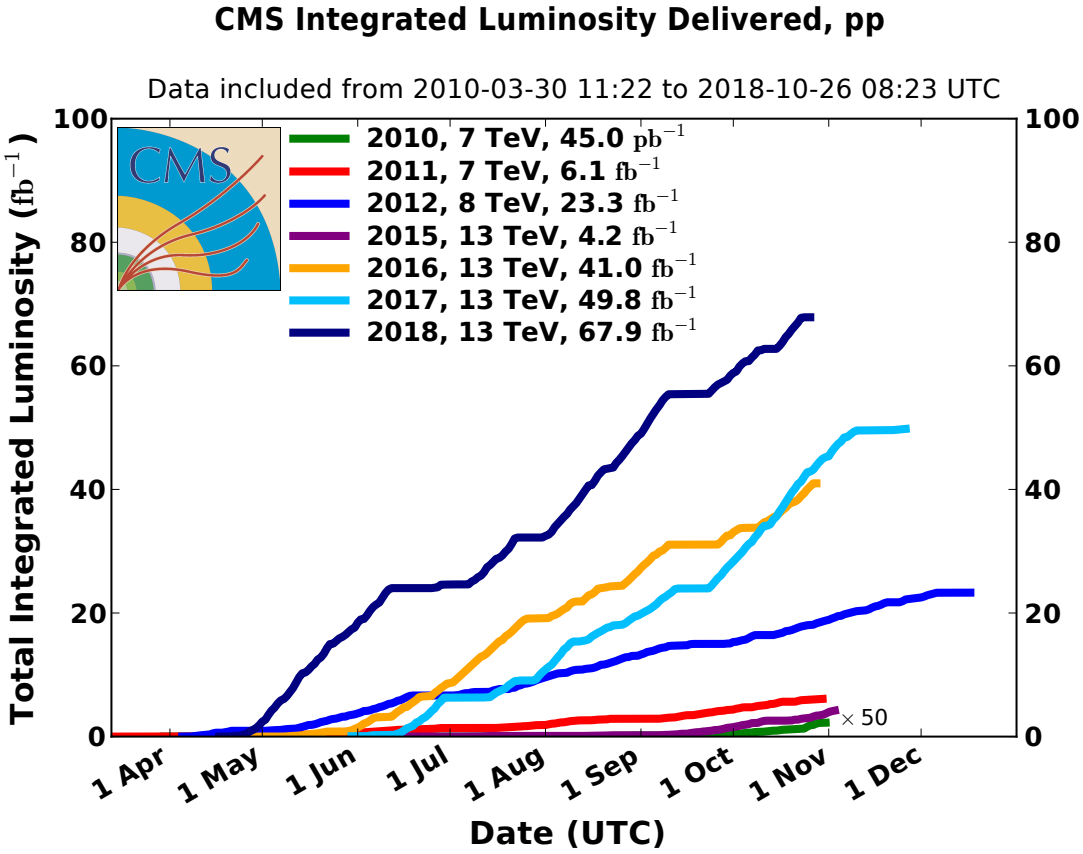

Figure 4.2: Integrated luminosity delivered by the LHC at the CMS interaction point in the years from 2010 to 2018 as a function of time. Taken from Ref. [126].

In this section, first the coordinate conventions used in CMS are introduced, followed by a detailed description of each detector component. The information in this section is obtained from Refs. [127, 128] unless stated otherwise.

4.2.1 The Coordinate System

For the CMS detector, a right-handed cartesian coordinate system is used. It originates in the nominal interaction point and center of the detector. The x-axis points towards the center of the LHC ring, the y-axis upwards, and the z–axis in counterclockwise direction along the beam axis. However, due to the angular dependencies of pp collisions and the detector geometry, it is most useful to use the radial distance r from the z–axis and two angles ϕ and θ instead of cartesian coordinates. The azimuthal angle ϕ is defined as the angle in the $x-y$–plane enclosed with the x-axis. The polar angle θ is defined as the angle enclosed with the z–axis. Because in pp collisions the initial-state momentum in z–direction is unknown, the coordinates used must be invariant

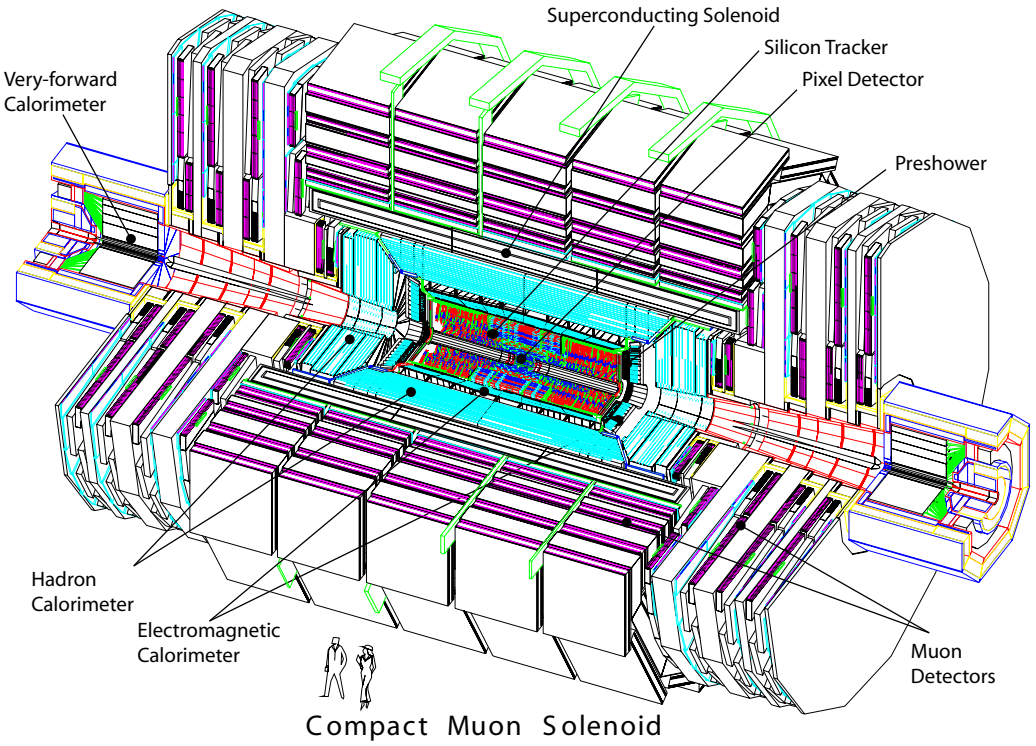

Figure 4.3: Schematic view of the CMS detector. Taken from Ref. [127].

under Lorentz-transformations along the beam axis. With r and ϕ already meeting this requirement, the pseudo-rapidity η is used instead of θ. It is defined as

$$\eta = -\ln\left(\tan\frac{\theta}{2}\right), \tag{4.4}$$

making differences in η invariant under Lorentz-boosts along the z–axis. The angular distance ΔR between two objects in the CMS detector is then defined as

$$\Delta R = \sqrt{(\Delta\phi)^2 + (\Delta\eta)^2} \tag{4.5}$$

and is also invariant under Lorentz-transformations in z–direction.

4.2.2 The Tracking System

The tracking system is the innermost component of the CMS detector, directly surrounding the interaction point. It is used to reconstruct the trajectory of charged particles produced in the collisions and hence facilitates the measurement of the charge-sign

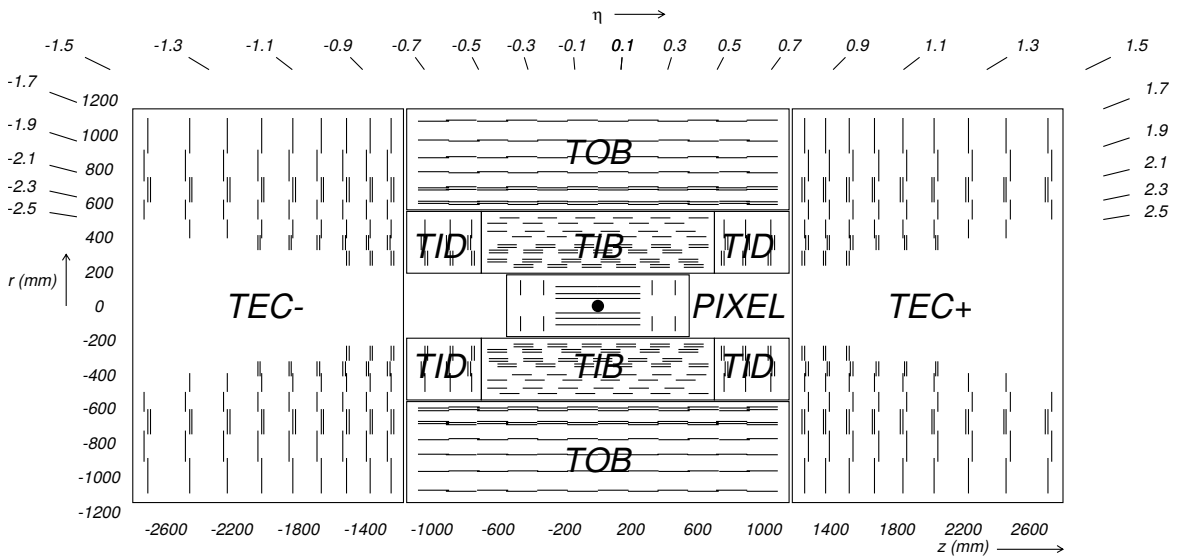

Figure 4.4: Layout of the CMS tracking system. Taken from Ref. [128].

and momentum of such particles as well as the identification of primary and secondary vertices. The tracker has a length of about 5.8 m, covers the region of $|\eta| < 2.5$, and consists of layers of two different silicon detectors, pixel and strip sensors. The layout of the tracking system is shown in figure 4.4.

The pixel detector is located closest to the beam axis and employs pixels of $100 \times 150\,\mu\text{m}^2$ size. In the 2016 data-taking period, it was made from three barrel layers at 4.4, 7.3, and 10.2 cm distance from the beam and two layers in each endcap, located at distances of 34.5 and 46.5 cm from the interaction point. In the technical stop before the 2017 data-taking period, the pixel detector was upgraded [129] and since then contains four barrel layers at $r = 3.0$, 6.8, 10.2, and 16.0 cm as well as three layers per endcap, at a z–distance of 29.1, 39.6, and 51.6 cm from the interaction point. The aim of the upgraded pixel system is to ensure a performance equally good or better in an LHC operational mode with a much higher instantaneous luminosity, and hence a much higher particle density in the tracker.

The strip tracker surrounds the pixel detector and consists of silicon strips grouped in two parts in the barrel, the *Tracker Inner Barrel* (TIB) and *Tracker Outer Barrel* (TOB). The TIB contains four layers of strip sensors of 320 μm thickness with a pitch of between 80 and 120 μm and covers the region of $|z| < 65$ cm. The TIB is followed by the TOB, which uses strips with an increased thickness and pitch of 500 μm and 120–180 μm, respectively. The TOB covers the area up to $|z| = 110$ cm. In the endcaps, the *Tracker Inner Disc* (TID) and *Tracker End Cap* (TEC) contain three and nine layers of strip sensors, respectively. As in the barrel, the TID uses thinner strips of

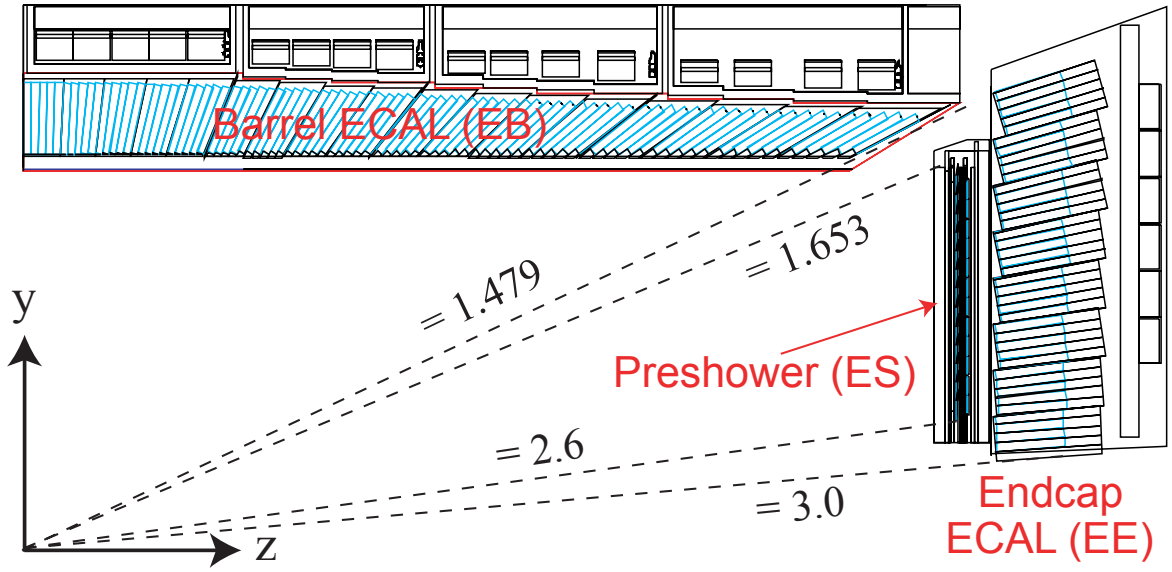

Figure 4.5: Schematic view of the CMS ECAL. Taken from Ref. [127].

320 μm thickness, while in the TEC 500 μm thick strips are used. Complementing the barrel detectors, the TEC covers the region of 120 cm $< |z| <$ 280 cm.

4.2.3 The Electromagnetic Calorimeter

The electromagnetic calorimeter (ECAL) surrounds the tracking system and aims at measuring the energy of mainly electrons and photons with highest precision. It is a hermetic, homogeneous calorimeter made of scintillating lead-tungstate ($PbWO_4$) crystals. 80% of the scintillation light is emitted within the bunch spacing time of 25 ns. In the design of the ECAL, a solution had to be found that allowed it to be placed inside the solenoid coil while still fully absorbing the energy of particles of interest. The choice of $PbWO_4$ is motivated by its short radiation length of $X_0 = 0.89$ cm and small Molière radius of 2.2 cm. This allows for the very compact yet highly granular construction of the ECAL. Similar to the tracker, also the ECAL is divided in a barrel (EB) and two endcap (EE) parts. A schematic view of the ECAL is presented in figure 4.5.

In the EB, which has an inner radius of 129 cm and extends up to $|\eta| < 1.479$, crystals with a front-face cross section of $22 \times 22\,\text{mm}^2$ and a length of 230 mm are used. The EE is made of crystals with front-face cross sections of $28.6 \times 28.6\,\text{mm}^2$ and lengths of 230 mm. It is placed at 314 cm distance from the interaction point along the beam pipe and covers the pseudorapidity region of $1.479 < |\eta| < 3.0$.

The CMS ECAL has an excellent energy resolution, which has been measured for

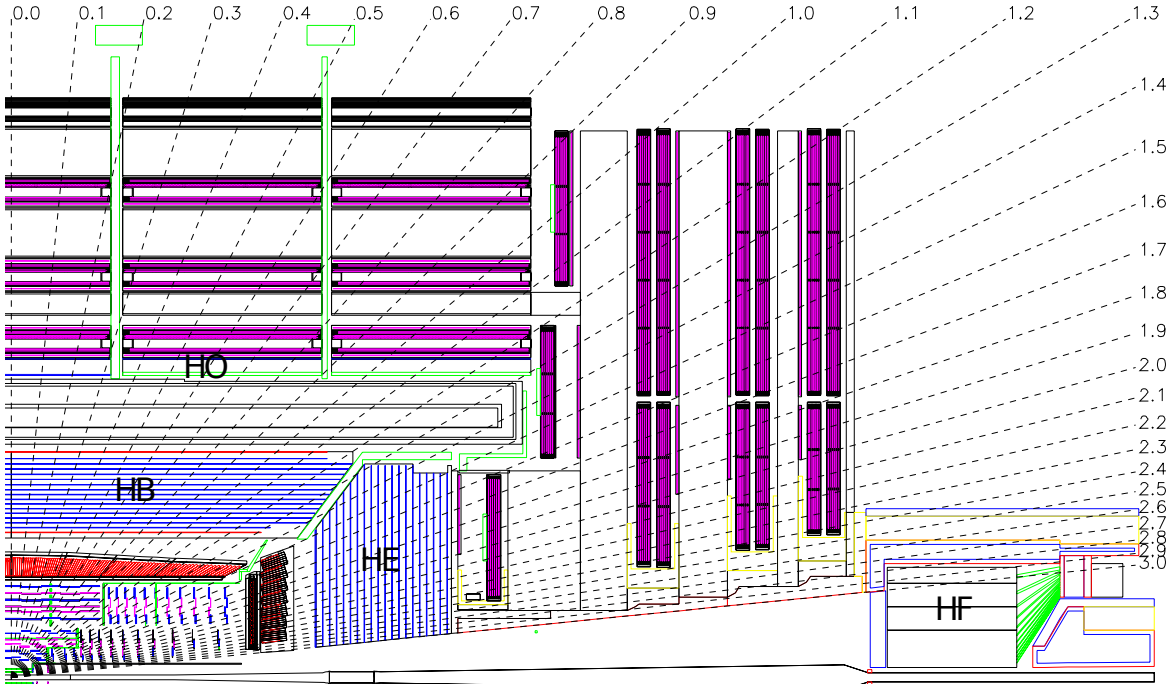

Figure 4.6: Schematic view of the CMS HCAL. Taken from Ref. [128].

electrons of varying incident energies. It can be parameterized as follows [128]:

$$\frac{\sigma_E}{E} = \frac{2.8\%}{\sqrt{E/\mathrm{GeV}}} \oplus \frac{12\%}{E/\mathrm{GeV}} \oplus 0.3\%. \tag{4.6}$$

Here, the first term takes into account stochastic effects from the shower development in the ECAL, the second term describes electronic noise, and the last term accounts for calibration errors and non-uniform light collection.

4.2.4 The Hadronic Calorimeter

The CMS hadronic calorimeter (HCAL) encloses the tracker and the ECAL, being the last detector component inside the magnetic field. Its purpose is measuring the energy of hadrons, which have a much larger typical interaction length λ_I than electrons and photons, and hence traverse the ECAL. For this reason, the HCAL was built as a sampling calorimeter consisting of alternating layers of brass absorber and plastic scintillator tiles. Its structure is shown in figure 4.6.

There are four different parts of the HCAL, two in the barrel and two in the forward region of the detector. The Hadron Barrel (HB) contains active material segmented into towers, each covering 0.087×0.087 in $\eta - \phi$, and covers the pseudorapidity up to $|\eta| = 1.3$. At $\eta = 0$, the HB absorber thickness corresponds to $5.8\lambda_\mathrm{I}$, which is effectively

increased with the absolute value of the pseudorapidity, and reaches a value of $10.6\lambda_\mathrm{I}$ at $|\eta| = 1.3$. The ECAL material in front of the HB corresponds to about $1.1\lambda_\mathrm{I}$. The Hadron Outer (HO) is made of scintillator material located outside the solenoid to stop particles having passed the HB and the magnet in a region of $|\eta| < 1.26$.

The Hadron Endcaps (HE) extend the HCAL coverage from $1.3 < |\eta| < 3.0$. The HE is also segmented into towers, of which each covers between 0.087×0.087 and 0.17×0.17 in the $\eta - \phi$ plane, depending on the pseudorapidity. Taking into account the ECAL material in front of the HE, the total calorimeter length corresponds to approximately $10\lambda_\mathrm{I}$. The forward region is completed by the Hadron Forward (HF) sub-detector, which covers the region closest to the beam pipe, $2.9 < |\eta| < 5.2$. It must be especially radiation hard and therefore consists of steel and quartz fibres as absorber and active medium, respectively. It is divided into towers of 0.175×0.175 in $\eta - \phi$, similarly to the inner part of the HE.

The combined energy resolution of the ECAL EB and HCAL HB systems has been measured with a pion test-beam and can be parameterized as [128]

$$\frac{\sigma_E}{E} = \frac{115.3\%}{\sqrt{E/\mathrm{GeV}}} \oplus 5.5\%. \tag{4.7}$$

4.2.5 The Solenoid

In order to bend the trajectories of charged particles and allow for a precise momentum reconstruction, the CMS detector contains a superconducting solenoid magnet enclosing the tracking system and both calorimeters. It is 12.9 m long and its inner diameter is 5.9 m. The magnet provides a homogeneous magnetic field of 3.8 T on its inside, while the outer magnetic field is returned by iron yokes alternating with the muon chambers. In this design, muon trajectories are bent in the opposite direction when traversing the muon chambers, allowing for an improved reconstruction of muon momenta.

4.2.6 The Muon System

The muon system is the outermost part of the CMS detector and is used to identify muons, as these are the only particles (except neutrinos) that pass the whole detector without significant energy loss. Three different types of gaseous detectors are used in the muon system: drift tubes (DT), resistive plate chambers (RPC), and cathode strip chambers (CSC). The layout of the muon system is sketched in figure 4.7.

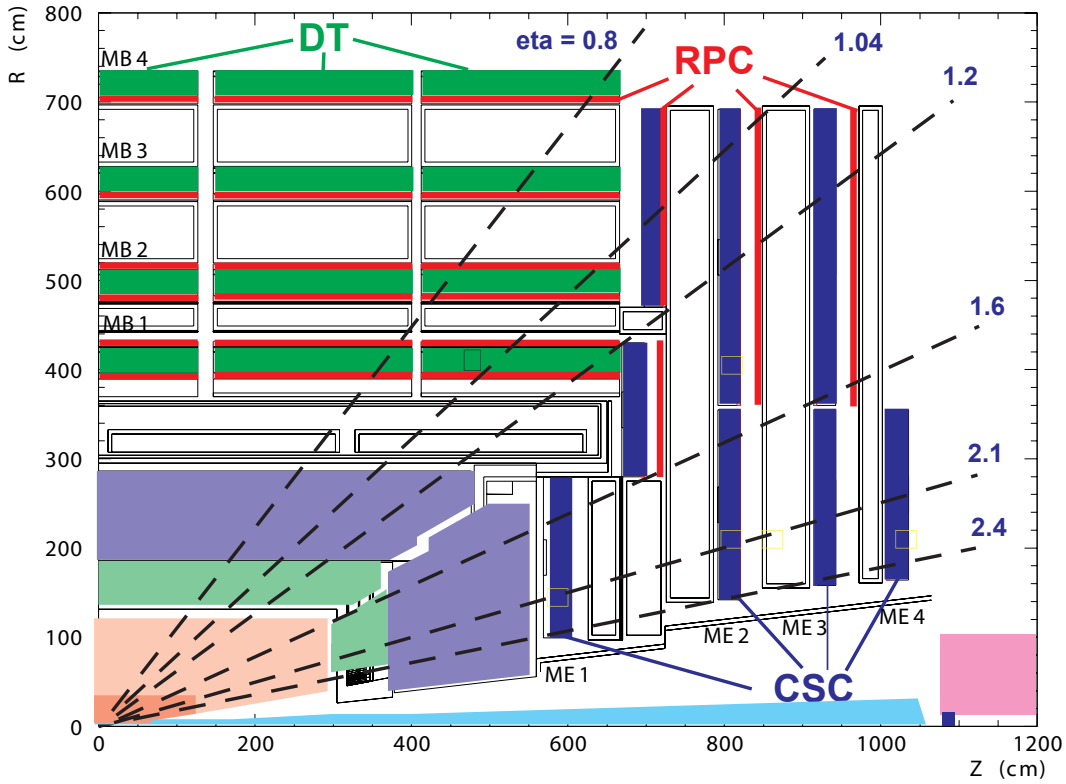

Figure 4.7: Layout of the CMS muon system. Taken from Ref. [127].

In the barrel part (MB), which covers the central region up to $|\eta| < 1.2$, DTs and RPCs are used. As mentioned above, the MB and the iron return yokes alternate, resulting in four separate muon stations. In the two inner layers, the RPCs enclose the DTs, while in the outer layers there is a single layer of RPCs per layer of DTs.

In the endcaps (ME), covering a region of $1.2 < |\eta| < 2.4$, mostly CSCs are used due to the higher particle flux. The ME is also divided into four stations, where RPCs complement the CSCs up to $|\eta| < 1.6$ in the inner three layers. The outermost layer of CSCs only covers the region closest to the beam.

4.2.7 The Trigger System

Due to the very high luminosity provided by the LHC, the proton bunch crossing rate is 40 MHz, which translates into $\mathcal{O}(10^9)$ pp interactions per second at design luminosity. Since it is not feasible to store events at such high rates, the CMS experiment employs a two-tiered trigger system. Its goal is to select potentially interesting events at high speed using only fast algorithms and a reduced set of information.

The first stage is the level-1 (L1) trigger, a hardware-based trigger using only information from the calorimeters and the muon system in a lower resolution. It must

decide to keep or discard an event within 3.2 μs and reduces the event rate to about 100kHz.

The second stage is the high-level trigger (HLT). The HLT is based on software and further analyzes events passing the L1 trigger. Here, information of all sub-detector systems is processed in a CPU farm in full granularity by more sophisticated algorithms. In the HLT, events have to pass multiple selection steps and are discarded as early as possible in order to reduce the computing time. By making one decision every 50 ms, the rate of events that are permanently stored is reduced to $\mathcal{O}(100\,\mathrm{Hz})$.

Chapter 5

Object Reconstruction

In order to analyze the data recorded by the CMS detector described in the previous chapter, the candidates of particles originating from the pp collisions must be reconstructed from raw electronic signals. Since different types of particles have distinct signatures in the various detector sub-systems, combining information from all of these systems is most advantageous to identify and reconstruct the properties of particles precisely. The CMS Collaboration employs a particle flow (PF) reconstruction method [130] for this purpose, which is described in section 5.1. In the subsequent sections, the reconstruction of primary vertices, electrons, muons, and jets is explained (sections 5.2 – 5.5), followed by a discussion of the jet energy calibration in section 5.6. Section 5.7 gives a description the missing transverse momentum, a variable used frequently in the following chapters.

5.1 The CMS Particle Flow Event Reconstruction

The CMS event reconstruction is based on a PF algorithm [130] making combined use of the detector sub-systems. The highly performant tracking system in a strong magnetic field, the hermetic calorimeters with a particularly good spatial ECAL resolution, and the dedicated muon system are the components making a PF-based event reconstruction especially successful. The algorithm first combines signals in single detector components to so-called PF elements, which are tracks from the inner tracker and the muon systems as well as clusters of calorimeter cells. In the second step, PF elements are linked together and the linked elements are finally identified as electrons, muons, charged or neutral hadrons, or photons.

First, tracks are reconstructed from hits in the inner tracking system using the iterative application of a combinatorial track finder based on the Kalman-filter technique,

which is described in detail in Ref. [131]. In each iteration, any hits associated with tracks identified in a previous iteration are not taken into account. By relaxing the requirements on track seeds in subsequent iterations, high overall efficiency is achieved while keeping the misidentification rate at a low level. The first iterations are purely seeded by doublets or triplets of pixel hits. By considering also hits in the strip detector or taking into account information from the muon chambers, efficiency for muons, particles inside very energetic jets, or particles originating from displaced vertices is recovered in later iterations.

Second, calorimeter cells are grouped into clusters. Calorimetric information is especially important to determine the energy of neutral particles, to identify electrons and find all the associated bremsstrahlung photons, and to improve the energy measurement of highly-energetic charged hadrons. The clustering procedure starts from seeds, which are identified as cells with local energy maxima that exceed a given threshold. Starting from a seed, all adjacent cells are clustered to the so-called topological cluster iteratively if their energy lies above twice the noise level. This clustering is done in all calorimeter sub-systems individually, except for the HF, where each cell is directly identified as a cluster.

Since most particles are expected to leave a signal in more than one detector component, the PF algorithm attempts to link the PF elements reconstructed previously. Links may be established between any pair of PF elements. An inner track and a calorimeter cluster are linked if the extrapolated track ends up inside the cluster within the uncertainty. The quality of such a link is quantified by the distance of the extrapolated track to the cluster in the $\eta - \phi$ plane. In case of ambiguous assignments of HCAL clusters to the same track, or several tracks to a single ECAL cluster, the best link is chosen. To account for photons from electrons emitting bremsstrahlung, ECAL clusters are linked to a track if the tangent to the track at any layer of the tracking system lies within the cluster. In this process, it is also accounted for photon conversion in the tracker material. Different calorimeter clusters are linked to each other if the cluster in the more granular calorimeter is inside the boundaries of the cluster in the less granular calorimeter. Potential ambiguities are again resolved by linking the clusters with the smallest distance. Last, multiple tracks can be linked if they share a common secondary vertex that fulfills certain criteria.

In the last step of the PF algorithm, the *blocks* of elements linked together, either directly or indirectly through common intermediate links, are identified as particles. The PF elements associated to a particle identified previously are not considered further. Muons are reconstructed solely from tracks in the inner tracker and/or in the

outer muon chambers. Electrons are identified as tracks combined with ECAL clusters. Photons, on the other hand, must be trackless clusters in the ECAL, taking into account linked HCAL clusters if the ratio of the energy deposits in both is compatible with the expectation of a photon-induced shower in the region covered by the tracker. Outside the tracker acceptance, any ECAL shower is assumed to arise from a photon if it is not linked to an HCAL cluster, otherwise it gives rise to a charged or neutral hadron. Any HCAL clusters not linked to a track are then identified as neutral hadrons. Finally, an HCAL cluster linked to a track indicates the presence of a charged hadron.

5.2 Reconstruction of Primary Vertices

In pp collisions at the LHC, it is necessary to identify primary vertices (PVs) of an event, which are the locations of inelastic interactions between two protons. At the LHC, multiple PVs are reconstructed in a given event due to the presence of not only the main hard interaction but also additional, softer interactions between protons in the same or adjacent bunch crossings.

In CMS, PVs are reconstructed based on the collection of tracks returned by the PF algorithm. In order for tracks to be used in the PV reconstruction, their transverse impact parameter significance with respect to the beam spot must be smaller than 5, they must have at least five hits in the tracking system, of which at least two must be pixel hits, and the normalized χ^2 of the track fit must be smaller than 20. The selected tracks are then clustered to PV candidates with a *deterministic annealing algorithm* [132]. Last, those PVs with at least two associated tracks are fitted to their tracks to obtain the optimal estimate of vertex parameters using an *adaptive vertex fitter* [133]. In this fit, each associated track is assigned a weight w between 0 and 1, where w is a measure for the probability of a given track to arise from the PV under consideration. The number of degrees of freedom of the fit is given by

$$n_{\mathrm{dof}} = -3 + 2 \sum_{i=1}^{N_{\mathrm{tracks}}} w_i, \tag{5.1}$$

which is a measure for the number of tracks that are likely associated to a given PV. All primary vertices considered in this thesis must satisfy $n_{\mathrm{dof}} \geq 4$ and be located close to the nominal interaction point, $\sqrt{x^2 + y^2} < 2\,\mathrm{cm}$ and $|z| < 24\,\mathrm{cm}$. In this thesis, only events with at least one such primary vertex are considered.

Of the fitted PVs passing the above criteria, the one that has the largest summed transverse momentum of physics objects associated to it is assumed to be the PV

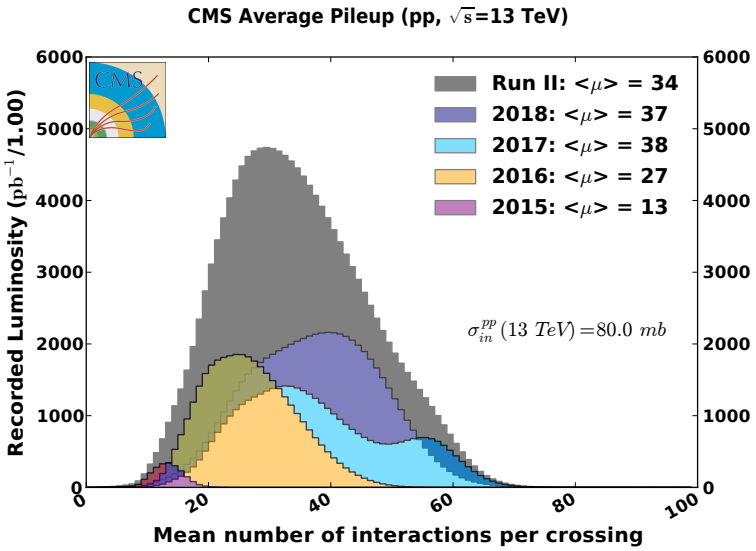

Figure 5.1: Distribution of the mean number of pp interactions per bunch crossing for the data-taking periods at $\sqrt{s} = 13\,\text{TeV}$. Taken from Ref. [126].

from the hard interaction (hereafter referred to as *leading* or *main* PV). Here, the physics objects are those obtained from the anti-k_T jet finding algorithm [134, 135] and the missing transverse momentum, calculated as the negative $\vec{p}_\text{T}$ sum of those jets. All other PVs in the event are assumed to originate from PU. In figure 5.1, the distribution of the mean number of pp interactions per bunch crossing is shown. In the 2016 data-taking period, on average 27 interactions took place per bunch crossing.

In order to mitigate the influence of particles from PU vertices in the event, CMS employs different techniques. A detailed comparison of such techniques in CMS can be found in Ref. [136]. The *charged hadron subtraction (CHS)* method [130] rejects charged hadrons associated to PU vertices from the jet clustering, while the impact of neutral hadrons is mitigated by employing jet-area based corrections [137–139] to the jet four-momentum (cf. section 5.6). Jets entirely composed of PU particles are rejected using a multivariate PU jet identification criterion [140]. Another approach is the *pileup per particle identification (PUPPI)* algorithm [141], which, unlike the techniques mentioned before, acts purely on particle level and also takes neutral hadrons into account. It assigns each particle a weight corresponding to the probability to originate from the leading PV. All objects and event observables computed from PF candidates then take the PUPPI weight into account and are hence expected to be more resilient against PU in CMS.

5.3 Identification of Electrons

The electron reconstruction in CMS [142] takes into account both tracks and ECAL clusters, accounting for photons from bremsstrahlung and photon conversion. Electron candidates can be seeded by ECAL clusters or tracks. In the former case, energetic ECAL clusters are used to aggregate *superclusters*, obtained by combining ECAL clusters in an $\eta - \phi$–region around the seed cluster. The supercluster is assumed to contain the energy of the electron and the parts it radiated before reaching the ECAL. From the initial seed, the expected tracker hits can be inferred. This seeding technique is most efficient for isolated and highly energetic electrons.

Seeding electron candidates with tracks recovers reconstruction efficiency for non-isolated or soft electrons. If the electron did not emit considerable amounts of bremsstrahlung in the tracking system, the Kalman-Filter track can be matched to an ECAL cluster well, returning a good measurement of the electron's momentum. On the other hand, if the amount of energy radiated is significant, the momentum obtained from the track fit will not match the energy deposited in the ECAL cluster. Such electron tracks are refitted with a Gaussian sum filter technique [143], which is more suited to handle the large and frequent energy losses due to emission of bremsstrahlung. As described in section 5.1, ECAL clusters matching tangents of the electron track at any layer of tracker material are taken into account as bremsstrahlung.

Electron candidates reconstructed by the algorithms explained above must satisfy an additional set of identification (ID) criteria, which are described in detail in Ref. [142]. The variables considered in the ID can be grouped into three categories. First, some variables account for the shape of the shower in lateral and transverse direction and restrict the fraction of energy deposited in the HCAL. Second, track-based observables from the Gaussian sum filter track and differences between the Kalman-Filter and Gaussian sum filter tracks allow distinguishing electrons from charged hadrons. Last, some variables compare the measurements from the track and the calorimeter cluster. The full set of variables used is explained below.

- The lateral shower shape is taken into account by the variable $\sigma_{\eta\eta}$, which must be sufficiently small.
- The differences in η and ϕ, $\Delta\eta$ and $\Delta\phi$, between the track and the ECAL supercluster must not be too large.
- The ratio H/E of energy of the electron deposited in the HCAL to the energy deposited in the ECAL must be small.

- The track's momentum and the cluster's energy are compared via the variable $|1/E - 1/p|$, which must be small.
- The distance of the electron from the leading PV in transverse and z–direction, d_0 and d_z, must be small.
- The number of missing hits in the electron track must not be greater than 1.
- The electron has to pass a conversion veto to enrich prompt electrons and reject those from photon conversion.
- The electron's relative combined PF isolation, taking into account all PF candidates around the electron in a distance of $\Delta R < 0.3$ and the electron p_{T}, can additionally be used, mostly to discriminate electrons inside jets.

By imposing differently strong requirements on the above variables, the CMS Collaboration has defined multiple *working points (WPs)*, where WPs have a larger reconstruction efficiency at the cost of an increased misidentification rate. In this analysis, the loose and tight WPs are used, which have efficiencies of approximately 90% and 70%, respectively. Finally, electrons are only considered in the presented analysis if they have $|\eta| < 2.4$.

5.4 Reconstruction of Muons

In CMS, muons are reconstructed as either *tracker muons*, *standalone muons*, or *global muons* [144]. A track is identified as a tracker muon if a track from the inner tracking system matches at least one hit in the outer muon chambers with a given quality. Conversely, standalone muons are constructed solely from hits in the muon stations. Global muons are obtained from standalone muon tracks that are compatible with tracks in the inner tracker. In this case, the two tracks are combined, which results in an improved muon momentum resolution for high transverse momenta compared to tracker muons. Global muons and tracker muons are merged if they share the same track in the inner tracking system.

Muon candidates reconstructed in the aforementioned ways are required to pass an additional set of ID criteria. Similar to the case of reconstructed electrons, multiple WPs have been defined by the CMS Collaboration, resulting in varying efficiencies and misidentification rates. Similarly to the case of electrons, also for the muons the loose and tight WPs are employed in this thesis. They are explained in the following.

A loose muon must be reconstructed as either a tracker or a global muon. This ID has the highest efficiency and targets prompt muons as well as muons from decays of heavy-flavor hadrons. The tight muon ID, on the other hand, has the lowest efficiency but yields the purest collection of prompt muons. A tight muon is defined as a loose muon passing the following additional quality requirements:

- The muon must be reconstructed as a tracker muon and as a global muon.
- The track of the tracker muon has hits in at least six layers of the inner tracker, out of which at least one must be a pixel hit.
- The muon must have at least two hits in the muon chambers matching its track in the inner tracker.
- The fit applied to the global muon must have a $\chi^2/\text{ndf} < 10$ and include at least one hit in the muon chambers.
- The muon must have a transverse and longitudinal distance from the leading PV of $d_0 < 0.2\,\text{cm}$ and $d_z < 0.5\,\text{cm}$, respectively.

In addition to the loose and tight ID WPs, a dedicated ID optimized for muons with a very high p_T of more than 200 GeV has been developed by the CMS Collaboration [144]. It does not make use of the PF event reconstruction technique, which takes into account the full event when reconstructing muons, but instead relies solely on muon track quantities. It is a modification of the tight ID WP and differs from it in the following criteria:

- The requirement of the muon to be reconstructed as a tracker muon is removed. Hence, the high-p_T muon must be a global muon.
- The requirement of χ^2/ndf on the global muon fit is removed.
- A new requirement on the maximum relative error σ_p/p on the momentum of the best muon track is added. Muons must have $\sigma_p/p < 0.3$.

The relative PF isolation of muons I_rel takes the transverse momenta of all PF candidates in a cone of radius $\Delta R < 0.4$ around the muon candidate into account and is defined as

$$I_\text{rel} = \frac{\sum_{h^\pm} p_\text{T} + \max(0,\ \sum_\gamma p_\text{T} + \sum_{h^0} p_\text{T} - 0.5 \sum_{h^\pm}^\text{PU} p_\text{T})}{p_\text{T}^{\mu\ \text{cand.}}}. \tag{5.2}$$

Here, $\sum_{h^\pm} p_\mathrm{T}$ is the p_T sum of all charged hadrons from the leading PV, $\sum_\gamma p_\mathrm{T}$ is the sum of the photon p_T around the muon candidate, and $\sum_{h^0} p_\mathrm{T}$ denotes the summed p_T of neutral hadrons. The term $\sum_{h^\pm}^\mathrm{PU} p_\mathrm{T}$ denotes the p_T sum of charged hadrons from PU vertices. Without employing algorithms such as PUPPI, it is only possible to identify charged PU particles using tracking information, not neutral ones. Hence, $0.5 \sum_{h^\pm}^\mathrm{PU} p_\mathrm{T}$ is used to approximate the contribution of neutral PU hadrons and subtract it from the overall sum in order to provide an isolation efficiency that shows no or only small dependence on the number of PU interactions in an event.

Last, only muons in the region covered by the tracking system, $|\eta| < 2.4$, are considered in this thesis.

5.5 Reconstruction of Jets

As outlined in section 2.1.2, colored particles produced in high-energy pp collisions are not observed freely but give rise to jets. These sprays of particles consist of roughly 65% charged hadrons, 25% photons, and 10% neutral hadrons [130]. In order to infer properties of the initiating particle, jets are reconstructed with dedicated jet clustering algorithms.

5.5.1 Jet clustering algorithms

Since it is crucial to enable comparison between theory and experimental data, jet clustering algorithms must fulfill a number of conditions ensuring finite QCD predictions. First, they have to be invariant under soft gluon radiation, i.e. the properties of a jet must not change if a soft gluon is emitted. Second, jet algorithms must be insensitive to collinear splittings of a particle in the jet, i.e. if a particle in the jet is replaced by two collinear particles with the same summed four-momentum, the jet properties must be retained. These criteria are referred to as *infrared* and *collinear safety*, respectively.

In the CMS Collaboration, a variety of infrared and collinear safe sequential clustering algorithms are used. Among them are the k_T [145, 146], Cambridge-Aachen [147], and anti-k_T [134, 135] algorithms. These algorithms take a list of particle four-momenta as inputs, which can be obtained from the particles reconstructed by the PF algorithm or also from generated particles when considering simulated events. All of the three clustering algorithms mentioned above consider the distance measures d_{ij} and $d_{i\mathrm{B}}$ between two particles i and j and between the particle i and the beam axis B, respectively.

They are defined as

$$d_{ij} = \min\left(k_{\mathrm{T},i}^{2n}, k_{\mathrm{T},j}^{2n}\right) \frac{\Delta R_{ij}^2}{R^2}, \tag{5.3a}$$

$$d_{i\mathrm{B}} = k_{\mathrm{T},i}^{2n}, \tag{5.3b}$$

with $k_{\mathrm{T},i}$ the transverse momentum of particle i, R a dimensionless parameter indicating the maximum jet radius, and $n \in \{-1,\ 0,\ 1\}$. The clustering is then performed in an iterative procedure. In each step, the distance d_{ij} is calculated for each pair of particles i and j and compared to the values of $d_{i\mathrm{B}}$ of all particles i. If one d_{ij} is smaller than the minimum of all $d_{i\mathrm{B}}$, the four-momenta of i and j are summed and the combination is considered as a single object in the subsequent steps. The original i and j are then deleted from the list of input particles. Otherwise (i.e. if a $d_{i\mathrm{B}}$ is smallest), i is considered a jet and removed from the inputs. This procedure is repeated until all particles have been clustered into jets.

The parameter n governs the order in which the particles are combined. If it is negative, priority is given to particles carrying large transverse momentum, while positive values lead to soft particles being clustered first. For $n = 0$, only the geometrical distance between particles i and j is relevant for the clustering. The anti-k_{T} (Cambridge-Aachen, k_{T}) algorithm uses a value of $n = -1$ (0, 1). In this thesis, jets clustered with the anti-k_{T} algorithm with a radius parameter of $R = 0.4$ and 0.8 are used, which are respectively referred to as AK4 and AK8 jets in the following.

In order to discriminate jets that arise from calorimetric detector noise instead of particles produced in pp collisions, the CMS Collaboration has defined a noise jet ID [140]. All jets considered in this thesis have to pass the loose WP, which imposes the following requirements depending on the jet's $|\eta|$:

If the jet is in a region covered by the tracker, $|\eta| < 2.4$,

- the respective fractions of energy carried by neutral hadrons, electrons, and photons must be smaller than 0.99,
- the fraction of energy carried by charged hadrons must be greater than 0.0, and
- at least one charged particle must be clustered to the jet.

If the jet lies in a region of $2.4 < |\eta| < 2.7$, where no tracking information is accessible, the respective fractions of energy carried by neutral hadrons and photons must be smaller than 0.99. This requirement is tightened for jets with $2.7 < |\eta| < 5.0$, where

these fractions must be smaller than 0.9. In this region, an additional requirement on the number of neutral particles clustered to the jet is introduced, i.e. the jet has to have at least 3 (11) neutral constituents, if $2.7 < |\eta| < 3.0$ ($3.0 < |\eta| < 5.0$).

5.5.2 Identification of bottom–quark–initiated jets

An important task in many LHC analyses is the identification of jets initiated by bottom quarks (b-tagging). Since top quarks are expected to decay into a bottom quark and a W boson, b-tagging provides a valuable handle to identify such decays in a kinematic regime where the bottom–quark–initiated jet (b-jet) is well-separated from the W decay products. The most important quantity exploited to identify b-jets is the lifetime of B hadrons, which is significantly larger than the one of other particles produced in pp collisions [4]. Due to their lifetime, B hadrons can propagate from the leading PV for a few mm before decaying. Their decay produces secondary vertices that are displaced with respect to the leading PVs and can be identified exploiting the excellent spatial resolution of the CMS tracking system.

The CMS Collaboration employs a number of methods to perform b-tagging [148], of which the Combined Secondary Vertex (CSVv2) algorithm is used in this thesis. It is a multivariate algorithm trained on a number of variables based on the tracks and secondary vertices of the jet. The track-based variables include the impact parameter significance and the transverse momentum of a track relative to the jet axis. The variables related to secondary vertices take into account, among others, its mass, its flight distance (significance), and the number of tracks originating from it. The multivariate algorithm combines all input variables and returns a single number ranging from 0 to 1 for a given jet, which can be interpreted as the probability of that jet to be a b-jet. Light quark- and gluon-jets are most likely to have a value close to 0. Placing a cut on the CSVv2 output variable allows to obtain samples of b-jets with varying efficiency and purity. In this thesis, the loose b-tagging WP is used, which has an efficiency of about 90% for correctly identifying b-jets and a rate of approximately 10% to wrongly b-tag a jet originating from a light quark or a gluon.

5.5.3 Reconstruction of Boosted Hadronic Top Quark Decays

This thesis focuses on searches for new particles decaying into top quarks. As the new particles are potentially very heavy compared to SM particles, the particles produced in its decay can receive a large Lorentz boost in transverse direction. Boosted top quarks decaying to quarks hence produce three quarks that are collimated in the direction

of movement of the top quark. In contrast to top quarks decaying at rest, whose decay products are well-separated and can be reconstructed as three distinct AK4 jets, boosted top quark decays are likely to be reconstructed as a single AK8 jet with large p_{T} that contains all of its decay products.

For the analysis of final states with boosted hadronic top quark decays, it is crucial to identify (tag) such jets as originating from a top quark decay and distinguish them from AK8 jets originating solely from clustering QCD radiation. For this purpose, the substructure of an AK8 jet is utilized. Jets originating from a top quark decay exhibit a distinct substructure with three sub-jets corresponding to the individual top quark decay products. Jets initiated by QCD radiation mostly do not have such a multi-prong substructure. Furthermore, the invariant mass of the jet constituents is sensitive to the origin of a jet and provides additional information used in discriminating jets of different origins.

In order to reject additional soft and collinear QCD radiation clustered to the AK8 jet, so-called *grooming* algorithms are used. In this thesis, the modified mass drop tagger [149] is employed, which is based on the soft drop algorithm [150]. The mass of the jet groomed with this algorithm is referred to as softdrop mass M_{SD} throughout this thesis.

Within the CMS Collaboration, a wide variety of algorithms is used for tagging top-quark-initiated jets (t-tagging). A comprehensive overview and comparison is given in Ref. [151]. In the presented work, t-tagging is used in the search for resonant $\mathrm{t\bar{t}}$ production, which is presented in chapter 8. Jets are considered to be t-tagged if they have $p_{\mathrm{T}} > 400\,\mathrm{GeV}$ and pass two additional criteria. First, their soft drop mass must be compatible with the top quark mass, i.e. $105\,\mathrm{GeV} < M_{\mathrm{SD}} < 210\,\mathrm{GeV}$. Second, the *N-subjettiness* variable τ_N [152] is considered. It represents a measure for the probability of a jet to consist of at most N sub-jets. Here, small values of τ_N indicate a high probability. Consequently, the ratio $\tau_{32} = \tau_3/\tau_2$ quantifies the probability of the jet to have 3 instead of 2 sub-jets. Values of $\tau_{32} \simeq 0$ are obtained for jets that are much more likely to have 3 rather than 2 sub-jets. High values of τ_{32} indicate no preference for either hypothesis. In this thesis, t-tagged jets are required to have $\tau_{32} < 0.65$, which efficienctly selects jets originating from top quark decays and discriminates jets arising from QCD radiation. In the following, jets passing all of the above criteria are referred to as t-tagged jets.

Figure 5.2: Representation of the factorized jet energy scale correction procedure used in CMS.

5.6 Jet Energy Calibration in CMS

The jets reconstructed in an event allow to infer properties of the quarks and gluons produced in the pp scattering. For this purpose, a precise calibration of the energy scale and resolution of jets is crucial. The CMS Collaboration employs a factorized jet energy correction (JEC) approach [139] to ensure the true and the measured jet energy scale (JES) and jet energy resolution (JER) agree. It is summarized in figure 5.2 and consists of multiple steps applied successively. The need for such a calibration is due to various sources.

First, the presence of PU interactions in addition to the main hard interaction causes jets to contain particles not only produced in the showering of the particle initiating the jet but also PU particles, which leads to a shift in the jet energy. Second, detector effects like non-uniformity in η, non-linearity in p_{T}, and electronic noise bias the jet energy measurement and need to be corrected for. Third, differences in the jet energy scale and resolution between data and simulated events are mitigated. Each of these steps is described in the following. All corrections are derived for AK4 jets clustered from PF particles with CHS applied (AK4 CHS jets).

5.6.1 Pileup Offset Correction

The first step in the CMS jet energy calibration is the correction for an offset in the jet energy scale due to PU, referred to as **L1 offset correction**. As mentioned above, clustering particles from PU interactions to jets of the primary hard interaction shifts the jet energy measured. The average energy offset is corrected through a multiplicative factor determined with the *hybrid jet area method*, which was first introduced in Ref. [139] and modified by the CMS Collaboration.

The correction factor is parameterized as a function of the uncorrected p_{T} of the jet, its pseudorapidity η, the effective jet area and the average energy density ρ in the event. The parameters in the correction factor are obtained from simulated events, where the particle-level (i.e. before simulating the interaction of particles with the detector material) energy offset is determined comparing the p_{T} of particle-level jets in simulated events of QCD multijet production with and without simulated PU. Finally, differences

in the energy offset between data and simulation are corrected with a data-to-simulation (data/MC) scale factor (SF) derived with the random cone (RC) method [153]. It exploits the fact that the average energy of particles contained in randomly-placed cones in η and ϕ corresponds to the average energy offset due to PU. Performing this measurement in simulation and minimum-bias data, a data/MC SF depending on η and ρ is obtained.

5.6.2 Simulated Detector Response Corrections

In the second step of the CMS jet energy calibration, the relative and absolute detector response is corrected, referred to as **L2 relative** and **L3 absolute correction**, respectively. Here, the pileup-induced energy offset has already been corrected as described previously. Simulated events are used to correct for detector effects that introduce a discrepancy between the true and the measured energy of jets.

In simulation, the true energy of a jet is accessible as the energy sum of generated particles clustered into the particle-level jet before the detector simulation. The reconstructed AK4 jets are matched to their corresponding particle-level jets within a radius of $\Delta R < 0.2$ in order to derive the detector response. It is defined as the ratio of the average measured and true jet energy and used to correct the reconstructed jet energy as a function of the reconstructed jet's η and the particle-level jet's p_{T}.

5.6.3 Relative and absolute residual corrections

After applying L1 and L2L3 corrections, residual differences in the mean detector response between data and simulation are corrected in the last step, referred to as **L2L3Res corrections**.

The L2Res relative correction aims at correcting the mean detector response as a function of $|\eta|$ of the jet, relative to the barrel region in $|\eta| < 1.3$, and is derived in QCD dijet events. This step is presented comprehensively in chapter 6 and briefly summarized here. The L3Res absolute correction corrects the detector response as a function of jet p_{T} in the barrel of the detector. It is derived in Z/γ+jet and QCD multijet events. The final L3Res correction is obtained from a combined fit to the results from all of these channels.

The L2L3Res corrections employ two different definitions of the detector response. In the first case, the p_{T} ratio $\mathcal{R}_{\mathrm{bal}}$ between a reference object and the probe jet is used, which ideally should be unity. Depending on the channel, the reference object is a jet in the barrel region (L2Res) or a Z boson, a photon, or a system of jet recoiling against

the probe jet (L3Res). This method is referred to as p_{T}-*balance method*.

The second method is called *missing transverse momentum projection fraction (MPF)* method and exploits the fact that ideal dijet, Z/γ+jet, and multijet events have no intrinsic source of missing transverse momentum. It is assumed that any missing transverse momentum in such events arises only from miscalibrated jets. In CMS, the MPF method is used to derive the nominal L2L3Res corrections and the p_{T}-balance method is used for validation and cross-checks.

In both methods, the response is measured in data and simulated events and corrected for potential additional jet radiation. The ratio of responses constitutes the final correction applied to jets in data.

5.6.4 Jet energy resolution correction

After the jet energy scale has been corrected, the JER is measured in data and simulated events in order to derive data/MC correction factors. Usually, the JER in simulation is better and needs to be smeared to match the one in data. For this procedure, first the JER is measured on particle-level jets in simulated events. Second, measurements of JER-sensitive variables allow the determination of data/MC correction factors as a function of $|\eta|$ of the jet. Those are applied to simulation in order to widen its detector response distribution.

5.7 Missing Transverse Momentum

The only stable SM particles that cannot directly be detected by the CMS detector are neutrinos. Since they do not interact with the detector material, they manifest themselves only in a transverse momentum imbalance in the event. Since the sum of transverse momenta in the initial state of pp collisions at the LHC is zero, momentum conservation requires the p_{T} sum of all final state particles to vanish. Since neutrinos are invisible in the detector, their presence leads to missing transverse momentum. As mentioned in section 5.6.3, also miscalibrated objects can cause missing transverse momentum. It is defined as the negative vectorial sum of the transverse momenta of all PF particles i in an event,

$$p_{\mathrm{T}}^{\mathrm{miss}} = \left|\vec{p}_{\mathrm{T}}^{\,\mathrm{miss}}\right| = \left|-\sum_i \vec{p}_{\mathrm{T},i}\right|. \tag{5.4}$$

It is obvious that the calculation of $p_{\mathrm{T}}^{\mathrm{miss}}$ relies on a precise measurement of the

individual transverse momenta of the PF particles. It is therefore important to propagate the correction of the absolute and relative jet energy scale (the L2L3 corrections) as well as the jet energy resolution correction to $p_{\mathrm{T}}^{\mathrm{miss}}$, which is referred to as *type-I* $p_{\mathrm{T}}^{\mathrm{miss}}$ correction. For this, the (uncalibrated) transverse momenta of PF candidates clustered to AK4 jets with $p_{\mathrm{T}} > 10\,\mathrm{GeV}$ are replaced by the p_{T} of corresponding jets with L2L3 correction applied. In simulated events, also JER smearing is applied before replacing the PF particles with the calibrated jets.

Chapter 6

Relative Residual Jet Energy Corrections

The relative residual jet energy corrections are part of the last step in the jet energy scale calibration sequence in CMS discussed previously in section 5.6. This L2Res correction is applied to L1L2L3 corrected jets, i.e. their energy scale has already been corrected for PU offset and the detector response. Furthermore, also the simulated jet energy resolution has already been smeared to match the resolution in data. Absolute and relative residual corrections now aim at correcting small remaining differences in the detector response between data and simulation and are applied to data only. The L2Res relative correction is derived in QCD dijet events relative to the barrel part of the detector in $|\eta| < 1.3$ and depends on $|\eta|$ of the jet. Jets within $|\eta| < 1.3$ are corrected with the L3Res corrections, which are derived in that central region as a function of jet p_{T}. In contrast to the calibration performed in earlier stages, the derivation of residual correction factors must be performed in both data and simulated events in order to correct for differences between the two.

In this chapter, a detailed description of the derivation of the L2Res relative residual jet energy scale correction is presented. It is based on the procedure described in Ref. [139] and includes improvements made for the data-taking in the year 2016. Section 6.1 introduces the estimators for the detector response already mentioned previously. In section 6.2, an overview over the data and simulated samples used is given before the event selection is explained in section 6.3. Afterwards, the derivation of the L2Res correction factors is presented in detail (section 6.4). The chapter closes with a discussion of relevant systematic uncertainties and a summary in sections 6.5 and 6.6, respectively. An earlier version of the corrections presented here was used in all CMS analyses published for the Rencontres de Moriond 2017 conference and in

most analyses using only the dataset recorded in the year 2016.

6.1 Response Estimators

The detector response is estimated in two complementary ways in the derivation of residual jet energy corrections, as mentioned in section 5.6.3. In this section, a more detailed discussion is presented.

The p_T-balance method compares the transverse momentum of a reference jet in the barrel region to that of a probe jet to be calibrated. In this method, the response $\mathcal{R}_\mathrm{bal}$ is defined as

$$\mathcal{R}_\mathrm{bal} = \frac{p_\mathrm{T}^\mathrm{probe}}{p_\mathrm{T}^\mathrm{ref}} \tag{6.1}$$

and expected to be 1 for perfectly calibrated jets.

The second approach, the MPF method, uses the projection of the vectorial missing transverse momentum in an event onto the transverse momentum of the reference jet to measure the detector response. In ideal dijet events, $p_\mathrm{T}^\mathrm{miss}$ could only arise from miscalibrated jets recoiling against the reference object. The MPF response $\mathcal{R}_\mathrm{MPF}$ is defined as

$$\mathcal{R}_\mathrm{MPF} = 1 + \frac{\vec{p}_\mathrm{T}^\,\mathrm{miss} \cdot \vec{p}_\mathrm{T}^\,\mathrm{ref}}{\left(\vec{p}_\mathrm{T}^\,\mathrm{ref}\right)^2}, \tag{6.2}$$

which yields unity in case of perfect calibration.

In order to minimize biases due to the wide energy resolution of the reference jet, both responses can be expressed using the average p_T of the reference and the probe jet, $\overline{p}_\mathrm{T} = (p_\mathrm{T}^\mathrm{ref} + p_\mathrm{T}^\mathrm{probe})/2$, in the numerator and denominator. When evaluating the responses in bins of $\overline{p}_\mathrm{T}$, the bias due to the JER and also initial- and final-state radiation (ISR and FSR, respectively) cancels to first order. Equation (6.1) then becomes

$$\mathcal{R}_\mathrm{bal} = \frac{1 + \langle \mathcal{A} \rangle}{1 - \langle \mathcal{A} \rangle}, \quad \text{with} \tag{6.3a}$$

$$\mathcal{A} = \frac{p_\mathrm{T}^\mathrm{probe} - p_\mathrm{T}^\mathrm{ref}}{2\overline{p}_\mathrm{T}}. \tag{6.3b}$$

Similarly, the MPF response in equation (6.2) is expressed as

$$\mathcal{R}_{\mathrm{MPF}} = \frac{1+\langle\mathcal{B}\rangle}{1-\langle\mathcal{B}\rangle}, \quad \text{with} \tag{6.4a}$$

$$\mathcal{B} = \frac{\vec{p}_{\mathrm{T}}^{\,\mathrm{miss}} \cdot \left(\vec{p}_{\mathrm{T}}^{\,\mathrm{ref}}/p_{\mathrm{T}}^{\mathrm{ref}}\right)}{2\overline{p}_{\mathrm{T}}}. \tag{6.4b}$$

In both cases, $\langle\mathcal{X}\rangle$ indicates the arithmetic mean of $\mathcal{X}$ in a given bin of $\overline{p}_{\mathrm{T}}$. The variables $\mathcal{A}$ and $\mathcal{B}$ are referred to as *asymmetry* in the p_{T}-balance and MPF method, respectively.

For increased statistical precision, not only ideal dijet events but also those with additional jet radiation are considered (cf. section 6.3). The amount of additional radiation is quantified by the variable α, which is defined as

$$\alpha = \frac{p_{\mathrm{T}}^{\text{third jet}}}{\overline{p}_{\mathrm{T}}}, \tag{6.5}$$

where $p^{\text{third jet}}$ is the transverse momentum of the jet with the third-largest p_{T} (third-leading jet).

As will be shown in section 6.4, the MPF response is much more resilient against additional jet radiation than the p_{T}-balance response, because the former essentially balances the reference jet against the entire, potentially miscalibrated hadronic recoil. In contrast, the p_{T}-balance method only considers two jets and is hence more susceptible to the impact of ISR or FSR on the transverse momentum balance. The nominal results presented in this chapter are therefore derived with the MPF method, the p_{T}-balance method is only used to estimate the systematic uncertainty in the choice of the derivation method.

6.2 Data and Simulated Samples

The L2Res corrections are derived from data and simulated QCD multijet events. The data sample analyzed was recorded with the CMS detector in the year 2016 at a center-of-mass energy of 13 TeV and corresponds to an integrated luminosity of $35.9\,\mathrm{fb}^{-1}$. Data are collected with two sets of triggers selecting dijet events with different requirements on the minimal $\overline{p}_{\mathrm{T}}$. The first trigger set is most efficient in dijet events in the central part of the detector while the second set targets dijet events with one of the two leading jets in the forward region. The list of online thresholds and offline requirements on $\overline{p}_{\mathrm{T}}$

detector region	online $\overline{p}_{\mathrm{T}}$ [GeV]	offline $\overline{p}_{\mathrm{T}}$ [GeV]
central	40	51
central	60	73
central	80	95
central	140	163
central	200	230
central	260	299
central	320	365
central	400	453
central	500	566
forward	60	100
forward	80	126
forward	100	152
forward	160	250
forward	220	319
forward	300	433

Table 6.1: Online thresholds and offline requirements on $\overline{p}_{\mathrm{T}}$ for the dijet triggers targeting events with both of the two leading jets in the central (upper part) or one of the two leading jets in the forward (lower part) region of the detector.

for the two sets of triggers is given in table 6.1. Events are required to pass at least one of the given triggers and the corresponding offline $\overline{p}_{\mathrm{T}}$ selection to be considered in the derivation of L2Res corrections. The value of $\overline{p}_{\mathrm{T}}$ is computed as the average transverse momentum of the two jets with the largest p_{T} (leading and sub-leading jet, respectively). Due to non-uniform conditions during data-taking, the data are split into four parts, referred to as RunBCD, RunEFearly, RunFlateG, and RunH. They correspond to integrated luminosities of 12.9, 6.8, 8.0, and $8.2\,\mathrm{fb}^{-1}$, respectively.

QCD multijet events are simulated with the PYTHIA 8 MC event generator. In order to increase the number of generated events with a jet in the forward region of the detector, two independent samples are used. The first sample has a physical distribution of jet $|\eta|$ and is used to derive L2Res corrections in the region of $|\eta| < 2.853$. The second sample contains only events with at least one jet in the forward region and is therefore used in the forward region with $|\eta| > 2.853$. Interactions are generated uniformly over a range of transferred momentum $\hat{p}_{\mathrm{T}}$ between 15 and 7000 GeV. This has the advantage of simulating a large number of events in regions of phase space that would otherwise only be sparsely populated, e.g. at very high jet p_{T}. Therefore, the statistical uncertainty in such regions is reduced significantly in simulated events. By applying an event weight calculated by the generator, a physical $\overline{p}_{\mathrm{T}}$ spectrum is obtained.

Furthermore, a second event weight is applied to match the weighted number of simulated events to the number of recorded events in data in bins of $\overline{p}_{\mathrm{T}}$, which are defined by the offline $\overline{p}_{\mathrm{T}}$ requirements. To be considered in this measurement, simulated events must pass the lowest offline $\overline{p}_{\mathrm{T}}$ requirement, i.e. $\overline{p}_{\mathrm{T}} > 51\,\mathrm{GeV}$.

6.3 Event Selection

For the selection of QCD dijet events, an offline event selection is applied. As mentioned above, reconstructed AK4 CHS jets are corrected with the L1 and L2L3 jet energy scale corrections and in simulated events, the jet energy resolution is smeared to match the one in data. The four-momenta of electrons and muons clustered to the jet are subtracted from its four-momentum. Events are selected as described in the following.

First, the data collected by the trigger and passing the offline $\overline{p}_{\mathrm{T}}$ requirement as well as all simulated events are required to contain at least one well-reconstructed PV and at least two jets passing the loose noise jet ID (cf. section 5.5.1). To ensure a dijet topology, the two leading jets in an event must be back-to-back in ϕ, $\Delta\phi(\text{jet 1, jet 2}) > 2.7$. Events with a highly imbalanced dijet system are rejected by requiring the asymmetry as defined in the p_{T}-balance method to fulfill $|\mathcal{A}| < 0.7$ to avoid bias in the determination of the L2Res corrections. Furthermore, events with high additional jet activity, which therefore are not sufficiently dijet-like, are rejected by imposing $\alpha < 0.3$. In order to enable the calculation of L2Res corrections relative to the barrel of the detector, it is required that at least one of the two leading jets is reconstructed in the barrel region within $|\eta| < 1.3$.

In order to discriminate simulated events in which PU interactions lead to a strong bias, simulated events are additionally required to pass at least one of the following criteria:

- The p_{T} of the leading generated particle-level jet (not clustering PU particles) is smaller than 150% of the transferred momentum of the primary interaction, $p_{\mathrm{T}}^{\text{gen-jet 1}} < 1.5 \cdot \hat{p}_{\mathrm{T}}$, or
- the p_{T} of the leading reconstructed jet is smaller than 150% of the p_{T} of the leading generated particle-level jet, $p_{\mathrm{T}}^{\text{rec-jet 1}} < 1.5 \cdot p_{\mathrm{T}}^{\text{gen-jet 1}}$.

The first criterion rejects events in which the leading jet has much more p_{T} than the transferred momentum of the primary interaction, hinting at the presence of a PU interaction even harder than the primary one. In this case, PU has a major impact on the jet content of the event and the assumption that the two leading jets in the

event form a balanced dijet system no longer holds. The second criterion rejects events in which the leading reconstructed jet contains a large fraction of PU particles or is strongly affected by noise. In both cases, it is not expected that the dijet system is balanced, and hence it cannot be used to determine response corrections.

6.4 Derivation of L2Res correction factors

The L2Res correction is performed relative to the response of the reference jet with $|\eta| < 1.3$. The other jet is defined as the probe jet and is to be calibrated. In case both jets have $|\eta| < 1.3$, one of them is chosen as the reference jet at random. Since the final correction factors are derived as a function of $|\eta|$ of the probe jet, all of the steps described below are performed in bins of $|\eta|$, with η referring to the pseudorapidity of the probe jet in the following.

The general strategy is to calculate the arithmetic mean of the asymmetries defined in equations (6.3b) and (6.4b) in bins of $|\eta|$ and $\overline{p}_\mathrm{T}$ in data and simulation. This allows to calculate the p_T-balance and MPF responses as defined in (6.3a) and (6.4a) as a function of $\overline{p}_\mathrm{T}$ in a given $|\eta|$ bin. After fitting the responses versus $\overline{p}_\mathrm{T}$, the ratio of the responses in simulation and data can be calculated in bins of $|\eta|$. This ratio would be equivalent to the final correction factor if only perfect dijet events were considered, i.e. $\alpha = 0$. Because this is highly unlikely, events with additional jet radiation are also considered, up to $\alpha = 0.3$. A dedicated correction procedure is applied to take the effect of additional jets perturbing the dijet balance into account. Finally, the ratio of responses corrected for this additional radiation then is the scale factor that corrects for small differences in the jet response in data and simulation versus $|\eta|$. Each of the steps is discussed in detail in the following.

6.4.1 Response calculation

In the first step, the asymmetries of the p_T-balance and MPF methods, $\mathcal{A}$ and $\mathcal{B}$, are calculated for all selected events in data and simulation. In both methods, their values are a measure of the degree of miscalibration of the probe jet with respect to the central reference jet. As mentioned before, the asymmetry is evaluated in bins of $|\eta|$ and $\overline{p}_\mathrm{T}$. Figure 6.1 shows the normalized asymmetry distributions of $\mathcal{A}$ and $\mathcal{B}$ in data of RunBCD and simulation in all $\overline{p}_\mathrm{T}$ bins for $2.17 < |\eta| < 2.32$. This choice of $|\eta|$ is for illustration only and the procedure is the same in all other bins of $|\eta|$.

The arithmetic mean values $\langle\mathcal{A}\rangle$ and $\langle\mathcal{B}\rangle$ are then calculated in each bin of $\overline{p}_\mathrm{T}$ and $|\eta|$ from those distributions. The p_T-balance and MPF responses can be computed double

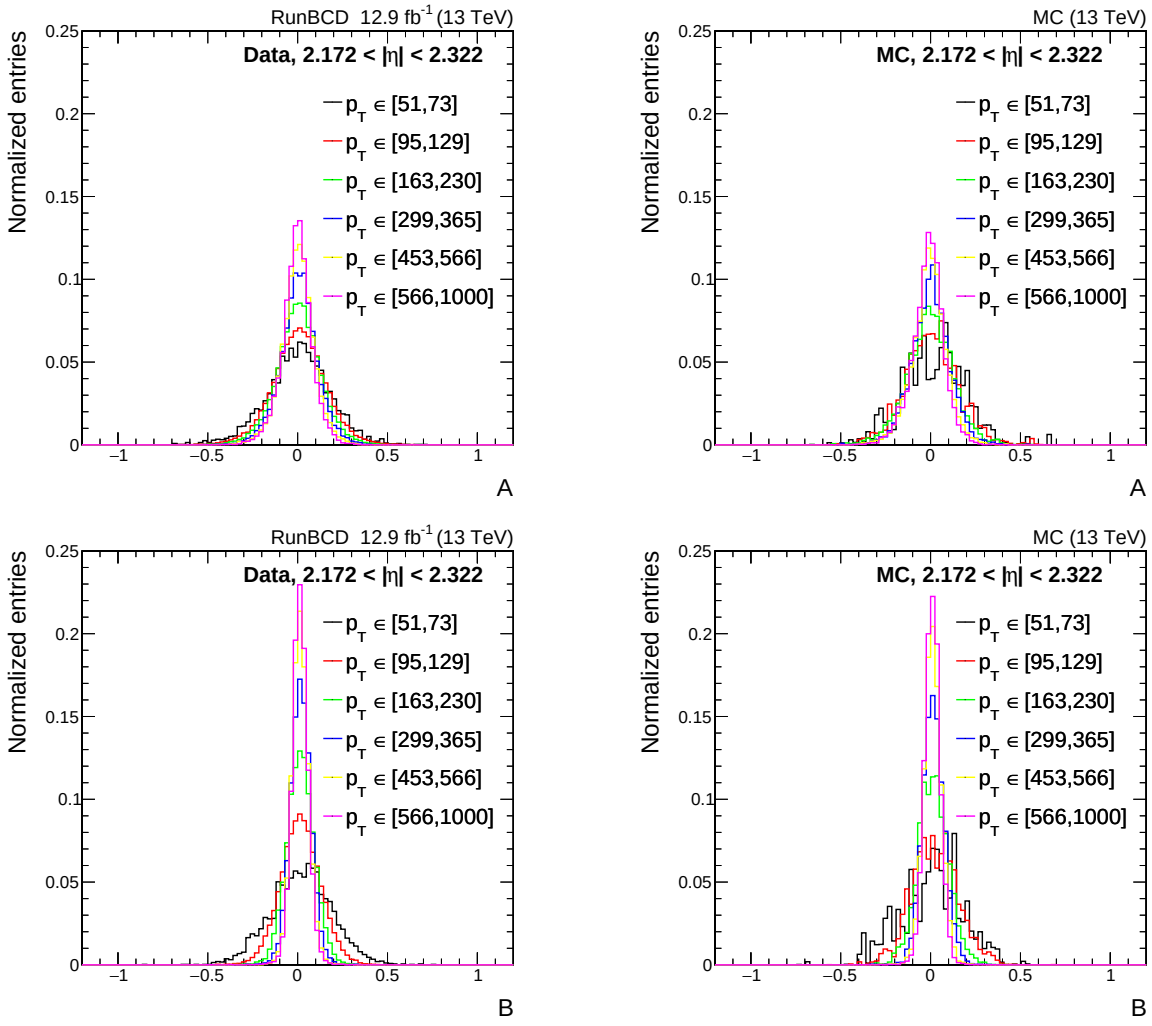

Figure 6.1: Distributions of $\mathcal{A}$ (upper row) and $\mathcal{B}$ (lower row) in data (left) and simulated events (right) in the bin of $2.17 < |\eta| < 2.32$. Different $\overline{p}_{\mathrm{T}}$ bins are displayed in different colors.

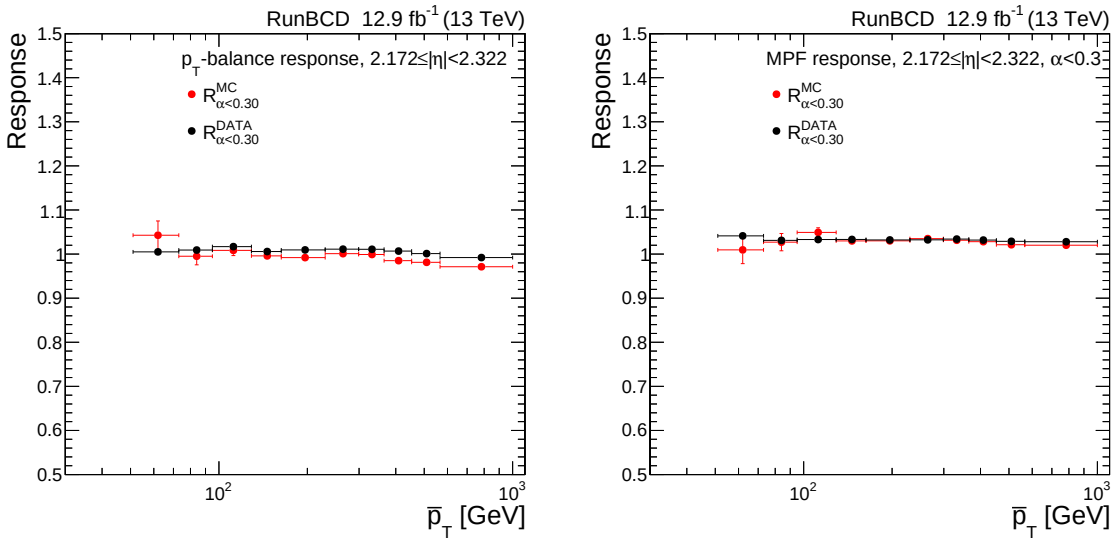

Figure 6.2: Response of the p_{T}-balance (left) and MPF (right) methods as a function of $\overline{p}_{\mathrm{T}}$ in $2.17 < |\eta| < 2.32$. The responses calculated in data and simulated events are shown in black and red, respectively.

differentially from those according to equations (6.3a) and (6.4a), respectively. The responses in data and simulation are shown as a function of $\overline{p}_{\mathrm{T}}$ and for $2.17 < |\eta| < 2.32$ in figure 6.2 for both methods.

6.4.2 Interpolation versus $\overline{p}_{\mathrm{T}}$

Since the L2Res correction factors are derived from the ratio of the responses in data and simulation, it is calculated as a function of $\overline{p}_{\mathrm{T}}$ in bins of $|\eta|$ from the individual responses shown in figure 6.2. Because the relative residual corrections are derived only as a function of $|\eta|$ to decrease the statistical uncertainty, any potential dependence on $\overline{p}_{\mathrm{T}}$ must be taken into account. Figure 6.3 shows the ratios of $\mathcal{R}_{\mathrm{bal}}$ and $\mathcal{R}_{\mathrm{MPF}}$ in simulation and data as a function of $\overline{p}_{\mathrm{T}}$ for $2.17 < |\eta| < 2.32$. The ratios feature a non-negligible dependence on $\overline{p}_{\mathrm{T}}$. For this reason, a log-linear fit to the ratio is performed taking into account bins above $\overline{p}_{\mathrm{T}} > 95\,\mathrm{GeV}$. For comparison, also the result of a constant fit is displayed. To reduce the results to a single value per bin of $|\eta|$, the constant and log-linear fits are evaluated at the mean $\overline{p}_{\mathrm{T}}$, $\langle \overline{p}_{\mathrm{T}} \rangle$, of all events in a given $|\eta|$ region. The potentially non-zero slope of the log-linear fit function is used later to derive a systematic uncertainty taking into account the $\overline{p}_{\mathrm{T}}$ dependence of the fit. The ratio of responses in simulation and data evaluated at $\langle \overline{p}_{\mathrm{T}} \rangle$ is shown in figure 6.4.

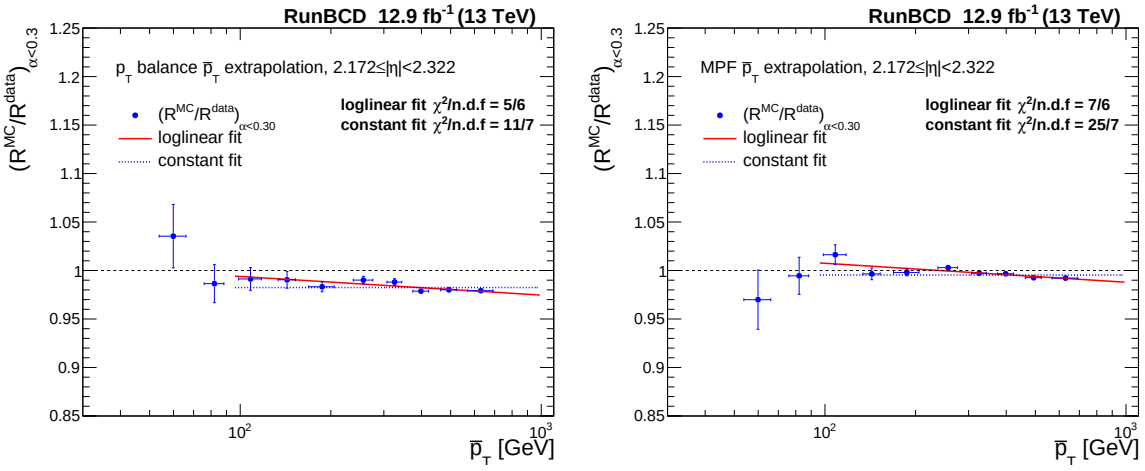

Figure 6.3: Ratio of the responses of the p_{T}-balance (left) and MPF (right) methods in simulation and data as a function of $\overline{p}_{\mathrm{T}}$ in $2.17 < |\eta| < 2.32$. The dashed line indicates a constant fit to the ratio while the red solid line indicates a log-linear fit.

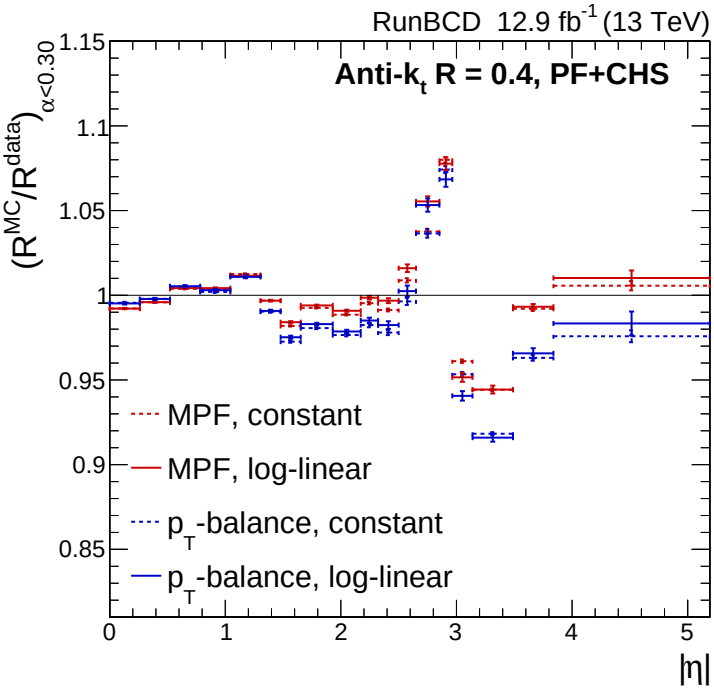

Figure 6.4: Ratio of the responses of the p_{T}-balance (blue) and MPF (red) methods in simulation and data after evaluating the constant (dashed) and log-linear (solid) fits at $\langle \overline{p}_{\mathrm{T}} \rangle$ as a function of $|\eta|$.

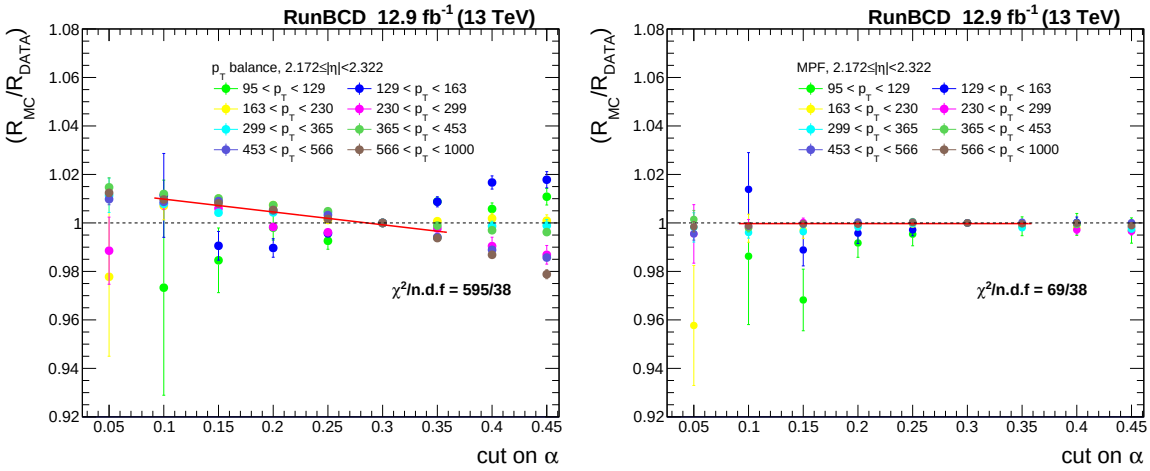

Figure 6.5: Ratio of the responses of the p_{T}-balance (left) and MPF (right) methods in simulation and data for $2.17 < |\eta| < 2.32$ as a function of α. Events with different $\overline{p}_{\mathrm{T}}$ are shown in different colors. The red line shows a linear fit taking into account all bins of $\overline{p}_{\mathrm{T}}$.

6.4.3 Correction for Additional Jet Radiation

As events with $\alpha < 0.3$ are considered in the derivation of the L2Res corrections, a correction taking into account the additional jet radiation must be derived. This is done by extrapolating the ratio of responses to the value at $\alpha \to 0$. The result will be a multiplicative factor k_{FSR} that is applied to each bin shown in figure 6.4. Formally, it is defined as the following double ratio.

$$k_{\mathrm{FSR}}(\alpha < 0.3) = \left(\frac{\mathcal{R}^{\mathrm{data}}(\alpha \to 0)}{\mathcal{R}^{\mathrm{MC}}(\alpha \to 0)} \right) / \left(\frac{\mathcal{R}^{\mathrm{data}}(\alpha < 0.3)}{\mathcal{R}^{\mathrm{MC}}(\alpha < 0.3)} \right) \tag{6.6}$$

In order to compute $\mathcal{R}(\alpha \to 0)$, the ratio of responses in simulation and data is considered not only in as a function of $\overline{p}_{\mathrm{T}}$ and $|\eta|$, but also α. The binning is inclusive in α, i.e. the content of a given bin corresponds to the number of events that have a value of α smaller than the upper bin edge. Figure 6.5 shows the ratio of responses of both methods for $2.17 < |\eta| < 2.32$ and all bins in $\overline{p}_{\mathrm{T}}$ as a function of α. The ratio of responses is normalized to unity in the bin at $\alpha < 0.3$ since the correction is derived for such events and the values in figure 6.4 have been computed in this range.

A linear fit is performed, taking into account all bins of $\overline{p}_{\mathrm{T}}$ in each region of $|\eta|$, which is indicated by the red line in figure 6.5. It considers all events with $0.1 < \alpha < 0.3$. Evaluating the fit at $\alpha = 0$ yields the desired correction in a given bin of $|\eta|$, which can be interpreted as the factor by which the ratio of responses would differ from the

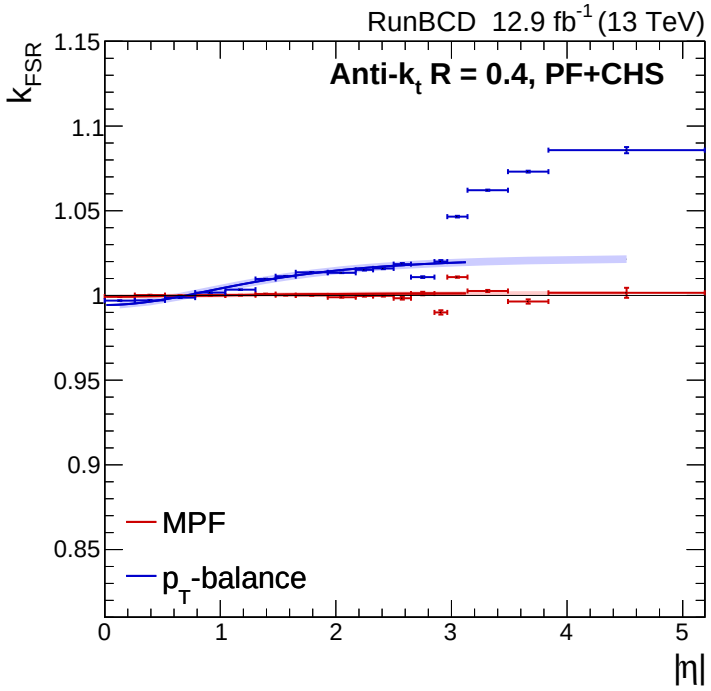

Figure 6.6: Correction factors k_{FSR} as a function of $|\eta|$ for the p_{T}-balance (blue) and MPF (red) methods. The lines indicate the fit to the binned values.

values in figure 6.4 if they had been derived on events with $\alpha = 0$. The resulting factors are extracted for each $|\eta|$ bin and shown in figure 6.6.

Since the values of k_{FSR} fluctuate statistically, a fit to the binned values is performed for both methods, taking into account all bins up to $|\eta| < 3.14$. The empirical function

$$f_{a,b,c}(|\eta|) = a \cdot \frac{b \cdot \cosh(|\eta|)}{1 + c \cdot \cosh(|\eta|)} \tag{6.7}$$

is used for this purpose. Evaluating the fitted function at the center of a given $|\eta|$ bin yields the final correction factor that must be multiplied to the values shown in figure 6.4 in order to obtain the final relative residual corrections. As expected, k_{FSR} is almost negligible for the MPF method while it takes sizeable values for the p_{T}-balance method.

The final relative residual jet energy scale corrections are shown in figure 6.7 as a function of $|\eta|$. The result obtained with the MPF method constitutes the nominal value and the result of the p_{T}-balance method serves as a cross-check. The statistical uncertainty in this result is propagated from the bare ratio of responses in data and simulation and the fit used to obtain the k_{FSR} correction. Good agreement between the two methods is observed across the full range of $|\eta|$. Most bins agree with unity within

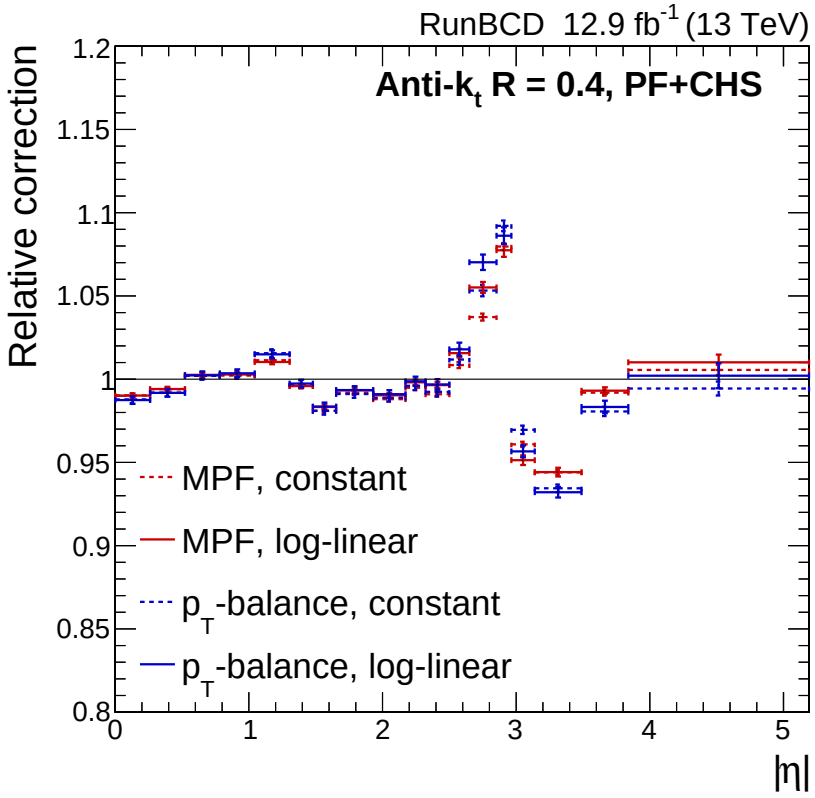

Figure 6.7: L2Res relative residual jet energy scale correction factors as a function of $|\eta|$ for the p_{T}-balance (blue) and MPF (red) methods. The dashed lines indicate values obtained with a constant fit to the ratio of responses versus p_{T}, while the solid lines represent the nominal result obtained from a log-linear fit.

3% and demonstrate the excellent precision of the CMS jet energy calibration. In the transition region between endcap and hadron forward HCAL coverage, the magnitude of the L2Res corrections takes values up to 10%.

6.5 Systematic Uncertainties

All systematic uncertainties considered for the L2Res correction factors are discussed briefly in the following.

6.5.1 Dependence on $\overline{p}_{\mathrm{T}}$

As described in section 6.4.2, the ratio of responses in simulation and data is first evaluated in bins of $|\eta|$ and $\overline{p}_{\mathrm{T}}$. Because the L2Res corrections are derived only as a function of $|\eta|$, a potential dependence of the detector response on $\overline{p}_{\mathrm{T}}$ is eliminated by evaluating

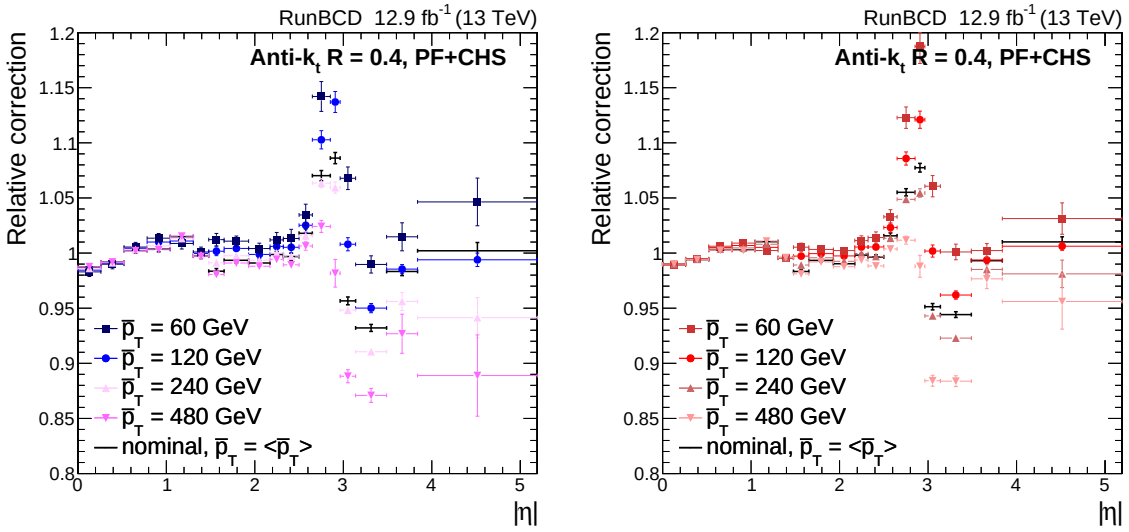

Figure 6.8: L2Res relative residual jet energy scale correction factors as a function of $|\eta|$ for the p_T-balance (left) and MPF (right) methods when evaluating the log-linear fit at different values of $\overline{p}_\mathrm{T}$. The nominal result shown in black corresponds to $\overline{p}_\mathrm{T} = \langle \overline{p}_\mathrm{T} \rangle$.

the log-linear fit described in section 6.4.2 at $\langle \overline{p}_\mathrm{T} \rangle$ in each bin of $|\eta|$. To determine the degree of $\overline{p}_\mathrm{T}$-dependence of that result, the log-linear fit is additionally evaluated at different values of $\overline{p}_\mathrm{T}$, i.e. $\overline{p}_\mathrm{T} \in \{\langle \overline{p}_\mathrm{T} \rangle,\ 60\,\mathrm{GeV},\ 120\,\mathrm{GeV},\ 240\,\mathrm{GeV},\ 480\,\mathrm{GeV}\}$, as shown in figure 6.8. The stronger the $\overline{p}_\mathrm{T}$-dependence in a given bin of $|\eta|$ is, the larger is the difference in the final correction factors.

In the region of $|\eta| < 2.5$, the L2Res correction factor shows only a small dependence on $\overline{p}_\mathrm{T}$, while in the transition region and the HF-covered part, deviations from the nominal result by up to 10% are observed. Half of the difference between the correction obtained with the log-linear fit and the constant fit is taken as a systematic uncertainty accounting for the $\overline{p}_\mathrm{T}$-dependence of the final result.

6.5.2 Jet Energy Resolution Uncertainty

For the derivation of the L2Res corrections, simulated events are used, in which the JER was smeared to match the JER in data. Because both, the MPF and the p_T-balance methods, are sensitive to differences in the JER between data and simulation, uncertanties in the JER scale factors are propagated to the L2Res measurement. For this, the JER correction factors used are varied within their total uncertainties and the impact on the final L2Res correction is considered as a systematic uncertainty.

6.5.3 Dependence on ISR and FSR

For a study of uncertainties in the simulation and modelling of additional ISR and FSR, a QCD multijet sample generated with a different generator (HERWIG++) is used. The difference between the L2Res correction factors derived with the nominal sample simulated with PYTHIA 8 and this additional sample is taken as the systematic uncertainty in modelling ISR and FSR.

6.5.4 Time Stability

The non-uniformity of the 2016 data over time is taken into account by comparing the luminosity-weighted average of the L2Res corrections with a fifth set of L2Res corrections, derived on the full 2016 data instead of four subsets of it. The difference between the two correction factors is taken as the systematic uncertainty due to the time (in)stability of the L2Res correction.

6.5.5 Method of Derivation

Because the MPF and p_{T}-balance methods should in principle yield the same values, the difference between the residual correction factors derived with the two methods (figure 6.7, blue and red markers) is taken as an additional systematic uncertainty.

6.5.6 Contribution to the Overall Jet Energy Scale Uncertainty

In figure 6.9, the overall uncertainty in the jet energy scale is shown as a function of η of the jet using a different, more recent, calibration than the one presented in this chapter, also derived on data recorded in the year 2016 [154]. However, it illustrates the contribution of uncertainties considered in the derivation of the L2Res corrections to the total JEC uncertainty. The *relative scale* contribution corresponds to the impact of JER and ISR and FSR on the L2Res correction as described previously, which has a dominant impact in the transition region around $|\eta| = 3$. The *method & sample* contribution is derived from multiple steps in the factorized JEC approach and takes into account the difference between corrections obtained with the p_{T}-balance and MPF methods as well as differences between individual measurements in regions where more than one measurement is available. This uncertainty has the dominant contribution to the overall JEC uncertainty in the region of $|\eta| > 2.5$. A minor contribution originates

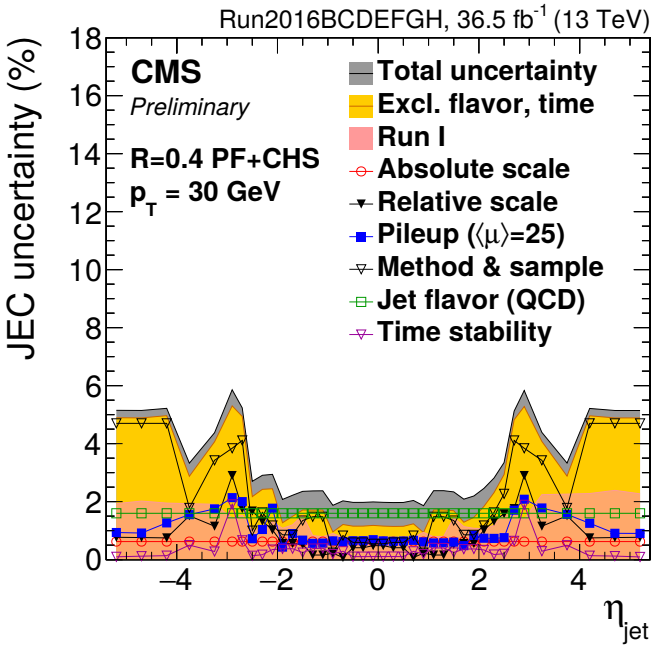

Figure 6.9: Contributions of different sources of uncertainties in the jet energy scale to the overall jet energy scale uncertainty derived on data recorded in the year 2016 as a function of η of the jet. A different L2Res calibration than the one presented in this chapter was used for this result. Taken from Ref. [154].

from the *time stability* of the L2Res and L3Res corrections. The other sources of uncertainties shown in figure 6.9 have no contribution from the L2Res correction factors. The uncertainty due to the dependence on $\overline{p}_{\mathrm{T}}$ of the L2Res correction factors is not shown in figure 6.9 because the L2Res corrections were provided as a function of $\overline{p}_{\mathrm{T}}$ in the calibration used for that result.

6.6 Summary

The relative residual jet energy scale corrections are a vital part in the factorized CMS jet energy correction scheme. They are derived in QCD dijet events for L1L2L3 corrected jets and aim at correcting small differences in the detector response between data and simulation relative to the central part of the detector. The response is computed with two complementary methods and corrected for the effect of additional jet radiation in the initial or final state. Four sets of $|\eta|$-dependent corrections are provided, corresponding to the four sets of data recorded under similar conditions. A number of systematic uncertainties is considered, which are small in the barrel of the detector and can take values of $\mathcal{O}(10\%)$ in the transition region and the most forward

region.

Chapter 7

Search for Pair-Produced Leptoquarks

In this chapter, a search for pair production of leptoquarks decaying to top quarks and muons is presented. As explained previously, this decay mode is essential in many BSM theories that aim at resolving the tension between the SM prediction and experimental data in the b-flavor sector (cf. chapter 3). It can also be used to explain the value of the anomalous magnetic moment of the muon, which would receive corrections from such an LQ.

First, an overview over the strategy of the presented analysis is given in section 7.1, followed by a description of the data and simulated samples analyzed (section 7.2). The measurement of the electron trigger efficiency is presented in section 7.3. Afterwards, the main event selection is introduced in section 7.4, and the LQ mass reconstruction is explained in section 7.5. The measurement of the lepton misidentification rates is presented in section 7.6. In section 7.7, the data-driven background estimation method is described, followed by a discussion of the systematic uncertainties in section 7.8. The results of this search and the combination with other LQ decay channels are highlighted in sections 7.9 and 7.10, respectively. Prospects for the HL-LHC are given in section 7.11. This chapter concludes with an outlook in section 7.12. The analysis presented in this chapter has been published in Ref. [83], the HL-LHC projection has been published in Refs. [155–157].

7.1 Analysis Overview

This section introduces the general analysis strategy of the search for pair-produced LQs in the tμ decay channel. This search makes use of a number of orthogonal signal

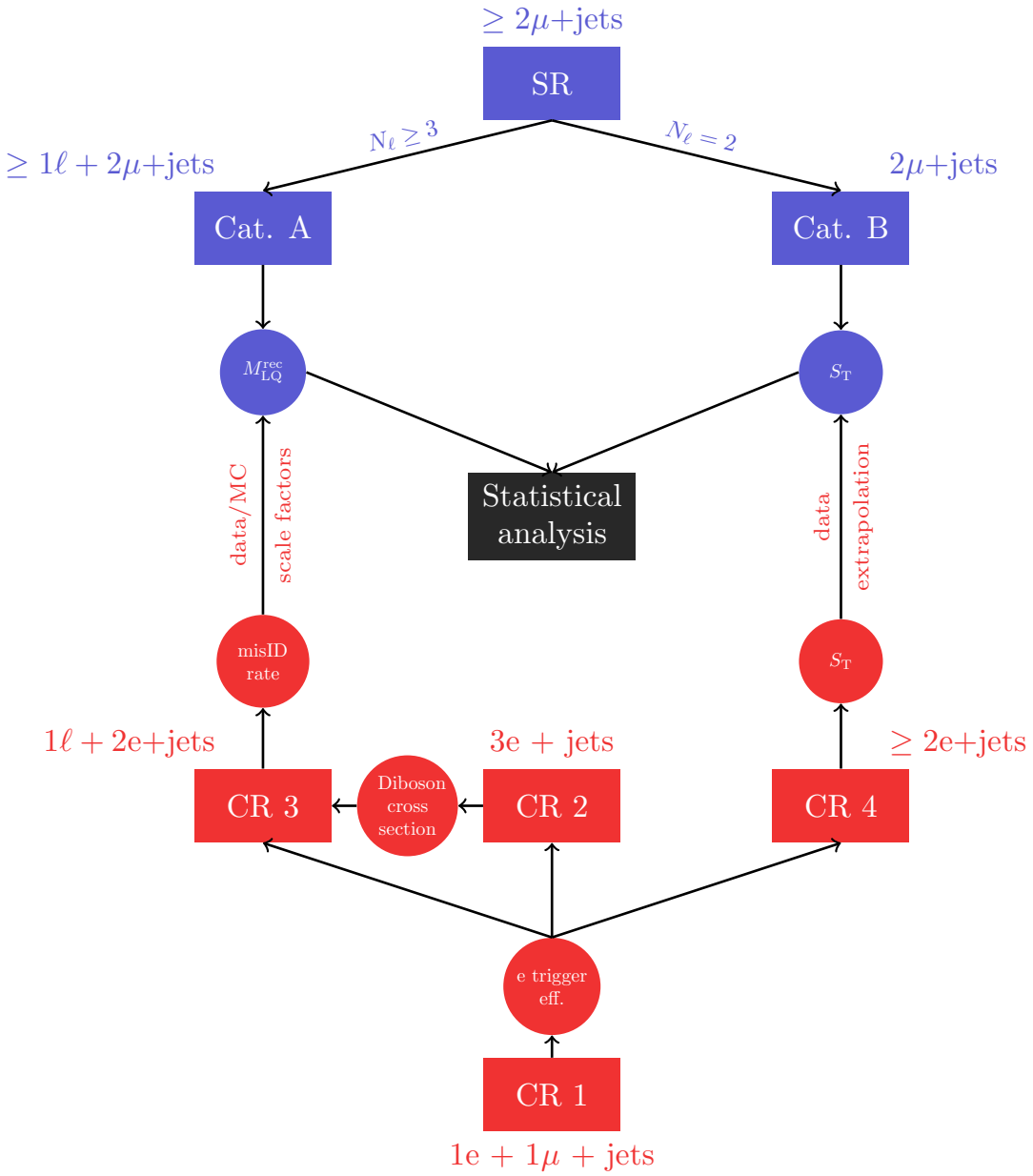

Figure 7.1: Illustration of the analysis strategy.

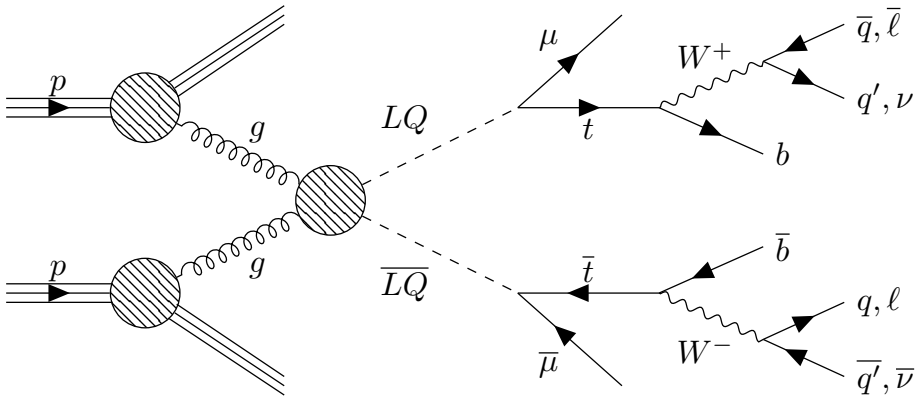

Figure 7.2: Leading-order Feynman diagram of the gluon-induced pair production of LQs, their decay to top quarks and muons, and the subsequent decay of the top quarks.

and control regions, which are briefly described here and explained in detail in the following sections. An illustration of the structure of the presented analysis is given in figure 7.1. The leading-order Feynman diagram of the decay of pair-produced LQs to top quarks and muons is shown in figure 7.2. In this analysis, all possible subsequent decays of the top quark pair are considered, which is reflected in the event selection.

Irrespective of the top quark decays, the expected signature of the decay of a pair of LQs contains at least two muons and multiple jets. The signal region (SR) is optimized for sensitivity to a potential LQ signal and therefore contains events fulfilling that expectation. The SR is further divided into two orthogonal categories targeting different decay modes of the top quark pair. They are combined statistically in a simultaneous maximum-likelihood (ML) fit to both categories in the end.

Events in category A must have at least one electron or muon in addition to the two muons required before and one pair of leptons with opposite-sign (OS) electric charge. Since this category contains events with at least three leptons, usually one or both of the top quarks in this category decay(s) to the final state with a lepton originating from the subsequent W boson decay (also referred to as *leptonic decay* in the following). In category A, the LQ mass is reconstructed ($M_{\mathrm{LQ}}^{\mathrm{rec}}$) and its distribution is used in the final statistical evaluation.

Category B contains all remaining events of the SR that do not fall into category A. The top quark pair is expected to decay to the all-jets final state (also referred to as *hadronic decay* in the following) in this category. Here, the variable S_{T} is used to discriminate signal from background in the final evaluation. It is defined as the scalar

sum of the transverse momenta of all electrons, muons, AK4 jets, and $p_{\mathrm{T}}^{\mathrm{miss}}$ in an event,

$$S_{\mathrm{T}} = \sum_{e,\mu,\mathrm{jets}} p_{\mathrm{T}} + p_{\mathrm{T}}^{\mathrm{miss}}. \tag{7.1}$$

Apart from the SR, this analysis exploits a number of control regions (CRs) for the derivation of the dominant background contributions directly from data (category B) or correcting for differences between data and simulation (category A). Ideally, such CRs reflect the kinematics of the SR and contain as little signal contamination as possible. Since the SR contains events with at least two muons, utilizing the final state with at least two electrons instead of muons is a natural choice to achieve both.

The data in the CRs is collected by different triggers than that in the SR (cf. section 7.2). Therefore, the efficiency of those triggers is first measured in a $\mathrm{t\bar{t}}+\mathrm{jets}$ enriched region (CR 1) relative to the trigger used in the SR. Differences in the efficiency between data and simulated events are corrected. The resulting data/MC scale factors are then used in all other CRs.

Since category A contains events with at least 3 leptons, the misidentification (misID) rate of electrons and muons in simulated events needs to be studied and potentially corrected. This is done in a CR requiring at least two electrons with a dielectron mass around M_{Z} (CR 3), which is therefore enriched in Drell-Yan + jets (DY + jets) events. The presence of one additional electron or muon is then used to measure the misID rate of the respective lepton flavor. The main background to that measurement are diboson events that can produce three or more prompt leptons. The production cross section of such events is controlled in a dedicated region (CR 2).

About 90% of the events in category B arise from $\mathrm{t\bar{t}}+\mathrm{jets}$ and DY + jets production. Their contribution is estimated in a data-driven procedure from a region (CR 4) with at least two electrons and otherwise kinematic requirements very similar to the ones in the SR. This leads to a strongly improved description of all kinematic variables in category B and largely reduced systematic uncertainties.

The results of this search are finally interpreted not only for the case of exclusive decays of $\mathrm{LQ} \to \mathrm{t}\mu$ but also in scenarios where one additional decay channel is considered, either $\mathrm{LQ} \to \mathrm{t}\tau$ or $\mathrm{LQ} \to \mathrm{b}\nu$.

7.2 Dataset and Simulated Events

In this search, data taken in pp collisions at $\sqrt{s} = 13\,\mathrm{TeV}$ by the CMS experiment in the year 2016 are analyzed. They correspond to an integrated luminosity of $L = 35.9\,\mathrm{fb}^{-1}$.

M_{LQ} [GeV]	σ [pb]	Generator	N
200	$6.06 \cdot 10^{1}$	PYTHIA	74079
300	$8.05 \cdot 10^{0}$	PYTHIA	73905
400	$1.74 \cdot 10^{0}$	PYTHIA	74516
500	$4.96 \cdot 10^{-1}$	PYTHIA	74478
600	$1.69 \cdot 10^{-1}$	PYTHIA	71639
700	$6.48 \cdot 10^{-2}$	PYTHIA	74723
800	$2.73 \cdot 10^{-2}$	PYTHIA	74571
900	$1.23 \cdot 10^{-2}$	PYTHIA	73216
1000	$5.86 \cdot 10^{-3}$	PYTHIA	73496
1200	$1.50 \cdot 10^{-3}$	PYTHIA	74730
1400	$4.32 \cdot 10^{-4}$	PYTHIA	74095
1700	$7.74 \cdot 10^{-5}$	PYTHIA	73934
2000	$1.55 \cdot 10^{-5}$	PYTHIA	74731

Table 7.1: Summary of the simulated samples of LQ pair production with $\mathrm{LQ} \to \mathrm{t}\mu$ decays used. Listed are the generated LQ mass, the production cross section σ, the name of the generator, and the number N of generated events.

The data were recorded by triggers requiring the presence of at least one lepton. In the SR, at least one isolated muon with an online p_{T} of at least 24 GeV is required by applying the logical *or* of two triggers, which differ only in the way the muon candidate is reconstructed.

In the CRs, the logical *or* of two triggers requiring at least one electron is used. The first trigger requires at least one isolated electron with online $p_{\mathrm{T}} > 27\,\mathrm{GeV}$, the second one requires at least one electron without any isolation requirement and an online $p_{\mathrm{T}} > 115\,\mathrm{GeV}$. The second trigger is used to recover efficiency at high electron p_{T}, where electrons are not isolated in the selected event topology.

The pair production of scalar leptoquarks with prompt decays to top quarks and muons is simulated with the PYTHIA 8.205 event generator at LO. Samples are generated for LQ masses between 200 and 2000 GeV. They are listed in table 7.1.

A large number of SM background processes is considered in this analysis. The complete list of all background samples used is given in table 7.2. The $\mathrm{t\bar{t}}+\mathrm{jets}$ production is simulated with POWHEG v2 [158] at NLO. Single top quark production is simulated for three different processes at NLO. The t-channel production mode is also generated with POWHEG v2 [159], the associated production of a single top quark and a W boson is simulated with POWHEG v1 [160], and single top quark production in the s-channel is generated with MadGraph5_aMC@NLO v2.2.2. In the former two processes, all decays of the generated particles are simulated, while in the latter only leptonic decays are considered. The MadGraph5_aMC@NLO event generator is also

Process	σ [pb]	Generator	N [10^6]
$t\bar{t}$ + jets	$8.3 \cdot 10^2$	POWHEG + PYTHIA	155.2
$W(\to \ell\nu)$ + jets, $\hat{p}_T \in [100, 250)$ GeV	$6.9 \cdot 10^2$	AMC@NLO + PYTHIA	176792.6
$W(\to \ell\nu)$ + jets, $\hat{p}_T \in [250, 400)$ GeV	$2.5 \cdot 10^1$	AMC@NLO + PYTHIA	617.7
$W(\to \ell\nu)$ + jets, $\hat{p}_T \in [400, 600)$ GeV	$3.1 \cdot 10^0$	AMC@NLO + PYTHIA	11.7
$W(\to \ell\nu)$ + jets, $\hat{p}_T \in [250, 400)$ GeV	$4.7 \cdot 10^{-1}$	AMC@NLO + PYTHIA	1.8
$DY(Z/\gamma \to \ell\ell)$ + jets, $H_T \in [70, 100)$ GeV	$2.2 \cdot 10^2$	MADGRAPH + PYTHIA	9.6
$DY(Z/\gamma \to \ell\ell)$ + jets, $H_T \in [100, 200)$ GeV	$1.8 \cdot 10^2$	MADGRAPH + PYTHIA	10.6
$DY(Z/\gamma \to \ell\ell)$ + jets, $H_T \in [200, 400)$ GeV	$5.0 \cdot 10^1$	MADGRAPH + PYTHIA	9.6
$DY(Z/\gamma \to \ell\ell)$ + jets, $H_T \in [400, 600)$ GeV	$7.0 \cdot 10^0$	MADGRAPH + PYTHIA	10.0
$DY(Z/\gamma \to \ell\ell)$ + jets, $H_T \in [600, 800)$ GeV	$1.7 \cdot 10^0$	MADGRAPH + PYTHIA	8.3
$DY(Z/\gamma \to \ell\ell)$ + jets, $H_T \in [800, 1200)$ GeV	$7.8 \cdot 10^{-1}$	MADGRAPH + PYTHIA	2.7
$DY(Z/\gamma \to \ell\ell)$ + jets, $H_T \in [1200, 2500)$ GeV	$1.9 \cdot 10^{-1}$	MADGRAPH + PYTHIA	0.6
$DY(Z/\gamma \to \ell\ell)$ + jets, $H_T \in [2500, \infty)$ GeV	$4.4 \cdot 10^{-3}$	MADGRAPH + PYTHIA	0.4
Single t, t-channel	$1.4 \cdot 10^2$	POWHEG + PYTHIA	6.0
Single $\bar{t}$, t-channel	$8.1 \cdot 10^1$	POWHEG + PYTHIA	3.9
Single t / $\bar{t}$, s-channel	$3.4 \cdot 10^0$	AMC@NLO + PYTHIA	3.4
Single t, tW-channel	$3.6 \cdot 10^1$	POWHEG + PYTHIA	6.9
Single $\bar{t}$, tW-channel	$3.6 \cdot 10^1$	POWHEG + PYTHIA	6.9
Diboson (WW$\to 2\ell 2\nu$)	$1.2 \cdot 10^1$	POWHEG + PYTHIA	2.0
Diboson (WW$\to \ell\nu$2q)	$5.0 \cdot 10^1$	POWHEG + PYTHIA	9.0
Diboson (WZ$\to \ell\nu$2q)	$1.1 \cdot 10^1$	AMC@NLO + PYTHIA	420.5
Diboson (WZ$\to 2\ell$2q)	$5.6 \cdot 10^0$	AMC@NLO + PYTHIA	233.1
Diboson (WZ$\to 3\ell\nu$)	$4.4 \cdot 10^0$	POWHEG + PYTHIA	2.0
Diboson (ZZ$\to 2\ell 2\nu$)	$5.6 \cdot 10^{-1}$	POWHEG + PYTHIA	8.8
Diboson (ZZ$\to 2\ell$2q)	$3.2 \cdot 10^0$	AMC@NLO + PYTHIA	77.9
Diboson (ZZ$\to 4\ell$)	$1.2 \cdot 10^0$	AMC@NLO + PYTHIA	20.5
$t\bar{t}$ + W$(\to \ell\nu)$	$2.0 \cdot 10^{-1}$	AMC@NLO + PYTHIA	3.5
$t\bar{t}$ + Z$(\to \ell\ell$ / $\nu\nu)$	$2.5 \cdot 10^{-1}$	AMC@NLO + PYTHIA	1.8
QCD, μ enr., $\hat{p}_T \in [15, 20)$ GeV	$3.8 \cdot 10^6$	PYTHIA	4.1
QCD, μ enr., $\hat{p}_T \in [20, 30)$ GeV	$3.0 \cdot 10^6$	PYTHIA	31.5
QCD, μ enr., $\hat{p}_T \in [30, 50)$ GeV	$1.7 \cdot 10^6$	PYTHIA	29.9
QCD, μ enr., $\hat{p}_T \in [50, 80)$ GeV	$4.4 \cdot 10^5$	PYTHIA	19.8
QCD, μ enr., $\hat{p}_T \in [80, 120)$ GeV	$1.1 \cdot 10^5$	PYTHIA	13.8
QCD, μ enr., $\hat{p}_T \in [120, 170)$ GeV	$2.5 \cdot 10^4$	PYTHIA	8.0
QCD, μ enr., $\hat{p}_T \in [170, 300)$ GeV	$8.7 \cdot 10^3$	PYTHIA	7.9
QCD, μ enr., $\hat{p}_T \in [300, 470)$ GeV	$8.0 \cdot 10^2$	PYTHIA	7.9
QCD, μ enr., $\hat{p}_T \in [470, 600)$ GeV	$7.9 \cdot 10^1$	PYTHIA	3.9
QCD, μ enr., $\hat{p}_T \in [600, 800)$ GeV	$2.5 \cdot 10^1$	PYTHIA	4.0
QCD, μ enr., $\hat{p}_T \in [800, 1000)$ GeV	$4.7 \cdot 10^0$	PYTHIA	4.0
QCD, μ enr., $\hat{p}_T \in [1000, \infty)$ GeV	$1.6 \cdot 10^0$	PYTHIA	4.0
QCD, EM enr., $\hat{p}_T \in [20, 30)$ GeV	$5.4 \cdot 10^6$	PYTHIA	9.2
QCD, EM enr., $\hat{p}_T \in [30, 50)$ GeV	$9.9 \cdot 10^6$	PYTHIA	4.7
QCD, EM enr., $\hat{p}_T \in [50, 80)$ GeV	$2.9 \cdot 10^6$	PYTHIA	23.5
QCD, EM enr., $\hat{p}_T \in [80, 120)$ GeV	$4.2 \cdot 10^5$	PYTHIA	35.8
QCD, EM enr., $\hat{p}_T \in [120, 170)$ GeV	$7.7 \cdot 10^4$	PYTHIA	77.8
QCD, EM enr., $\hat{p}_T \in [170, 300)$ GeV	$1.9 \cdot 10^4$	PYTHIA	11.5
QCD, EM enr., $\hat{p}_T \in [300, \infty)$ GeV	$1.4 \cdot 10^3$	PYTHIA	7.4
QCD, bc $\to$ e, $\hat{p}_T \in [15, 20)$ GeV	$2.5 \cdot 10^5$	PYTHIA	2.7
QCD, bc $\to$ e, $\hat{p}_T \in [20, 30)$ GeV	$3.3 \cdot 10^5$	PYTHIA	10.9
QCD, bc $\to$ e, $\hat{p}_T \in [30, 80)$ GeV	$4.1 \cdot 10^5$	PYTHIA	15.3
QCD, bc $\to$ e, $\hat{p}_T \in [80, 170)$ GeV	$3.8 \cdot 10^4$	PYTHIA	15.0
QCD, bc $\to$ e, $\hat{p}_T \in [170, 250)$ GeV	$2.6 \cdot 10^3$	PYTHIA	9.5
QCD, bc $\to$ e, $\hat{p}_T \in [250, \infty)$ GeV	$7.1 \cdot 10^2$	PYTHIA	9.8

Table 7.2: Summary of the simulated samples of SM background processes. Listed are the simulated process, the production cross section σ including filter efficiencies and K factors (see text), the name of the generator, and the number N of weighted events.

used to simulate the production of a top quark pair in association with a heavy gauge boson ($t\bar{t}+V$) and of a W boson with additional jet radiation (W + jets) at NLO. For the generation of the production of two heavy gauge bosons and jets (diboson) at NLO, MadGraph5_amc@nlo and powheg v2 [161, 162] are used and only decays that result in at least one lepton in the final state are considered. The simulation of DY + jets processes, $Z/\gamma^{\star} \to \ell\ell$, is performed with MadGraph5_amc@nlo at LO. A flat so-called K factor is applied to scale the production cross section of such events from LO to NLO, $K = 1.23$. Last, QCD multijet events are generated with pythia at LO. In the QCD simulation, the generated events are filtered and only those that contain at least one muon or electron are considered in the analysis. The filtering efficiency ranges between 0.02 and 16.5%.

For generating events at LO (NLO), the NNPDF3.0 [16] PDFs at LO (NLO) are used. For all samples mentioned above, the parton shower and hadronization is simulated with pythia. The UE is modelled using the CUETP8M1 [163, 164] tune for pythia for all samples but $t\bar{t}$ + jets and single top quark production in the t-channel, where the CUETP8M2T4 [165] tune is used instead. Simulated events are reweighted to match the number of simulated interactions per bunch-crossing to the number of PU interactions in data. The distribution of the number of PU interactions per event in data is a superposition of Poisson distributions derived from the inelastic pp cross section [166]. Considering different data-taking periods with varying instantaneous luminosities, Poisson distributions around the mean number of expected PU interactions $\mu = \mathcal{L} \cdot \sigma_{\mathrm{pp}}$, using $\sigma_{\mathrm{pp}} = 69.2\,\mathrm{mb}$, are constructed. The event weights applied to simulation are defined as the ratio of the distribution of the number of true interactions in simulation and the superposition of the Poisson distributions in data.

In order to compare the simulated SM prediction to the recorded data, all simulated events are reweighted according to the cross section σ of the simulated process and the integrated luminosity $L = 35.9\,\mathrm{fb}^{-1}$ of the dataset. The weight w applied to each event is defined as $w = \frac{\sigma \cdot L}{N}$, where N is the weighted number of generated events in the respective sample. For N, event weights applied by the generator itself are taken into account.

7.3 Electron Trigger Efficiency Measurement

The measurement of the efficiency of the combination of electron triggers used in the main CRs of this analysis is carried out in a dedicated CR. It contains events with exactly one electron and one muon in the final state. A tag-and-probe method in events

of $\mathrm{t\bar{t}}+\text{jets}$ production is then used to measure the efficiency of the electron triggers with respect to the one of the muon trigger used in the SR. The efficiency of the muon trigger has been measured by the CMS Collaboration [144], which also provided data/MC scale factors to correct for differences between data and simulation.

7.3.1 Event Selection

The event selection aims at selecting events of $\mathrm{t\bar{t}}+\text{jets}$ production, where both of the two top quarks undergo a leptonic decay and produce the final state with exactly one muon and one electron. In this way, the muon can be used as a tagged lepton (henceforth referred to as *tag*) and the electron acts as the probe, which is to measure the efficiency of the electron triggers.

The tagged muon (probe electron) is required to fulfil the tight ID criteria for muons (electrons), have $p_\mathrm{T} > 30(10)\,\mathrm{GeV}$, $|\eta| < 2.4$. Additionally, muons and electrons must be isolated. Here, the isolation criterion included in the tight ID is used for electrons, while muons are required to have a relative isolation $I_\mathrm{rel} < 0.15$ (cf. equation (5.2)). Importantly, the electron requirements except for the p_T cut are the same as in the CRs using the single-electron triggers. The choice of the tag to be a muon facilitates selecting a sample of events unbiased with respect to the electron triggers under study.

For the same reason, the single-muon triggers used in the SR are employed for collecting data in this CR. Because the efficiency of those triggers has been corrected to be the same in data and simulated events, the measurement of the electron trigger efficiency can be carried out relative to the single-muon triggers. Differences between data and simulation can then be attributed to the single-electron triggers studied here.

Apart from the trigger and the lepton selection, the presence of at least two AK4 jets with a minimum p_T of 30 GeV and $|\eta| < 2.4$ is required. Because the requirement of exactly two leptons of opposite flavor can on tree-level only be satisfied by the SM $\mathrm{t\bar{t}}$, single top quark production in the tW channel, and rare diboson and $\mathrm{t\bar{t}}+\mathrm{V}$ processes, no further selection criteria need to be applied. The full set of selection requirements is again listed below.

- Events are recorded with the combination of muon triggers used in the SR
- Exactly one muon fulfilling the tight ID and with $p_\mathrm{T} > 30\,\mathrm{GeV}$, $|\eta| < 2.4$, and $I_\mathrm{rel} < 0.15$ is present in the event.
- Exactly one electron fulfilling the tight ID with the corresponding isolation criterion and with $p_\mathrm{T} > 10\,\mathrm{GeV}$, and $|\eta| < 2.4$ is present in the event.

- At least two AK4 jets with $p_{\mathrm{T}} > 30\,\mathrm{GeV}$, and $|\eta| < 2.4$ are present in the event.

In figure 7.3, control distributions of the events passing this selection are shown. A sample of $\mathrm{t\bar{t}}+\mathrm{jets}$ events with a purity of about 90% is selected by the above criteria. The subdominant source of background are events from single top quark production in association with a W boson, which can also produce two prompt leptons of different flavor on tree level. The contribution of diboson and $\mathrm{t\bar{t}}+\mathrm{V}$ production is negligibly small. Using events in this region of phase space for measuring the efficiency has the advantage of a relatively large number of events even at very high transverse momenta of the probe as shown in figure 7.3 (upper left). The selected events are used to derive the electron trigger efficiencies as described below.

7.3.2 Efficiency and Correction Factor Measurement

Ideally, the electron triggers would record each event that passes the offline selection detailed above and contains an electron with p_{T} above the trigger threshold. However, the real trigger efficiency can depend on the properties of the detector and the triggering object. Therefore, the trigger efficiency is measured as a function of different variables of the reconstructed electron. After having applied the event selection, the trigger efficiency ϵ is defined as the fraction of events additionally passing the trigger,

$$\epsilon = \frac{N_{\mathrm{events}}\,(\mathrm{trigger} + \mathrm{selection})}{N_{\mathrm{events}}\,(\mathrm{selection})}, \tag{7.2}$$

where the numerator represents the number of events passing the event selection as well as the electron trigger combination. The denominator contains all events that pass the event selection, irrespective of the electron triggers. Hence, by definition $\epsilon \leq 1$.

In figure 7.4 (upper row), the trigger efficiency in data and simulated events is shown as a function of p_{T} of the electron in two different binnings. Around the respective trigger threshold of each of the two individual triggers, the turn-on in the efficiency is clearly visible. The data/MC ratio is flat at high electron momenta above $p_{\mathrm{T}}^{\mathrm{e}} = 30\,\mathrm{GeV}$, i.e. after the efficiency plateau of the isolated trigger is reached. The logical combination of the isolated trigger at low and the non-isolated trigger at high transverse momenta indeed prevent a drop in efficiency over the full kinematic range. Due to the presence of two efficiency turn-on regions, the measurement of the efficiency as a function of other variables is also split into two regions, $30\,\mathrm{GeV} < p_{\mathrm{T}}^{\mathrm{e}} < 120\,\mathrm{GeV}$ and $p_{\mathrm{T}}^{\mathrm{e}} > 120\,\mathrm{GeV}$.

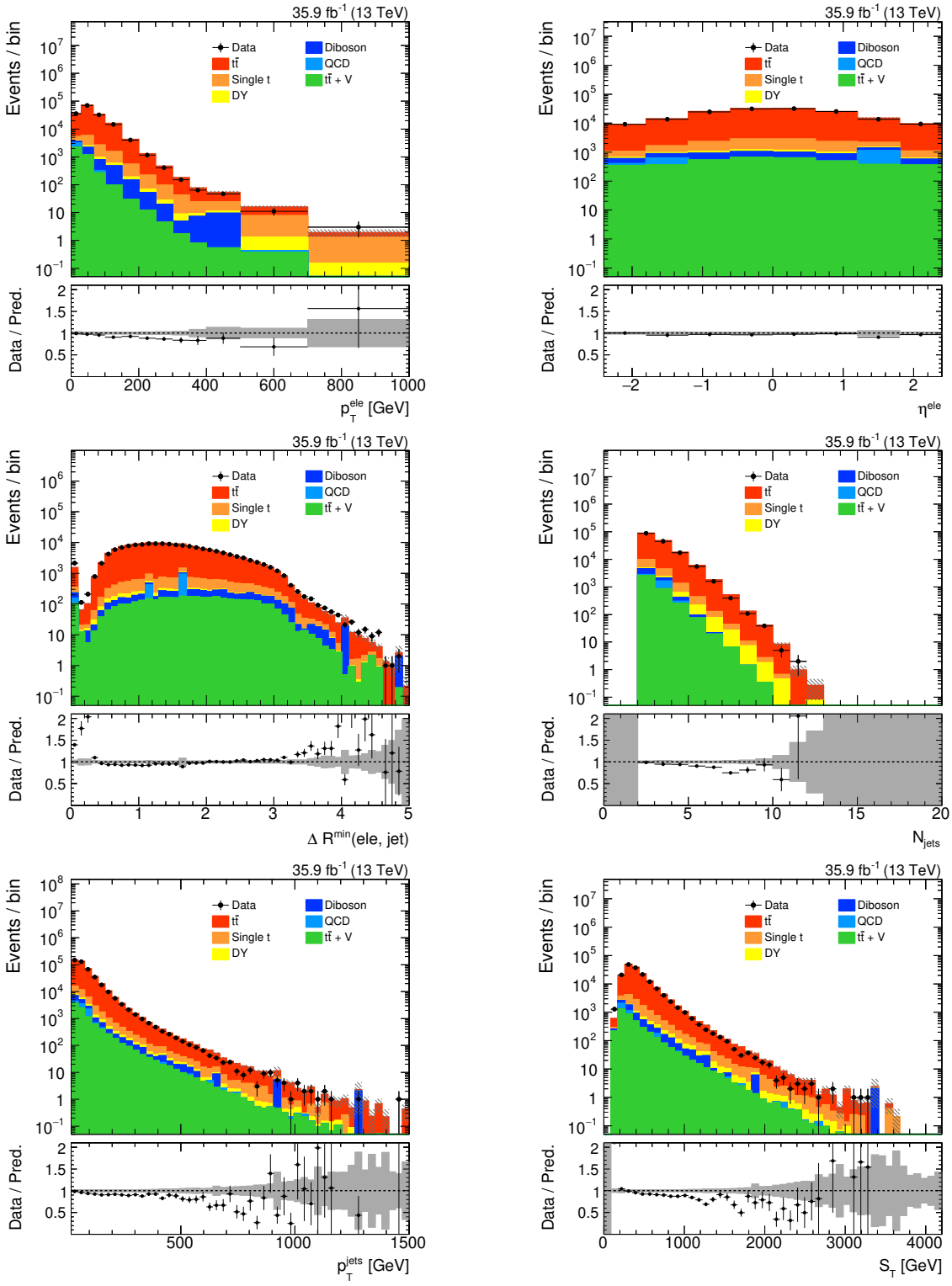

Figure 7.3: Distributions of $p_{\mathrm{T}}^{\mathrm{e}}$ (upper left), η^{e} (upper right), the distance between the electron and the closest jet (middle left), the number of AK4 jets (middle right), the p_{T} of all AK4 jets (lower left), and S_{T} (lower right) for all events passing the event selection for the trigger efficiency measurement. The lower panels show the ratio of data and simulation, the grey area corresponds to the statistical uncertainty in the SM prediction.

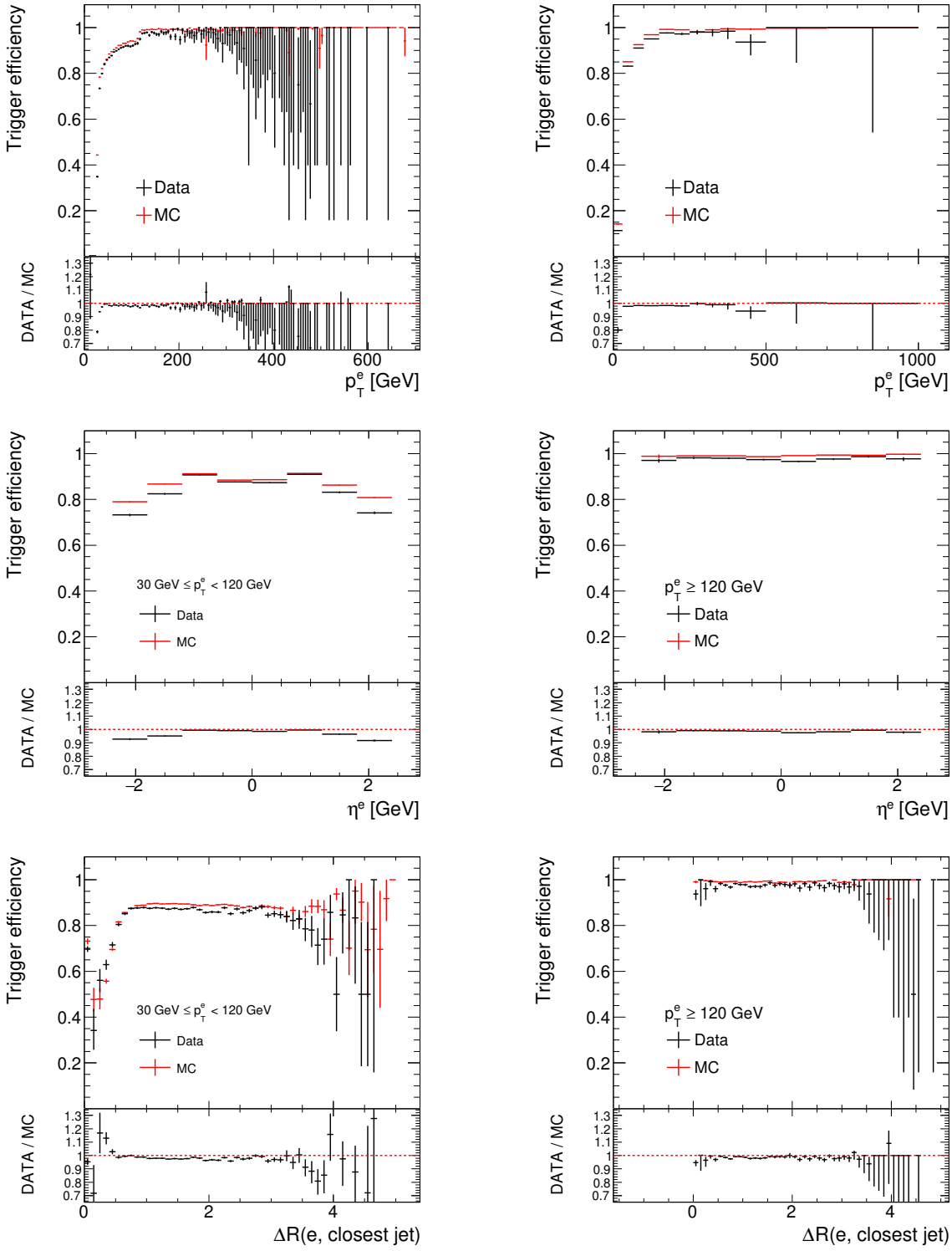

Figure 7.4: Efficiencies of the electron trigger combination in data (black) and simulated events (red) as a function of the p_{T} of the reconstructed electron in two different binnings (upper row), η of the electron in the low-p_{T} and high-p_{T} regions (middle left and right, respectively), and ΔR^{min}(e, jet) in the low-p_{T} and high-p_{T} regions (lower left and right, respectively). The lower panels show the ratio of efficiencies in data and simulation.

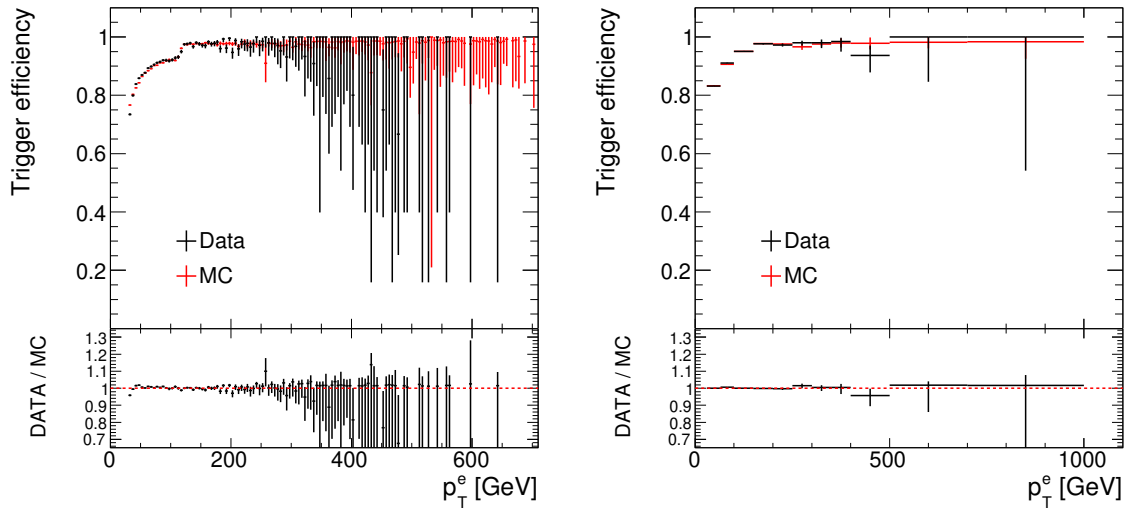

Figure 7.5: Efficiencies of the electron trigger combination in data (black) and simulated events (red) as a function of p_{T} of the reconstructed electron in fine (left) and coarse (right) binning. The simulated efficiency has been corrected to match the one in data as described in the text. The lower panels show the ratio of efficiencies in data and simulation.

In order to take the geometry of the detector into account, the efficiency is also measured as a function of η^{e}. It is shown in figure 7.4 (middle) for the low- and high-p_{T} regimes (left and right, respectively). In accordance with the behavior shown in figure 7.4 (upper row), the overall efficiency is different from unity only in the low-p_{T} region. At high-p_{T}, both efficiencies are constantly high with values of about 1.

Last, the trigger efficiency is derived as a function of the distance in R between the electron and the closest jet, $\Delta R^{\mathrm{min}}\,(\mathrm{e,\,jet})$. It is shown in figure 7.4 (lower row) for the two kinematic regimes. Since the low-p_{T} trigger requires the electron candidates to be isolated, the trigger efficiency is low for events in which the electron has a jet in its close proximity. Especially in highly-boosted $\mathrm{t\bar{t}}+\mathrm{jets}$ events, the top quark decay products are collimated and hence the value of $\Delta R^{\mathrm{min}}\,(\mathrm{e,\,jet})$ is expected to shrink with increasing $p_{\mathrm{T}}^{\mathrm{e}}$. Due to the isolation criterion on the low-p_{T} trigger, the trigger efficiency would be lower also for highly boosted events. However, it can be observed that at high $p_{\mathrm{T}}^{\mathrm{e}}$, thanks to logical combination with the non-isolated trigger, the trigger efficiency is independent of $\Delta R^{\mathrm{min}}\,(\mathrm{e,\,jet})$ and similar for data and simulated events.

Due to the good agreement of data and simulation as a function of $\Delta R^{\mathrm{min}}\,(\mathrm{e,\,jet})$, data/MC correction factors are only applied as a function of p_{T} and η of the reconstructed electron. Because the electron triggers show two distinct efficiency turn-on regions in figure 7.4, two sets of scale factors measured as a function of η^{e} are applied,

corresponding to the low- and high-p_{T} regime already introduced. They correspond to the data/MC ratio shown in the lower panels of figure 7.4 (middle row).

In order to verify that those scale factors indeed correct for all biases introduced by the electron triggers, a validation is performed. Here, the correction factors are applied to all events passing the trigger and the corrected trigger efficiency in simulation is again compared to the one in data. It is expected that data and simulation agree within the statistical uncertainties now. This comparison is shown in figure 7.5 as a function of the p_{T} of the reconstructed electron. Indeed, very good agreement between data and the corrected simulation is observed across the full kinematic range. The small shape difference in the region of $30\,\mathrm{GeV} < p_{\mathrm{T}}^{\mathrm{e}} < 50\,\mathrm{GeV}$ suggests that dedicated corrections for such low-p_{T} events could improve the description of the data. However, it has been verified that this would have negligible impact on the final scale factors and kinematic distributions.

7.4 Event Selection in the Signal Region

The event selection in the SR is split into two parts, the *pre-selection* and the *full selection*, which are presented in the following.

7.4.1 Pre-Selection

Events in the signal region have been recorded by the combination of single isolated muon triggers as explained previously. In simulated events, these triggers are emulated to provide a similar selection efficiency. Events are selected in a kinematic region where the trigger operates at the plateau of its efficiency by the criteria described below. The efficiency of the combination of triggers used has been measured by the CMS Collaboration in data and simulation [144]. Data/MC scale factors have been derived as a function of muon p_{T} and $|\eta|$, which correct the efficiency in simulated events to match the one in data.

In the SR, the list of reconstructed physics objects in an event is cleaned before applying an event selection or calculating variables describing the event kinematics. Muons are only considered if they pass the tight ID working point, have $p_{\mathrm{T}} > 30\,\mathrm{GeV}$, $|\eta| < 2.4$, and are isolated, i.e. their relative isolation fulfills $I_{\mathrm{rel}} < 0.15$. Electrons must fulfill the loose ID working point also considering the relative isolation and in addition have $p_{\mathrm{T}} > 30\,\mathrm{GeV}$ and $|\eta| < 2.4$. Last, AK4 jets are required to pass the loose noise jet ID working point and fulfill $p_{\mathrm{T}} > 30\,\mathrm{GeV}$ and $|\eta| < 2.4$. The efficiency of the requirement on the muon ID and its isolation, as well as the electron reconstruction

and identification efficiency, has been measured by the CMS Collaboration in data and simulation [144]. Similar to the muon trigger efficiency SF, the respective data/MC SFs are applied as a function of p_{T} and $|\eta|$ of each muon or electron in an event.

The decay of pair-produced LQs coupling to top quarks and muons produces two isolated muons in the final state. Depending on the LQ mass, the muon's p_{T} can take values between $\mathcal{O}(10\,\mathrm{GeV})$ and $\mathcal{O}(1\,\mathrm{TeV})$. Therefore, the requirement of at least two isolated muons passing the criteria mentioned above is a natural choice to select events of LQ pair production.

The production of two top quarks in the decay of the LQs leads to at least two additional jets in the final state. Selecting events with at least two AK4 jets hence is in accordance with the expected signature of LQ signal irrespective of the $\mathrm{t\bar{t}}$ decay mode.

Moreover, LQ events tend to exhibit a larger overall event activity, which increases with the LQ mass under consideration. A measure of the activity in the event is given by the variable S_{T} defined in equation (7.1). Requiring a minimum value of $S_{\mathrm{T}} > 350\,\mathrm{GeV}$ hardly affects signal events while rejecting a large number of background events. A summary of all pre-selection criteria is given below.

- At least two isolated muons with $p_{\mathrm{T}} > 30\,\mathrm{GeV}$, $|\eta| < 2.4$, and $I_{\mathrm{rel}} < 0.15$ must be present in an event, $N_{\mu} \geq 2$.
- At least two AK4 jets with $p_{\mathrm{T}} > 30\,\mathrm{GeV}$ and $|\eta| < 2.4$ must be present in an event, $N_{\mathrm{jets}} \geq 2$.
- A minimum value of S_{T} is required, $S_{\mathrm{T}} > 350\,\mathrm{GeV}$.

In figure 7.6, the signal selection efficiency of each requirement imposed in the pre-selection is shown as a function of the generated LQ mass. It is apparent that the requirement of at least two muons with $p_{\mathrm{T}} > 30\,\mathrm{GeV}$ has the largest impact on the signal efficiency. At low LQ masses, where the decay of LQs to a top quark and a muon is close to the kinematic threshold, the two prompt muons are not expected to have very large transverse momenta, hence the selection efficiency at such low masses is smallest. At very high LQ masses, the efficiency of this criterion reaches a plateau of about 80%.

7.4.2 Final selection

Requirements on a number of different variables are considered in the final event selection and discussed in the following. Because in the decay chain of the LQ pair two bottom quarks are expected to be produced on tree-level, it is an intuitive choice to

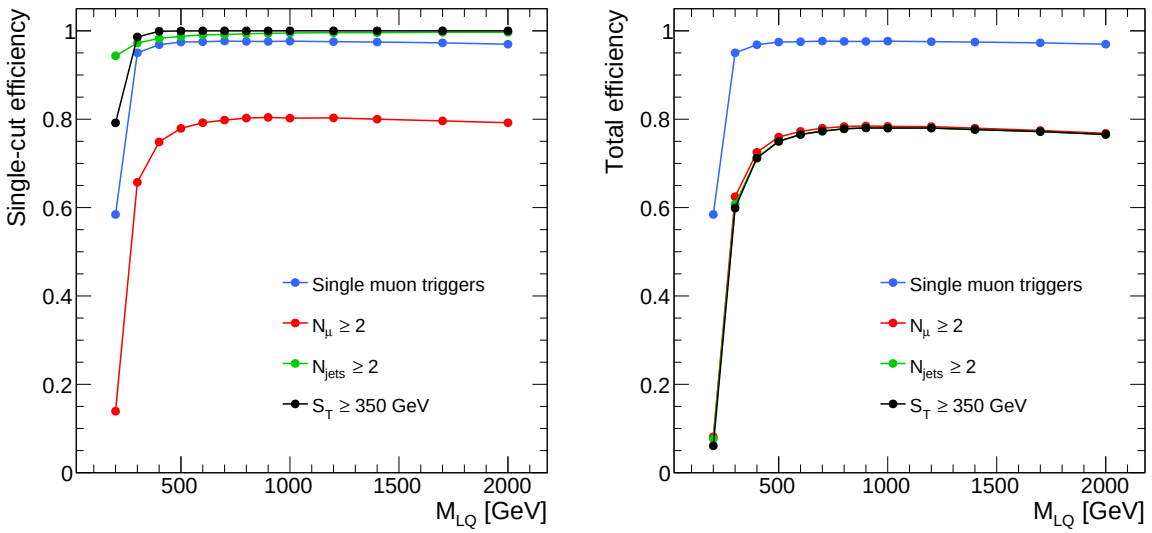

Figure 7.6: Signal selection efficiencies of each requirement imposed in the pre-selection as a function of the generated LQ mass. On the left, the efficiencies are calculated relative to the previous selection step. On the right, the efficiencies are calculated with respect to all generated events.

require the presence of b-tagged jets. Of the considered backgrounds, only events featuring the production of either single or pairs of top quarks are expected to contain b-jets as well. The number of b-tagged jets satisfying the loose b-tagging WP in events passing the pre-selection is shown in figure 7.7 (left).

Given that events of DY + jets production are the dominant source of background after the pre-selection, the invariant dimuon mass, $M_{\mu\mu}$, is another promising variable to eliminate a large fraction of background while keeping most of the signal events. The distribution of $M_{\mu\mu}$ is shown in figure 7.7 (right).

In the decay channel considered in this thesis, a pair of LQs always produces two well-isolated prompt muons. Because LQs are often expected to be heavier than SM particles, these muons can receive large Lorentz boosts depending on the mass difference between the LQ and the top quark. The resulting high transverse momentum can be used to identify a potential signal and reject SM backgrounds of any origin. Here, the variable $S_{\mathrm{T}}^{\mathrm{lep}}$, which is defined as

$$S_{\mathrm{T}}^{\mathrm{lep}} = \sum_{\mathrm{e},\mu} p_{\mathrm{T}}, \tag{7.3}$$

is considered. The distribution of $S_{\mathrm{T}}^{\mathrm{lep}}$ is shown in figure 7.8. By requiring a minimum value of $S_{\mathrm{T}}^{\mathrm{lep}}$ in the event selection, signal events can be selected more efficiently compared to SM backgrounds, which peak at low values of $S_{\mathrm{T}}^{\mathrm{lep}}$ and fall off exponen-

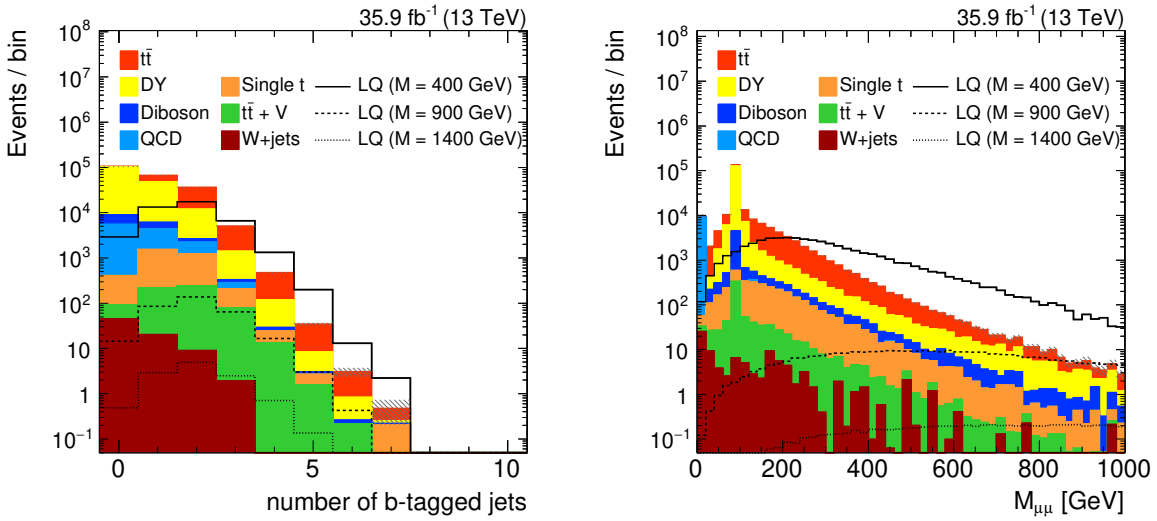

Figure 7.7: Distributions of the number of jets passing the loose b-tagging WP (left) and the invariant mass of all dimuon pairs (right) in simulated events passing the pre-selection.

tially. Especially events from $\mathrm{t\bar{t}}+\mathrm{jets}$ production can be discriminated since they are expected to contain only up to two prompt leptons with lower p_{T} in the final state compared to the signal.

The thresholds imposed on the three variables discussed above were chosen such that they maximize the sensitivity to a potential LQ signal. For this purpose, the expected significance of the LQ signal was computed as a function of the LQ mass for a set of different cuts on each variable individually. The expected significance was obtained from a log-likelihood ratio using Wilks' theorem with the THETA software package [167]. The distribution of S_{T} was used and only statistical uncertainties and systematic uncertainties in the integrated luminosity and SM production cross sections discussed in section 7.8 were considered.

The final event selection is determined by considering all permutations of those criteria. The expected significance of each combination of requirements is computed as described above. In addition, also the expected cross section upper limits are computed. A detailed description of the limit-setting procedure is given in section 7.9. Both the significances and the limits are compared for an integrated luminosity of $35.9\,\mathrm{fb}^{-1}$ and assuming unit branching fraction for the decay $\mathrm{LQ}\to\mathrm{t}\mu$. They are shown in figure 7.9. In the computation of the expected significance, the LQ signal strength is set to 0.25 instead of 1 for $300\,\mathrm{GeV}\leq M_{\mathrm{LQ}}\leq 600\,\mathrm{GeV}$ for numerical reasons.

Applying any of the suggested event selection criteria improves the sensitivity to LQ signal. Comparing the different selections, the requirement of $M_{\mu\mu}>111\,\mathrm{GeV}$

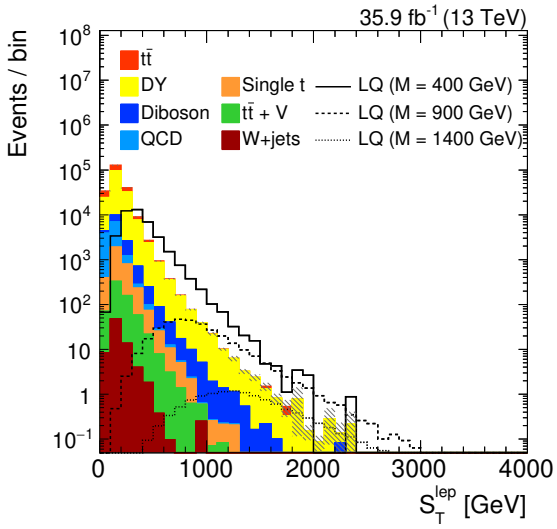

Figure 7.8: Distribution of $S_{\mathrm{T}}^{\mathrm{lep}}$ in simulated events passing the pre-selection.

yields the largest improvement in terms of both expected significance and cross section upper limits due to rejecting most of the DY + jets events Requiring $S_{\mathrm{T}}^{\mathrm{lep}} > 200\,\mathrm{GeV}$ also improves the sensitivity for LQs with $M_{\mathrm{LQ}} \geq 300\,\mathrm{GeV}$ while slightly degrading the performance for the lowest mass point of $M_{\mathrm{LQ}} = 200\,\mathrm{GeV}$, where no high-$p_{\mathrm{T}}$ leptons are expected in the signal. Enforcing the presence of at least one b-tagged jet always results in slightly improved sensitivity. Additionally, it serves the purpose of eliminating the remaining events of QCD and W+jets production. The CMS Collaboration has measured the efficiency of tagging b-jets to be different in data and simulated events, and data/MC correction factors are applied to simulation in order to correct for this effect [148]. In conclusion, the simultaneous application of all three requirements listed above results in the best expected significance and cross section upper limits over a large range of LQ masses. For clarity, the full event selection is listed below. The signal region of this search is defined by all events passing it.

- Events contain at least two muons with $p_{\mathrm{T}} > 30\,\mathrm{GeV}$, $|\eta| < 2.4$, and $I_{\mathrm{rel}} < 0.15$
- Events contain at least two AK4 jets with $p_{\mathrm{T}} > 30\,\mathrm{GeV}$ and $|\eta| < 2.4$.
- Events satisfy $S_{\mathrm{T}} > 350\,\mathrm{GeV}$.
- Events contain at least one AK4 jet satisfying the loose CSVv2 b-tagging WP.
- Events satisfy $M_{\mu\mu} > 111\,\mathrm{GeV}$.
- Events satisfy $S_{\mathrm{T}}^{\mathrm{lep}} > 200\,\mathrm{GeV}$.

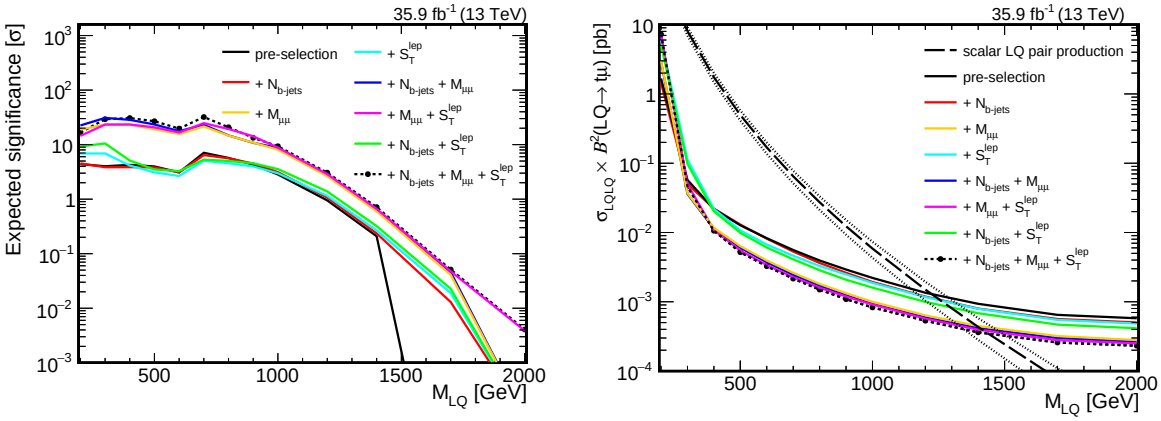

Figure 7.9: Expected significances of a scalar LQ signal (left) and cross section upper limits on scalar LQ pair production (right) for different event selections as a function of the LQ mass For calculating significances, the signal strength for masses of $300\,\text{GeV} \leq M_{\text{LQ}} \leq 600\,\text{GeV}$ is set to 0.25 instead of 1.

Figure 7.10 shows the signal selection efficiencies of the full selection as a function of the generated LQ mass. It rises steeply with the generated LQ mass and reaches a plateau of about 75% for very high LQ masses. Here, all criteria applied after the pre-selection have an efficiency of more than 90% for LQ masses of $M_{\text{LQ}} = 500\,\text{GeV}$ and above. The event categorization and LQ mass reconstruction (c.f. sections 7.4.3 and 7.5) will later improve the sensitivity to a low-mass LQ signal.

In figure 7.11, distributions of variables characterizing the selected final state are shown in data, simulated SM background and three different LQ signals of varying mass. In general, it is visible that the decay of an LQ pair is expected to produce a final state with higher jet (figure 7.11, upper left) and muon multiplicity (figure 7.11, upper right) compared to the SM background. In the distribution of the muon multiplicity, only very few events of the SM background are expected to contain more than two muons, while the LQ signal shows a considerable number of events with three or four muons. Additionally, the LQ signal is expected to produce jets and muons with larger p_{T} than the SM background processes.

The distribution of S_{T} is observed to be particularly sensitive to the presence of a hypothetical LQ signal. As this variable takes into account the transverse momenta of all reconstructed objects in the event, LQ events are expected to have high S_{T} compared to the background. Not only is it possible to distinguish signal from background, but also can different signal hypotheses be distinguished well from each other in this distribution.

Generally, the data are described well by the simulated SM prediction. A global deficit of simulated events of about 5% is observed and also a trend in the ratio of data

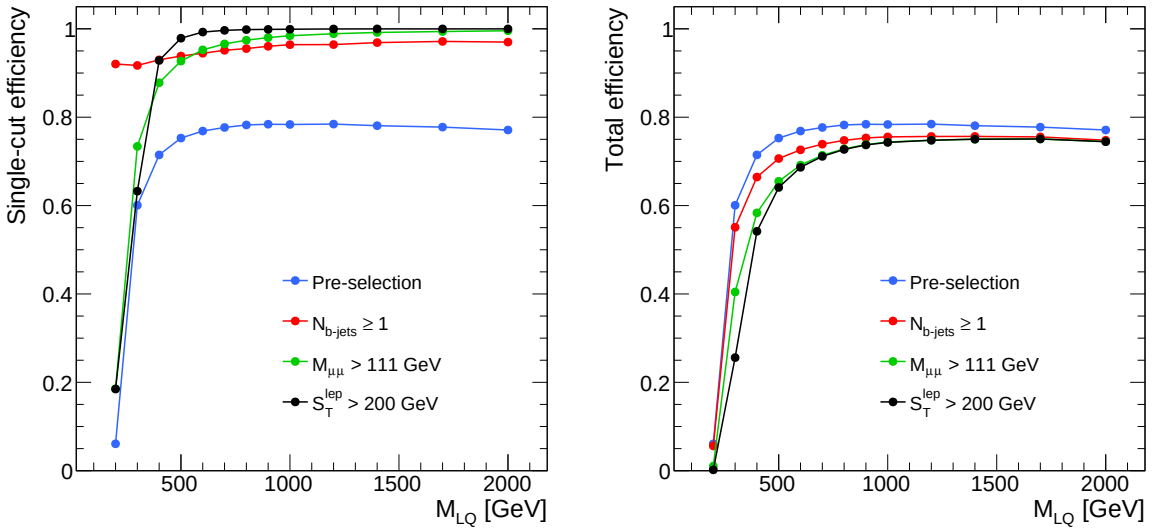

Figure 7.10: Signal selection efficiencies of each requirement imposed in the full selection as a function of the generated LQ mass. On the left, the efficiencies are calculated relative to the previous selection step. On the right, the efficiencies are calculated with respect to all generated events.

and background in some distributions. It is related to a mismodelling of the simulated SM prediction in the selected region of phase space. The need for a dedicated data-driven estimation of the major $t\bar{t}+$jets and DY$+$jets background is apparent from the disagreement between data and the prediction. That procedure is explained in section 7.7.

7.4.3 Event Categorization

All events passing the full event selection are categorized into two categories, A or B. The categories aim at different decay modes of the top quark pair produced in the LQ decays. In category A, the $t\bar{t}$ system is assumed to decay to the semi-leptonic or di-leptonic final states, producing at least one electron or muon in addition to the two muons already required in the event selection. Additionally, in this category, events must have a lepton pair with OS charge. Since the presence of three or more prompt leptons is highly unlikely in SM background processes, this category has a large signal-to-background ratio. Category B contains all events in the SR that are not assigned to category A. Here, events in which both top quarks decay hadronically are collected.

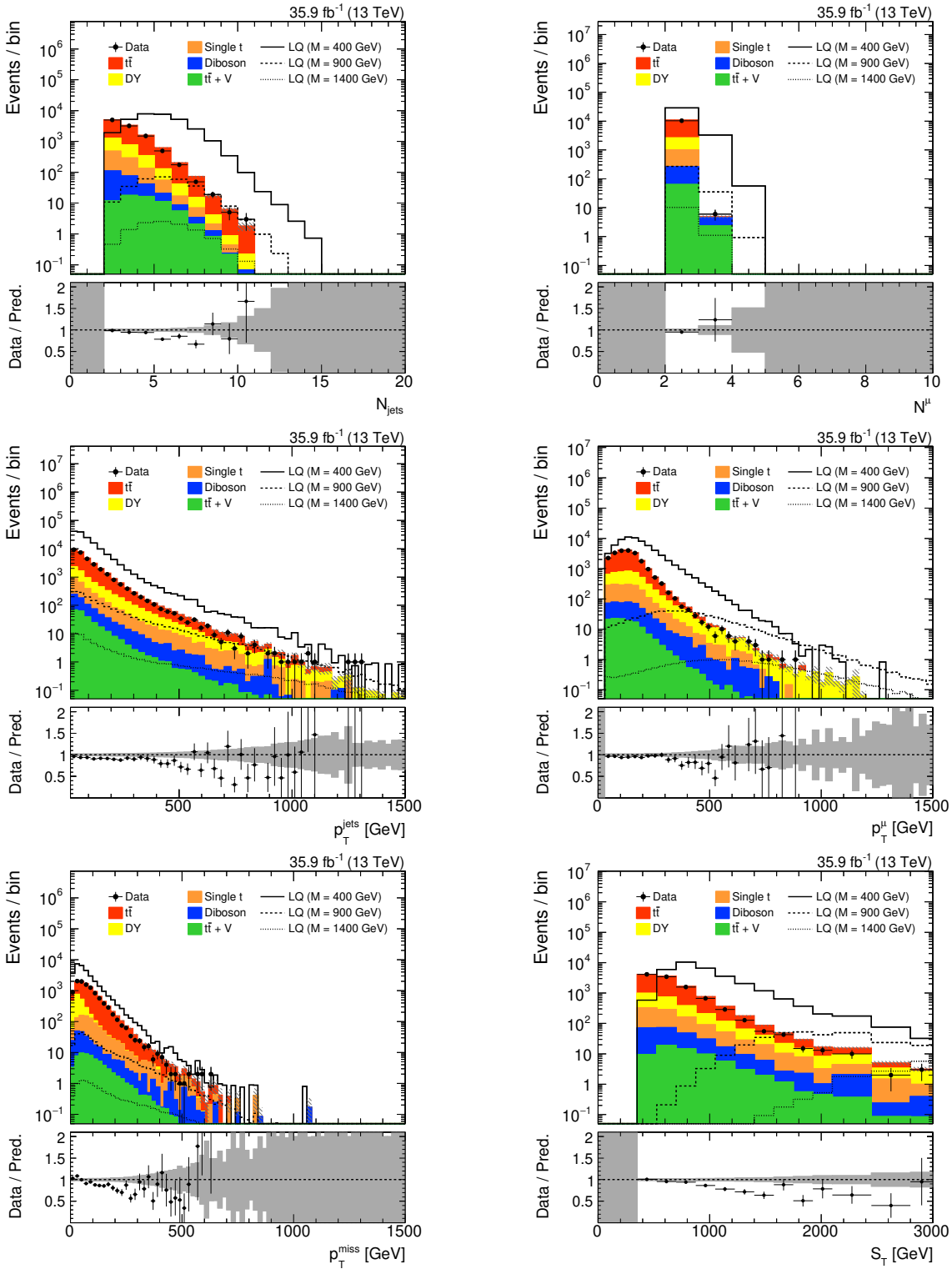

Figure 7.11: Distributions of N_{jets} (upper left), N_μ (upper right), $p_{\text{T}}^{\text{jets}}$ (middle left), p_{T}^{μ} (middle right), $p_{\text{T}}^{\text{miss}}$ (lower left), and S_{T} (lower right) for all events passing the full event selection. The lower panels show the ratio of data and simulation, the grey area corresponds to the statistical uncertainty in the SM prediction.

7.5 Reconstruction of the Leptoquark Mass

In order to discriminate a potential signal from the SM backgrounds, it is a natural choice to use the reconstructed mass of the LQs produced in an event. The basic idea of the LQ reconstruction is to combine reconstructed objects to form top quark candidates. Those are combined with muons to obtain LQ candidates, whose mass is the variable of interest.

For the reconstruction of the LQ mass, it assumed that one of the two top quarks in the LQ decay chain produces an electron or muon in the final state while the other one decays to quarks. Consequently, the LQ reconstruction is only performed in events of category A. Although signal events with both top quarks producing leptons also end up in category A, but do not satisfy the assumption of a semi-leptonic $\mathrm{t\bar{t}}$ decay, they are still passed through the reconstruction algorithm. The increased number of signal events in the distribution of the reconstructed LQ mass has been shown to increase the signal sensitivity even if the reconstruction is done under the assumption of a different decay mode. The reconstruction algorithm contains three steps.

7.5.1 Reconstruction of the Neutrino Momentum

Since exactly one neutrino is expected to be produced in the semi-leptonic $\mathrm{t\bar{t}}$ decay, its transverse momentum can be inferred by the measurement of $p_{\mathrm{T}}^{\mathrm{miss}}$. The neutrino's momentum in z-direction, $p_{z,\nu}$, can be calculated from the requirement that the invariant mass of the lepton from the top quark decay (henceforth referred to as *additional lepton*) and the neutrino equals the W boson mass,

$$P_{\mathrm{W}}^2 = M_{\mathrm{W}}^2 = (P_\ell + P_\nu)^2 , \tag{7.4}$$

with P_i the four-momentum of the particle i. Since the only unknown variable in this quadratic equation is $p_{z,\nu}$, the solution is given by

$$p_{z,\nu}^{\pm} = \frac{\mu\, p_{z,\ell}}{p_{T,\ell}^2} \pm \sqrt{\frac{\mu^2 p_{z,\ell}^2}{p_{T,\ell}^4} - \frac{E_\ell^2\, p_{T,\nu}^2 - \mu^2}{p_{T,\ell}^2}}, \tag{7.5}$$

where $\mu = M_W^2/2 + p_{T,\ell}\, p_{T,\nu} \cos\Delta\phi$, and $\Delta\phi$ the azimuthal angle between the vectorial missing transverse momentum and the additional lepton. Equation (7.5) can have zero, one, or two real solutions. In the first case, the real part of the complex solution is considered. In case it has two real solutions, both are considered and the procedure

described in the following is repeated for each of them.

7.5.2 Reconstruction of the Top Quark Candidates

The second step is the reconstruction of top quark candidates. The candidates for the top quark decaying to the final state containing an electron or muon[1], t_{lep}, are reconstructed by considering the additional lepton, the neutrino, and a combination of AK4 jets in the event. The combinations of AK4 jets must respect that at least one jet in the event is always reserved for the hadronically decaying top quark t_{had}. Furthermore, if an event has more than seven jets, only the seven leading jets are considered in total, leaving up to six to be associated to the t_{lep}.

If an event contains more than one additional lepton, or if that lepton is a muon, the assignment of the lepton associated to t_{lep} is ambiguous. In case an event contains at least one electron, the leading electron is always considered as the additional lepton entering t_{lep}, since it can never originate from the LQ decay. If an event does not contain any electrons but instead at least three muons, the three leading ones are considered for building t_{lep} candidates. Two of them must have OS charge according to the requirements on events in category A. Only the two muons with same-sign (SS) charge are potentially produced by the decay of the t_{lep}. In such events, both possible assignments of one of the SS charge muons to the t_{lep} are considered, which doubles the number of candidates.

For each element in the list of t_{lep} candidates, a number of t_{had} candidates is reconstructed. Only AK4 jets are considered for the t_{had}. Being restricted to the same set of AK4 jets as for the t_{lep} candidate, only those are considered that have not been used for the associated t_{lep} candidate. The final result of this second step is a list of pairs of top quark candidates, each consisting of one t_{lep} and one t_{had} candidate. Their four-momenta are calculated as the sum of the four-momenta of the constituents, i.e.

$$P_{t_{lep}} = \sum_i P_{i,\text{jet}} + P_\ell + P_\nu, \tag{7.6a}$$

$$P_{t_{had}} = \sum_i P_{i,\text{jet}}. \tag{7.6b}$$

[1]Top quarks decaying to the final state with a τ lepton that further decays to an electron or muon are taken into account implicitly as well. In such cases, the assumption that the electron or muon originates promptly from the W boson decay in the top quark decay chain is violated, mostly resulting in a reduced reconstruction quality. Hadronically decaying τ leptons are not considered.

7.5.3 Reconstruction of the Leptoquark Candidates

The pairs of reconstructed top quark candidates are combined with muons in the last step in order to form LQ candidates. In the following, the LQ candidate containing the t_{had} (t_{lep}) candidate is referred to as LQ_{had} (LQ_{lep}). The muon to be combined with the t_{lep} candidate is chosen based on its charge. As can be seen in figure 7.2, the additional lepton produced in the top quark decay always has OS charge compared to the prompt muon from the decay of the associated LQ. The presence of an OS muon is required for events in category A. Therefore, the OS muon is combined with the t_{lep} candidate to form the LQ_{lep} candidate. The remaining muon is combined with the t_{had} candidate to form the LQ_{had} candidate. The four-momenta of the LQ candidates are defined as the sum of the four-momenta of the associated top quark candidate and the muon,

$$P_{\mathrm{LQ_{lep}}} = P_{\mathrm{t_{lep}}} + P_{\mu_{\mathrm{OS}}}, \tag{7.7a}$$

$$P_{\mathrm{LQ_{had}}} = P_{\mathrm{t_{had}}} + P_{\mu_{\mathrm{SS}}}. \tag{7.7b}$$

The LQ mass reconstructed in each event is finally defined as the averaged invariant mass of the LQ candidate pair, i.e.

$$M_{\mathrm{LQ}}^{\mathrm{rec}} = \frac{M_{\mathrm{LQ_{lep}}} + M_{\mathrm{LQ_{had}}}}{2}. \tag{7.8}$$

After combining muons and top quark candidates, in each event a list of pairs of LQ candidates is available. From this list, the pair of candidates is chosen that is most compatible with the hypothesis of a pair of LQs decaying as assumed, which is quantified by a χ^2 term. It consists of three terms, each testing a different property of the LQ candidate pair and is defined as

$$\chi^2 = \left(\frac{M_{\mathrm{t_{lep}}} - \overline{M}_{\mathrm{t_{lep}}}}{\sigma_{\mathrm{lep}}}\right)^2 + \left(\frac{M_{\mathrm{t_{had}}} - \overline{M}_{\mathrm{t_{had}}}}{\sigma_{\mathrm{had}}}\right)^2 + \left(\frac{\Delta M_{\mathrm{LQ}}^{\mathrm{rel}} - \overline{\Delta M}_{\mathrm{LQ}}^{\mathrm{rel}}}{\sigma_{\Delta M}}\right)^2. \tag{7.9}$$

Here, $M_{\mathrm{t_{lep}}}$ and $M_{\mathrm{t_{had}}}$ are the invariant masses of the t_{lep} and t_{had} candidate, respectively. The variable $\Delta M_{\mathrm{LQ}}^{\mathrm{rel}}$ is the relative difference in the invariant mass of the

Variable	Expected value	Width
$M_{\mathrm{t_{lep}}}$	173 GeV	22 GeV
$M_{\mathrm{t_{had}}}$	174 GeV	16 GeV
$\Delta M_{\mathrm{LQ}}^{\mathrm{rel}}$	-0.013	0.088

Table 7.3: Expected values and widths of the variables used in equation (7.9).

two LQ candidates in one pair, defined as

$$\Delta M_{\mathrm{LQ}}^{\mathrm{rel}} = \frac{M_{\mathrm{LQ_{had}}} - M_{\mathrm{LQ_{lep}}}}{M_{\mathrm{LQ}}^{\mathrm{rec}}}. \tag{7.10}$$

The value of χ^2 becomes small if the invariant masses of the top quark candidates are close to the expected values and the two LQ candidates have a similar invariant mass. The expected values and widths on reconstruction level in equation (7.9) are determined in simulated events using MC truth information and listed in table 7.3. Finally, the best pair of LQ candidates in an event is defined as the one that has the smallest value of χ^2 in equation (7.9). The value of $M_{\mathrm{LQ}}^{\mathrm{rec}}$ only of this best pair is used to discriminate between a potential LQ signal and the SM backgrounds in the final statistical evaluation presented in section 7.9. Throughout this thesis, it is distinguished between the variables M_{LQ} and $M_{\mathrm{LQ}}^{\mathrm{rec}}$. The former refers to the true LQ mass generated in an event, and the latter is the mass reconstructed according to the procedure described in this section.

The distribution of $M_{\mathrm{LQ}}^{\mathrm{rec}}$ is shown for four different generated values of M_{LQ}, $M_{\mathrm{LQ}} \in \{400, 800, 1200, 1700\}\,\mathrm{GeV}$, in figure 7.12 (left) for all events passing the preselection and fulfill the additional criteria of category A. Each of the four distributions is normalized to unit area. All of them exhibit a sharp peak at the true LQ mass and a width that increases with the value of M_{LQ}. This is expected due to p_{T}-dependent detector effects, for instance an increased jet energy resolution. However, the width relative to the generated LQ mass is constant in very good approximation. The distribution of $M_{\mathrm{LQ}}^{\mathrm{rec}}$ for the SM backgrounds and three different LQ signals is shown in figure 7.12 (right) for all events passing the full selection and the additional criteria of category A. It is expected to observe a large number of signal events in this category. Compared to the SM background, the peaking behaviour of $M_{\mathrm{LQ}}^{\mathrm{rec}}$ makes this variable particularly sensitive to the potential presence of an LQ signal.

In order to compare the sensitivity of the categories A and B to a potential LQ signal, the distributions of $M_{\mathrm{LQ}}^{\mathrm{rec}}$ and S_{T} as shown in figure 7.13 are used, respectively, to calculate expected upper limits on the LQ pair production cross section. They have

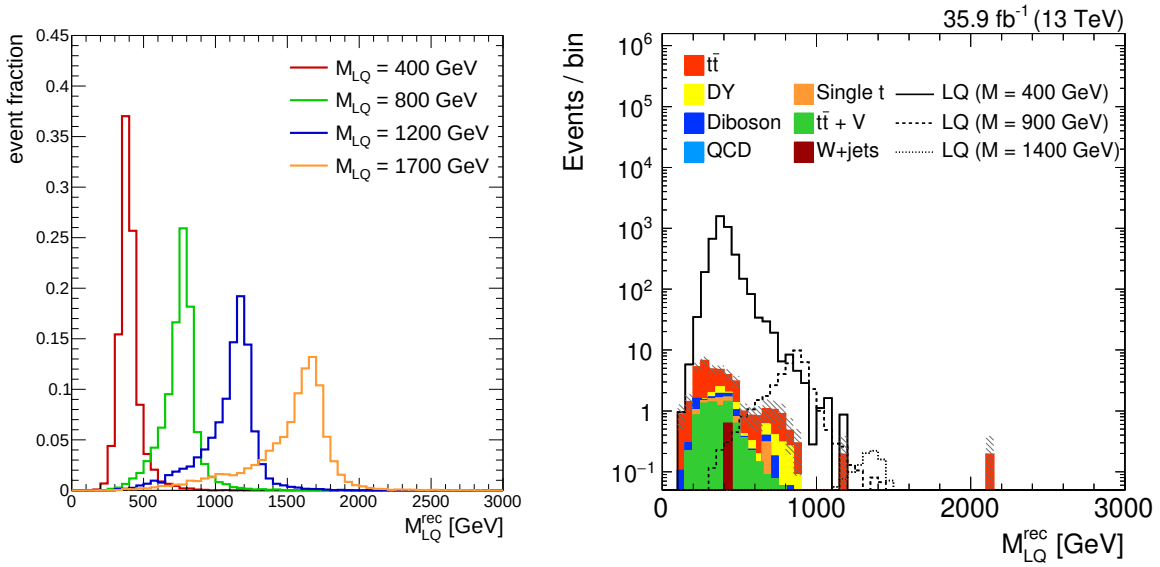

Figure 7.12: Left: Distributions of $M_{\mathrm{LQ}}^{\mathrm{rec}}$ after the pre-selection obtained from the best pair of LQ candidates for four different generated LQ masses. Each distribution is normalized to unit area. Right: Distribution of $M_{\mathrm{LQ}}^{\mathrm{rec}}$ for the SM backgrounds and three different signals for events passing the full selection and criteria of category A.

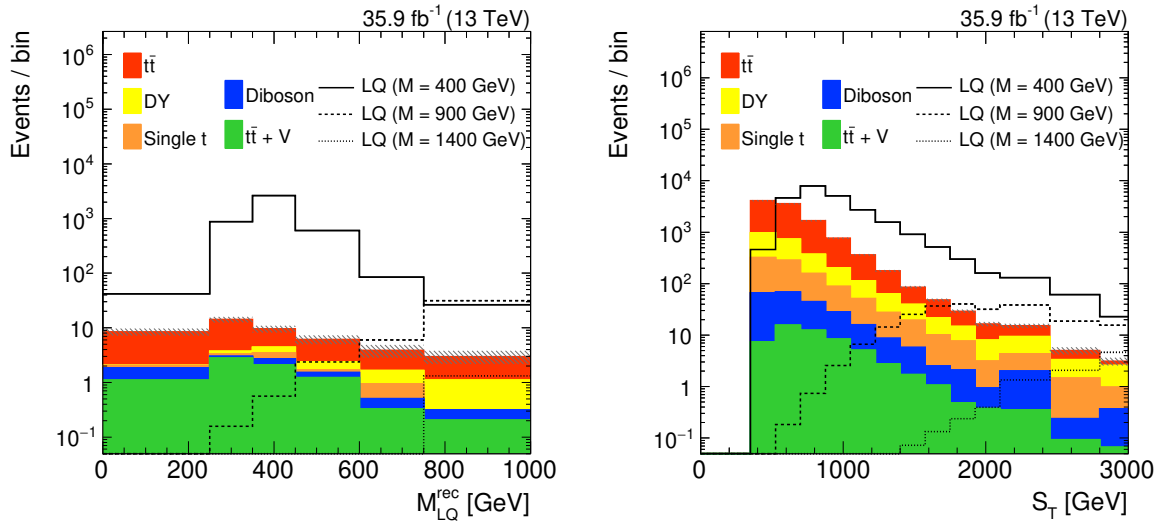

Figure 7.13: Distributions of $M_{\mathrm{LQ}}^{\mathrm{rec}}$ (left) and S_{T} (right) for events after the full selection in category A and B, respectively.

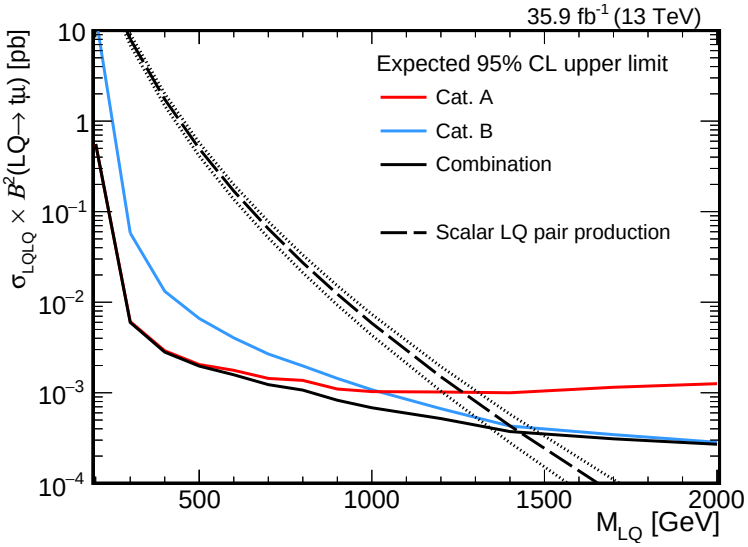

Figure 7.14: Expected cross section upper limits on LQ pair production under the assumption of unit branching fraction for the decay $\mathrm{LQ} \to \mathrm{t}\mu$ from category A, B, and their combination. The dashed line shows the pair production cross section of scalar LQs at NLO [77].

a binning that ensures a minimum number of events per bin. The expected limits from the individual categories and their statistical combination are shown in figure 7.14. Compared to the best limit shown in figure 7.9 (right), the sensitivity to a potential LQ signal is enhanced especially at low values of M_{LQ}.

This gain is explained by two factors. First, a large number of expected signal events provides strong sensitivity over the small SM backgrounds in category A. Second, the shape of the reconstructed LQ mass for $M_{\mathrm{LQ}} \geq 300\,\mathrm{GeV}$ is easily distinguished from the SM expectation, which is comparably flat. The large bin widths and limited axis range used for the distribution of $M_{\mathrm{LQ}}^{\mathrm{rec}}$ in order to suppress large statistical uncertainties result in improved sensitivity only at low M_{LQ}.

7.6 Measurement of the Lepton Misidentification Rate

As category A contains events with at least three leptons, the expected SM backgrounds in this category consist of rare processes able to produce three or more prompt leptons on tree level, i.e. $\mathrm{t\bar{t}} + \mathrm{V}$ or diboson production. On the other hand, other processes can enter this category either via the presence of non-prompt leptons from heavy-flavor hadron decays (HF decays) or other objects, such as jets or coincidental detector noise, misidentified as leptons.

The small number of expected background events in category A is visible in figure 7.13 (left). The largest fraction of SM backgrounds originates from processes that cannot produce more than two prompt leptons on tree-level. It has been validated that the simulation describes HF decays in data well. It is therefore crucial to measure the misidentification rates of leptons in data and simulated events and correct for differences between them. Since events of DY + jets production with at least three reconstructed leptons are utilized for this purpose, the dominant source of background is diboson production. As described in section 7.6.1, first a diboson CR is defined in order to validate and correct the diboson production cross section. Afterwards, the measurement of the misidentification rates is performed, which is described in sections 7.6.2 and 7.6.3.

7.6.1 Correction of the Diboson Production Cross Section

Since the misidentification rates of electrons and muons are very small, the simulated contribution of diboson events must match the real one in data precisely in order not to bias the measurement. For validating and correcting the diboson contribution, a dedicated CR is employed.

To select events of diboson production that feature similar kinematic properties as those constituting the background in the measurement of the lepton misidentification rates, the presence of exactly three electrons that have $p_{\mathrm{T}} > 30\,\mathrm{GeV}$ and fulfill the tight ID is required. At least one pair of electrons must have an invariant mass in a window of 20 GeV around M_{Z}, i.e. $M_{\mathrm{ee}} \in [71, 111]\,\mathrm{GeV}$. This criterion selects events in which at least one real Z boson was produced. Events with additional muons with $p_{\mathrm{T}} > 30\,\mathrm{GeV}$ passing the loose ID are discarded. Because the misidentification rates are measured in events with $S_{\mathrm{T}} > 350\,\mathrm{GeV}$ and at least two jets that have $p_{\mathrm{T}} > 30\,\mathrm{GeV}$, the same requirements are also imposed in this CR. Of all selected jets, no more than two are allowed to pass the loose b-tagging WP. This criterion mainly rejects events of $\mathrm{t\bar{t}}$ + jets and $\mathrm{t\bar{t}} + \mathrm{V}$ production with one or more jets wrongly identified as b-jets. Last, events are required to have at least 60 GeV of missing transverse momentum to ensure a selection orthogonal to that used in the measurement of the misidentification rates. In summary, the following criteria are applied in this CR:

- Events must have exactly three electrons with $p_{\mathrm{T}} > 30\,\mathrm{GeV}$ and $|\eta| < 2.4$ passing the tight ID.
- Events must not contain any muons with $p_{\mathrm{T}} > 30\,\mathrm{GeV}$ and $|\eta| < 2.4$ passing the loose ID.

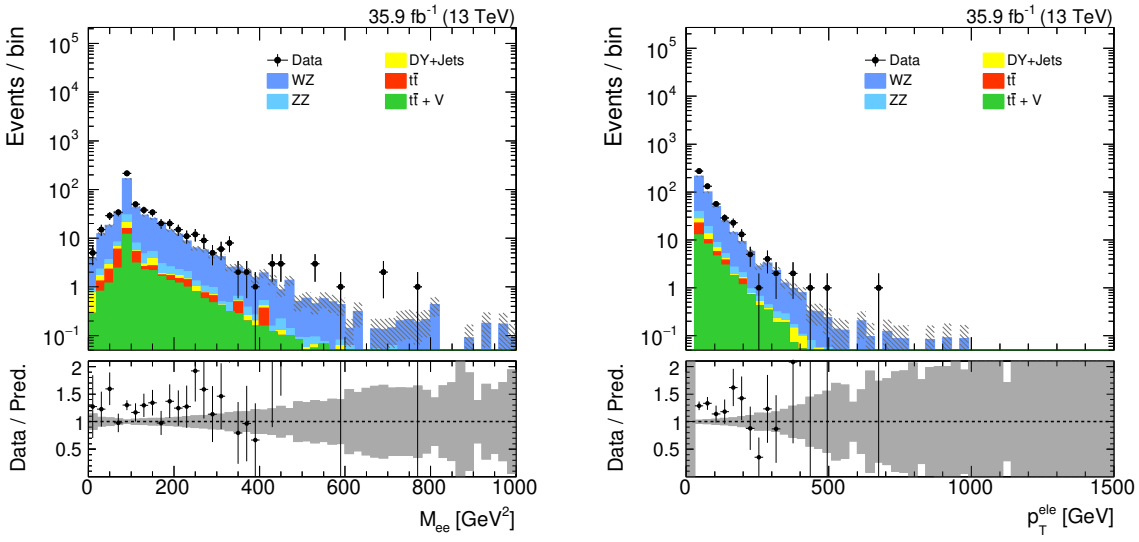

Figure 7.15: Distributions of the invariant dielectron mass for all three pairs of electrons (left) and the transverse momentum of all selected electrons (right) passing the selection for the CR enriched in events of diboson production. The lower panels show the ratio of data and simulation, the grey area corresponds to the statistical uncertainty in the SM prediction.

- Events must contain at least two jets with $p_{\mathrm{T}} > 30\,\mathrm{GeV}$ and $|\eta| < 2.4$.
- Events must not contain more than two jets passing the loose b-tagging WP.
- The invariant dielectron mass must satisfy $M_{\mathrm{ee}} \in [71, 111]\,\mathrm{GeV}$ for at least one pair of electrons.
- Events must satisfy $S_{\mathrm{T}} > 350\,\mathrm{GeV}$.
- Events must satisfy $p_{\mathrm{T}}^{\mathrm{miss}} > 60\,\mathrm{GeV}$.

The selected sample consists of events of diboson production to about 90%. Events with three electrons and a minimum value of missing transverse momentum are most likely to originate from the associated WZ production, which serves as a proxy for the total background from diboson production in the following. Figure 7.15 shows the distributions of M_{ee} of all three pairs of electrons and the transverse momentum of all selected electrons for events passing the above selection.

The shape of the simulated SM backgrounds agrees well with the recorded data. However, the simulation predicts about 30% less events than observed. Such a deficit of diboson events would lead to considerably biased lepton misidentification rate measurements. Therefore, a data/MC scale factor s_{diboson} is derived, which is applied to all events from diboson production in the following measurements. First, the simulated

non-diboson contribution is subtracted from data. The scale factor is then obtained from the ratio of the remaining data and the simulated diboson events. It is measured to be $s_{\text{diboson}} = 1.31 \pm 0.11$ and applied to all diboson events in the measurement of the electron and muon misidentification rates.

7.6.2 Measurement of the Electron Misidentification Rate

In order to select a data sample enriched in events that contain misidentified electrons, events of DY + jets production with at least two electrons in the final state are selected. If such events contain three or more electrons, one of them has most likely been misidentified. The probability of a jet to be misidentified as an electron is measured in data and simulation in the following.

Events containing between two and three electrons with $p_{\text{T}} > 30\,\text{GeV}$ and $|\eta| < 2.4$ are considered for that purpose. The electrons are required to pass the loose ID, which is the same requirement as for electrons in category A of the SR. Furthermore, events are required to have $p_{\text{T}}^{\text{miss}} < 60\,\text{GeV}$ in order to select events of DY + jets production, where no neutrino is expected in the final state. This requirement ensures no overlap between this CR and the one used to correct the diboson production cross section. All other requirements remain unchanged with respect to those in section 7.6.1. Hence, a very similar kinematic regime is selected in both CRs, which is essential for the applicability of s_{diboson}.

The requirement of $M_{\text{ee}} \in [71, 111]\,\text{GeV}$ is crucial for this measurement. It selects events in which a real Z boson has been produced and hence contain two prompt electrons. Starting from the selection described above, the per-jet electron misidentification rate is measured in events that contain exactly three electrons. Figure 7.16 shows the distributions of the transverse momenta of all jets (left) and electrons (right) in events that pass the above selection and have exactly three electrons. The underestimation of data demonstrates the need for a dedicated measurement and correction of the electron misidentification rate in simulation.

Considering DY + jets events, the two electrons whose invariant mass is closest to the value of $M_{\text{Z}} \simeq 91\,\text{GeV}$ are assumed to be prompt electrons in data. These electrons are labelled *paired* in the following. The quality of this assumption is validated in simulated events passing the above selection, where MC truth information is used to identify prompt electrons from the Z boson decay. In events with exactly two reconstructed electrons, they are always assumed to originate from the Z boson decay.

If three electrons are reconstructed in an event, they are matched to generator-level particles to determine their origin. If a reconstructed electron is matched to a

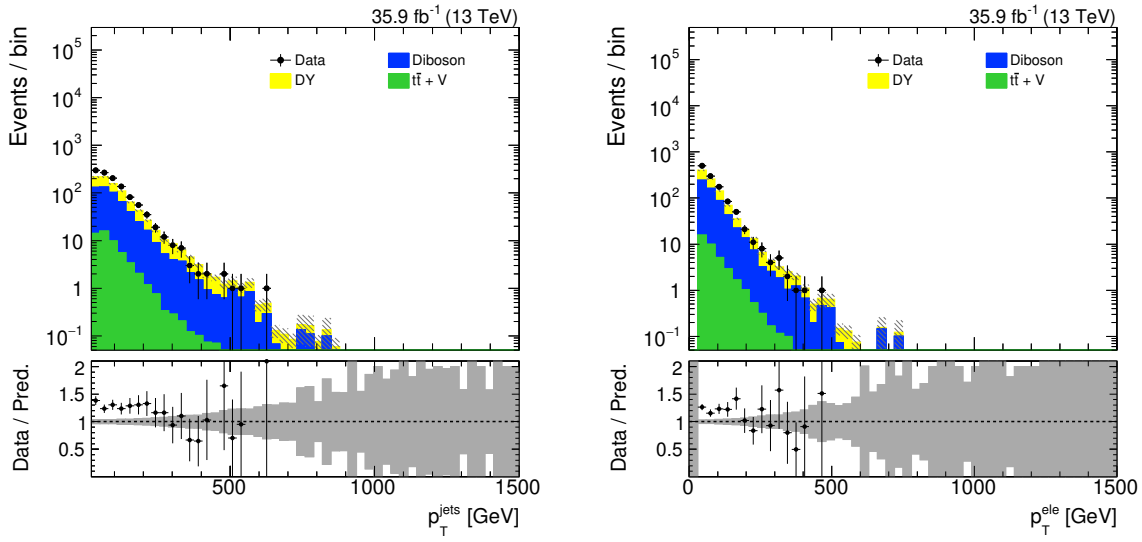

Figure 7.16: Distributions of the transverse momenta of all jets (left) and electrons (right) in events that pass the event selection and have exactly three electrons.

generated electron within $\Delta R < 0.1$, it is assumed to be a prompt electron. Otherwise, if it is matched to a generated τ lepton, bottom quark, or c quark within $\Delta R < 0.2$, it is assumed to be a decay product of the respective particle. Electrons matched to either of the aforementioned particles are labelled as *matched* and considered to be real electrons. All others are labelled *unmatched* and taken to be misidentified.

It is verified that paired electrons are indeed matched in most cases and unpaired ones are not. In figure 7.17, electrons in the selected events containing three electrons are split into four categories. Matched and unmatched electrons are compared with paired and unpaired ones. The two left bins contain matched electrons while the two right bins contain those that are unmatched, i.e. misidentified. The first bin at -2 is filled for all matched electrons that are also paired. The neighboring bin at -1 contains matched and unpaired electrons. Unmatched electrons that are still paired are filled into the bin at $+1$ and electrons that are both unmatched and unpaired receive a value of $+2$.

According to this definition, electrons from DY + jets events in the bins at ± 2 support the hypothesis that unpaired electrons are misidentified and vice versa. The electrons that are misidentified but still paired (at a value of $+1$) correspond to the cases in which the hypothesis is wrong. Conversely, for each such unmatched and paired electron in DY + jets events, there must be a matched and unpaired one (corresponding to the value -1). However, this bin is also populated by events from diboson production, where three matched leptons can be produced on tree level, one of which

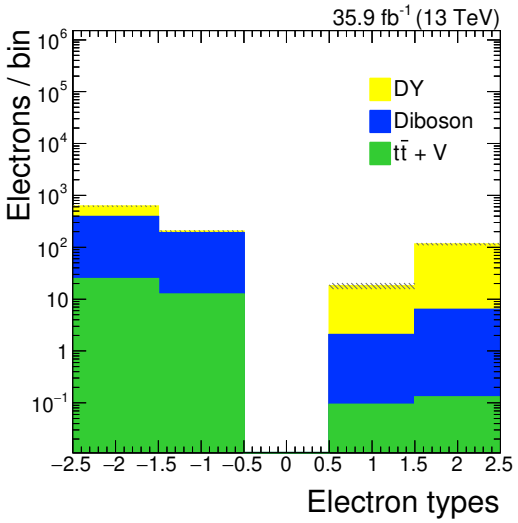

Figure 7.17: Types of electrons in events with three electrons passing the full selection. The bin at -2 is filled in case the electron is matched and paired. The bin at -1 is filled in case the electron is matched and unpaired. The bin at $+1$ is filled in case the electron is unmatched and paired. The bin at $+2$ is filled in case the electron is unmatched and unpaired.

must always be unpaired by definition.

90% of the electrons that are unmatched and unpaired originate from events of DY + jets production. These electrons are used to determine the misidentification rate of electrons in simulated events. In data, all unpaired electrons are considered. To account for the cases of unpaired but matched electrons, the corresponding number of electrons is subtracted from data using simulated events. To determine the per-jet-misidentification rate, unpaired electrons are matched to reconstructed jets within $\Delta R < 0.4$ in order to identify the jet that has been misidentified. The matching efficiency for truly misidentified electrons is close to unity. Only jets that could be matched to reconstructed electrons according to this criterion are considered in the following.

The per-jet misidentification rate ϵ is measured in three bins of transverse momentum of the jet. In simulation, ϵ is defined as the number of jets corresponding to unpaired and unmatched electrons in events with three reconstructed electrons divided by the total number of jets in events with two or three reconstructed electrons,

$$\epsilon^{\mathrm{MC}} = \frac{N^{\mathrm{MC}}_{\text{unpaired, unmatched}}}{N^{\mathrm{MC}}_{\text{total}}}. \tag{7.11}$$

In data, the simulated number of jets corresponding to unpaired but matched (i.e. real)

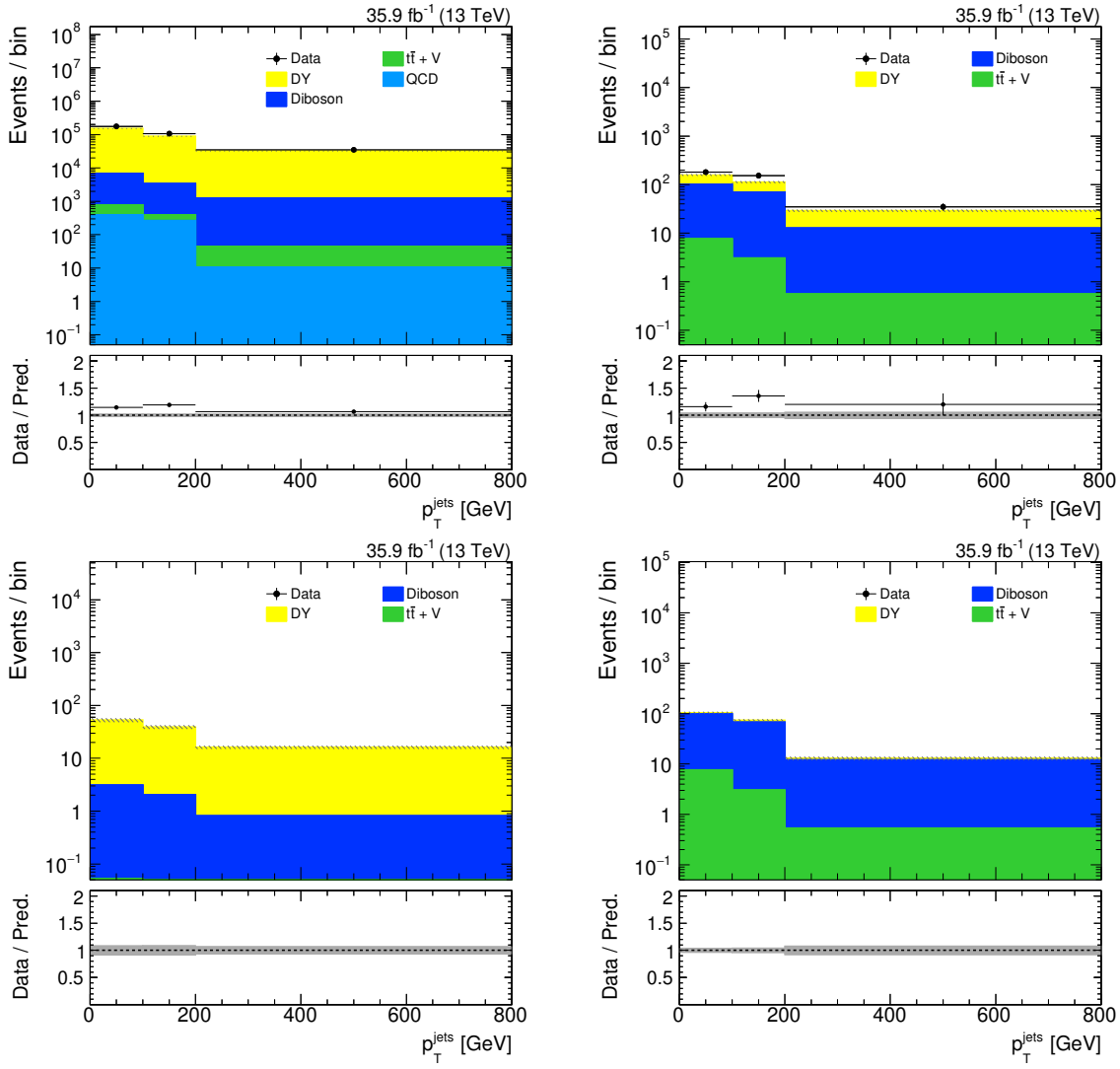

Figure 7.18: Distributions of the transverse momenta of all jets in the binning used for deriving the per-jet electron misidentification rate. The upper left distribution corresponds to $N^{\mathrm{MC}}_{\mathrm{total}}$ and $N^{\mathrm{data}}_{\mathrm{total}}$, the upper right distribution corresponds to $N^{\mathrm{MC}}_{\mathrm{unpaired}}$ and $N^{\mathrm{data}}_{\mathrm{unpaired}}$. The distributions in the lower row show $N^{\mathrm{MC}}_{\mathrm{unpaired,\ unmatched}}$ (left) and $N^{\mathrm{MC}}_{\mathrm{unpaired,\ matched}}$ (right).

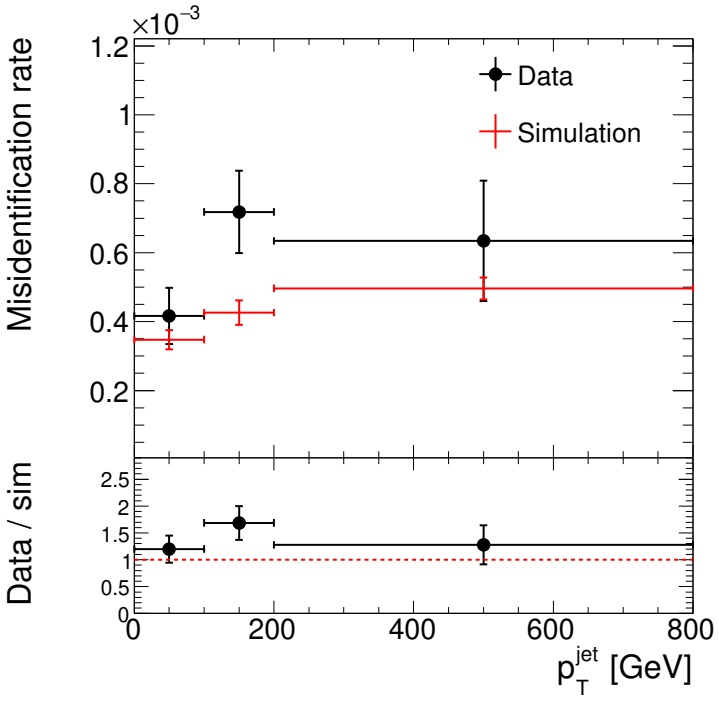

Figure 7.19: Per-jet electron misidentification rate measured in data (black) and simulated events (red) as a function of the jet matched to the misidentified electron. The lower panel shows the ratio of data and simulation.

electrons is subtracted in the numerator,

$$\epsilon^{\text{data}} = \frac{N^{\text{data}}_{\text{unpaired}} - N^{\text{MC}}_{\text{unpaired, matched}}}{N^{\text{data}}_{\text{total}}}. \tag{7.12}$$

The number of jets matched to each of the four classes of electrons defined before is shown in figure 7.18 for simulated events and, where applicable, data.

The per-jet misidentification rate of electrons is presented in figure 7.19. In simulated events, the number of electrons matched to τ lepton or heavy quark decays is assigned an additional conservative uncertainty of 30% in order to account for potential small differences in their description between data and simulation. The fraction of such electrons is of $\mathcal{O}(0.05\%)$.

The simulated misidentification rate takes systematically smaller values than that observed in data. Therefore, the ratio of the per-jet misidentification rates in data and simulated events is applied as a data/MC scale factor to all jets that are matched to a misidentified electron in the signal region. Events in category A are particularly affected as discussed previously.

7.6.3 Measurement of the Muon Misidentification Rate

Similar to the procedure described in the previous section, also the muon misidentification rate is measured in data and simulated events. It is expected to be even smaller due to the excellent detectors and algorithms for muon detection and reconstruction employed by the CMS Collaboration. As opposed to electrons, which are reconstructed in the ECAL and hence more susceptible to misidentification of jets, the muon reconstruction relies on the inner tracker and the muon system outside the solenoid. The impact of detector noise and jets penetrating the HCAL and reaching the muon system on the muon reconstruction needs to be measured in order to correct for a mis-modelling of these effects in simulation. This measurement closely follows the procedure described in the previous section. In contrast to the procedure in the electron channel, the presence of a misidentified muon is inferred from events that contain a muon in addition to two electrons in DY + jets events. The event selection only differs in the requirement of exactly two electrons with $p_{\mathrm{T}} > 30\,\mathrm{GeV}$ and $|\eta| < 2.4$ that fulfill the loose ID. At most one additional isolated muon with $p_{\mathrm{T}} > 30\,\mathrm{GeV}$, $|\eta| < 2.4$, and $I_{\mathrm{rel}} < 0.15$ passing the tight ID is allowed to be present. These muon quality criteria correspond to those applied in the signal region.

The definition of misidentified muons can be simplified, as in the presence of a muon there is no ambiguity in identifying the misidentified lepton. All events without an additional muon are assumed to contain only prompt electrons. In case a muon is present in DY + jets events in data or simulation, it is assumed that it has been misidentified. The muon misidentification rate is measured inclusively and without matching to jets. It is defined as

$$\epsilon^{\mathrm{MC}} = \frac{N^{\mathrm{MC}}_{1\mu,\ \mathrm{unmatched}}}{N^{\mathrm{MC}}_{\mathrm{total}}} \tag{7.13}$$

and

$$\epsilon^{\mathrm{data}} = \frac{N^{\mathrm{data}}_{1\mu} - N^{\mathrm{MC}}_{1\mu,\ \mathrm{matched}}}{N^{\mathrm{data}}_{\mathrm{total}}} \tag{7.14}$$

in simulation and data, respectively.

It is measured to be $\epsilon^{\mathrm{MC}} = 0.0041 \pm 0.0010\,\%$ and $\epsilon^{\mathrm{data}} = 0.0082^{+0.0143}_{-0.0082}\,\%$ about one order of magnitude smaller than the misidentification rate for electrons. Similarly as before, the number of non-prompt muons from τ lepton or heavy quark decays is assigned an additional uncertainty of 30% in simulation. The data/MC scale factor

of $s_{\mu\ \mathrm{misID}} = \epsilon^{\mathrm{data}}/\epsilon^{\mathrm{MC}} = 2.0^{+3.5}_{-2.0}$ is applied for each unmatched simulated muon in the signal region.

7.7 Background Estimation

After the backgrounds in category A of the SR have been corrected for a mismodelling of the lepton misidentification rate, in this section the data-driven estimation of the dominant backgrounds in category B is presented. The background in that category is mainly composed of events of $\mathrm{t\bar{t}}+\mathrm{jets}$ and $\mathrm{DY}+\mathrm{jets}$ production with a share of more than 90%. These backgrounds in the distribution of S_{T} will be derived from data as described in this section. The remaining minor contributions arise due to single t, diboson, and $\mathrm{t\bar{t}}+\mathrm{V}$ events.

Since the event selection of the SR focuses on a particular region of phase space, distributions of kinematic variables and production cross sections of the simulated SM background can significantly differ from the truth in data. A data-driven background estimation reduces the dependance on phenomenologically modelled processes like hadronization and correctly predicted fiducial production cross sections. Overall, the normalization and shape of distributions in category B of the SR are expected to match the underlying truth in data after the application of data-driven methods. This and the largely reduced uncertainties in the modelling of the SM backgrounds leads to improved sensitivity to a potential LQ signal.

7.7.1 Event Selection

In order to select events in a similar kinematic regime as in the SR and at the same time suppress events of LQ pair production, the final state with at least two electrons instead of muons is a natural choice. Contamination of this CR with signal events and overlap with the SR is avoided by rejecting events that contain muons. The further event selection is chosen to resemble the one in the SR as closely as possible in order not to introduce kinematic biases.

The CR contains all events satisfying the following requirements:

- Events must have at least two electrons with $p_{\mathrm{T}} > 30\,\mathrm{GeV}$ and $|\eta| < 2.4$ passing the tight ID with the isolation requirement.
- Events must not contain any muons with $p_{\mathrm{T}} > 30\,\mathrm{GeV}$, $|\eta| < 2.4$, and $I_{\mathrm{rel}} < 0.15$ passing the loose ID.

- Events must contain at least two AK4 jets with $p_T > 30\,\text{GeV}$ and $|\eta| < 2.4$.
- Events must contain at least one AK4 jet passing the loose b-tagging WP.
- Events must satisfy $S_T > 350\,\text{GeV}$.
- Events must satisfy $S_T^{\text{lep}} > 200\,\text{GeV}$.
- Events must satisfy $M_{ee} > 111\,\text{GeV}$ for any pair of electrons.

In figure 7.20, control distributions of characteristic variables are shown for events in the CR passing the above selection. Of the events passing the selection, about 78% arise from $t\bar{t}$ + jets production. The second-largest contribution with a fraction of roughly 14% is due to DY + jets events. As expected, the overall background composition is very similar to the one in the SR. Furthermore, the contamination of this CR with events of LQ pair production is negligibly small.

Overall, a slight discrepancy in the normalization of data and simulated events is observed. About 5% more events are predicted than were recorded in data. The normalization offset is mainly introduced by the requirement of at least two electrons. Also in the shapes of some distributions differences between data and simulation are observed. Comparing the distributions of kinematic variables in the SR (figure 7.11) and CR (figure 7.20), very similar behavior is observed.

The fact that those deviations are present also in the signal-depleted CR indicates that the observed disagreement is caused by mismodelling of the SM prediction rather than the presence of an LQ signal. Furthermore, the observed deviations between simulation and real data, especially in the distribution of S_T, demonstrate the need for a data-driven background estimation in this region of phase space.

In order to extrapolate the distribution of S_T in data from the CR into the SR, the shapes of these distributions, it has to be verified that the shapes of both distributions agree well. Since the differences between the final states with electrons and muons are assumed to be well-modelled in simulation, the shapes of the S_T distributions are compared in simulated events of $t\bar{t}$ + jets and DY + jets production between the SR and CR. Both backgrounds are collectively referred to as $t\bar{t}$ +DY + jets events in the following.

Figure 7.21 shows the shapes of the S_T distributions in simulated events of $t\bar{t}$ + jets, DY + jets, and the combined $t\bar{t}$ +DY + jets production in two different binnings. They do not agree within their statistical uncertainties. Events in the CR tend to have higher values of S_T compared to the SR. This trend is particularly evident when comparing $t\bar{t}$ + jets events, but also present in DY + jets production. The different trends in

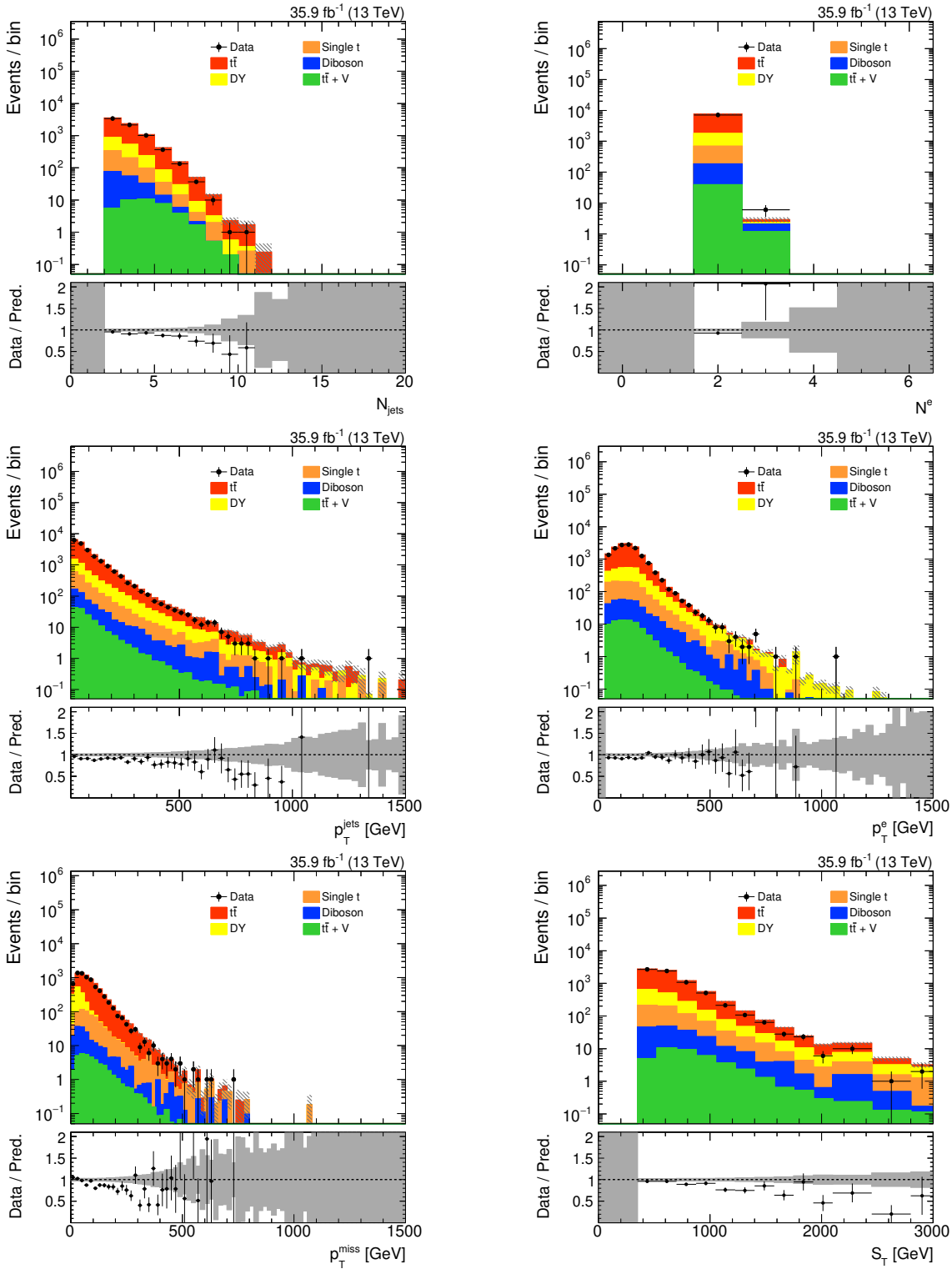

Figure 7.20: Distributions of N_{jets} (upper left), N_{e} (upper right), $p_{\text{T}}^{\text{jets}}$ (middle left), p_{T}^{e} (middle right), $p_{\text{T}}^{\text{miss}}$ (lower left), and S_{T} (lower right) for all events passing the full event selection in the CR. The lower panels show the ratio of data and simulation, the grey area corresponds to the statistical uncertainty in the SM prediction.

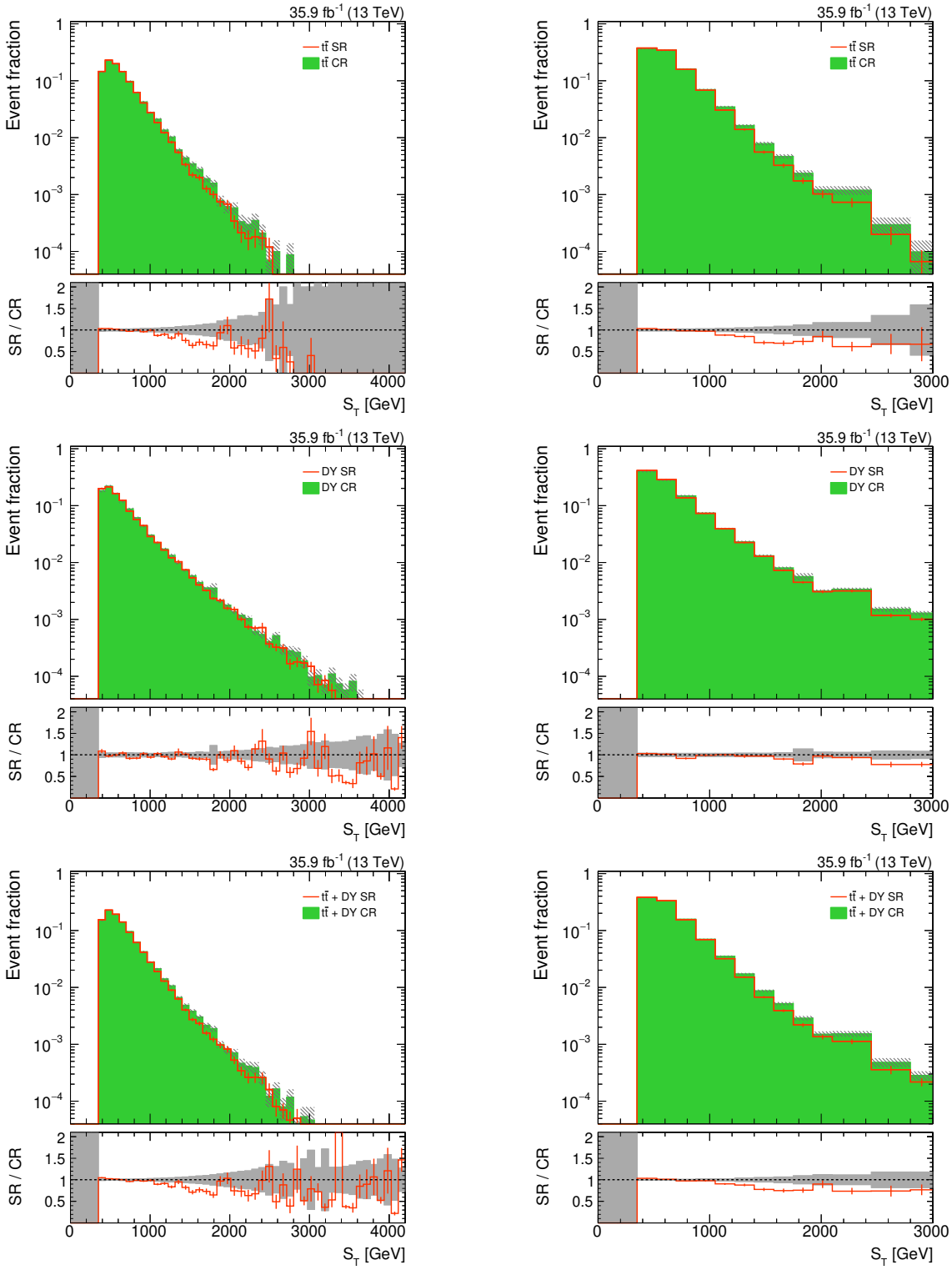

Figure 7.21: Shape comparison of the S_{T} distributions of simulated $\mathrm{t\bar{t}}+$jets (upper), DY + jets (middle), and combined $\mathrm{t\bar{t}}$ +DY + jets (lower) events between the SR (red) and CR (green) for narrow bins (left) and the binning used in the final statistical interpretation (right). Both distributions are normalized to unit area. The lower panels show the ratio of SR and CR, the grey area and the error bars correspond to the respective statistical uncertainty.

the shape comparisons between $\mathrm{t\bar{t}}+\mathrm{jets}$ and $\mathrm{DY}+\mathrm{jets}$ events cause the background estimation to depend on the assumed background composition in the SR and CR and hence on the production cross sections of both processes. This dependence is taken into account as described in section 7.8.

The different shapes in the SR and CR were found to be caused by different reconstruction efficiencies of electrons and muons, respectively, as a function of S_T. A function depending on S_T is derived on simulated events of $\mathrm{t\bar{t}}+\mathrm{DY}+\mathrm{jets}$ production in the SR and CR in order to correct for this effect.

7.7.2 Derivation of the Data-Driven Background Estimate

The correction function $\alpha(S_\mathrm{T})$ takes into account differences in the shape and normalization of the S_T distribution in both regions. Data in the CR weighted with the value of $\alpha(S_\mathrm{T})$ after the minor backgrounds have been subtracted then constitute the SM prediction of $\mathrm{t\bar{t}}+\mathrm{DY}+\mathrm{jets}$ events in the SR. The function $\alpha(S_\mathrm{T})$ is derived as follows.

In the first step, an empirical function F is fitted to the distribution of S_T in the SR (of events in category B) and the CR. The function has seven free parameters $a...g$ and depends on S_T, $F = F_{a...f}(S_\mathrm{T})$. The parameterization consists of a Landau function describing the peak of the distribution at low S_T and an exponential function for the tail towards high values of S_T. Both terms are connected via an error function serving as a turn-on, governing the transition between both functions. The full function is given by

$$\begin{aligned} F_{a...g}(S_\mathrm{T}) = a \cdot \mathrm{Landau}(S_\mathrm{T}, b, c) \cdot \left[1 - \frac{1+\mathrm{Erf}\left(\frac{S_\mathrm{T}-d}{e}\right)}{2}\right] + \\ + \exp(f \cdot S_\mathrm{T} + g) \cdot \left[\frac{1+\mathrm{Erf}\left(\frac{S_\mathrm{T}-d}{e}\right)}{2}\right]. \end{aligned} \tag{7.15}$$

Here, the parameters a, b and c determine the normalization, peak position, and width of the Landau function, respectively. The term $\mathrm{Erf}\left(\frac{S_T-d}{e}\right)$ refers to an error function depending on S_T. The parameter d affects the position of its root and e controls its steepness in the root. Last, the parameters f and g are used in the polynomial argument of the exponential function. It is important to note that the terms in square brackets serve as turn-on and turn-off functions, as by definition the term $\frac{1+\mathrm{Erf}(x)}{2}$ can take values between zero and one. The error functions in equation (7.15) have the same argument, which ensures logical consistency during the transition from the peak

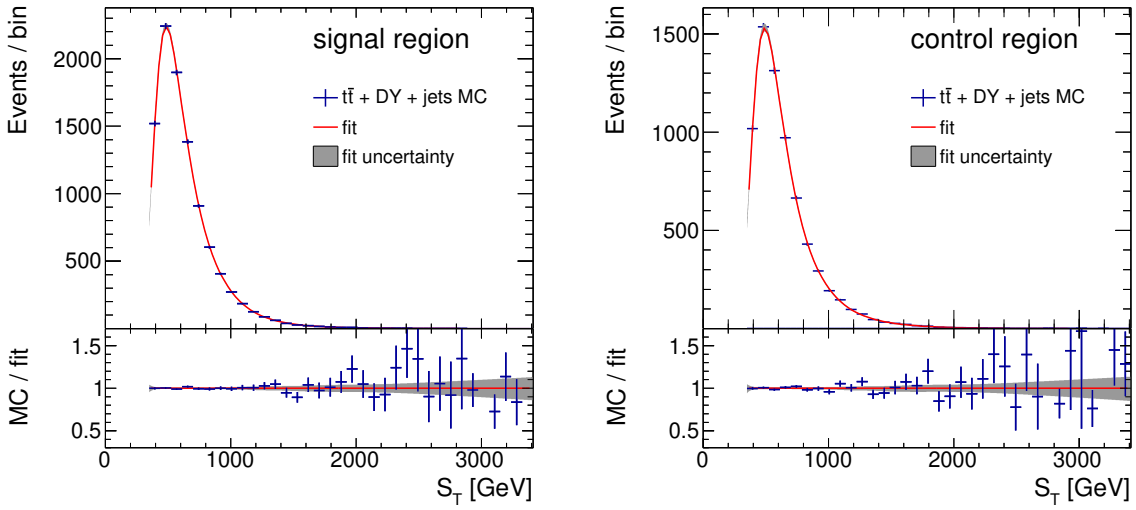

Figure 7.22: Distributions of S_T in the SR (left) and CR (right). The blue markers correspond to simulated $\mathrm{t\bar{t}}+\mathrm{DY}+\mathrm{jets}$ events, the error bars indicate the statistical uncertainty. The resulting function of the fit of F to the distributions is shown as a red line, its statistical uncertainty corresponds to the grey band. The lower panels show the ratio of simulated events to the fit.

region to the exponential tail.

The fit takes into account values of S_T between 350 and 3400 GeV. The distributions of S_T in simulated events of $\mathrm{t\bar{t}}+\mathrm{DY}+\mathrm{jets}$ production and the fitted function F are shown in figure 7.22 for the SR (left) and the CR (right). In the SR, the fit returns a value of $\chi^2/\mathrm{ndof} = 20/28$ while in the CR, $\chi^2/\mathrm{ndof} = 29/28$ is obtained. In both cases, the fit function models the distribution of S_T well.

In order to estimate the uncertainty on the final extrapolation function $\alpha(S_\mathrm{T})$, the statistical uncertainty of both fit functions is evaluated and later propagated to the calculation of $\alpha(S_\mathrm{T})$. The parameters of the fit are decorrelated from each other in order to obtain independent parameters that can be varied within their uncertainties individually. The resulting functions F, obtained with one parameter varied up and down by one standard deviation, respectively, are used to estimate the statistical uncertainty in the nomial fit result. For seven free parameters, 14 varied functions are considered in total. At every value of S_T, the deviations to higher or lower values of the function from all 14 variations are added in quadrature to determine the final uncertainty in the nominal result.

The final function $\alpha(S_\mathrm{T})$, used to extrapolate data from the CR into the SR, is

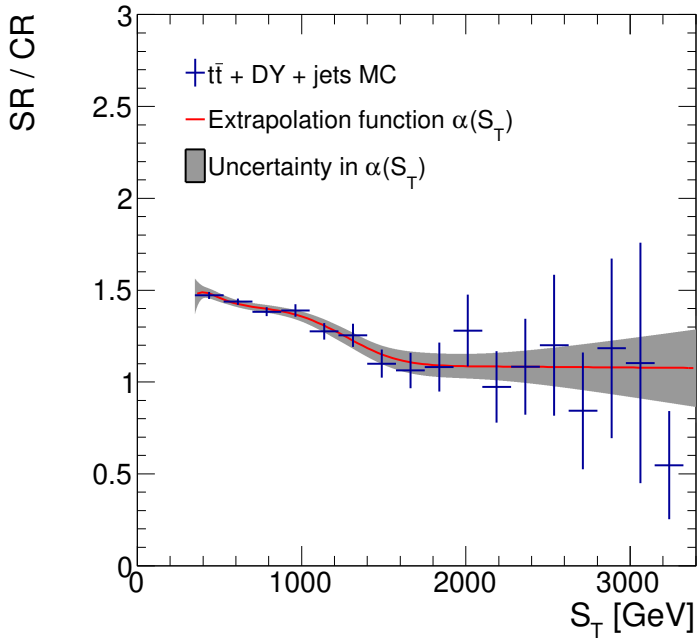

Figure 7.23: Extrapolation function $\alpha(S_\mathrm{T})$. The red line represents the nominal value and the grey area indicates its statistical uncertainty. The ratio of $\mathrm{t\bar{t}}+\mathrm{DY}+\mathrm{jets}$ simulated events in the SR and CR is shown in blue for comparison.

defined as the ratio of the functions in the SR and CR,

$$\alpha(S_\mathrm{T}) = \frac{F_\mathrm{SR}(S_\mathrm{T})}{F_\mathrm{CR}(S_\mathrm{T})}. \tag{7.16}$$

The uncertainty in $\alpha(S_\mathrm{T})$ is propagated from the uncertainties in the individual fit functions. The extrapolation function and its statistical uncertainty is shown in figure 7.23. The ratio of $\mathrm{t\bar{t}}+\mathrm{DY}+\mathrm{jets}$ simulated events in the SR and CR is shown for comparison. It is observed that $\alpha(S_\mathrm{T})$ describes the ratio of SR and CR well. The uncertainty on $\alpha(S_\mathrm{T})$ is small in regions containing a large number of simulated events around $S_\mathrm{T} = 500\,\mathrm{GeV}$ and increases towards higher values due to larger uncertainties in the fits. Systematic uncertainties due to the choice of parameterization of the S_T spectrum were found to be well covered by the statistical uncertainty. Hence, no additional systematic uncertainty is considered.

7.7.3 Application to Data

In order to obtain the final estimation of the SM $t\bar{t}$ +DY + jets backgrounds from data, the extrapolation discussed above is applied to data in the CR. First, the fraction of the simulated prediction of all other processes in the CR is subtracted from data bin by bin in the distribution of interest. The statistical uncertainties of the data and all subtracted processes are added in quadrature to account for this procedure. The resulting uncertainty is considered to be the statistical uncertainty of the remaining data in the CR.

Second, the remaining events in data are assigned event weights obtained from evaluating the function $\alpha(S_{\mathrm{T}})$ at the value of S_{T} of the respective events. The result is considered to be the contribution of events of $t\bar{t}$ +DY + jets production in the distribution of interest in category B of the SR. Performing this procedure with the distribution of S_{T}, the final $t\bar{t}$ +DY + jets background prediction for the sensitive variable used in category B is obtained. The impact of the data-driven background estimation on the systematic uncertainties and the final results is discussed in the following sections (cf. sections 7.8 and 7.9).

7.7.4 Validation in Data

In order to validate the method detailed above directly in data, a validation region (VR) is defined. The event selection for the CR as described in section 7.7.1 is applied. However, in order to select a statistically independent sample of events, the requirement on $S_{\mathrm{T}}^{\mathrm{lep}}$ is inverted, i.e. $S_{\mathrm{T}}^{\mathrm{lep}} < 200\,\mathrm{GeV}$. This VR has a negligible contamination with events of LQ pair production. Although inverting the requirement on $S_{\mathrm{T}}^{\mathrm{lep}}$ affects the distribution of S_{T}, the VR can be used to verify that the method presented above works well and yields an accurate prediction of the background from $t\bar{t}$ +DY + jets events.

In the following, the whole procedure described previously is applied to the CR and the VR, where the VR is treated like the SR. The same parameterization of the fit function (equation (7.15)) is used, only the fit range is restricted to $350\,\mathrm{GeV} < S_{\mathrm{T}} < 2000\,\mathrm{GeV}$, because inverting the $S_{\mathrm{T}}^{\mathrm{lep}}$ requirement reduces the number of events with larger values of S_{T} in the VR. Figure 7.24 shows the fits in the VR and CR, respectively. The ratio of these fits is used to extrapolate data from the CR into the VR.

The final distribution of S_{T} in the VR is presented in figure 7.25 with purely simulated backgrounds (left) and with the $t\bar{t}$ +DY + jets contribution estimated from data (right). When deriving the dominant backgrounds from data, very good agreement be-

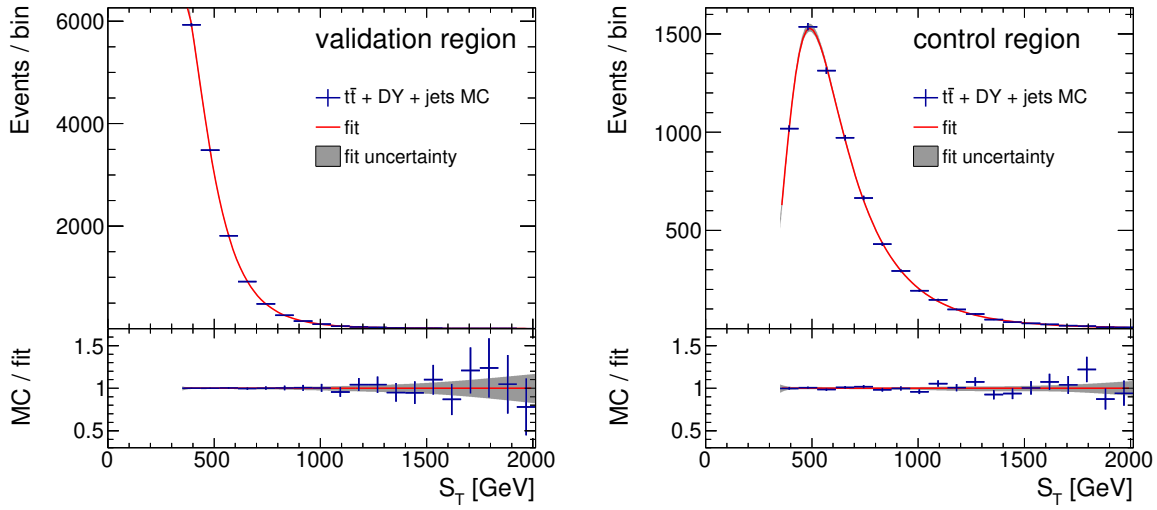

Figure 7.24: Distributions of S_T in the VR (left) and CR (right). The blue markers correspond to simulated $t\bar{t}$ +DY + jets events, the error bars indicate the statistical uncertainty. The resulting function of the fit of F to the distributions is shown as a red line, its statistical uncertainty corresponds to the grey band. The lower panels show the ratio of simulated events to the fit.

tween data and background is observed. This indicates that the background estimation method provides a solid and unbiased prediction in the SR as well.

7.7.5 Application to the Signal Region

After validating the performance of the data-driven background estimation method in the dedicated VR, it is used to predict the $t\bar{t}$ +DY + jets background in category B of the SR. In figure 7.26, control distributions in the SR are shown, where the contribution of $t\bar{t}$ +DY + jets events is predicted from data instead of simulation.

Very good agreement both in the shape and the normalization of data and the SM prediction is observed. Compared to the distributions shown in figure 7.11, no trend in the ratio of data and the prediction is observed anymore. This is due to the fact that the data-driven background estimate is applied to the major part of the SM background. Since data are not affected by mismodelling in simulation of the region of phase space under consideration, the disagreement observed before disappeared. This background estimation technique will also be used for the distribution of S_T in category B of the SR in the final statistical evaluation discussed in section 7.9.

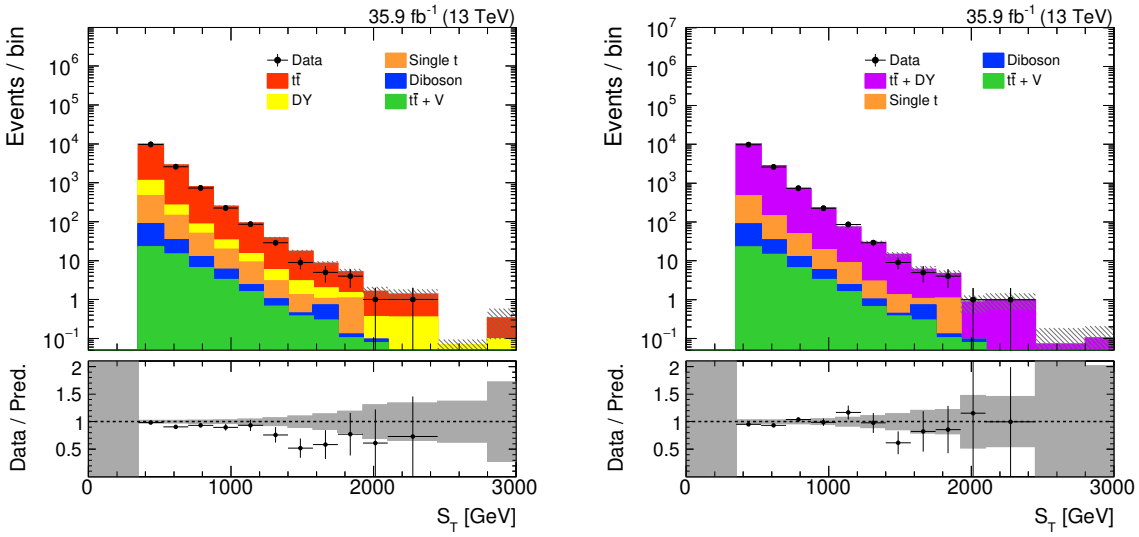

Figure 7.25: Distributions of S_{T} in the VR for purely simulated backgrounds (left) and with the $\mathrm{t\bar{t}}+\mathrm{DY}+\mathrm{jets}$ contribution estimated from data (right). The lower panels show the ratio of data and the background, the grey area corresponds to the statistical uncertainty in the SM prediction.

7.8 Systematic Uncertainties

In this analysis, various systematic uncertainties affect the final distributions of $M_{\mathrm{LQ}}^{\mathrm{rec}}$ in category A and S_{T} in category B. They can either have an effect only on the rate of the different processes or affect the shape of the distributions in addition. For each systematic uncertainty discussed in the following, modified distributions of $M_{\mathrm{LQ}}^{\mathrm{rec}}$ and S_{T} are derived, which correspond to the distributions with a given source of uncertainty varied up and down by one standard deviation. They are taken into account in the final statistical evaluation as described in section 7.9.

The data-driven background estimate of $\mathrm{t\bar{t}}+\mathrm{DY}+\mathrm{jets}$ events in category B is affected by some uncertainties differently than the simulated events in both categories. For each varied source of uncertainty, the full extrapolation procedure described in section 7.7 is repeated with the varied distributions of S_{T} in the SR and CR. In the following, all sources of systematic uncertainties are presented and the evaluation of their impact is discussed in detail.

- **Luminosity:** The value of the integrated luminosity of $L = 35.9\,\mathrm{fb}^{-1}$ of the dataset recorded by the CMS Collaboration in 2016 and analyzed in this search is measured with an uncertainty of 2.5% [168]. The value of L is used to weight simulated events such that they yield the number of events expected from their respective production cross sections. The nominal value is therefore varied by

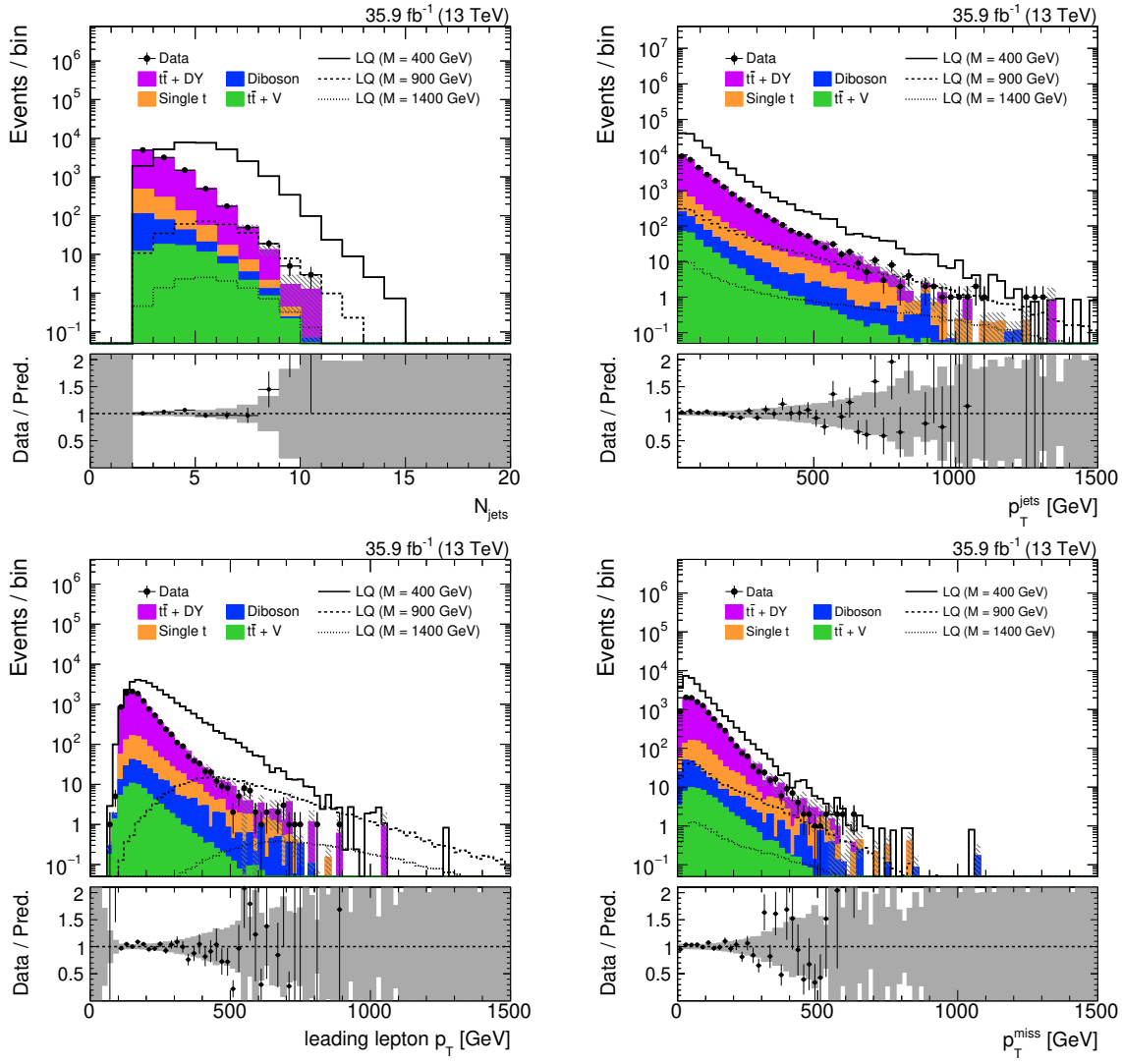

Figure 7.26: Distributions of N_{jets} (upper left), $p_{\text{T}}^{\text{jets}}$ (upper right), p_{T} of the leading lepton (lower left), and $p_{\text{T}}^{\text{miss}}$ (lower right) for events passing the full selection of category B of the SR. The background from $\mathrm{t\bar{t}}+\mathrm{DY}+\text{jets}$ production is predicted from data as described in the text. The lower panels show the ratio of data and the background, the grey area corresponds to the statistical uncertainty in the SM prediction.

±2.5% to estimate the impact of this uncertainty on the final distributions. Only the normalization of simulated events is affected, because changes in the global normalization cancel exactly in the ratio of simulated events used to derive the extrapolation function $\alpha(S_T)$ (cf. equation (7.16)) and the normalization of data is constant.

- **SM production cross sections:** The following conservative estimates for the uncertainties in the production cross sections of SM processes are used. They are based on Refs. [169–177]:
  - $t\bar{t}$ + jets production: 5.6%
  - DY + jets production: 10%
  - Single top quark production: 10%
  - Diboson production: 20%
  - $t\bar{t}$ + V production: 25%

  These uncertainties affect only the normalization of the simulated SM backgrounds. Of the data-driven prediction of $t\bar{t}$ +DY + jets events in category B, both the shape and the normalization are affected. First, by varying the fraction of $t\bar{t}$ and DY + jets events in the SR and CR, the individual contributions of both backgrounds to the shape difference between the SR and CR are modified, which changes the extrapolation function. Second, also the normalization of the minor backgrounds affects the normalization and shape of the data-driven prediction. This is due to subtracting their contribution from data in the CR in the extrapolation.

- **Pileup:** Simulated events are reweighted based on the number of simulated interactions per bunch crossing and the number of PU interactions in data. The latter distribution is derived from the inelastic pp scattering cross section, for which a value of $\sigma_{pp} = 69.2\,\text{mb}$ is assumed [166]. This value has an associated uncertainty of ±4.6%, which is used to create alternative Poisson profiles. The reweighting is repeated with the varied PU profiles for data and the result is propagated to the final sensitive distributions. This uncertainty affects the normalization and shape of all simulated events and the data-driven background estimate.

- **Jet energy corrections:** The jet energy scale and resolution corrections are varied up and down within their uncertainties [139]. The JES uncertainties depend on p_T and η of a jet while the JER uncertainties only depend on the jet's η. The

modified JEC is propagated to the type-I correction of the missing transverse momentum. The entire analysis is repeated with the varied JECs and their impact on the final distributions is evaluated. This uncertainty affects the normalization and shape of all simulated events and the data-driven background estimate.

- **Electron efficiencies:** Uncertainties in the electron reconstruction, ID, and trigger efficiencies [142] are taken into account by varying the respective data/MC scale factor up and down within its total uncertainty. Here, additional systematic uncertainties of 1% in the reconstruction and ID efficiencies and 2% in the trigger efficiency are added to the statistical uncertainties in quadrature. These uncertainties only affect the normalization and shape of simulated events in category A and the data-driven background estimate in category B.

- **Muon efficiencies:** Uncertainties in the muon ID, isolation, tracking, and trigger efficiencies [144] are taken into account by varying the respective data/MC scale factor up and down within its total uncertainty. Here, additional systematic uncertainties of 1% in the ID efficiency and 0.5% in the isolation and trigger efficiencies are added to the statistical uncertainties in quadrature. These uncertainties affect the normalization and shape of all simulated events and the data-driven background estimate.

- **Lepton misidentification rates:** Uncertainties in the misidentification rates of electrons and muons are taken into account by varying the respective data/MC scale factor up and down within its total uncertainty. It is composed of the statistical uncertainty and an additional uncertainty of 30% on the contribution of real, non-prompt leptons originating from τ lepton or heavy quark decays as described in section 7.6. The uncertainty associated to muons affects the normalization and shape of all simulated events and the data-driven background estimate. The uncertainty related to electrons only affects the normalization and shape of simulated events in category A and the data-driven background estimate in category B.

- **Efficiencies of b-tagging:** Uncertainties in the efficiency of identifying jets as originating from bottom quark hadronization [148] are taken into account by varying the corresponding data/MC scale factor up and down within its statistical uncertainty. The uncertainties in the efficiencies of correctly tagging bottom-quark-initiated jets and mistagging c quark-initiated jets are taken to be fully correlated and the respective scale factors are varied simultaneously. The uncertainty in the efficiency of mistagging jets initiated by light quarks or gluons

is assumed to be fully uncorrelated and the corresponding scale factor is varied independently. These uncertainties affect the normalization and shape of all simulated events and the data-driven background estimate.

- **Background estimation method:** The uncertainty associated with the data-driven estimation of the contribution of $t\bar{t}+\mathrm{DY}+\mathrm{jets}$ events in category B is evaluated by varying the extrapolation function $\alpha(S_\mathrm{T})$ up and down within its statistical uncertainties. Repeating the extrapolation of the data from the CR into the SR with the modified function yields varied templates for the prediction of $t\bar{t}+\mathrm{DY}+\mathrm{jets}$ events in category B. Simulated events are not affected by this uncertainty.

- **Renormalization and factorization scales:** The uncertainty in the choice of renormalization and factorization scales (μ_r and μ_f, respectively) in the simulation of events is taken into by independently varying both up and down by a factor of 2 with respect to the nominal value. This leads to a set of eight varied configurations in addition to the nominal one. The two configurations with scales varied in opposite directions are discarded as unphysical. The remaining six varied distributions and the nominal choice are considered in the following. The envelope of the seven distributions in each bin of the final distributions is taken as the systematic uncertainty due to the choice of μ_r and μ_f. This uncertainty is considered separately for each source of background considered as the default choice of μ_r and μ_f is different for all processes. The normalization and shape of all simulated events and the data-driven background estimate are affected by this uncertainty.

- **Parton distribution functions:** The choice of the PDF used for generating events [16, 178] is the last source of uncertainty considered in this analysis. Its impact is evaluated by considering 100 sets of varied PDFs provided for this purpose. Correspondingly, 100 variations of each of the final distributions are generated. In each bin, the $\pm1\sigma$ uncertainty due to the choice of the PDF is given by the symmetric standard deviation calculated from the 100 variations with respect to the nominal distribution. This uncertainty affects the normalization and shape of all simulated events and the data-driven background estimate.

The nominal distributions of $M_\mathrm{LQ}^\mathrm{rec}$ and S_T in category A and B, respectively, together with the variations corresponding to the uncertainties discussed above, are shown in figures 7.27 and 7.28 for selected relevant uncertainties.

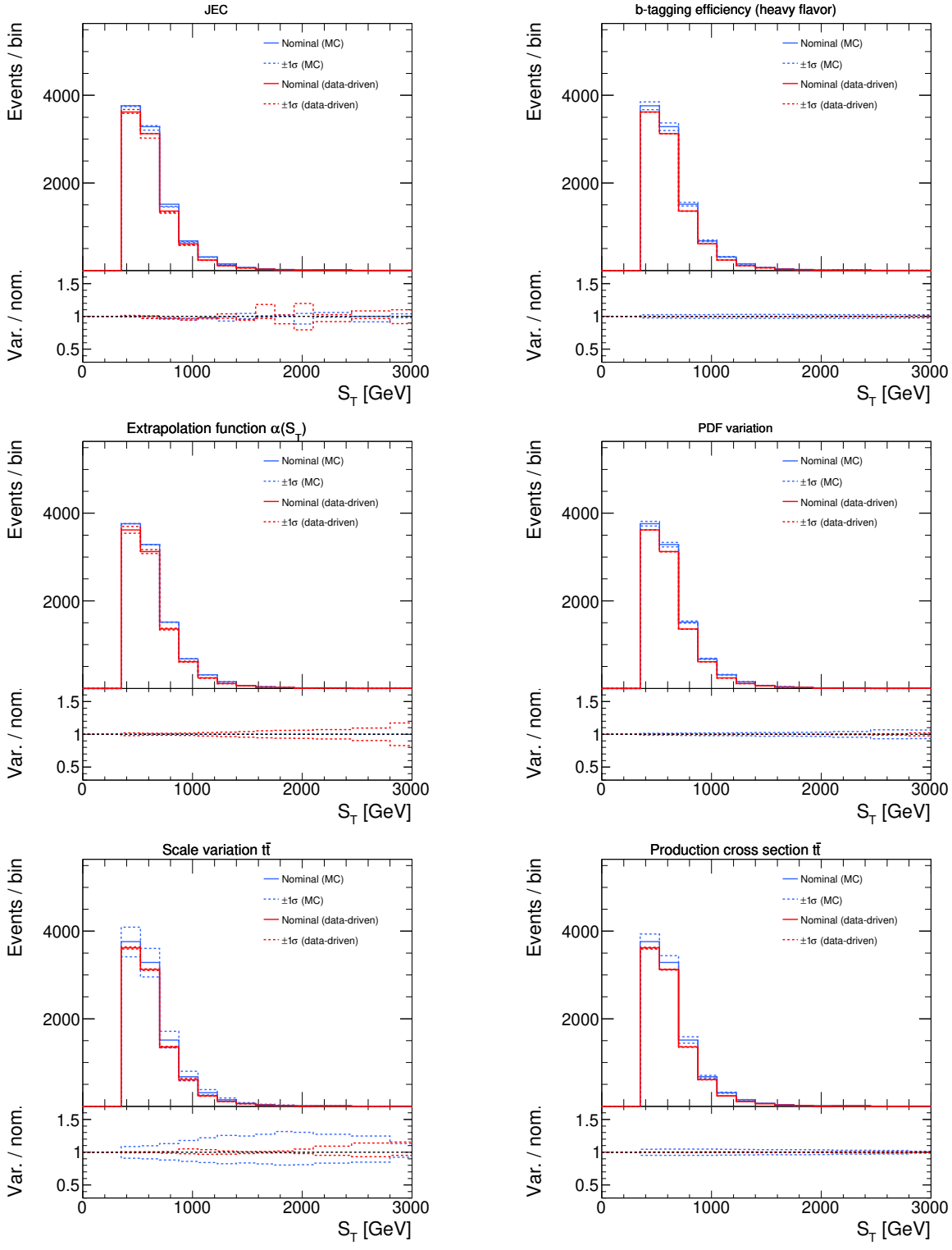

Figure 7.27: Distributions of S_T of the nominal (solid) and systematically varied (dashed) templates for simulated $\mathrm{t\bar{t}}$ +DY + jets events (blue) and the data-driven estimate (red). Shown are variations due to the uncertainty in the JEC (upper left), b-tagging efficiency (upper right), extrapolation function $\alpha(S_\mathrm{T})$ (middle left), choice of PDF (middle right), choice of μ_r and μ_f for $\mathrm{t\bar{t}}$ production (lower left), and $\mathrm{t\bar{t}}$ production cross section (lower right). The lower panels show the ratio of the varied templates and the nominal ones.

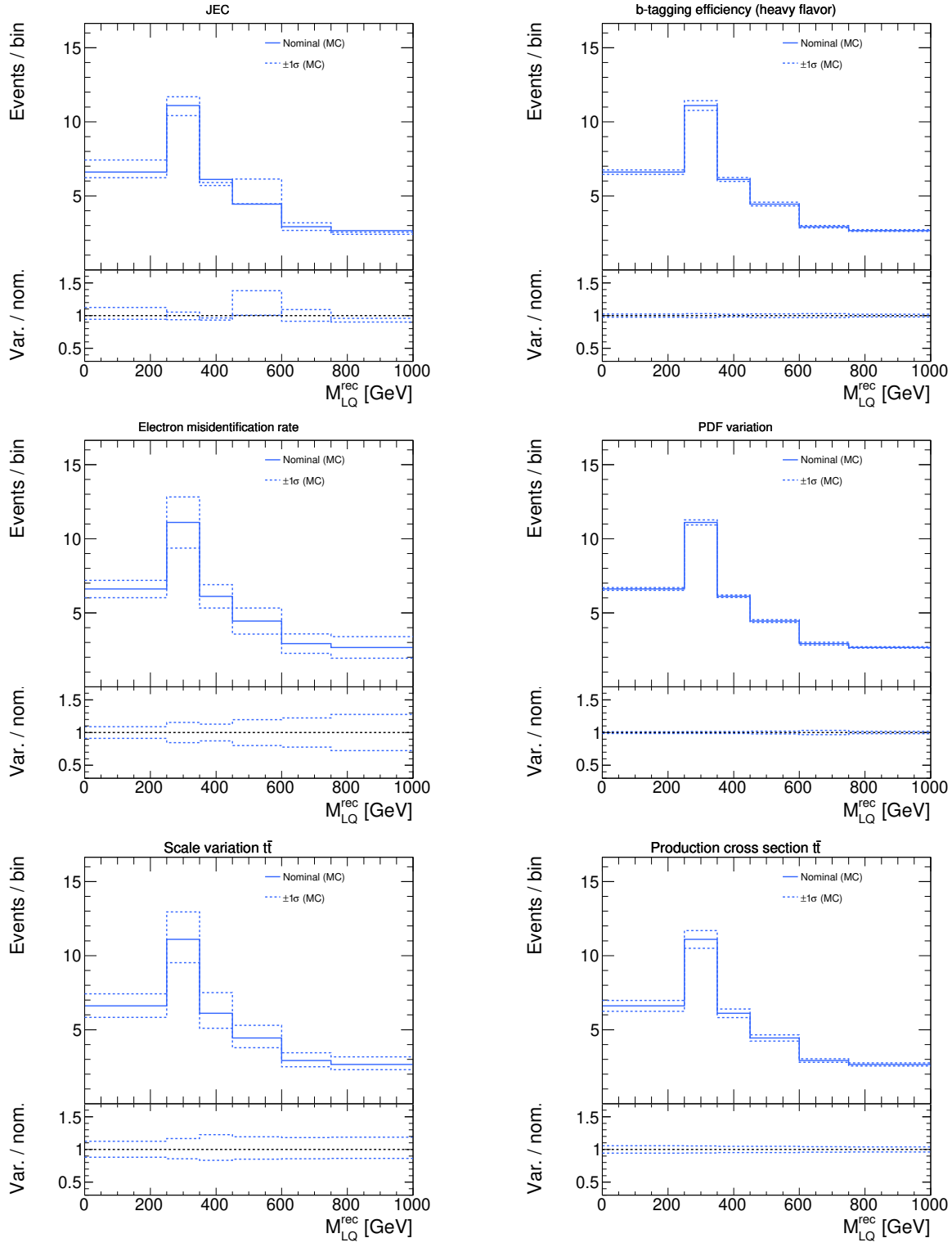

Figure 7.28: Distributions of $M_{\mathrm{LQ}}^{\mathrm{rec}}$ of the nominal (solid) and systematically varied (dashed) templates for simulated $\mathrm{t\bar{t}}+\mathrm{jets}$ events. Shown are variations due to the uncertainty in the JEC (upper left), b-tagging efficiency (upper right), electron misidentification rate (middle left), choice of PDF (middle right), choice of μ_{r} and μ_{f} for $\mathrm{t\bar{t}}$ production (lower left), and $\mathrm{t\bar{t}}$ production cross section (lower right). The lower panels show the ratio of the varied template and the nominal one.

In category A, their influence on simulated events of $\mathrm{t\bar{t}}+\text{jets}$ production is shown, while for category B, the simulated background from $\mathrm{t\bar{t}}+\mathrm{DY}+\text{jets}$ events is compared to the data-driven prediction. It is visible, that the extrapolation from data is much less affected by almost all systematic uncertainties. In particular, the otherwise dominant uncertainty in the choice of μ_r and μ_f is reduced in comparison to simulated events. This is due to the ratio used in the definition of the extrapolation function in equation (7.16). Uncertainties affecting both the SR and CR cancel to a large degree in this formula, which decreases the dependence of $\alpha(S_\mathrm{T})$ on systematic uncertainties. Although the data-driven prediction is affected by the uncertainty in $\alpha(S_\mathrm{T})$, the great reduction of other systematic uncertainties is beneficial in total. Uncertainties with an effect only in the SR or CR are not reduced by the data-driven background estimation method.

For the simulated backgrounds in category A, the dominant systematic uncertainties are due to the choice of μ_r and μ_f as well as the lepton misidentification rates. In the major backgrounds estimated from data in category B, the uncertainties in the extrapolation function and lepton efficiencies have the largest impact. The minor backgrounds estimated from simulation are most affected by the modelling uncertainties related to the choice of μ_r and μ_f and the PDF. For simulated events of LQ pair production, the uncertainties in lepton and b-tagging efficiencies are dominant. All systematic uncertainties discussed in this section are statistically accounted for in the final interpretation of the results as described in the following section.

7.9 Results

The distributions of $M_\mathrm{LQ}^\mathrm{rec}$ in category A and S_T in category B of the SR are used in a statistical procedure to quantify the presence of a potential LQ signal. Both allow for a clear distinction between SM processes and the expected contribution from events of LQ pair production. In order to obtain the final SM prediction in both categories, a simultaneous binned ML template fit of the backgrounds to the data is performed with the THETA software package [167]. All systematic uncertainties discussed in the previous section are considered as nuisance parameters in the fit. A log-normal prior distribution is used for uncertainties only affecting the rate of a given process. Uncertainties in both the shape and normalization are modelled by Gaussian priors. The statistical uncertainty in the SM backgrounds is taken into account by defining one additional nuisance parameter with a Gaussian prior for each bin in the distributions of $M_\mathrm{LQ}^\mathrm{rec}$ and S_T.

The values of the nuisance parameters corresponding to the best fit of the back-

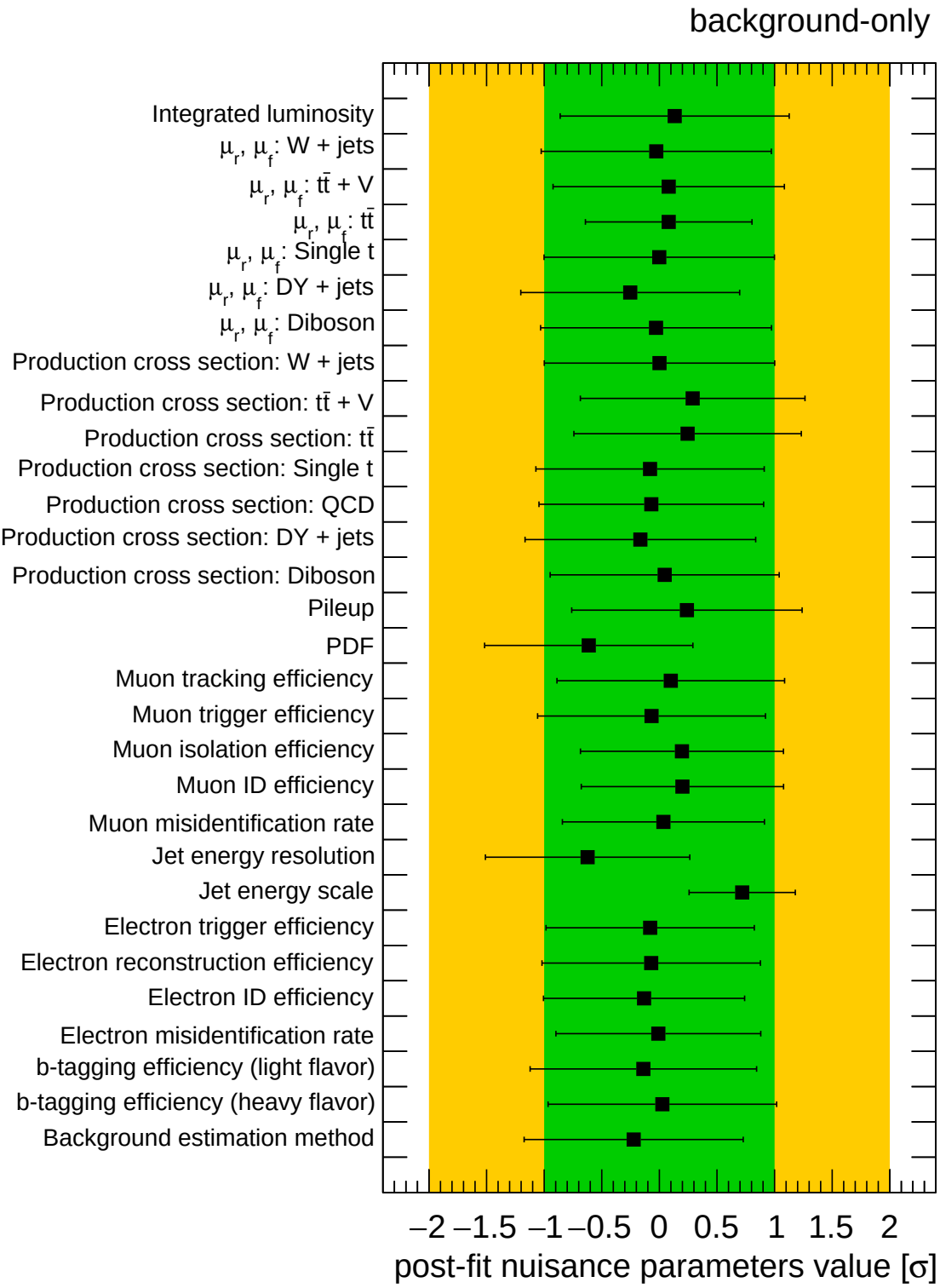

Figure 7.29: Values of the nuisance parameters after the background-only fit to the data. The values are given in units of their prior uncertainty, the error bars correspond to the post-fit uncertainties.

ground to the data are shown in figure 7.29. The error bars correspond to the post-fit uncertainties of the nuisance parameters. All post-fit nuisance parameters agree with their priors well within one standard deviation, only few shifts by more than 0.5 standard deviations are observed. This result confirms the good modelling of data by the prediction of SM backgrounds derived for this analysis in both categories. Furthermore, it is visible that the systematic uncertainties are not constrained considerably by the fit. This behavior is due to the small impact of systematic uncertainties as a result of the data-driven background prediction in category B.

The final distributions of $M_{\mathrm{LQ}}^{\mathrm{rec}}$ and S_{T} after the fit are shown in figure 7.30. Here, the uncertainties shown correspond to the total uncertainties, which are the quadratic sum of the statistical and systematic uncertainties. Very good agreement between data and the fitted SM prediction is found and no signal of LQ pair production is observed. The difference between data and the predicted background is smaller than two standard deviations of the total uncertainty in every bin, most bins agree within one standard deviation. As indicated by the post-fit nuisance parameter values, the data-driven background estimation in category B leads to an accurate description of the data.

In the absence of a signal, upper limits on the product of the LQ pair production cross section and the squared branching fraction $\mathcal{B}^2$ at 95% CL are derived as a function of the LQ mass. Here, it is assumed that LQs exclusively decay to top quarks and muons, i.e. $\mathcal{B}(\mathrm{LQ} \to \mathrm{t}\mu) = 1$. A Bayesian likelihood-based method [167, 180, 181] is used for this purpose. It performs a statistical combination of all bins of the two distributions considered. In addition to the nuisance parameters described above, the LQ pair production cross section is assigned a nuisance parameter without prior constraints, i.e. with a flat prior distribution.

Toy distributions of $M_{\mathrm{LQ}}^{\mathrm{rec}}$ and S_{T} are sampled from the post-fit nuisance parameter values and uncertainties in pseudo-experiments. They are used to determine the distribution of expected upper limits on the LQ pair production cross section under the background-only hypothesis for exclusive LQ decays to top quarks and muons. Observed exclusion limits are derived from the recorded data. Figure 7.31 presents the observed limits and the median and regions expected to contain 68 and 95% of the distribution of expected limits under the background-only hypothesis. Good agreement between the observed and expected exclusion limits is observed across all values of M_{LQ}. The limits for $M_{\mathrm{LQ}} = 200\,\mathrm{GeV}$ are considerably weaker than the ones for higher masses. This effect is introduced by requiring two muons with $p_{\mathrm{T}} > 30\,\mathrm{GeV}$. Due to the large top quark mass, the final state with top quarks and muons is produced near

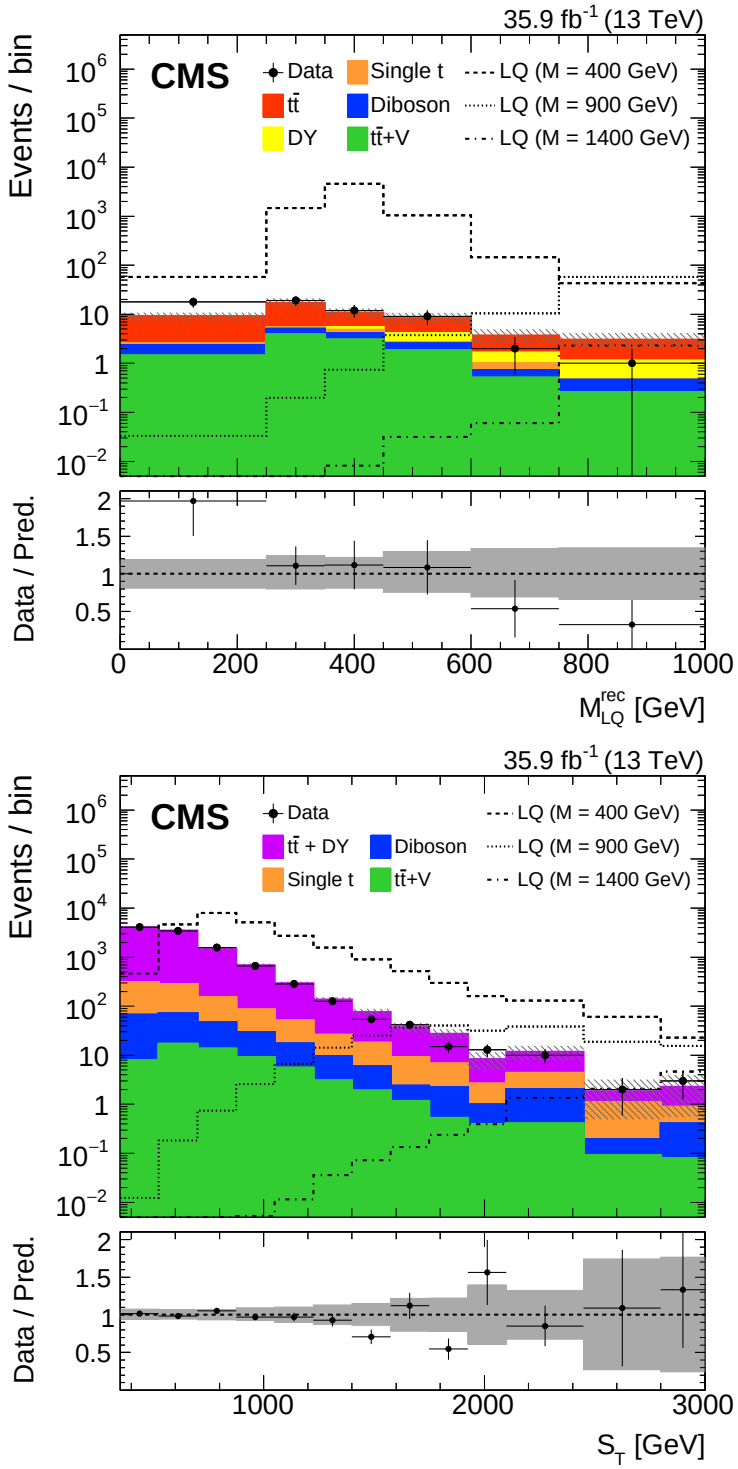

Figure 7.30: Distributions of $M_{\mathrm{LQ}}^{\mathrm{rec}}$ (upper) and S_{T} (lower) in categories A and B, respectively, of events passing the full selection. The background from events of $\mathrm{t\bar{t}}+\mathrm{DY}+\mathrm{jets}$ production in category B is estimated from data. All backgrounds are scaled according to the post-fit values of the nuisance parameters in the background-only fit. The lower panels show the ratio of data and the SM prediction, the grey area corresponds to the total uncertainty in the SM prediction. Published in Ref. [83] and available online in HEPDATA [179].

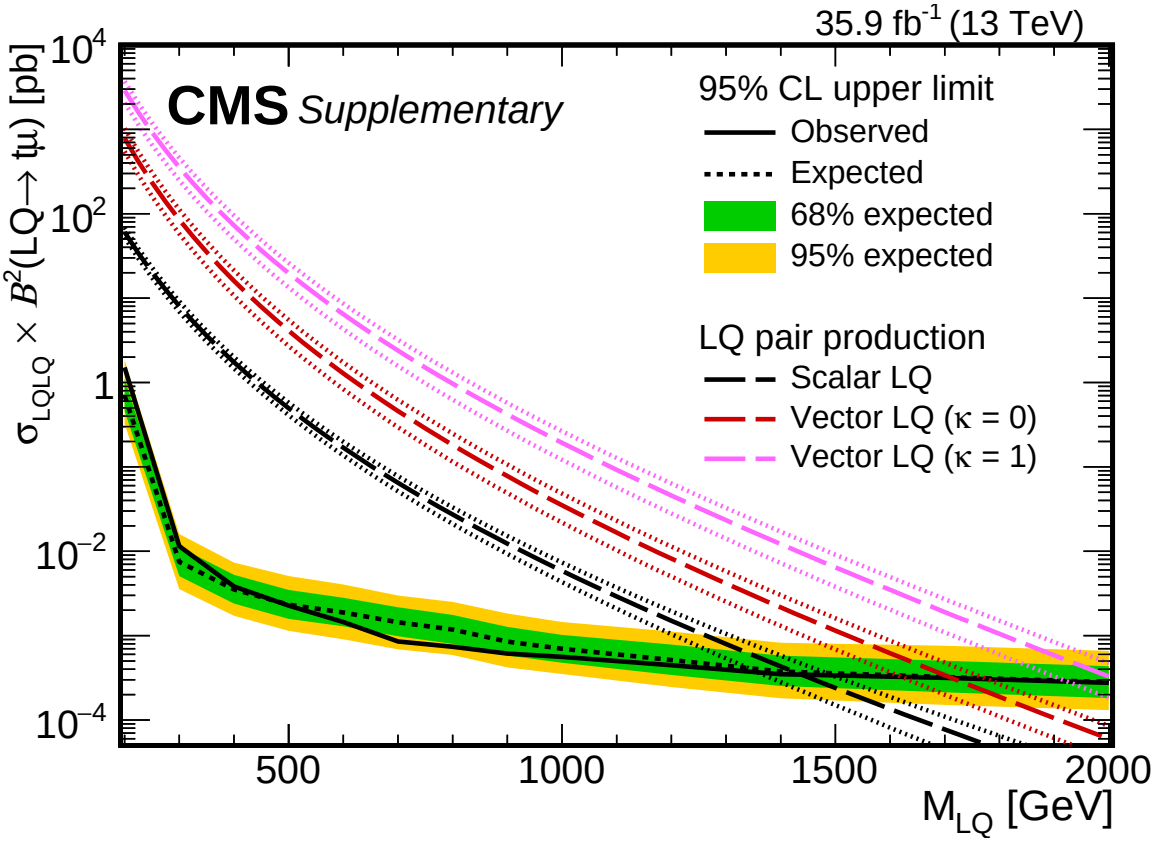

Figure 7.31: Expected and observed upper limits on the product of the LQ pair production cross section and $\mathcal{B}^2$ at the 95% CL as a function of the LQ mass. Unit branching fraction for the decay LQ $\to$ tμ is assumed. The black (colored) dashed lines show the pair production cross section of scalar (vector) LQs at NLO [77] (LO [78]). Published with Ref. [83].

the kinematic threshold for such low LQ masses. Hence, the selection efficiency is significantly reduced for the lowest LQ mass considered. As stated in section 7.5, the sensitivity to low LQ masses is driven by category A while at high M_{LQ}, category B provides the largest sensitivity.

The presented limits on the cross section were derived for scalar LQ pair production. However, it has been verified that the acceptance and kinematic distributions in events of vector LQ pair production are compatible with the scalar case. Hence, the limits shown in figure 7.31 are interpreted in the context of scalar and vector LQs. Comparing the theoretical production cross section with the experimental cross section upper limits, lower limits on the LQ mass are set. Pair-produced scalar LQs decaying exclusively to top quarks and muons are excluded up to masses of $M_{\mathrm{LQ}} = 1420\,\mathrm{GeV}$ at 95% CL. Due to the higher pair production cross section, vector LQs with the same decay mode are excluded below $M_{\mathrm{LQ}} = 1710\,\mathrm{GeV}$ and $M_{\mathrm{LQ}} = 2000\,\mathrm{GeV}$ for $\kappa = 0$ and

$\kappa = 1$, respectively. These limit constitute the results of the first direct search for LQ pair production in the $\mathrm{LQ} \to \mathrm{t}\mu$ decay channel. The mass limits on scalar LQs are improved by more than 600 GeV compared to the limits obtained in a reinterpretation [75] of a search for supersymmetry [182]. The limits placed by the presented analysis are the most stringent limits in the $\mathrm{LQ} \to \mathrm{t}\mu$ decay mode to date.

7.10 Combination with Other Decay Modes

The parameter space constrained can be increased significantly by considering not only the decay of LQs to top quarks and muons but also other final states that could be produced in the decay of the same LQ state with charge $-1/3$. For this purpose, the result of the search presented here is combined with those of two other analyses. The first is a search for scalar LQs in the $\mathrm{LQ} \to \mathrm{t}\tau$ decay channel [85]. Pair-produced scalar LQs decaying exclusively to top quarks and τ leptons are excluded below masses of 900 GeV at 95% CL by that search. Constraining the LQ to decay to top quarks and either muons or τ leptons, cross section upper limits are placed in the plane of M_{LQ} and B. In this case, $\mathcal{B}(\mathrm{LQ} \to \mathrm{t}\mu) = 1 - \mathcal{B}(\mathrm{LQ} \to \mathrm{t}\tau)$ holds.

A full statistical combination of the two decay channels considered is performed. Simulated samples of LQ pair production with subsequent decays to top quarks and muons or τ leptons for varying values of $\mathcal{B}(\mathrm{LQ} \to \mathrm{t}\mu)$ are assembled by reweighting samples of simulated LQ pair production and subsequent decays to the $\mathrm{t}\mu\mathrm{t}\mu$, $\mathrm{t}\tau\mathrm{t}\tau$, or $\mathrm{t}\mu\mathrm{t}\tau$ final states. All weights are listed in table 7.4. The weight applied to the events of a given sample equals the squared branching fraction of the respective decay mode. Hence, the second column of table 7.4 corresponds to weights applied to events in the $\mathrm{LQLQ} \to \mathrm{t}\mu\mathrm{t}\mu$ decay mode, the third column shows the weights for the $\mathrm{LQLQ} \to \mathrm{t}\tau\mathrm{t}\tau$ channel, and the fourth column contains the weights for the $\mathrm{LQLQ} \to \mathrm{t}\mu\mathrm{t}\tau$ sample.

Because the event selections of the analysis presented here and the search in the $\mathrm{LQ} \to \mathrm{t}\tau$ channel are orthogonal, the categories employed in both analyses can be combined statistically in a simultaneous binned maximum-likelihood template fit. The same procedure as described in the previous section is applied. Systematic uncertainties considered in both analyses are considered as fully correlated across all search categories. For each value of $\mathcal{B}(\mathrm{LQ} \to \mathrm{t}\mu)$, the expected and observed cross section upper limits at 95% CL are determined. The resulting observed limits in the plane of M_{LQ} and $\mathcal{B}(\mathrm{LQ} \to \mathrm{t}\mu)$ are shown in figure 7.32. The mass exclusion limits are determined by the intersection of the LQ pair production cross sections for scalar or vector LQs with the observed limit.

β	β^2	$(1-\beta)^2$	$1-\beta^2-(1-\beta)^2$
0.0	0.0	1.0	0.0
0.1	0.01	0.81	0.18
0.2	0.04	0.64	0.32
0.3	0.09	0.49	0.42
0.4	0.16	0.36	0.48
0.5	0.25	0.25	0.5
0.6	0.36	0.16	0.48
0.7	0.49	0.09	0.42
0.8	0.64	0.04	0.32
0.9	0.81	0.01	0.18
1.0	1.0	0.0	0.0

Table 7.4: Values of β used for the combination (left column) and weights used for reweighting the sample with LQLQ $\to$ tμtμ (tτtτ, tμtτ) decays (columns 2–4). Here, β denotes the value of $\mathcal{B}(\mathrm{LQ} \to \mathrm{t}\mu)$.

The sensitivity is driven by this analysis for values of $\mathcal{B}(\mathrm{LQ} \to \mathrm{t}\mu) > 0.1$ and by the search in the LQ $\to$ tτ channel for smaller values. For all values of $\mathcal{B}(\mathrm{LQ} \to \mathrm{t}\mu)$, pair-produced LQs decaying to top quarks and either muons or τ leptons below masses of $M_{\mathrm{LQ}} = 900\,\mathrm{GeV}$ are excluded at 95% CL. For vector LQs, the exclusion limits are even higher due to the increased production cross section. For all values of κ or $\mathcal{B}(\mathrm{LQ} \to \mathrm{t}\mu)$ considered, pair-produced vector LQs are excluded below $M_{\mathrm{LQ}} = 1190\,\mathrm{GeV}$.

Since an LQ with charge $-1/3$ could also decay to a down-type quark and a neutrino, the analysis presented here is also combined with results from a reinterpretation [82] of a search for pair-production of bottom squarks decaying to SM bottom quarks and the lightest supersymmetric particle, which is assumed to interact only via the weak force. For vanishing masses of the lightest supersymmetric particle, the final state of that analysis corresponds to the final state of LQ pair production and subsequent decays in the LQ $\to$ bν channel. That analysis excluded pair-produced scalar LQs below masses of 1080 GeV at 95% CL.

Unlike in the combination with the LQ $\to$ tτ channel, in this case only the strongest upper limit on the LQ pair production cross section, set either by the analysis presented here or in the LQ $\to$ bν channel, is considered. Here, it is assumed that LQs can only decay to the tμ or bν final state, i.e. $\mathcal{B}(\mathrm{LQ} \to \mathrm{t}\mu) = 1 - \mathcal{B}(\mathrm{LQ} \to \mathrm{b}\nu)$. The cross section limit in the tμ channel is scaled with $\mathcal{B}^2\,(\mathrm{LQ} \to \mathrm{t}\mu)$ while the limit in the bν channel is scaled with $\mathcal{B}^2\,(\mathrm{LQ} \to \mathrm{b}\nu) = (1 - \mathcal{B}(\mathrm{LQ} \to \mathrm{t}\mu))^2$. For each value of $\mathcal{B}(\mathrm{LQ} \to \mathrm{t}\mu)$, the strongest of the two limits is considered.

In figure 7.33, the resulting observed upper limits on the pair production cross

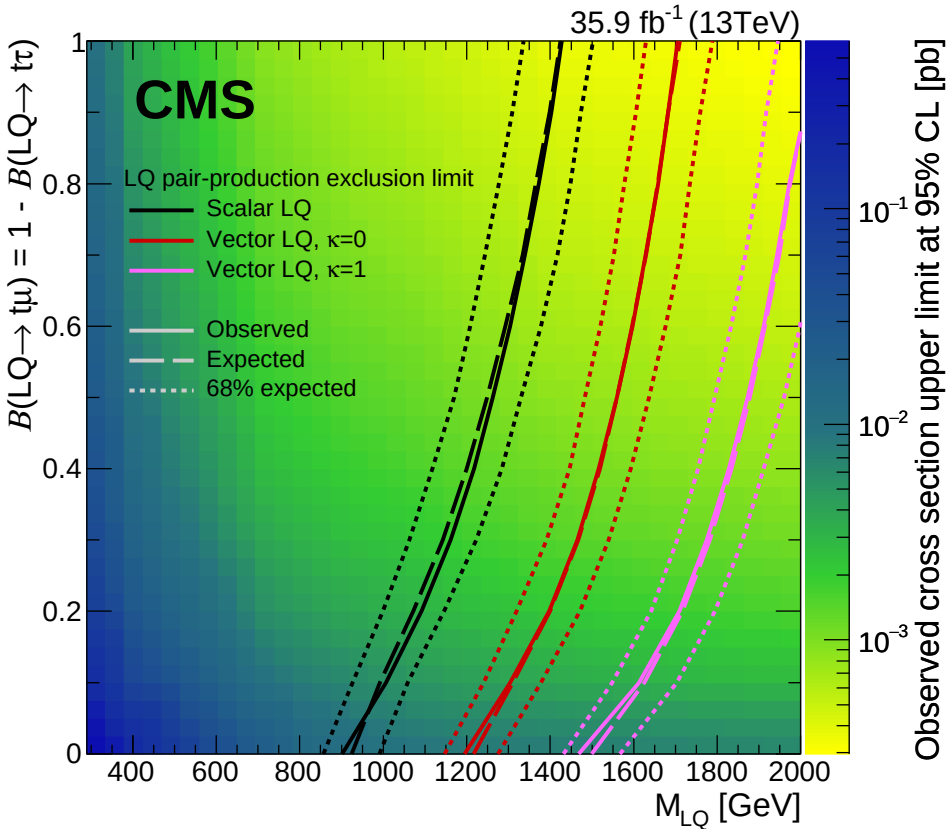

Figure 7.32: Observed upper limits on the LQ pair production cross section for LQs decaying into a top quark and a muon or a τ lepton at 95% CL in the M_{LQ}–$\mathcal{B}(\mathrm{LQ} \to \mathrm{t}\mu)$ plane. The black (colored) lines show the lower mass exclusion limits for scalar (vector) LQs. They are derived using the prediction for the scalar and vector LQ signal calculated at NLO [77] and LO [78], respectively. Published in Ref. [83] and available online in HEPDATA [179].

section of LQs are shown in the plane of M_{LQ} and $\mathcal{B}(\mathrm{LQ} \to \mathrm{t}\mu)$. The sensitivity in this combination is driven by the $\mathrm{LQ} \to \mathrm{t}\mu$ channel for values of $\mathcal{B}(\mathrm{LQ} \to \mathrm{t}\mu) > 0.3$ and by the $\mathrm{LQ} \to \mathrm{b}\nu$ channel otherwise. The transition region around $\mathcal{B}(\mathrm{LQ} \to \mathrm{t}\mu) = 0.3$ shows the weakest limits because none of the two analyses is sensitive to events with exactly one muon and one neutrino from the LQ decays. Across all values of $\mathcal{B}(\mathrm{LQ} \to \mathrm{t}\mu)$, pair-produced scalar LQs decaying either to top quarks and muons or bottom quarks and neutrinos are excluded below masses of $M_{\mathrm{LQ}} = 980\,\mathrm{GeV}$ at 95% CL. The pair production of vector LQs is excluded for LQ masses below $M_{\mathrm{LQ}} = 1340\,\mathrm{GeV}$ for all values of $\mathcal{B}(\mathrm{LQ} \to \mathrm{t}\mu)$ and κ in this configuration.

In summary, combining results obtained in multiple LQ decay channels increases the LQ parameter space that can be constrained. For the first time, all couplings of

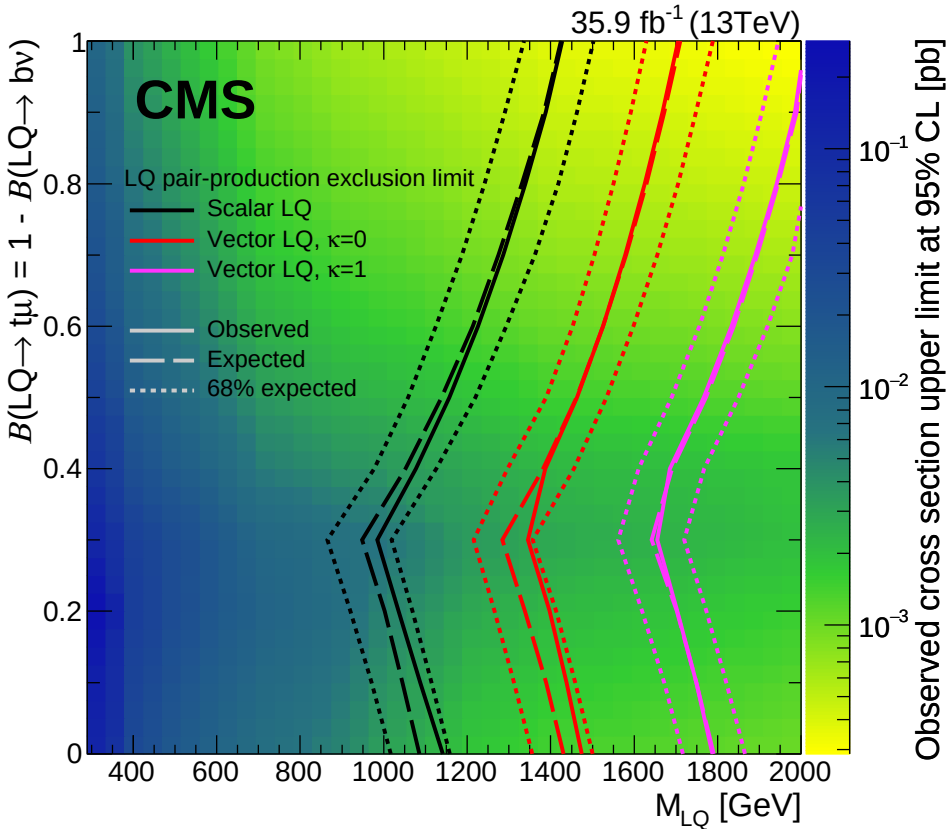

Figure 7.33: Observed upper limits on the LQ pair production cross section for LQs decaying into a top quark and a muon or a bottom quark and a neutrino at 95% CL in the M_{LQ}–$\mathcal{B}(\mathrm{LQ} \to \mathrm{t}\mu)$ plane. The black (colored) lines show the lower mass exclusion limits for scalar (vector) LQs. They are derived using the prediction for the scalar and vector LQ signal calculated at NLO [77] and LO [78], respectively. Published in Ref. [83] and available online in HEPDATA [179].

LQs with a charge of $-1/3$ to third-generation quarks relevant to explain the anomalies measured in the b-flavor sector are examined. Limits are derived as a function of the branching fraction of the LQ decay and its mass. Scalar (vector) LQs of charge $-1/3$ that decay in the $\mathrm{LQ} \to \mathrm{t}\mu$ and either $\mathrm{LQ} \to \mathrm{t}\tau$ or $\mathrm{LQ} \to \mathrm{b}\nu$ channels are excluded below masses of $M_{\mathrm{LQ}} = 900$ (1190) GeV for all possible branching fractions between those decay modes.

7.11 Prospects for the High Luminosity LHC

With the upcoming upgrade of the LHC, it will be operated at $\sqrt{s} = 14\,\mathrm{TeV}$ and much higher instantaneous luminosities [183]. A dataset corresponding to about $L =$

$3000\,\text{fb}^{-1}$ is expected to be recorded with such conditions. The expected reach in sensitivity of the analysis presented in the previous sections and the search for pair-produced scalar LQs decaying to top quarks and τ leptons [85] is estimated in this section. Both, expected exclusion limits and discovery significances are projected based on the analyses of the CMS dataset recorded in the year 2016, which corresponds to an integrated luminosity of $35.9\,\text{fb}^{-1}$. Similar as for that dataset, the analyses in the two channels are combined statistically. Projected exclusion limits and discovery significances are then derived in the plane of M_{LQ} and $\mathcal{B}(\text{LQ} \to \text{t}\mu)$.

In this section, first an overview over the upgraded CMS detector is given. Afterwards, the projection strategy is discussed and finally, the projected exclusion limits and discovery significances are presented.

7.11.1 The Upgraded CMS Detector

The HL-LHC will be operated at instantaneous luminosities of up to $7.5 \cdot 10^{34}\,\text{cm}^{-2}\text{s}^{-1}$, which exceeds the peak luminosity reached in the Run-II data-taking period by more than a factor of 3. The increased instantaneous luminosity leads to a much larger number of pp interactions per bunch crossing. While under Run-II conditions an average number of 34 interactions per bunch crossing was observed, up to 200 PU interactions are expected at the HL-LHC. Correspondingly, the expected particle flux in the individual detector systems is expected to increase significantly.

In order to cope with the HL-LHC running conditions, all components of the CMS detector will undergo major upgrades [184–188]. The goal of the upgrade is to provide the radiation hardness required for operation under HL-LHC conditions while optimally exploiting the physics potential of the high instantaneous luminosity.

The upgraded tracking system will cover a region of pseudorapidity up to $|\eta| = 4$ with increased granularity and radiation tolerance. Information from the tracker will be included at the L1 triggering stage. The ECAL crystals will be cooled to lower temperatures than currently, allowing for better noise mitigation in the readout. The upgraded readout will facilitate the use of timing information while the improved front-end electronics will allow for signals from single crystals to be used in the L1 trigger. In the HCAL, the readout system and the scintillator material close to the beam line will be replaced. The readout electronics in the muon system will be improved in order to increase its speed and radiation hardness. The new implementation of gaseous muon chambers in the endcap region will improve the detector acceptance and performance of the muon reconstruction. A new timing detector will be inserted between the tracker and ECAL, which is expected to reduce the impact of PU on the vertex reconstruction.

The upgraded L1 triggering system is expected to record events at a much higher rate of 750 kHz with an increased latency. The HLT is expected to record events at an increased rate of 7.5 kHz.

The performance of the physics object reconstruction and identification with the upgraded CMS detector is summarized in Ref. [189]. For this projection, it is assumed that the object reconstruction using the improved detector components is sufficiently robust against the presence of the increased number of PU interactions. Therefore, no additional systematic uncertainties are taken into account in this context.

7.11.2 Projection Strategy

The results from the search for pair-produced LQs decaying to top quarks and muons presented in the previous sections are projected to higher integrated luminosities as expected from the HL-LHC. Additionally, also the results from the search for pair-produced LQs decaying to top quarks and τ leptons [85] are projected.

For this purpose, the expected distributions of the SM backgrounds and the LQ signal used in the final limit-setting procedure are to higher values of L with a factor f. This scaling factor is defined as $L^{\text{target}}/35.9\,\text{fb}^{-1}$, where L^{target} is the integrated luminosity under consideration and takes values of 100, 300, and $3000\,\text{fb}^{-1}$. The value $35.9\,\text{fb}^{-1}$ corresponds to the dataset recorded in 2016 by the CMS detector. According to Poisson statistics, the statistical uncertainty in the distributions is scaled by a factor of $\sqrt{f}$, which results in the relative statistical uncertainty scaled by a factor of $1/\sqrt{f}$.

The increased energy of $\sqrt{s} = 14\,\text{TeV}$ in the HL-LHC data-taking period is also taken into account. Here, a multiplicative event weight w is applied to each event passing the full selection of the respective analysis. Due to the increased pp center-of-mass energy, a smaller value of the proton's momentum fraction x is required to be carried by the initial-state partons in order to maintain the same partonic center-of-mass energy $\sqrt{\hat{s}} = \sqrt{x_1 x_2 s}$, at which a given event was simulated. Under the assumption of $x_1 = x_2 = x$, the transition of $\sqrt{s} = 13\,\text{TeV} \rightarrow \sqrt{s'} = 14\,\text{TeV}$ causes a shift in x according to $x \rightarrow x' = \sqrt{s}/\sqrt{s'} \cdot x = 13/14 \cdot x$. The weight w takes into account the changed value of the underlying PDFs when evaluated at x or x'. It is defined as

$$w = \frac{x_1' f(x_1', Q, f_1) \cdot x_2' f(x_2', Q, f_2)}{x_1 f(x_1, Q, f_1) \cdot x_2 f(x_2, Q, f_2)}, \tag{7.17}$$

where x_i refers to the momentum fraction of the initial state parton i and f_i denotes its flavor. For each process and in each category considered in the final statistical

Uncertainty	Value at $3000\,\text{fb}^{-1}$ [%]
Luminosity	1
SM production cross sections	2.8–12.5
b-tagging (b/c)	1
b-tagging (light)	5
JES	1–2.5
JER	3–6
e, μ efficiencies	1
e, μ misidentification	1–16
τ identification	2.5
τ energy scale	3
τ charge misidentification	2
Background extrapolation	$\text{LQ} \to \text{t}\mu$: 1.2–3.6
	$\text{LQ} \to \text{t}\tau$: ≤ 1

Table 7.5: Scaled relative systematic uncertainties in the "YR18 syst." scenario at $L^{\text{target}} = 3000\,\text{fb}^{-1}$. Published in Ref. [155].

interpretation of the two analyses, a new histogram corresponding to the one used in the final fit is filled. The weight w is used to weight events populating each distribution. The resulting distribution of weights as a function of the respective variables is used to reweight the final distributions that are used in the limit setting procedure. As a result of this reweighting procedure, the differential production cross sections of the SM backgrounds and LQ signal are modified to the match those at a center-of-mass energy of 14 TeV. The production cross sections of the backgrounds and, in particular, the LQ pair production signal is increased. Events with high transverse momentum transfer are especially affected. The average weights are compatible with the predicted increase in the production cross section between 13 and 14 TeV. Overall, a gain in sensitivity of about 5% is achieved by increasing the center-of-mass energy to 14 TeV with respect to 13 TeV.

For this projection, also the impact of reduced systematic uncertainties is taken into account. Two scenarios are considered for this purpose. In the first scenario, which is referred to as "YR18 syst." in the following, the relative experimental systematic uncertainties are scaled with $1/\sqrt{f}$ until they reach a defined lower limit. This limit is estimated based on studies on the object performance with the upgraded CMS detector at HL-LHC run conditions [189]. The values of the scaled relative experimental uncertainties considered for $L^{\text{target}} = 3000\,\text{fb}^{-1}$ are presented in table 7.5. The sensitivity of the search in the $\text{LQ} \to \text{t}\mu$ channel is most affected by the uncertainty in the b-tagging and lepton efficiencies. The uncertainty in the τ lepton ID is dominant in the $\text{LQ} \to \text{t}\tau$ channel. No lower limits are assumed for the scaled uncertainties in the background

extrapolations in both analyses as those uncertainties are purely statistical. The uncertainty in the background extrapolation function $\alpha(S_{\mathrm{T}})$ of the analysis of the $\mathrm{LQ} \to \mathrm{t}\mu$ decay channel is obtained from a constant fit to the ratio of uncertainties of the extrapolation function derived from histograms corresponding to integrated luminosities of 35.9 and $3000\,\mathrm{fb}^{-1}$, respectively. The theoretical uncertainties in the choice of μ_{r}, μ_{f}, and the PDFs are halved at $L^{\mathrm{target}} = 3000\,\mathrm{fb}^{-1}$. In the second scenario, which is denoted "stat. only", no systematic uncertainties are considered. This case represents the scenario of ultimate precision and is therefore considered overly optimistic. However, it offers the possibility of estimating the ultimate reach of the analyses conducted in the 2016 dataset.

7.11.3 Projected Results

The statistical analysis for the limit derivation of the two individual analysis channels is performed as described in section 7.9. The expected discovery significances are computed from a log-likelihood ratio with the THETA package. In both cases, the same distributions as used in the analyses of the 2016 dataset are considered. In figure 7.34, the expected discovery significances in the $\mathrm{LQ} \to \mathrm{t}\mu$ and $\mathrm{LQ} \to \mathrm{t}\tau$ channels are shown for the "YR18 syst." and "stat. only" scenarios. The result for $35.9\,\mathrm{fb}^{-1}$ is obtained from templates only corrected for the higher center-of-mass energy but not for the value of the integrated luminosity or the uncertainties.

The discovery potential of both analyses is expected to be increased greatly by analyzing a dataset corresponding to $3000\,\mathrm{fb}^{-1}$. The LQ mass expected to be in reach for a discovery with 5σ significance is expected to be raised by more than 500 GeV, up to a value of 1700 GeV in the $\mathrm{LQ} \to \mathrm{t}\mu$ decay channel. An improvement of 400 GeV is expected in the $\mathrm{LQ} \to \mathrm{t}\tau$ channel, where LQs up to masses of 1200 GeV are expected to be discovered at the 5σ level. Considering the result in the $\mathrm{LQ} \to \mathrm{t}\mu$ decay mode, it is expected that the expected discovery significance becomes largely limited by the remaining systematic uncertainties at very high integrated luminosities. This is indicated by the large difference between the two scenarios displayed in figure 7.34 (upper). On the other hand, this behavior is not observed in the $\mathrm{LQ} \to \mathrm{t}\tau$ analysis, which suggests that the statistical uncertainty has a major impact on the analysis even when analyzing very large datasets.

The projected cross section upper limits at 95% CL on LQ pair production and exclusive decays to top quarks and muons or τ leptons are shown in figure 7.35 for the "YR18 syst." and "stat. only" scenarios. A kink is visible in the expected limits derived in the analysis of the $\mathrm{LQ} \to \mathrm{t}\mu$ decay channel in the "YR18 syst." scenario. Due

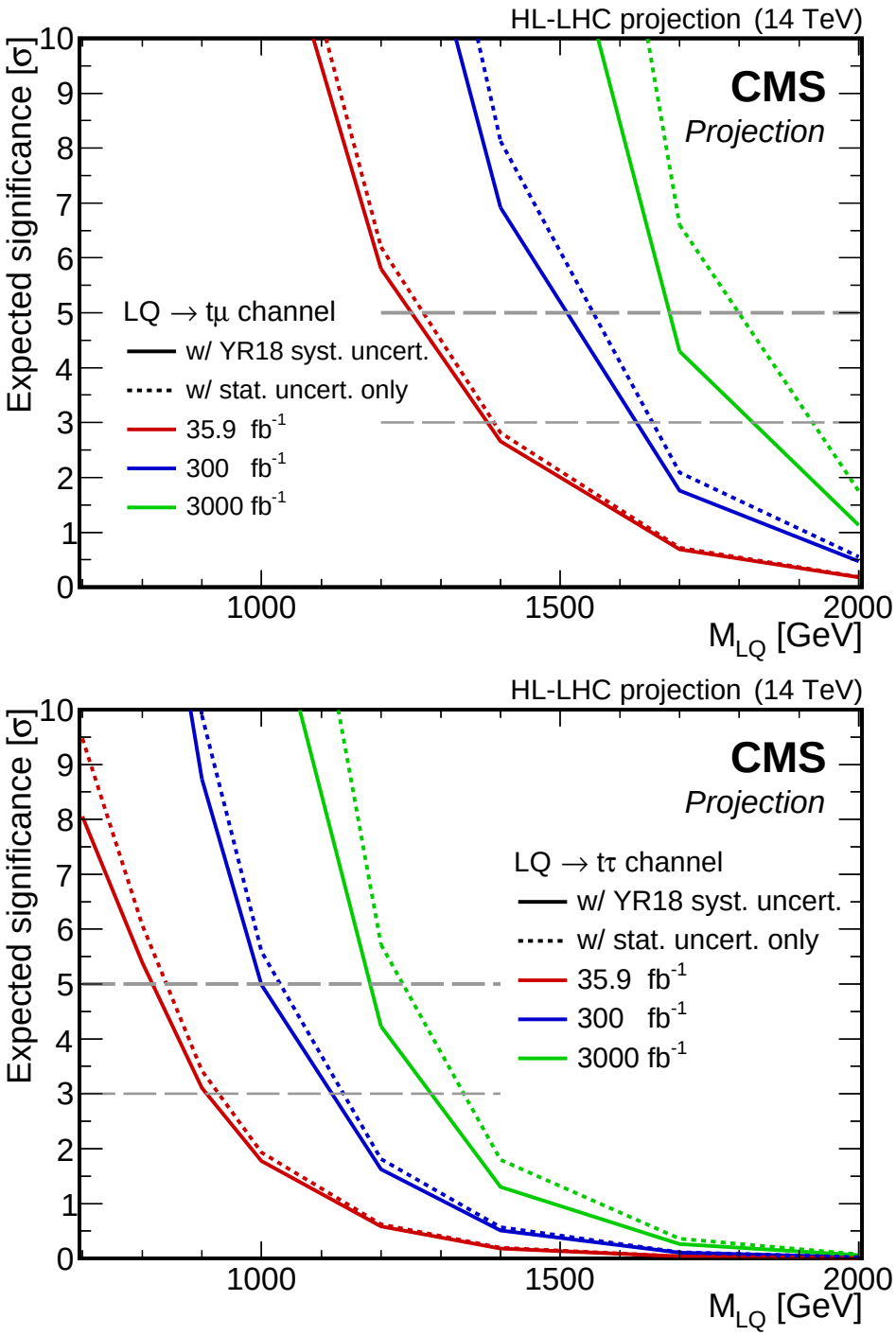

Figure 7.34: Expected discovery significances in the LQ $\to$ tμ (upper) and LQ $\to$ tτ (lower) decay channels for the "YR18 syst." (solid) and "stat. only" (dashed) scenarios. Three different values of L^{target} are considered. All results were obtained with templates for $\sqrt{s} = 13\,\text{TeV}$ that were scaled to $\sqrt{s} = 14\,\text{TeV}$. Published in Ref. [155].

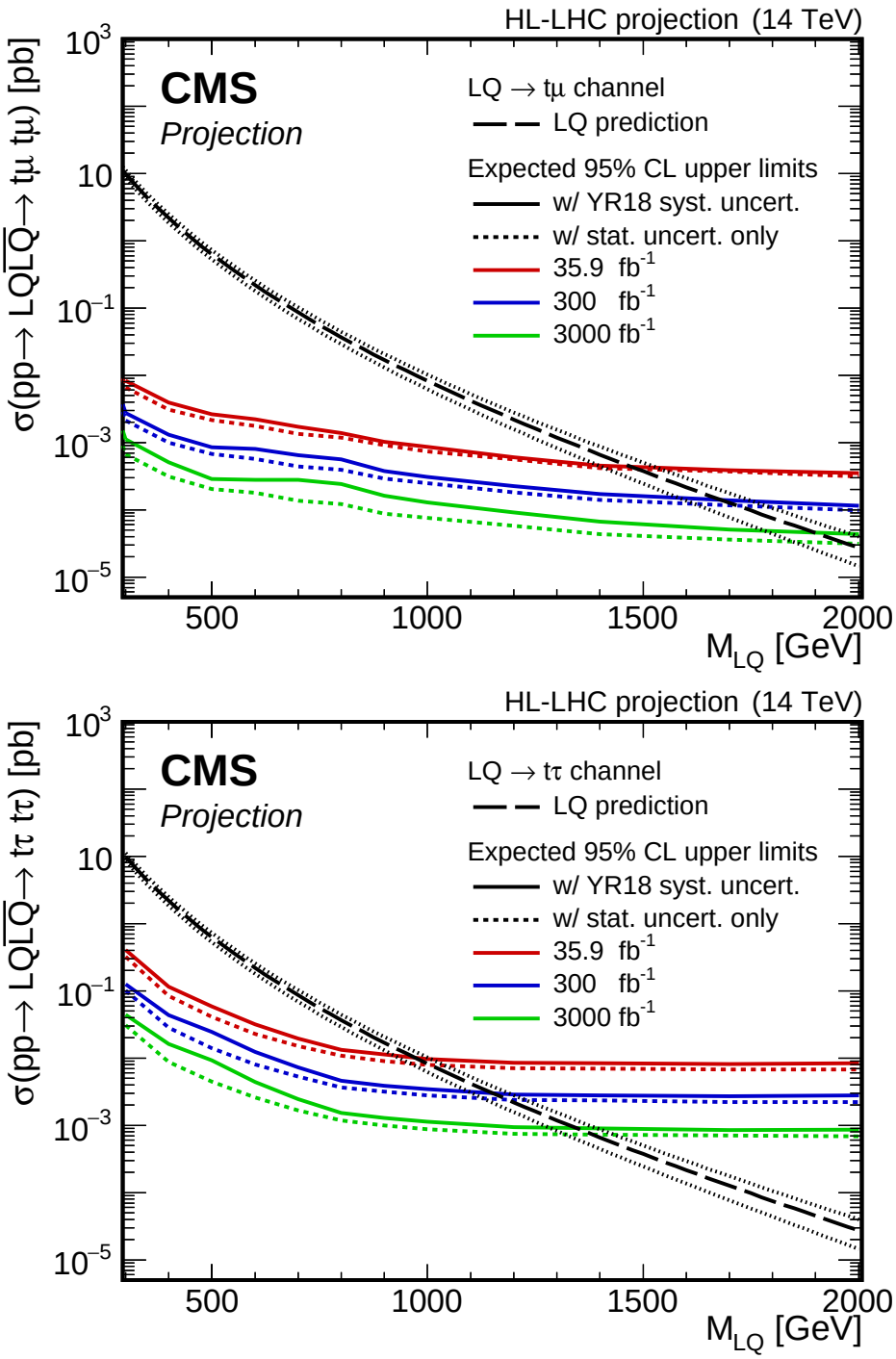

Figure 7.35: Expected pair production cross section upper limits at 95% CL in the $\mathrm{LQ} \to \mathrm{t}\mu$ (upper) and $\mathrm{LQ} \to \mathrm{t}\tau$ (lower) decay channels for the "YR18 syst." (solid) and "stat. only" (dashed) scenarios. Three different values of L^{target} are considered. All results were obtained with templates for $\sqrt{s} = 13\,\text{TeV}$ that were scaled to $\sqrt{s} = 14\,\text{TeV}$. Published in Ref. [155].

to employing two categories, A and B, in this analysis, the exclusion limits depend on the sensitivity in both of these categories. With increasing integrated luminosity, the sensitivity to LQ masses around 700 GeV provided by category A becomes limited by systematic uncertainties. This is visible in the region where both categories contribute equally to the overall expected limit, i.e. $M_{\mathrm{LQ}} \simeq 700\,\mathrm{GeV}$.

It is expected to exclude LQs decaying exclusively to top quarks and muons up to masses of about 1900 GeV at integrated luminosities of $3000\,\mathrm{fb}^{-1}$. This represents a gain of more than 500 GeV compared to the result obtained in the analysis of data corresponding to $35.9\,\mathrm{fb}^{-1}$ (cf. section 7.9). A similar improvement is expected to be made in the $\mathrm{LQ} \to \mathrm{t}\tau$ decay channel, where LQs of masses below $M_{\mathrm{LQ}} = 1400\,\mathrm{GeV}$ are expected to be excluded with $L^{\mathrm{target}} = 3000\,\mathrm{fb}^{-1}$, improving the current limit by 500 GeV.

The combination of the analyses in the individual LQ decay modes provides sentitivity to the full range of possible branching fraction for decays to either final state (cf. section 7.10). The projected discovery significance and cross section upper limit on LQ pair production at 95% CL is shown in figure 7.36 in the plane of M_{LQ} and $\mathcal{B}(\mathrm{LQ} \to \mathrm{t}\mu)$. An integrated luminosity of $3000\,\mathrm{fb}^{-1}$ is assumed in both cases. The gain when going from the "YR18 syst." to the "stat. only" scenario is clearly visible. This behavior is expected with the observation that the analysis in the $\mathrm{LQ} \to \mathrm{t}\mu$ decay channel drives the sensitivity for a large range of branching fractions and is limited by the scaled systematic uncertainties at $3000\,\mathrm{fb}^{-1}$. A discovery at the 5σ level is expected to be possible for LQs below masses of 1200 GeV independent of the branching fraction to the two final states under consideration. In the absence of LQ signal, LQs below masses of 1400 GeV are expected to be excluded at 95% CL for all possible branching fractions to $\mathrm{t}\mu$ and $\mathrm{t}\nu$.

In summary, improvements in the discovery potential and, if no evidence for the presence of an LQ signal is found, in the exclusion limits of between 400 and 500 GeV in the LQ mass are expected for analyses of the HL-LHC dataset. Systematic uncertainties will become more important as the statistical uncertainty will be largely reduced in a dataset of that size. With the analysis strategies unaltered, the projections presented here represent lower estimates of the potential reach of the two analyses considered.

7.12 Outlook

In order to increase the sensitivity of the search presented in this chapter in the future, analyzing the full dataset recorded in pp collisions of $\sqrt{s} = 13\,\mathrm{TeV}$ in the years 2016–

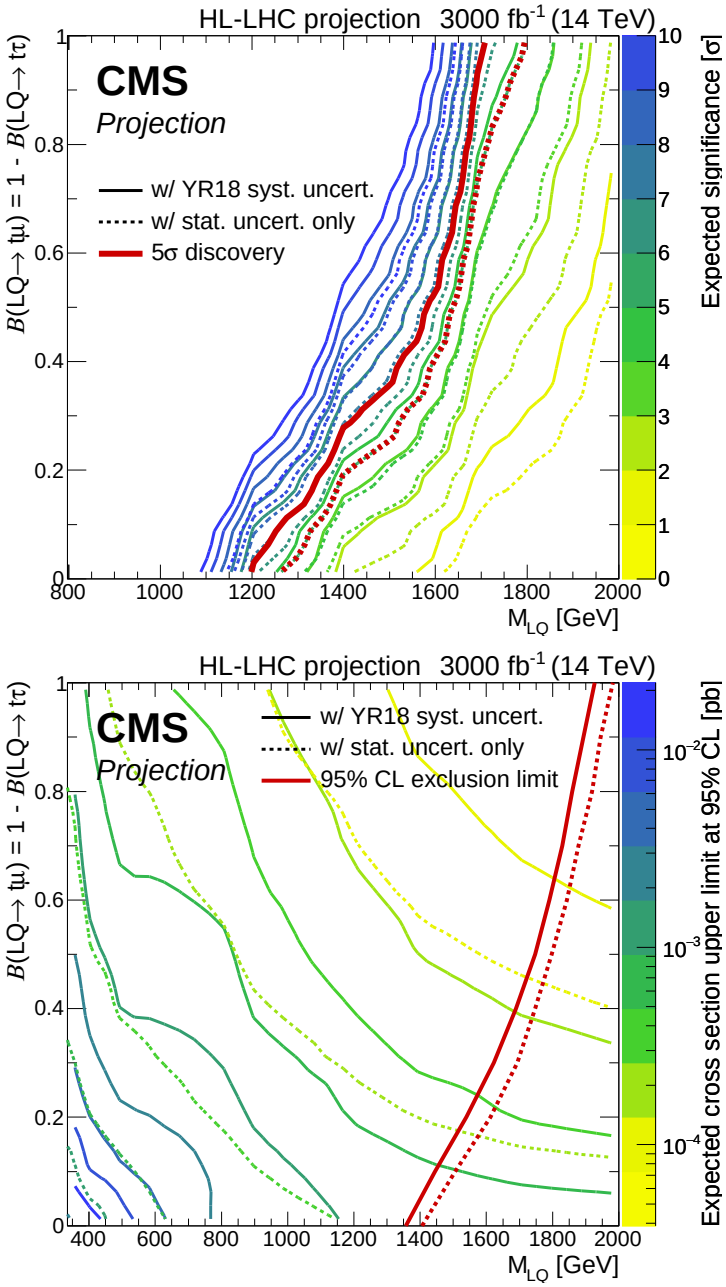

Figure 7.36: Expected significances (upper) and pair production cross section upper limits at 95% CL (lower) in the plane of M_{LQ} and $\mathcal{B}(\mathrm{LQ} \to \mathrm{t}\mu)$ at $3000\,\mathrm{fb}^{-1}$ for the "YR18 syst." (solid) and "stat. only" (dashed) scenarios. A value of $L^{\mathrm{target}} = 3000\,\mathrm{fb}^{-1}$ is considered. Color-coded lines represent lines of a constant expected significance or cross section upper limit, respectively. The red lines indicate the 5σ discovery level (upper) and the mass exclusion limit (lower). Published in Ref. [155].

2018 would be beneficial. In total, it corresponds to an integrated luminosity of more than $130\,\mathrm{fb}^{-1}$. Statistically combining data from the three years of data-taking would allow to probe higher LQ masses than those studied currently. However, significant improvements can only be achieved by refining the analysis strategy. A number of aspects of the analysis presented here could profit significantly from a larger amount of data beyond the effect of an improved statistical precision alone.

In this analysis, a common event selection is used for all three possible decay modes of the $\mathrm{t\bar{t}}$ system. This choice is due to the small expected number of SM background events with more than two leptons in the final state. However, with a dataset larger by a factor of 4, or even 100 as it would be the case for the HL-LHC data-taking, the three $\mathrm{t\bar{t}}$ decay modes could be analyzed separately. Event selections optimized individually would grant a better ratio of LQ signal to SM backgrounds and thus enhance the search sensitivity. Especially decays of the $\mathrm{t\bar{t}}$ system to the dileptonic final state analyzed in a separate category is expected to yield a large gain as the SM contribution to a category with four leptons in the final state is very rare.

As the region of LQ masses beyond $M_{\mathrm{LQ}} = 1420\,\mathrm{GeV}$ has not been excluded by this analysis, it is of particular interest for future searches. The decay products of such heavy LQs are expected to receive a considerable Lorentz boost due to the large mass difference between the LQ and the top quark. In this case, the decay products of the boosted top quark would produce a very collimated final state, hadronic decays would be expected to be reconstructed within a single, large jet. These final states are not optimally reconstructed in the presented analysis, where the hadronic top quark decay products are considered as individual AK4 jets. Dedicated algorithms for tagging such jets are extensively studied within the CMS Collaboration [151] and make use of the distinct substructure of the large jet arising from the top quark decay. Applying and optimizing this technique would be one of the most promising improvements to the current analysis. In order to maintain sensitivity to the low-mass LQ signal, separate categories could be defined based on the presence of a top-tagged jet. Individually optimizing the event selection for those categories would further increase the expected reach of a future analysis.

In general, the application of advanced data analysis techniques such as deep neural networks would also be expected to result in an optimized event selection. However, using simulated events of LQ pair production would introduce a model dependence to the result, which could significantly impair its reinterpretability in different models. As presented in the following chapter, it is possible to apply machine learning techniques in a model-agnostic way such that the gain in sensitivity originates solely from an

improved SM background classification.

The possibility to reinterpret and combine the results of searches for LQs is a crucial property for such analyses. Because LQs are expected to couple to more than exactly one quark-lepton-pair, utilizing the statistical potential of a combination of searches would maximize the sensitivity to LQs for all possible decay modes. Particular priority should be given to a combination of analyses examining couplings to third-generation quarks and any lepton family. Most models that aim at resolving the b-flavor anomalies (cf. chapter 3) predict such couplings to be dominant. Although simultaneous couplings of LQs to top quarks and muons or electrons are tightly constrained by flavor data, the $\mathrm{LQ} \to \mathrm{te}$ decay mode is the only one that has never been investigated when considering LQs of charge $-1/3$ and dominant couplings to top quarks. With the goal of providing experimental constraints for all possible LQ decay branching fractions, the full LQ coupling space favored by theoretical models could be studied systematically. The possibility to reinterpret the data in a variety of LQ theories will provide valuable guidance for identifying and closing gaps that are uncovered by the analyses currently conducted.

Chapter 8

Improvements of the Search for $t\bar{t}$ Resonances with a DNN Event Classifier

In this chapter, a simulation-based study of the search for resonant top quark pair production in the final state with exactly one muon and jets is presented. An example of a Feynman diagram for the process studied in this analysis is shown in figure 8.1. The existence of such resonances with masses at the TeV scale, which can be probed with LHC data, is postulated by many models extending the SM (cf. section 3.2). In this chapter, the published result of the CMS analysis using the 2016 dataset is presented in section 8.1. Afterwards, the simulated samples used in this study are introduced in section 8.2. The event selection and results obtained following the 2016 analysis strategy are detailed in section 8.3. Improvements using a DNN event classifier are studied in 8.4. This chapter closes with a summary and outlook in section 8.5.

8.1 Published CMS Results

Searches for new heavy resonances decaying to a pair of top quarks have been performed previously at the Tevatron [190–195] and by the ATLAS and CMS Collaborations [196–203]. The most stringent limits on resonant $t\bar{t}$ production were set by the CMS Collaboration [204] in a search analyzing the dataset recorded in the year 2016, corresponding to $35.9\,\mathrm{fb}^{-1}$. A combination of all three possible decay modes of the $t\bar{t}$ system was performed, increasing the sensitivity with respect to the results obtained in the individual decay channels.

In figure 8.2 (left), the expected exclusion limits on the g_{KK} production cross section

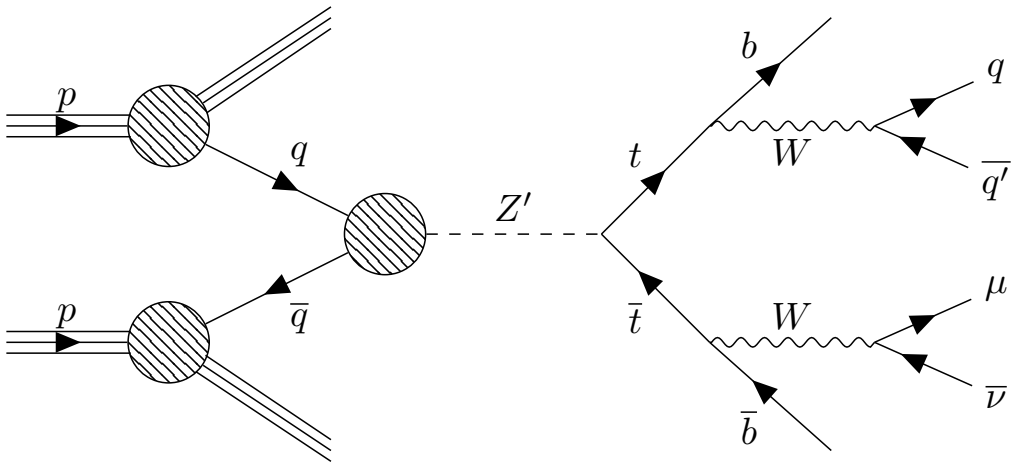

Figure 8.1: Feynman diagram for the production of a new heavy resonance Z' decaying to a pair of top quarks. The subsequent decay of the top quarks to the final state with one muon and jets is shown.

are shown as a function of the $\mathrm{g_{KK}}$ mass ($M_{\mathrm{g_{KK}}}$) under the assumption of unit branching fraction for the decay $\mathrm{g_{KK}} \to \mathrm{t\bar{t}}$ for the individual $\mathrm{t\bar{t}}$ decay channels and their statistical combination. It is visible that the dilepton channel contributes mostly at very small masses while the single-lepton and all-hadronic channels perform similarly and drive the limits at high $M_{\mathrm{g_{KK}}}$. In figure 8.2 (right), the observed and expected cross section upper limits for exclusive decays in the $\mathrm{g_{KK}} \to \mathrm{t\bar{t}}$ channel are shown as a function of $M_{\mathrm{g_{KK}}}$. KK excitations of the gluon are ruled out below a mass of 4.55 TeV for the same decay mode. Similarly, masses below 3.80, 5.25, and 6.65 TeV have been excluded for color-singlet Z' bosons decaying exclusively to a pair of top quarks with relative widths of 1, 10, and 30%, respectively.

8.2 Simulated Samples

The simulated samples analyzed in this study are scaled to correspond to the data that have been recorded by the CMS experiment in pp collisions at a center-of-mass energy of $\sqrt{s} = 13\,\mathrm{TeV}$ in the year 2017, corresponding to an integrated luminosity of $41.5\,\mathrm{fb}^{-1}$.

Signal events of s-channel $\mathrm{g_{KK}}$ production with subsequent decays to a pair of top quarks are simulated with the PYTHIA 8.230 event generator at LO, following the couplings presented in Ref. [205]. The LO production cross section is scaled with an K factor of $K = 1.3$ [206] to approximate NLO QCD contributions. Masses of the $\mathrm{g_{KK}}$

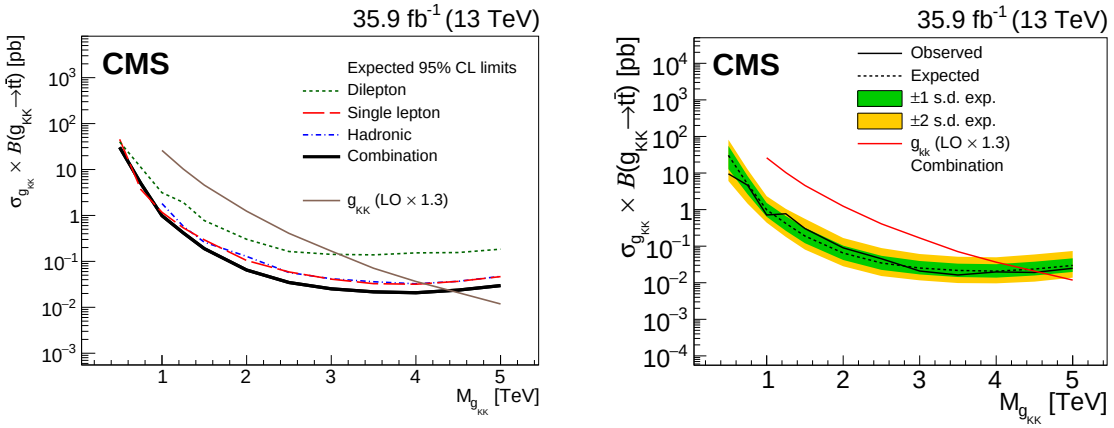

Figure 8.2: Left: Expected exclusion limits of the previous CMS search [204] on the g_{KK} production cross section as a function of $M_{g_{KK}}$ under the assumption of unit branching fraction for the decay $g_{KK} \to t\bar{t}$ for the individual $t\bar{t}$ decay channels and their statistical combination. The brown line depicts the prediction for the g_{KK} production cross section corrected with an NLO K factor of 1.3. Right: Observed and expected cross section upper limits of the previous CMS search [204] for exclusive decays in the $g_{KK} \to t\bar{t}$ channel as a function of $M_{g_{KK}}$.

between 0.5 and 8 TeV are generated. A complete list of the signal samples used is given in table 8.1.

The relevant SM background processes considered in this search include single and pair production of top quarks and additional strong radiation, the production of heavy gauge bosons in association with jets, and QCD multijet events. The simulation of events of $t\bar{t}$ + jets production is performed with POWHEG v2 at NLO. Single top quark production is simulated at NLO for three different channels. The s-channel production mode with a subsequent decay to the leptonic final state is generated with MADGRAPH5_AMC@NLO v2.4.3, the t-channel process and associated production of a top quark and a W boson are simulated with POWHEG v2 and include all possible decay chains. Events of DY + jets and W + jets production are generated with MADGRAPH5_AMC@NLO at LO. Last, QCD multijet production is simulated with PYTHIA at LO. Here, generated events are filtered to obtain a sample enriched with non-prompt muons produced in electroweak hadron decays. The filtering efficiency ranges between 0.6 and 13.2%.

For all simulated events, the NNPDF3.1 [207] PDF sets at NNLO precision are used. The fragmentation and hadronization is simulated with PYTHIA and the CP5 [208] tune is used to model the UE. The impact of additional pp interactions in the same or adjacent bunch-crossings is simulated with PYTHIA. Simulated events are reweighted

$M_{\mathrm{g_{KK}}}$ [GeV]	σ [pb]	N
500	$3.59 \cdot 10^{2}$	200000
750	$8.11 \cdot 10^{1}$	184000
1000	$2.61 \cdot 10^{1}$	200000
1250	$1.03 \cdot 10^{1}$	192000
1500	$4.57 \cdot 10^{0}$	200000
2000	$1.24 \cdot 10^{0}$	200000
2500	$4.08 \cdot 10^{-1}$	188000
3000	$1.68 \cdot 10^{-1}$	200000
3500	$7.09 \cdot 10^{-2}$	192000
4000	$3.65 \cdot 10^{-2}$	184000
4500	$2.08 \cdot 10^{-2}$	194000
5000	$1.18 \cdot 10^{-2}$	197000
5500	$7.25 \cdot 10^{-3}$	194000
6000	$4.92 \cdot 10^{-3}$	200000
6500	$3.47 \cdot 10^{-3}$	197000
7000	$2.53 \cdot 10^{-3}$	196000
7500	$1.90 \cdot 10^{-3}$	192000
8000	$1.45 \cdot 10^{-3}$	200000

Table 8.1: Summary of the simulated samples of s-channel $\mathrm{g_{KK}}$ production used with subsequent decays to a pair of top quarks. The simulated $M_{\mathrm{g_{KK}}}$, the production cross section corrected with an NLO K factor of 1.3, and the number of generated events is given.

to match the number of generated interactions per bunch-crossing to the number of PU interactions in the data recorded in the year 2017. Furthermore, all events are reweighted according to the production cross section of the respective simulated process and the integrated luminosity of $41.5\,\mathrm{fb}^{-1}$ as described in section 7.2. Table 8.2 lists all samples of simulated events considered in this analysis.

Process	σ [pb]	Generator	N [10^6]
$t\bar{t}(\to \ell\nu\,\ell\nu) + \text{jets}$	$8.8 \cdot 10^1$	POWHEG + PYTHIA	5011.2
$t\bar{t}(\to \ell\nu\,qq) + \text{jets}$	$3.7 \cdot 10^2$	POWHEG + PYTHIA	33368.5
$t\bar{t}(\to qq\,qq) + \text{jets}$	$3.8 \cdot 10^2$	POWHEG + PYTHIA	38054.5
$W(\to \ell\nu)$ + 1 jet	$8.1 \cdot 10^3$	MADGRAPH + PYTHIA	29.9
$W(\to \ell\nu)$ + 2 jets	$2.8 \cdot 10^3$	MADGRAPH + PYTHIA	19.9
$W(\to \ell\nu)$ + 3 jets	$9.9 \cdot 10^2$	MADGRAPH + PYTHIA	19.6
$W(\to \ell\nu)$ + 4 jets	$5.5 \cdot 10^2$	MADGRAPH + PYTHIA	11.2
$DY(Z/\gamma \to \ell\ell)$ + 1 jet	$8.7 \cdot 10^2$	MADGRAPH + PYTHIA	32.5
$DY(Z/\gamma \to \ell\ell)$ + 2 jets	$3.1 \cdot 10^2$	MADGRAPH + PYTHIA	11.6
$DY(Z/\gamma \to \ell\ell)$ + 3 jets	$1.1 \cdot 10^2$	MADGRAPH + PYTHIA	4.8
$DY(Z/\gamma \to \ell\ell)$ + 4 jets	$4.4 \cdot 10^1$	MADGRAPH + PYTHIA	4.3
Single t, t-channel	$1.4 \cdot 10^2$	POWHEG + PYTHIA	5.8
Single $\bar{t}$, t-channel	$8.1 \cdot 10^1$	POWHEG + PYTHIA	3.9
Single t / $\bar{t}$, s-channel	$3.7 \cdot 10^0$	AMC@NLO + PYTHIA	35.4
Single t, tW-channel	$3.6 \cdot 10^1$	POWHEG + PYTHIA	263.8
Single $\bar{t}$, tW-channel	$3.6 \cdot 10^1$	POWHEG + PYTHIA	270.8
QCD, μ enr., $\hat{p}_T \in [20,30)$ GeV	$2.5 \cdot 10^6$	PYTHIA	28.0
QCD, μ enr., $\hat{p}_T \in [30,50)$ GeV	$1.4 \cdot 10^6$	PYTHIA	28.6
QCD, μ enr., $\hat{p}_T \in [50,80)$ GeV	$3.8 \cdot 10^5$	PYTHIA	23.9
QCD, μ enr., $\hat{p}_T \in [80,120)$ GeV	$8.9 \cdot 10^4$	PYTHIA	23.0
QCD, μ enr., $\hat{p}_T \in [120,170)$ GeV	$2.1 \cdot 10^4$	PYTHIA	20.7
QCD, μ enr., $\hat{p}_T \in [170,300)$ GeV	$7.0 \cdot 10^3$	PYTHIA	39.2
QCD, μ enr., $\hat{p}_T \in [300,470)$ GeV	$6.1 \cdot 10^2$	PYTHIA	17.5
QCD, μ enr., $\hat{p}_T \in [470,600)$ GeV	$5.9 \cdot 10^1$	PYTHIA	18.1
QCD, μ enr., $\hat{p}_T \in [600,800)$ GeV	$1.8 \cdot 10^1$	PYTHIA	16.1
QCD, μ enr., $\hat{p}_T \in [800,1000)$ GeV	$3.3 \cdot 10^0$	PYTHIA	15.4
QCD, μ enr., $\hat{p}_T \in [1000,\infty)$ GeV	$1.1 \cdot 10^0$	PYTHIA	10.4

Table 8.2: Summary of the simulated samples of SM background processes. The simulated process, the production cross section, the name of the generator, and the number of weighted events is given.

8.3 Event Selection

The event selection applied in this search follows the one used in the analysis of the 2016 dataset in large parts. The results obtained with simulated samples assuming an integrated luminosity of $41.5\,\mathrm{fb}^{-1}$ in the single-muon final state are compared to those of the published CMS result using the 2016 dataset [204].

8.3.1 Pre-Selection

Simulated events are required to pass a trigger requiring the presence of a muon with $p_\mathrm{T} > 50\,\mathrm{GeV}$ and no isolation criterion. To ensure operation at the efficiency plateau of the trigger, the presence of exactly one muon fulfilling $p_\mathrm{T} > 55\,\mathrm{GeV}$, $|\eta| < 2.4$, and passing the high-p_T ID is required offline. The efficiency of the trigger requirement and the high-p_T ID have been measured in data and simulation by the CMS Collaboration [144]. The resulting data/MC scale factors are applied to simulated events to correct for the effect of differing efficiencies between data and simulation throughout this chapter.

In addition to the muon, a neutrino is expected in the targeted final state, which would manifest itself in a transverse momentum imbalance of the event. A minimum value of $p_\mathrm{T}^\mathrm{miss} > 50\,\mathrm{GeV}$ is required in order to select events in which the $\mathrm{t\bar{t}}$ system decays to the ℓ+jets final state. Events containing additional electrons or muons are discarded to avoid contributions from di-leptonic $\mathrm{t\bar{t}}$ decays. The same ID and kinematic requirements are imposed on muons for this purpose. Electrons are vetoed if they pass the tight ID WP without the isolation criterion and have $p_\mathrm{T} > 50\,\mathrm{GeV}$ and $|\eta| < 2.5$.

In order to account for the hadronic activity expected in a highly-boosted $\mathrm{t\bar{t}}$ decay, requirements on jets in the event are imposed as well. All AK4 jets with PUPPI PU subtraction applied (AK4 PUPPI jets) that fulfill the tight noise jet ID WP and have $p_\mathrm{T} > 30\,\mathrm{GeV}$ and $|\eta| < 2.4$ are considered in this analysis. At least two such jets must be present in pre-selected events, one of which must satisfy $p_\mathrm{T} > 50\,\mathrm{GeV}$. In addition to AK4 jets, AK8 PUPPI jets with $p_\mathrm{T} > 400\,\mathrm{GeV}$ and $|\eta| < 2.4$ that pass the tight noise jet ID WP are used in a later stage of this analysis. In summary, events satisfying the criteria given below are selected in the pre-selection.

- Events must contain exactly one muon passing the high-p_T ID WP with $p_\mathrm{T} > 55\,\mathrm{GeV}$ and $|\eta| < 2.4$, $N_\mu = 1$.
- Events must not contain any electrons passing the tight ID WP without isolation criterion having $p_\mathrm{T} > 50\,\mathrm{GeV}$ and $|\eta| < 2.5$, $N_\mathrm{e} = 0$.

- Events must satisfy $p_{\mathrm{T}}^{\mathrm{miss}} > 50\,\mathrm{GeV}$.
- Events must contain at least two AK4 PUPPI jets passing the tight noise jet ID WP that have $p_{\mathrm{T}} > 30\,\mathrm{GeV}$ and $|\eta| < 2.4$, $N_{\mathrm{jets}} \geq 2$.
- Events must have at least one jet with $p_{\mathrm{T}} > 50\,\mathrm{GeV}$.

In figure 8.3, control distributions after applying the pre-selection are shown. About 75% of the events selected at this stage of the analysis originate from QCD multijet production. The production of W+jets and $\mathrm{t\bar{t}}+\mathrm{jets}$ contribute with 15 and 10%, respectively. Minor backgrounds are due to $\mathrm{DY}+\mathrm{jets}$ and single top quark production.

Although the majority of events originates from QCD multijet production, it is visible that they contribute mostly in the phase space of small p_{T}^{μ} and $p_{\mathrm{T}}^{\mathrm{miss}}$. Also the expected number of jets is smaller in QCD events than in SM $\mathrm{t\bar{t}}+\mathrm{jets}$ production or the signal. Events that contain a highly energetic muon or a large amount of $p_{\mathrm{T}}^{\mathrm{miss}}$ are most likely to arise from W+jets and $\mathrm{t\bar{t}}+\mathrm{jets}$ production. In contrast to the SM expectation, signal events of a heavy resonance decaying to a pair of top quarks are expected to produce a larger number of AK4 and especially AK8 jets with $p_{\mathrm{T}} > 400\,\mathrm{GeV}$. Due to the large Lorentz boost of the top quarks in such events, which increases with the mass of the hypothetical resonance, increasingly more AK4 and AK8 jets with large p_{T} are expected to be reconstructed. Similarly, the muon and neutrino produced in the leptonic top quark decay are expected to carry a larger amount of p_{T}, resulting in increased values of p_{T}^{μ} and $p_{\mathrm{T}}^{\mathrm{miss}}$. In all events passing the pre-selection, the invariant mass of the $\mathrm{t\bar{t}}$ system is reconstructed, which is a variable particularly sensitive to the hypothetical signal.

8.3.2 Reconstruction of the $\mathrm{t\bar{t}}$ system

The $\mathrm{t\bar{t}}$ system is reconstructed following the technique described in sections 7.5.1 and 7.5.2. Of the two top quarks, exactly one is assumed to decay to the leptonic final state with a muon. The other one is assumed to decay to the all-jets final state.

In the first step, the z-component of the neutrino's three-momentum is reconstructed. Under the assumption that the neutrino, leaving the detector without interaction with the detector material, is the only source of $p_{\mathrm{T}}^{\mathrm{miss}}$ in an event, its longitudinal momentum is calculated according to equation (7.5).

Candidates for the top quark decaying to the leptonic final state are then reconstructed from the muon, the reconstructed neutrino, and all possible permutations of between one and six out of the seven leading AK4 jets in the event. In events where $N_{\mathrm{jets}} < 7$, only up to $N_{\mathrm{jets}} - 1$ jets are considered for each candidate.

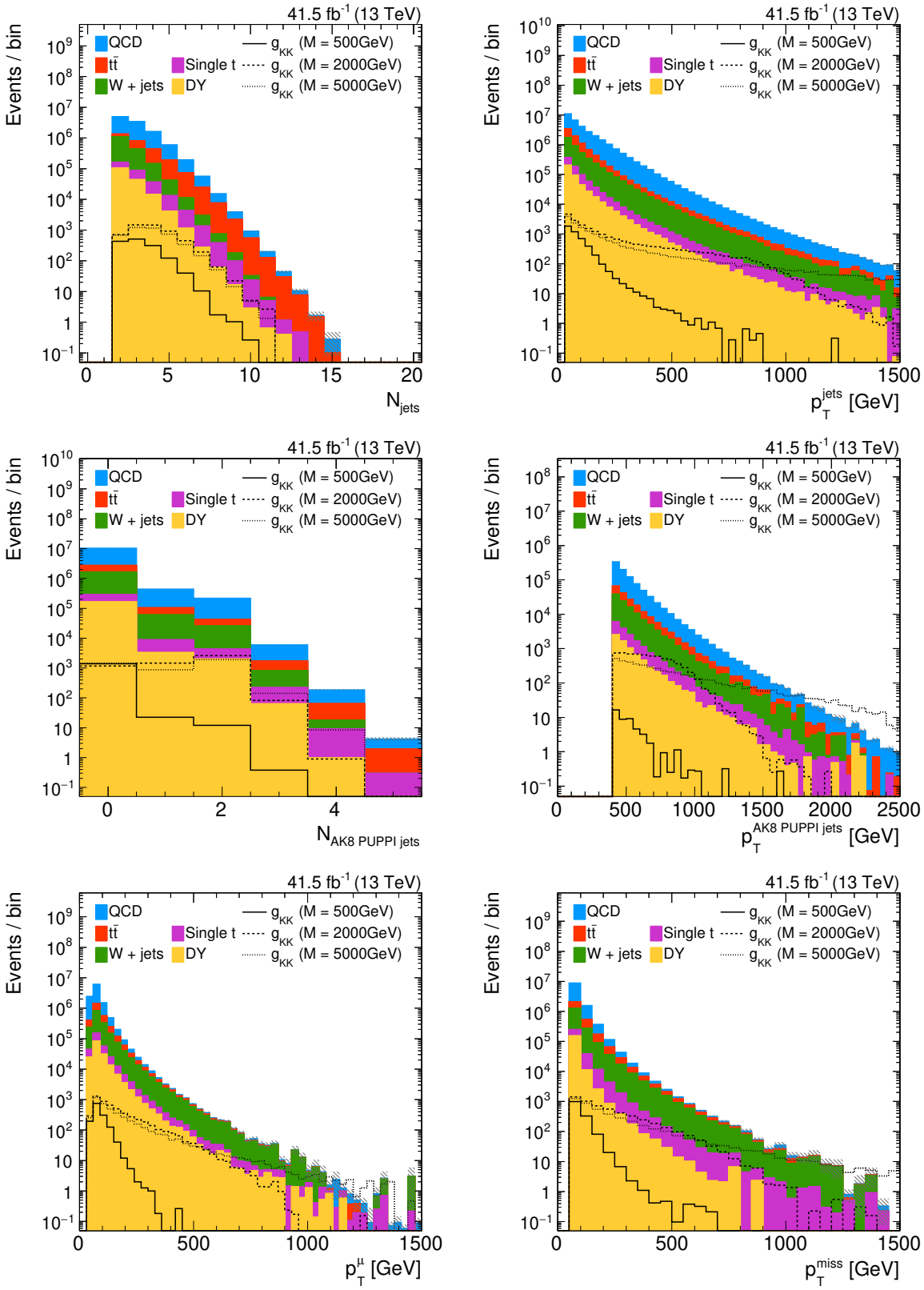

Figure 8.3: Distributions of N_{jets} (upper left), $p_{\text{T}}^{\text{jets}}$ (upper right), $N_{\text{AK8 PUPPI jets}}$ (middle left), $p_{\text{T}}^{\text{AK8 PUPPI jets}}$ (middle right), p_{T}^{μ} (lower left), and $p_{\text{T}}^{\text{miss}}$ (lower right) for all simulated events passing the pre-selection. The simulated signal predictions are normalized to a production cross section of 1 pb.

For each leptonic top quark candidate, a number of candidates for the top quark decaying to the all-jets final state is reconstructed. If at least one AK8 jet tagged as originating from a boosted top quark decay (cf. section 5.5.3) is found in the event, its four-momentum is used. This category of events is referred to as the *boosted* category in the following. Otherwise, all possible permutations of the seven leading AK4 jets that are not used in reconstructing the leptonic top quark candidate are considered. This kinematic region is referred to as *resolved* regime in the following.

In order to quantify the compatibility of the pairs of top quark candidates with the hypothesis of correctly reconstructing the $\mathrm{t\bar{t}}$ system, a χ^2 variable is calculated for each pair. It is given by

$$\chi^2 = \left(\frac{M_{\mathrm{t_{lep}}} - \overline{M}_{\mathrm{t_{lep}}}}{\sigma_{\mathrm{lep}}}\right)^2 + \left(\frac{M_{\mathrm{t_{had}}} - \overline{M}_{\mathrm{t_{had}}}}{\sigma_{\mathrm{had}}}\right)^2, \tag{8.1}$$

where the expected values and widths are determined from MC truth information in simulated events. For the value of $M_{\mathrm{t_{had}}}$ in the boosted regime, the softdrop mass (cf. section 5.5.3) of the t-tagged jet is used. For events in the boosted regime, i.e. events that contain a t-tagged AK8 jet, values of $\overline{M}_{\mathrm{t_{lep}}} = 173\,\mathrm{GeV}$, $\sigma_{\mathrm{lep}} = 29\,\mathrm{GeV}$, $\overline{M}_{\mathrm{t_{had}}} = 177\,\mathrm{GeV}$, and $\sigma_{\mathrm{had}} = 17\,\mathrm{GeV}$ are obtained. In the resolved regime, where the top quark decaying to the all-jets final state is reconstructed from a combination of AK4 jets, $\overline{M}_{\mathrm{t_{had}}} = 175\,\mathrm{GeV}$, and $\sigma_{\mathrm{had}} = 20\,\mathrm{GeV}$ are used instead. The values for $\overline{M}_{\mathrm{t_{lep}}}$, σ_{lep} remain unchanged.

Finally, only the pair of top quark candidates that minimizes the χ^2 variable is used in this analysis and is referred to as *best* pair in the following. The distribution of the invariant mass $M_{\mathrm{tt}}^{\mathrm{rec}}$ of the best pair is shown in figure 8.4 (left) for four different signal mass hypotheses. In figure 8.4 (right), the distribution of $M_{\mathrm{tt}}^{\mathrm{rec}}$ is shown for the SM backgrounds and three signal mass hypotheses. For both distributions, events passing the pre-selection are used.

In figure 8.4 (left), the resonant signal of hypothetical $\mathrm{g_{KK}}$ bosons with low masses is clearly visible. However, for high masses of $M_{\mathrm{g_{KK}}} = 4\,\mathrm{TeV}$, the expected signal signature in the distribution of $M_{\mathrm{tt}}^{\mathrm{rec}}$ becomes less resonant due to the strongly falling PDFs of the proton and the convolution of the PDFs with the Breit-Wigner shape of an s-channel resonance (cf. equation (2.16)). As a result, very heavy new particles would manifest themselves as a non-resonant enhancement of the distribution of $M_{\mathrm{tt}}^{\mathrm{rec}}$ at large values.

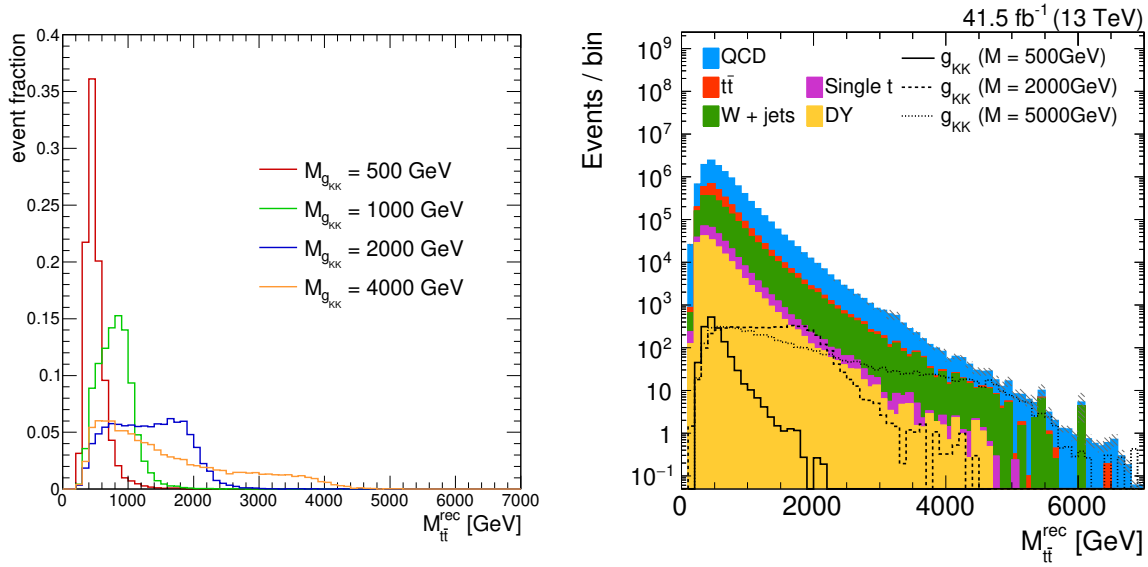

Figure 8.4: Left: Normalized distributions of $M_{\mathrm{t\bar{t}}}^{\mathrm{rec}}$ for four different signal mass hypotheses. Right: Distribution of $M_{\mathrm{t\bar{t}}}^{\mathrm{rec}}$ for SM backgrounds and three signal mass hypotheses. For both distributions, events passing the pre-selection are used.

8.3.3 Full Selection

As shown in figure 8.3, events of QCD multijet and W+jets production constitute the major part of the expected background after the pre-selection. The muons produced in QCD multijet events, e.g. via heavy-flavor quark decays, are expected to be surrounded by considerable hadronic activity and hence to be non-isolated. Since the muon reconstructed in signal events is also expected to be non-isolated due to the potentially large Lorentz boost of the top quark system, the muon's relative isolation cannot be used to distinguish signal from the SM background. Instead, two other variables are used to distinguish muons produced in QCD multijet events from those produced in boosted top quark decays. Muons originating from heavy quark decays are expected to be produced very close to the accompanying jet and to carry little transverse momentum relative to that jet. The distance of the lepton to the closest AK4 jet with $p_{\mathrm{T}} > 30\,\mathrm{GeV}$ ($\Delta R_{\mathrm{min}}\,(\ell,\mathrm{j})$) and the transverse momentum of the lepton projected onto the axis of the same jet ($p_{\mathrm{T,\,rel}}\,(\ell,\mathrm{j})$) are considered for this purpose. Selected events must satisfy $\Delta R_{\mathrm{min}}\,(\ell,\mathrm{j}) > 0.4$ || $p_{\mathrm{T,\,rel}}\,(\ell,\mathrm{j}) > 25\,\mathrm{GeV}$. This criterion is referred to as *2D selection* in the following. Furthermore, the sum of the muon's transverse momentum and $p_{\mathrm{T}}^{\mathrm{miss}}$ is required to satisfy $p_{\mathrm{T}}^{\mu} + p_{\mathrm{T}}^{\mathrm{miss}} > 150\,\mathrm{GeV}$. Considering $p_{\mathrm{T}}^{\mathrm{miss}}$ in addition to p_{T}^{μ} further adds discrimination power against events of QCD multijet production since no intrinsic $p_{\mathrm{T}}^{\mathrm{miss}}$ is expected in such events. In summary, the requirements discussed above discard

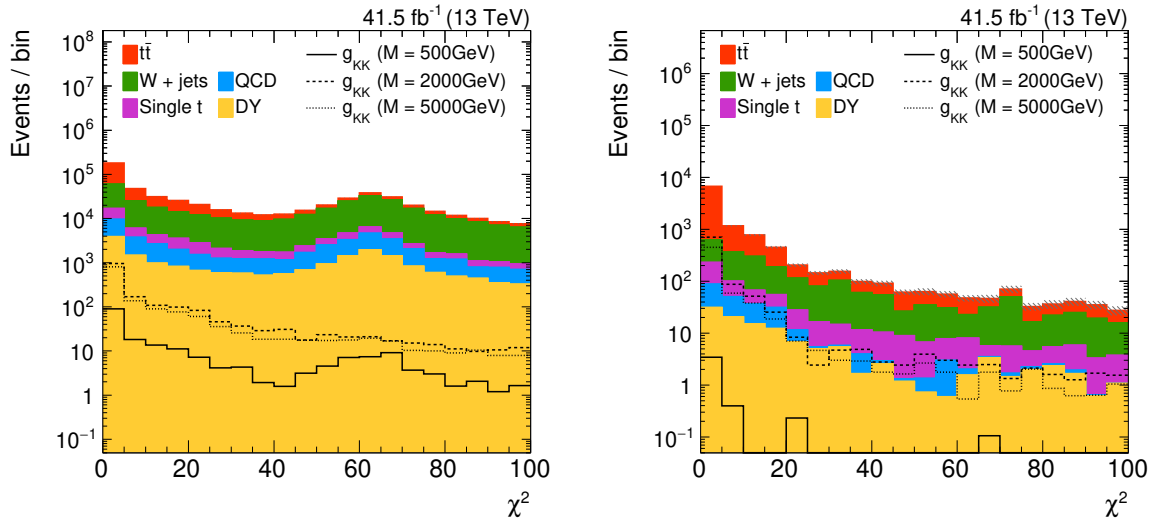

Figure 8.5: Distribution of χ^2 of the best top quark candidate pair for the resolved (left) and boosted (right) category. All events passing the full event selection without the requirement of $\chi^2 < 30$ are shown. The simulated signal predictions are normalized to a production cross section of 1 pb.

the major fraction of QCD multijet events passing the pre-selection. Events of $t\bar{t}$ + jets and W+jets production constitute the major backgrounds after applying this criterion.

Due to the large Lorentz boost of the two top quarks produced by the hypothetical new resonance, the jets originating from their decay have potentially very large p_T. On the other hand, the distribution of the jet transverse momentum falls exponentially towards high values of p_T in all SM processes. Hence, the requirement of the p_T-(sub)leading AK4 jet to have $p_T > 150$ (50) GeV is in accordance with the expected signal kinematics and well-suited to suppress the SM backgrounds irrespective of their origin.

The last requirement imposed on events in the full event selection targets the reconstruction of M_{tt}. The degree of compatibility of the best pair of top quarks returned by the reconstruction algorithm with the hypothesis of a $t\bar{t}$ decay to the μ + jets final state is quantified by the corresponding value of χ^2. The distribution of χ^2 of the best top quark candidate pair for all events passing the above event selection is shown in figure 8.5 for the resolved and boosted category, respectively. By construction, all events, especially those of SM $t\bar{t}$ + jets production and the signal, show a large peak at 0. The secondary peak at a value of about $\chi^2 = 60$ is obtained for reconstructed top quark masses of about $M_{t_{had}} \simeq 20$ GeV, which occurs frequently if only a single AK4 jet is considered for the hadronic top quark candidate. The requirement of $\chi^2 < 30$ for the best pair of top quark candidates in an event hence rejects all non–$t\bar{t}$ SM backgrounds

efficiently.

Kinematic distributions of events passing the full event selection are shown in figure 8.6. The signal expected from resonant $\mathrm{t\bar{t}}$ production can clearly be distinguished from the SM prediction for high resonance masses. For a mass close to the kinematic threshold of $\mathrm{t\bar{t}}$ production, the expected signal closely resembles SM $\mathrm{t\bar{t}}+\mathrm{jets}$ production. Due to the similarity between the expected signal and SM $\mathrm{t\bar{t}}+\mathrm{jets}$ production, after the full event selection about 50% of the expected SM background arises from $\mathrm{t\bar{t}}+\mathrm{jets}$ events. About 35% is due to W+jets production, the production of single top quarks, $\mathrm{DY}+\mathrm{jets}$, and QCD multijet events contribute to a minor degree. The full event selection is summarized below. All events passing it are considered in the final statistical analysis presented in section 8.3.5.

- The event must pass the pre-selection.
- The muon in selected event must fulfill $\Delta R_{\mathrm{min}}(\ell,\mathrm{j}) > 0.4 || p_{\mathrm{T,\,rel}}(\ell,\mathrm{j}) > 25\,\mathrm{GeV}$.
- The sum of the transverse momentum of the muon and $p_{\mathrm{T}}^{\mathrm{miss}}$ must satisfy $p_{\mathrm{T}}^{\mu} + p_{\mathrm{T}}^{\mathrm{miss}} > 150\,\mathrm{GeV}$.
- The leading AK4 jet must have $p_{\mathrm{T}} > 150\,\mathrm{GeV}$.
- The sub-leading AK4 jet must have $p_{\mathrm{T}} > 50\,\mathrm{GeV}$.
- In the reconstruction of the $\mathrm{t\bar{t}}$ system, the best pair of top quark candidates must satisfy $\chi^2 < 30$.

8.3.4 Pileup Mitigation

In comparison to the event selection applied in the analysis of the 2016 dataset, a different PU mitigation algorithm is used in this work. While previously, the CHS method was used, this result is obtained with the PUPPI algorithm (cf. section 5.2). Especially in events with 30 or more PU interactions, the PUPPI algorithm leads to a better and more stable performance compared to CHS. For example, the jet substructure variables used in tagging AK8 jets as originating from boosted decays of top quarks of heavy bosons have been shown to depend less on the number of PU interactions when employing PUPPI as opposed to CHS. Similarly, the resolution of $p_{\mathrm{T}}^{\mathrm{miss}}$ is improved and more robust against the influence of PU. Also the number of AK4 jets reconstructed with PUPPI PU mitigation applied is expected to be closer to the true number of jets produced in an event due to the more efficient suppression of jets clustered from PU particles. This would lead to reduced combinatorics in the

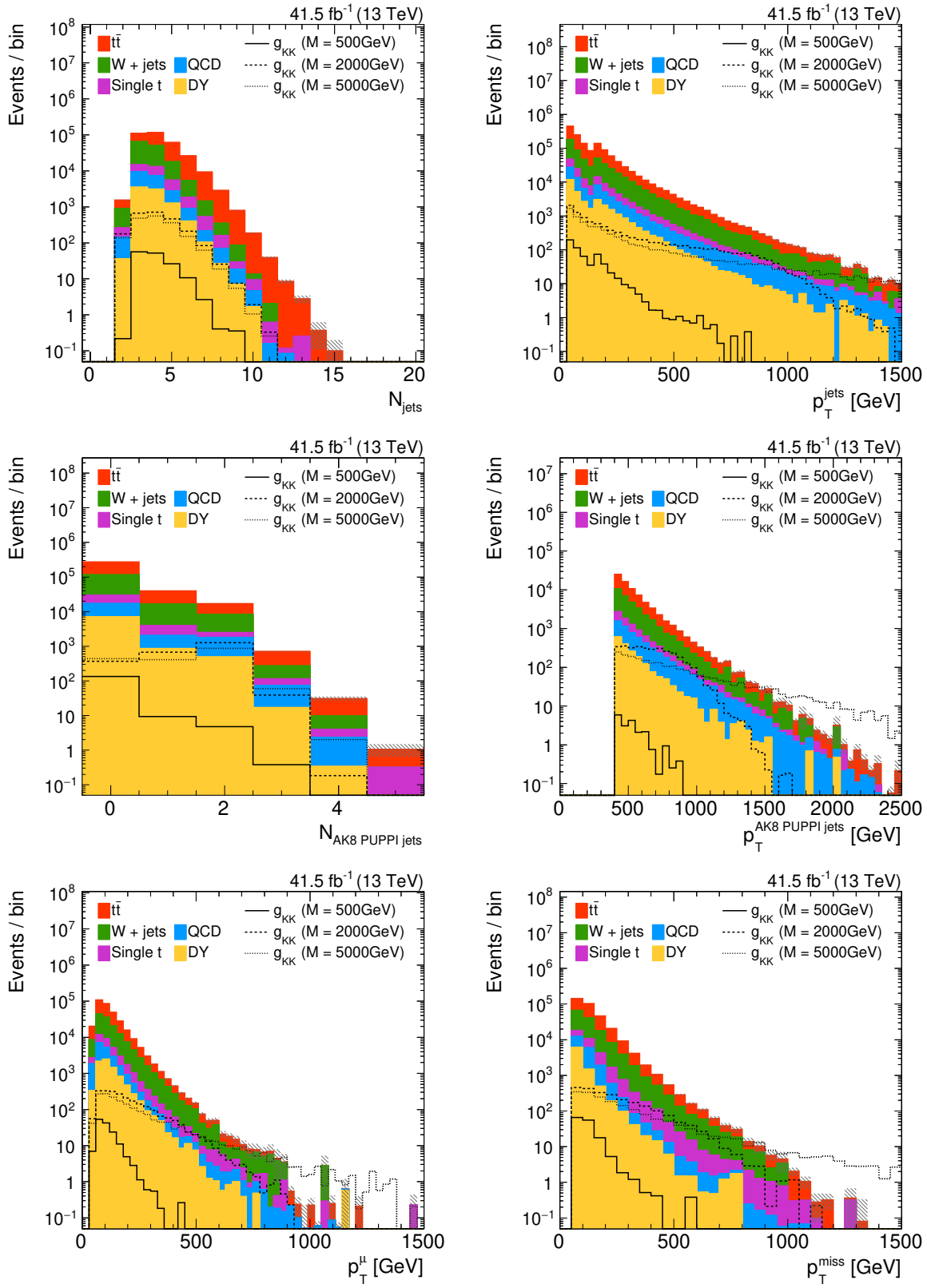

Figure 8.6: Distributions of N_{jets} (upper left), $p_{\text{T}}^{\text{jets}}$ (upper right), $N_{\text{AK8 PUPPI jets}}$ (middle left), $p_{\text{T}}^{\text{AK8 PUPPI jets}}$ (middle right), p_{T}^{μ} (lower left), and $p_{\text{T}}^{\text{miss}}$ (lower right) for all simulated events passing the full event selection. The simulated signal predictions are normalized to a production cross section of 1 pb.

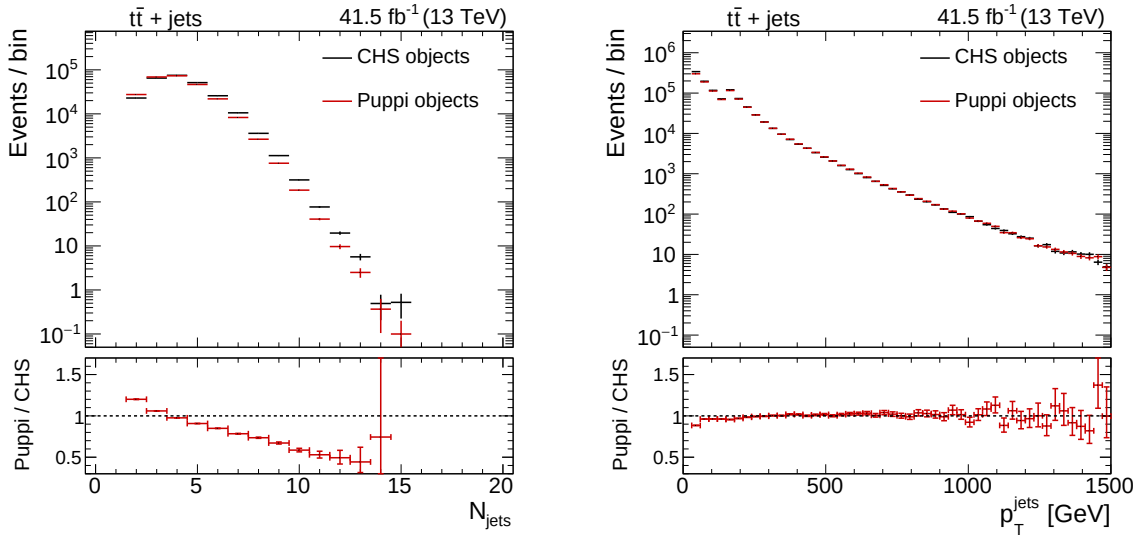

Figure 8.7: Comparison between the CHS and PUPPI event selection in $\mathrm{t\bar{t}}+$jets simulated events for the distribution of the number of AK4 jets (left), and the p_T of all AK4 jets (right). In the lower panels, the ratio of the distributions obtained with PUPPI and CHS is shown.

reconstruction of the $\mathrm{t\bar{t}}$ system, and would help to determine the correct combination of jets.

From the above examples, improved results are expected from utilizing PUPPI algorithm instead of CHS. In order to study the effect of both PU suppression algorithms, a dedicated comparison is performed. For this purpose, the full event selection explained in the previous section is repeated using AK4 and AK8 CHS jets instead of applying PUPPI. The requirement of $\chi^2 < 30$ is omitted in order to avoid an influence of the reconstruction of the $\mathrm{t\bar{t}}$ system. The value of $p_\mathrm{T}^\mathrm{miss}$ is calculated from PUPPI-rescaled four-momenta of the PF candidates as well, effectively modifying equation (5.4).

In general, the overall selection efficiency is reduced by about 5% in the PUPPI selection. This is due to the effects visible in the distributions of the number of reconstructed AK4 jets and their p_T shown in figure 8.7 for $\mathrm{t\bar{t}}+$jets simulated events. Events using the PUPPI algorithm tend to have a lower jet multiplicity compared to CHS (figure 8.7 left). This is a direct consequence of the fact that more jets are removed from the event when a more efficient PU mitigation technique is applied. Applying the PUPPI algorithm results in fewer AK4 jets reconstructed with low p_T (figure 8.7 right) compared to CHS. In simulated events of $\mathrm{t\bar{t}}+$jets production, jets with low p_T are more likely to originate from clustered PU particles than jets with high p_T. Consequently, employing a better PU mitigation results in a more efficient rejection of such low-p_T jets originating from PU, which explains the behavior observed in figure 8.7

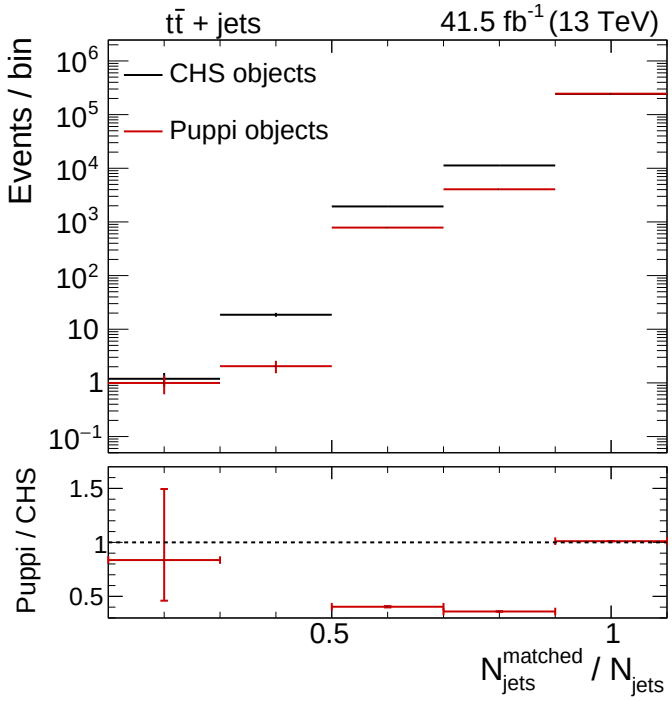

Figure 8.8: Comparison between the CHS and PUPPI event selection in $\mathrm{t\bar{t}}$ + jets simulated events for the distribution of $N_{\text{jets}}^{\text{matched}}/N_{\text{jets}}$. In the lower panel, the ratio of the distributions obtained with PUPPI and CHS is shown.

(right). Requiring a minimum p_{T} of 30 GeV for all AK4 jets causes the smaller number of reconstructed AK4 jets, which in turn results in a smaller overall selection efficiency.

In figure 8.8, the distribution of $N_{\text{jets}}^{\text{matched}}/N_{\text{jets}}$ is shown. Here, the number of matched AK4 jets, $N_{\text{jets}}^{\text{matched}}$, is defined as the number of reconstructed jets that can be matched to a generator-level jet with $p_{\mathrm{T}} > 20\,\text{GeV}$ and $|\eta| < 2.4$ within a distance of $\Delta R < 0.4$. The p_{T} threshold for generator-level jets is chosen smaller than that of reconstructed jets to take into account the jet energy resolution, which can cause jets to be reconstructed with a larger p_{T} than that of the corresponding generator-level jet. Comparing the distributions obtained with PUPPI and CHS, both algorithms have the same number of events in which all reconstructed jets could be matched. These events mostly have a relatively small number of reconstructed jets, which then have high p_{T}. For such high-p_{T} jets, the difference between both PU mitigation algorithms is negligible (cf. figure 8.7, right). On the other hand, with the PUPPI algorithm, the fraction of events in which not all jets can be matched is decreased by more than 50%, demonstrating the improved efficiency of removing jets that originate from PU. Because these jets are removed from the reconstruction of the $\mathrm{t\bar{t}}$ system, the correct combination of jets originating from the top quark decays is more likely to be found in the reconstruction procedure when employing the PUPPI algorithm. With this PU

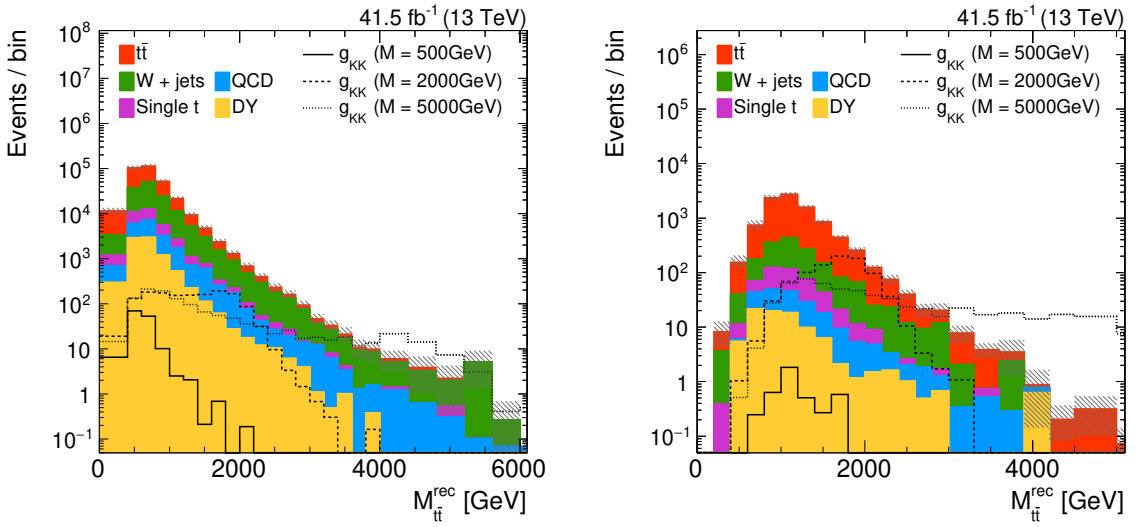

Figure 8.9: Distribution of $M_{\mathrm{tt}}^{\mathrm{rec}}$ in the resolved (left) and boosted (right) category after applying the full event selection. The simulated signal predictions are normalized to a production cross section of 1 pb. The hatched areas indicate the total uncertainty, composed of statistical and systematic uncertainties.

mitigation technique, the analysis results are also expected to be robust against the influence of PU and improved substructure variables as well as $p_{\mathrm{T}}^{\mathrm{miss}}$ pave the way for analyzing events recorded in the presence of more PU interactions than in the 2016 dataset.

8.3.5 Systematic Uncertainties and Statistical Interpretation

Events passing the full event selection detailed in section 8.3.3 are considered in the statistical interpretation in order to quantify the expected sensitivity to a potential signal. Events are categorized into a resolved and boosted region as outlined before. If at least one AK8 jet in the event is tagged as originating from a boosted hadronic top quark decay, the event is assigned to the boosted category. If no such jet is found, it is assigned to the resolved category. In both regions, the distributions of $M_{\mathrm{tt}}^{\mathrm{rec}}$, which are shown in figure 8.9, are used for the statistical analysis. As described in section 7.9, a Bayesian method is used to set expected upper limits on the production cross section of a heavy KK excitation of the gluon decaying to a pair of top quarks with a branching fraction of unity. The statistical and systematic uncertainties are treated as described in section 7.9 as well. In this analysis, the uncertainties listed below are considered, which follow the approach of the published CMS result [204] and are estimated as discussed in section 7.8 unless specified otherwise:

- The value of the integrated luminosity of $L = 41.5\,\mathrm{fb}^{-1}$ is varied by $\pm 2.3\%$ [209].
- Conservative uncertainties in the SM production cross sections for events of $\mathrm{t\bar{t}}+\mathrm{jets}$ (20%), $\mathrm{W}+\mathrm{jets}$ (25%), $\mathrm{DY}+\mathrm{jets}$ (25%), single top quark (50%) and QCD multijet (100%) production as used in the analysis of the 2016 dataset [204].
- Uncertainty in the inelastic pp cross section used for PU reweighting.
- Uncertainties in the jet energy scale and resolution.
- Uncertainties in the muon ID and trigger efficiency.
- Uncertainties due to reweighting of the distribution of the output of the CSVv2 algorithm with data/MC scale factors measured by the CMS Collaboration as applied in Ref. [204]. Nine individual sources of systematic uncertainties affecting the shape of the distribution of the CSVv2 output are considered, including contributions from the jet energy scale, impurities of the event samples used to derive the scale factors, and statistical fluctuations.
- Uncertainty in the choice of the renormalization and factorization scales.
- Uncertainty in the choice of PDF.

The post-fit nuisance parameter values as returned by the ML fit of the SM background to pseudo-data sampled from the final distributions are shown in figure 8.10. The post-fit parameters are compatible with their prior values. An anti-correlation between the nuisance parameter for the choice of μ_r and μ_f for W+jets events and that for $\mathrm{t\bar{t}}+\mathrm{jets}$ events and the production cross section of W+jets and $\mathrm{t\bar{t}}+\mathrm{jets}$ events is observed. Because these two sources of SM background are dominant after the full event selection, the systematic uncertainties mainly addressing the shape and normalization their distributions of $M_\mathrm{tt}^\mathrm{rec}$ can be constrained in the fit. Aside from these systematic uncertainties, most other uncertainties are not constrained significantly due to the lack of background-enriched CRs. This argument motivates the development of the DNN-based event classifier as presented in section 8.4. CRs enriched in specific SM backgrounds and used in the final ML fit can constrain systematic uncertainties significantly and consequently improve the expected sensitivity to a potential signal. Additionally, employing a DNN-based event selection would allow for the recovery of the signal selection efficiency, which is impaired by the conventional selection strategy followed in this section.

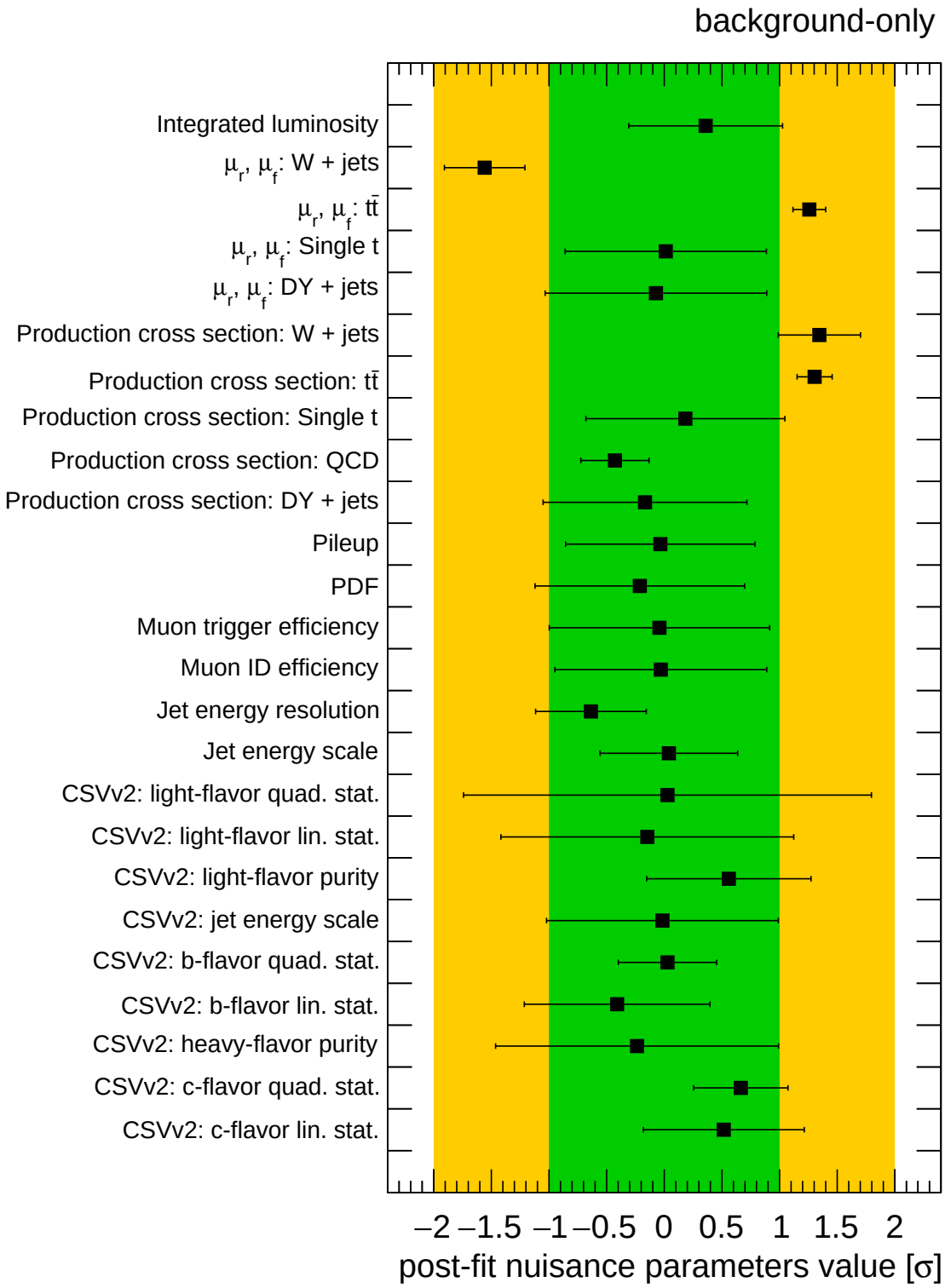

Figure 8.10: Values of the nuisance parameters after the background-only fit to pseudo-data. The values are given in units of their prior uncertainty, the error bars correspond to the post-fit uncertainties.

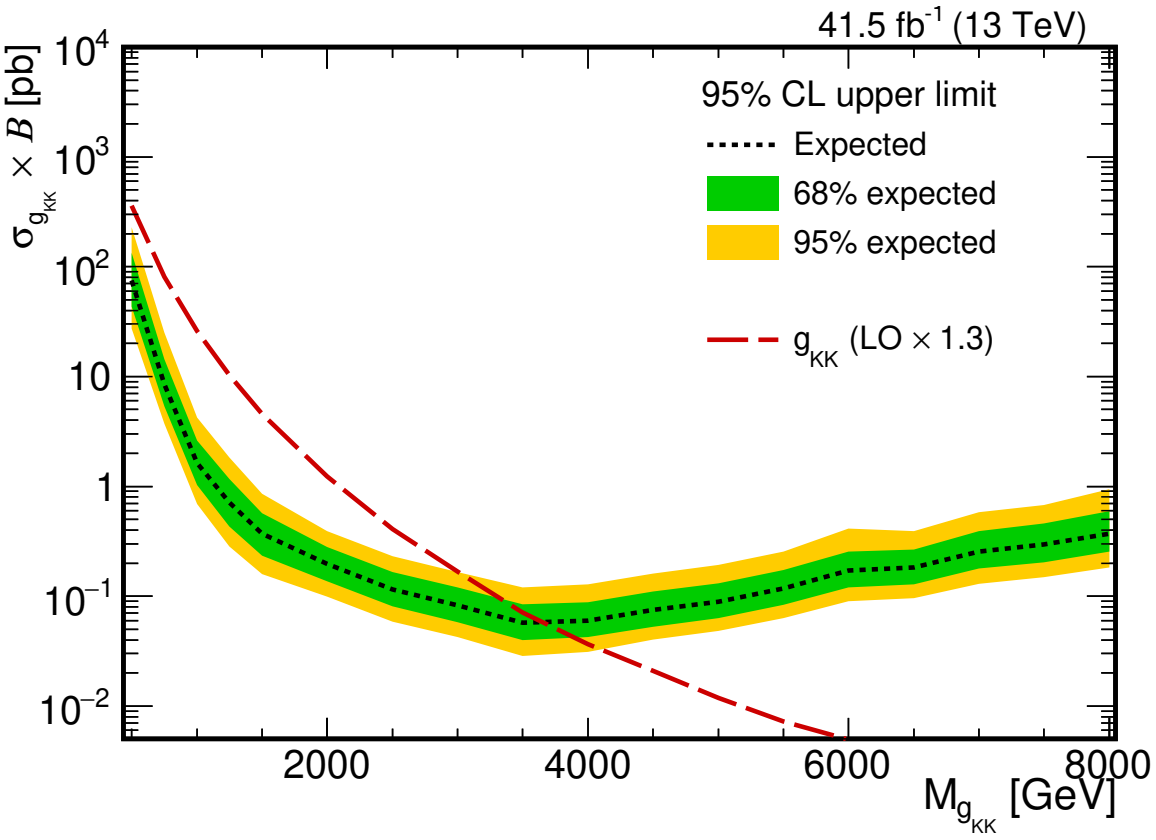

Figure 8.11: Expected upper limits on the product of the g_{KK} production cross section and $\mathcal{B}$ at the 95% CL as a function of the g_{KK} mass using the conventional analysis strategy similar to Ref. [204]. Unit branching fraction for the decay $g_{KK} \to t\bar{t}$ is assumed. The red dashed line depicts the prediction for the g_{KK} production cross section [205] corrected with an NLO K factor of 1.3 [206].

In the absence of a signal, the expected upper limits shown in figure 8.11 on the production cross section of a $\mathrm{g_{KK}}$ with unit branching fraction for the subsequent decay $\mathrm{g_{KK}} \to \mathrm{t\bar{t}}$ are placed as a function of $M_{\mathrm{g_{KK}}}$. Masses below 3.68 TeV are expected to be excluded for the resonance considered. Similar sensitivity is reached compared to the result obtained in the μ+jets final state in the analysis of 2016 data. The main reason for the slightly weaker result presented here is due to the larger impact of systematic uncertainties in the limit-setting procedure due to missing CRs for the major backgrounds. In 2016, a boosted decision tree (BDT) specifically optimized for identifying events from W+jets production was used. It allowed to discriminate this source of background and facilitated the definition of background-enriched CRs for constraining systematic uncertainties in the final fit to data. However, a promising technique utilizing DNNs is presented in the following section, which can extend the sensitivity of this analysis beyond the limits obtained with the 2016 dataset and the W+jets BDT.

8.4 Deep Neural Network Event Classification

In this section, an improved technique to classify not only W+jets events but all sources of SM background to this search is presented. It is based on a DNN with fully-connected layers. An overview over deep learning and deep neural networks can be found, for example, in Ref. [210]. The DNN used in this search is trained in a model-independent way, i.e. without considering signal events, and optimized to classify the five sources of SM background taken into account in this analysis. Following a model-independent approach has the benefit of making the results obtained with this algorithm easily re-interpretable as no particular model assumptions are used in the event categorization. The analysis sensitivity is optimized by this approach by replacing the one-dimensional selection requirements applied after the pre-selection (cf. section 8.3.3) by criteria imposed on the DNN output distributions. The advantage of this strategy is twofold. First, CRs enriched in events originating from a given SM process can be defined by considering the corresponding DNN output distribution. Second, the signal inefficiencies introduced by the conventional one-dimensional selection steps are reduced, allowing for an increased sensitivity. This effect is largest for low values of $M_{\mathrm{g_{KK}}}$, the regime where the shape of the hypothetical signal most closely resembles the SM background.

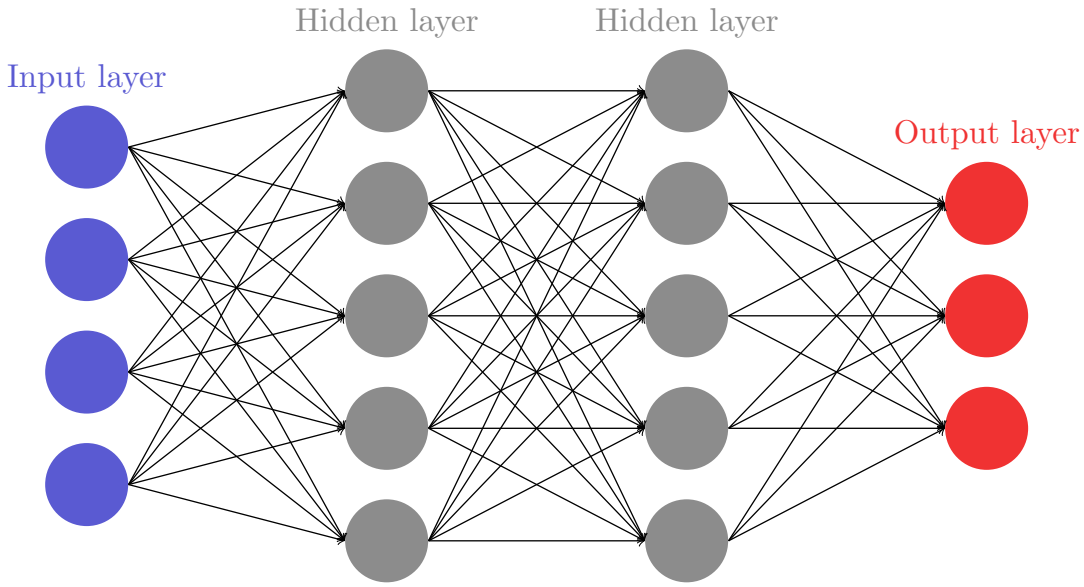

Figure 8.12: Sketch of the general structure of the DNNs used in this thesis.

8.4.1 Model-Independent DNN Classifier

The goal of the algorithm presented in this section is the classification of events as originating from one out of a given number of physical processes. All events passing the pre-selection are considered potential input to the DNN algorithm. As only the basic signal topology is reflected in the pre-selection, this choice represents a good compromise between a high signal selection efficiency and reduced computing time for training a multitude of neural networks.

The general structure of the DNNs considered in this work consists of three parts and is depicted in figure 8.12. The first layer contains the input variables passed to the DNN. The layers between the first and the last layer are referred to as *hidden layers*. The final layer of the DNN contains the DNN output and is referred to as *output layer*. In this thesis, only fully connected layers are considered, i.e. the output of a given node is passed as input to each of the nodes in the following layer. The number of hidden layers and the number of units (*nodes*) per hidden layer are hyperparameters of the DNN and will be optimized in the following. The number of nodes in the output layer corresponds to the number of classes the DNN is trained to classify. For the activation function of the hidden layers, the *rectified linear unit* (ReLU) is used, which is defined as $a(x) = \max(0, x)$. For c^{th} node in the output layer, the *softmax* function is used instead, which is defined as $a(x^c) = e^{x^c} / \sum_{c=1}^{M} e^{x^c}$. Here, M denotes the number of output nodes. Because of the normalization factor in the denominator of this function, the values of all nodes in the output layer sum up to 1. This allows to interpret the

output values as probabilities as explained below.

As opposed to conventional event selection strategies, where high-level variables are computed and used in a cut-based selection, one of the advantages of using a DNN algorithm is its ability to approximate the optimal discriminator for a given task simultaneously considering a number of comparably low-level input variables. In this work, 59 input variables are passed to the DNN. These include per-muon, per-AK4-jet, per-AK8-jet, and per-event quantities. They are shown in Appendix A, (figures A.1 – A.10), the full list of input variables is given below.

- p_T, η, ϕ, E, I_rel, $\Delta R_\mathrm{min}\,(\ell,\mathrm{j})$, and $p_{\mathrm{T,\,rel}}\,(\ell,\mathrm{j})$ of the muon in an event.
- p_T, η, ϕ, m, and the value of the CSVv2 discriminator of the three leading AK4 jets in an event. The jet mass is computed as the invariant mass of all of its constituents.
- p_T, η, ϕ, m_SD, τ_1, τ_2, τ_3, and the number of constituents of the three leading AK8 jets in an event.
- S_T, $S_\mathrm{T}^\mathrm{had}$, $S_\mathrm{T}^\mathrm{lep}$, $p_\mathrm{T}^\mathrm{miss}$, the number of reconstructed primary vertices, the total number of reconstructed AK4 and AK8 jets, and the entries S_{ij} of the (symmetric) sphericity tensor [211, 212] in an event. Here, $S_{ij} = S_{ji} = \left(\sum_\alpha p_\alpha^i p_\alpha^j\right) / \left(\sum_\alpha |p_\alpha|^2\right)$ with p^i the i^th component of the three-momentum of an AK4 jet in an event and where the index α runs over all AK4 jets in an event.

In events that contain less than three AK4 or AK8 jets, default values of 0 are used for the respective quantities associated with it. Because a value of 0 corresponds to a physically possible value for some of the variables, it has been verified that the exact choice of the default value does not significantly impact the DNN classification performance.

In total, about $18 \cdot 10^6$ generated events of the five SM background processes considered pass the pre-selection. Event weights taking into account the integrated luminosity of $41.5\,\mathrm{fb}^{-1}$, the production cross section of the respective process, and differences between data and simulation in various distributions are taken into account throughout the training and application of all DNNs presented in the following. Any given set of simulated events used as input to the DNN consists of a random mixture of events from the processes considered and is split into three statistically independent sub-samples. They contain a fraction of 4/6, 1/6, and 1/6 of the considered weighted events passing the pre-selection and are referred to as *training, test,* and *validation set*, respectively, in the following. Only the training sample is used to train the DNN weights. The test and

validation sets are used to optimize the hyperparameters of the DNN by quantifying and comparing the quality of performance of a set of trained DNN.

In order to avoid numeric instabilities, the distributions of the input variables (also referred to as *input features*) of each set of events are pre-processed before being passed to the DNN. In the pre-processing stage, each distribution of input features is scaled such that the mean μ' and standard deviation σ' of the scaled sample takes values of 0 and 1, respectively. The corresponding transformation of a variable x is given by $x \to x' = (x - \mu)/\sigma$, where μ and σ denote the mean and standard deviation of the unscaled distribution. The parameters μ and σ are derived only on events in the training sample, but applied to all three samples in the same way, such that no systematic bias between the samples is introduced.

The goal of the DNN training is the correct classification of events as originating from one out of five possible SM background processes, i.e. QCD, $\mathrm{t\bar{t}}$, W+jets, DY + jets, or single top quark production. As simulated events are used in the training, validation, and testing process, the true origin (*class*) of all events is known. Five output nodes of the DNN are defined, each of which corresponds to one of the five possible event classes. Due to the choice of activation function for the output layer, the output of a given node corresponds to the probability of an event to belong to the corresponding class. As the objective function J (also referred to as *loss function*) to be minimized during the training procedure, the categorical cross-entropy is used, which is defined as

$$J = \frac{1}{N} \sum_{i=1}^{N} \sum_{c=1}^{M} \left[-y_i^c \log\left(p_i^c\right) \right], \tag{8.2}$$

where N and M are the number of generated events in the sample considered and the number of possible classes (here, $M = 5$), respectively. The class label y_i^c of an event is 1 if c corresponds to the true class and 0 otherwise. The DNN prediction p_i^c is a real number between 0 and 1 for all c. In a perfect classifier, $p_i^c = y_i^c$ for all c and $J = 0$. The degree of dissimilarity between y_i and p_i is therefore quantified by J, which additionally averages over all events in a given sample. This has the advantage of making J comparable between sets containing varying numbers of events.

For training the DNN and minimizing the loss function, the ADAM minimizer [213] is used. First, each DNN with a given configuration of hyperparameters is trained for 500 epochs, i.e. each event in the training set is passed 500 times through the network. The value of J after each epoch, evaluated on both the training and the validation set, is compared. Because the validation set is never used in the training procedure, the loss

evaluated on the validation set serves as an indicator for the classification performance on unseen events and for potential overfitting of the DNN. Considering the values of J evaluated on the training and the validation set, it is possible to choose the optimal set of hyperparameters of the DNN for a given task as detailed in the following.

To apply the DNN in the physical analysis to the same events that were used for the training, it must perform similarly on both sets. For this purpose, it is necessary to regularize the DNN, preventing it from overfitting and ensuring similar performance on previously seen and unseen events. In this thesis, the dropout technique [214] is used for regularization. Here, a given fraction (*dropout rate*) of hidden nodes is randomly disabled during the training, which corresponds to effectively training an ensemble of DNNs, all with a different internal structure. Consequently, the DNN is less prone to overfitting. The dropout rate is one of the hyperparameters of the DNN and subject to optimization in the following.

In order to find the optimal set of hyperparameters for the DNN, a multitude of different networks is trained and their performances are compared. In the first step, the parameters tuned for optimal performance are the number of hidden layers (1, 2, 3, or 4), the number of nodes per hidden layer (64, 256, 512, or 1024), the number of events passed through the network before updating its weights, or *batch-size*, (2^9, 2^{13}, or 2^{17}), and the dropout rate (2%, 8%, 20%, 50%). One DNN is trained for each combination of these four parameters. Later, a finer grid of values around the preliminary optimum is examined.

As the events in the training set are a subset of the events the DNN will be applied to in the physics analysis, it is important to ensure equal performance on events in the training and the validation set. For the optimal set of hyperparameters, the loss J is therefore required to take the same value in the training and validation set at some point during the 500 epochs of training. The value of J at the point of equal loss on the training and validation set is used to quantify the performance of the DNN and to determine the optimal values of the hyperparameters. The optimum was found to be reached when using two hidden layers, each consisting of 512 nodes, a batch-size of 2^{17}, and a dropout rate of 50%.

Because for two of the four parameters the largest allowed value is chosen, a second optimization is performed, around the preliminary optimum given above. Here, the batch-size can take values of 2^{16}, 2^{17}, or 2^{18}, the dropout rate can be 30%, 40%, ..., 90%, and the learning rate of the ADAM optimizer is allowed to take values of 0.0010 (default), 0.0005, and 0.0002. The optimal set of hyperparameters is now found to be a batch-size of 2^{17}, a dropout rate of 60%, and a learning rate of 0.0005. As none of

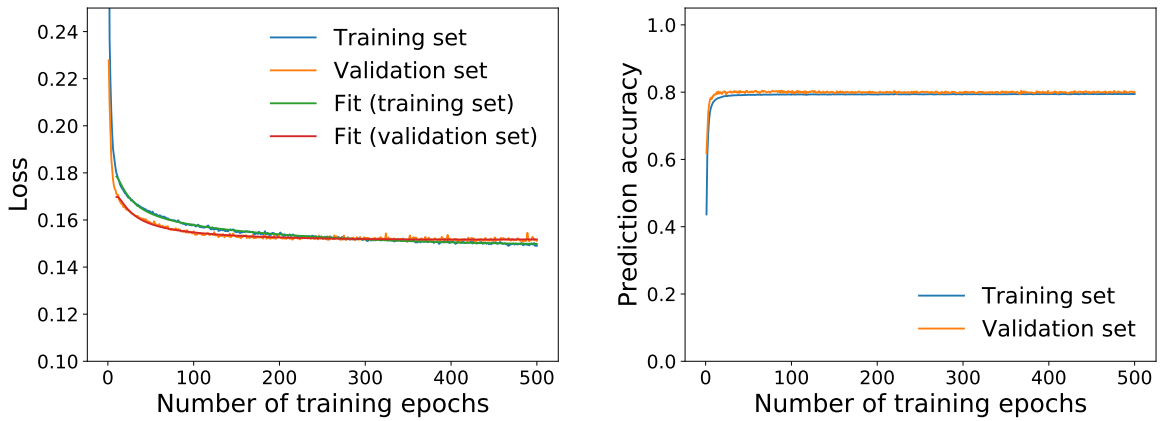

Figure 8.13: Left: Loss for the model-independent DNN evaluated on the training and the validation set and the corresponding fitted functions as a function of the number of training epochs. Right: Prediction accuracy of the model-independent DNN in the training and the validation set as a function of the number of training epochs.

the parameters is at its prior boundaries, the DNN obtained with these parameters is used in the following.

In figure 8.13 (left), the loss evaluated on the training and the validation set is shown as a function of the number of training epochs. The loss functions are fitted with an empirical function $f(x) = ax^2 + bx + c + d/x + e/x^2$ in order to determine the intersection of both loss functions. After training for 288 epochs, the loss function reaches a value of 0.152 on both the training and the validation set. Therefore, the DNN trained for 288 epochs is used in the following. In figure 8.13 (right), the prediction accuracy, determined as the fraction of events where for which the output node with the highest value corresponds to the true class, is shown. The accuracy rises steeply during the first training epochs and reaches a plateau of about 80% on the training and validation sets after about 20 epochs. Although the accuracy does not improve, the decreasing loss indicates that the classification performance still improves with the number of training epochs.

8.4.2 Performance of the Model-Independent DNN

The distributions of the DNN output for each of the five output nodes are shown in figure 8.14. The DNN was trained to predict a value close to 1 for events of QCD, $t\bar{t}$, DY + jets, W+jets, and single t production in node 0, 1, 2, 3, and 4, respectively. In all other nodes, the DNN response should be close to 0. Excellent classification performance is observed in all output nodes.

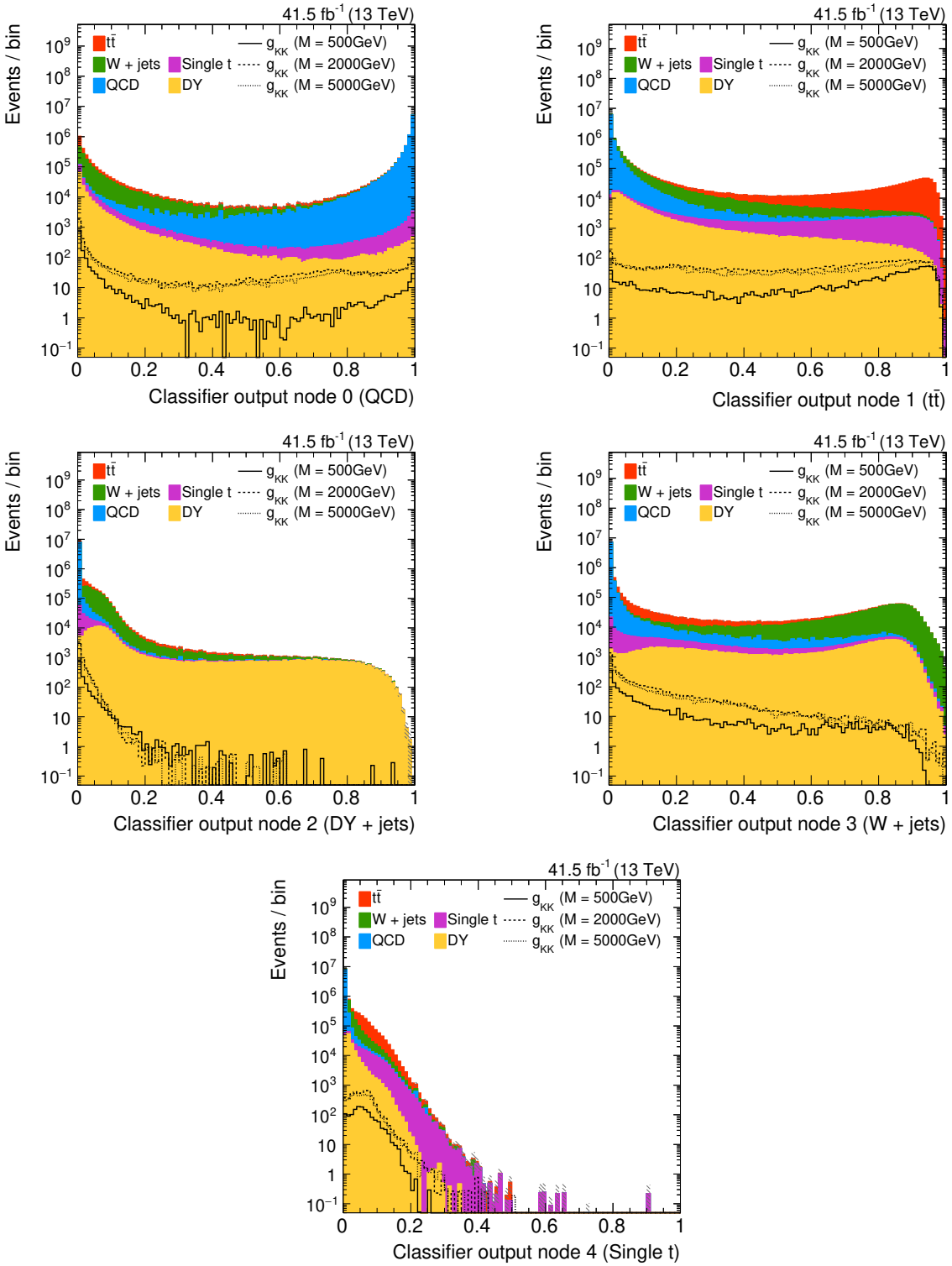

Figure 8.14: Distributions of the model-independent DNN output for each of the five output nodes.

Especially the distribution of the DNN output in node 0 shows a pronounced peak at values of 1 for events of QCD multijet production and at 0 for all other SM backgrounds. Events of $\mathrm{t\bar{t}}+\mathrm{jets}$ and W+jets production are also found to be assigned an output close to 1 in their respective nodes (1 and 3) and close to 0 in all other nodes. Remarkably, in nodes 1 and 3, also events of single top quark production and $\mathrm{DY}+\mathrm{jets}$ production are assigned similar values, respectively. Consequently, the shape of their distributions closely resembles that of $\mathrm{t\bar{t}}+\mathrm{jets}$ and W+jets events, respectively. Considering the output nodes 2 and 4, corresponding to $\mathrm{DY}+\mathrm{jets}$ and single t events, less discrimination power is reached for these sources of SM background. In both nodes, the respective targeted SM process is often wrongly assigned a value close to 0. While in the distribution corresponding to node 2 it is still possible to identify a pure region mostly populated by $\mathrm{DY}+\mathrm{jets}$ events, only a negligible fraction of single t events is assigned a value above 0.5 in the output distribution of node 4.

The frequent misclassification of events of $\mathrm{DY}+\mathrm{jets}$ and single top quark production is due to two reasons. First, together they only constitute a fraction of about 5% of the total number of expected SM background events. In the pre-selection, most events of $\mathrm{DY}+\mathrm{jets}$ production are discarded by the requirement of exactly one muon to be present in selected events. Also the branching fraction of single top quarks to decay via a W boson to the final state with a muon is small with about 11% [4]. Additionally, the production cross section of single t events is very small compared to that of the major backgrounds of QCD multijet, $\mathrm{t\bar{t}}+\mathrm{jets}$, and W+jets production. Second, the kinematics of single t and $\mathrm{DY}+\mathrm{jets}$ events closely resemble those of $\mathrm{t\bar{t}}+\mathrm{jets}$ and W+jets production, respectively, such that a clear distinction is not easily possible. This is reflected by the similar value assigned to both $\mathrm{t\bar{t}}+\mathrm{jets}$ and single t events in node 1 and W+jets and $\mathrm{DY}+\mathrm{jets}$ events in node 3. Taken together, the small expected number of event of such processes in the pre-selected sample passed as input to the DNN results in a weaker classification performance for these processes. Because such events only have a minor contribution to the overall loss function J, the correct classification of events originating from the dominant SM background processes is given clear preference.

The expected signal of the decay of a heavy $\mathrm{g_{KK}}$ is also passed through the DNN, although it has never been used for the training of the DNN. It is observed that no output node has particularly good sensitivity to the hypothetical signal, which is a consequence of the signal-agnostic DNN training. However, the shapes of the output distributions of SM $\mathrm{t\bar{t}}+\mathrm{jets}$ events and the signal are very similar in node 1. Especially the low-mass signal corresponding to $M_{\mathrm{g_{KK}}} = 500\,\mathrm{GeV}$, near the kinematic threshold

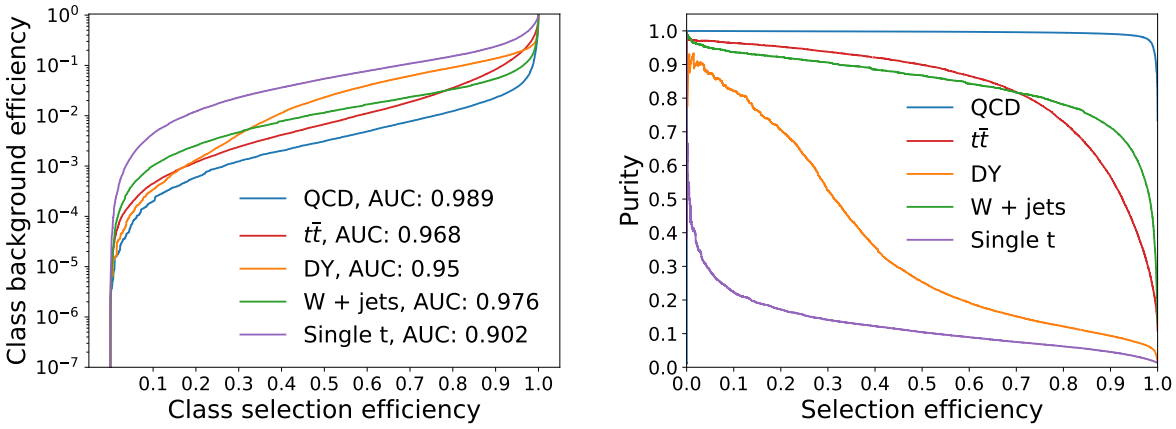

Figure 8.15: Left: ROC curves of the model-independent DNN showing the misclassification rate as a function of the selection efficiency for a given SM process. The AUC for each class is given in the legend. Right: Purity of the selected sample as a function of the selection efficiency of a given SM process for the model-independent DNN.

of $t\bar{t}$ production, is likely to be identified as originating from $t\bar{t}$ + jets production. At higher masses, the output value becomes more uniformly distributed, indicating less similarity to the kinematics of SM $t\bar{t}$ + jets events.

The DNN behavior proves that the DNN is indeed able to classify events as originating from different physical processes. Characteristic quantities of such processes have been learned by the DNN and it shows the expected behavior for events of a new class of events, which was not used in the training stage. Using the distributions of the value of the five output nodes, it is possible to classify SM backgrounds efficiently and to define an event selection that is model-independent and could be reinterpreted easily in searches for a different signal than $g_{KK} \to t\bar{t}$.

The performance of the event classification can be quantified by computing the misclassification rate (background selection efficiency) as a function of the selection efficiency for a given SM process. This function is referred to as *receiver operating characteristic (ROC)* curve and is shown in figure 8.15 (left). It is obtained by considering the distribution of the output value of the node associated to the respective event class for events in the test sample. Selecting events with an output value higher than a given threshold, the selection efficiency is defined as the fraction of selected events of the class of interest with respect to the total number of such events. Conversely, the background selection efficiency is defined as the fraction of selected events of a different class than the one under study. By varying the threshold, the ROC curve is obtained as a set of points with different selection efficiencies and misclassification rates. The integral of this curve is also referred to as *area under the curve (AUC)* and

is a measure for the classification performance. Ideal classifiers have AUC = 1, while random classifiers have AUC = 0.5. In figure 8.15 (right), also the purity of a selected sample is shown as a function of the selection efficiency for events of a given class. It is defined as the fraction of events of the process of interest in the selected sample with respect to the total number of selected events.

In order to define background-enriched CRs based on the DNN output values, which can be used to constrain systematic uncertainties in the final ML fit, it is crucial to select events of one class with a high efficiency and simultaneously obtain a pure sample of such events. As shown in figure 8.15 (right), this is only possible for three of the five SM processes under consideration in this classification scheme. However, as mentioned above, events of single top quark and DY + jets production are misclassified due to their small contributions to the overall value of the loss function and are kinematically similar to $\mathrm{t\bar{t}}$ + jets and W+jets production, respectively.

8.4.3 Application in the $\mathrm{t\bar{t}}$ analysis

The output distributions shown in figure 8.14 are well–suited to apply one-dimensional selections in order to define CRs enriched in the corresponding SM background processes. These CRs will be fitted simultaneously in the final statistical evaluation together with the SR to constrain systematic uncertainties and provide optimal sensitivity to the influence of individual SM processes

In the following, the DNN output distributions for events passing the pre-selection are used. One CR per DNN output node is defined by applying a threshold to each of the output nodes of the DNN. The SR is defined to contain all events that do not enter any of the CRs. The thresholds are found by an algorithm optimizing the significance, calculated as $S/\sqrt{S+B}$ in the SR, where S is the number of events expected of a $\mathrm{g_{KK}} \to \mathrm{t\bar{t}}$ signal with $M_{\mathrm{g_{KK}}} = 4\,\mathrm{TeV}$ and B is the number of events expected from the SM backgrounds. The algorithm iteratively considers all one-dimensional cuts on all DNN output distributions. It returns the upper or lower threshold for one distribution that results in the largest increase in significance in the SR and excludes that node from further consideration. After one cycle, the algorithm is applied a second time and it is verified that the chosen thresholds are indeed optimal.

The optimal selection for the DNN considering five event classes returned by the optimization algorithm consequently involves one-dimensional requirements on each of the five DNN output variables o_i, where $i = 0, 1, ..., 4$. For the definition of the CRs, the order of applying the respective requirements needs to be taken into account. At each selection step given in the following, a new CR is formed by events having

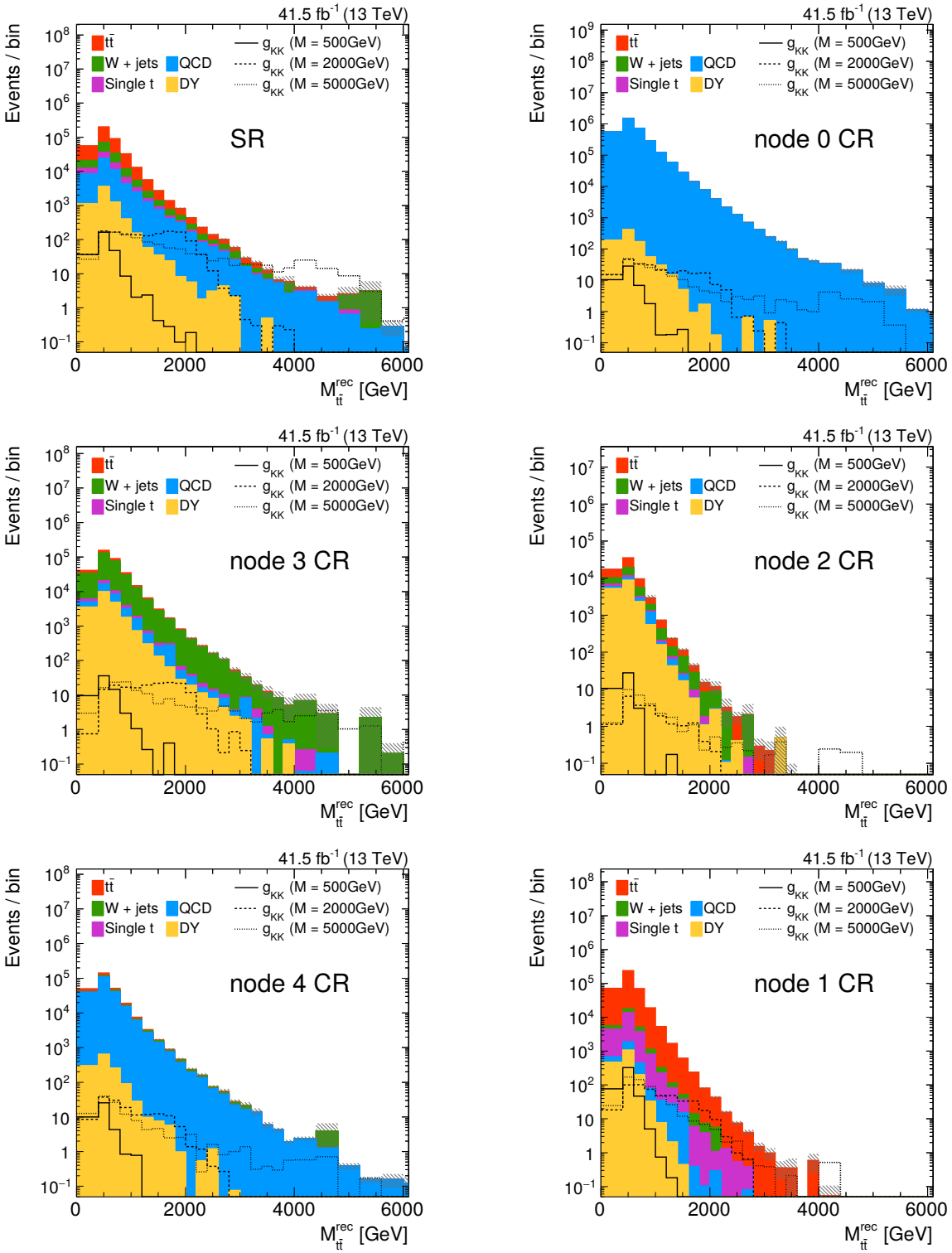

Figure 8.16: Distributions of $M_{\mathrm{tt}}^{\mathrm{rec}}$ in the resolved category in the SR and the five CRs defined by applying successive one-dimensional selections on the DNN output distributions. The model-independent DNN trained with five event classes is used.

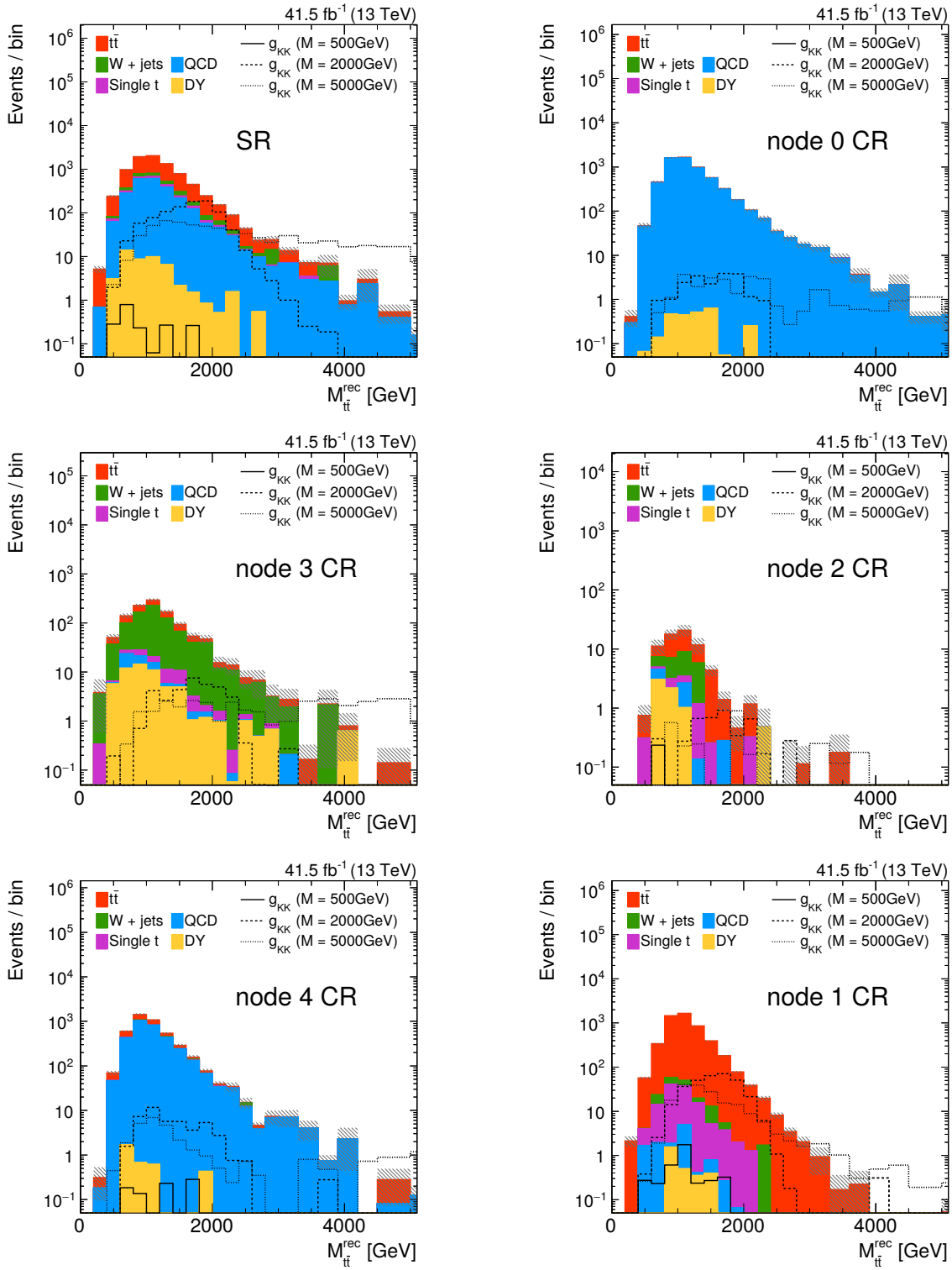

Figure 8.17: Distributions of $M_{\mathrm{tt}}^{\mathrm{rec}}$ in the boosted category in the SR and the five CRs defined by applying successive one-dimensional selections on the DNN output distributions. The model-independent DNN trained with five event classes is used.

passed all previous steps but failing the current one. Events in the SR are required to fulfill $o_0 < 0.91$, $o_3 < 0.46$, $o_2 < 0.06$, $o_4 > 0.02$, and $o_1 < 0.84$ in that order. It is important to note, that the algorithm is unable to select a CR enriched in events of single top quark production. Instead, by requiring $o_4 > 0.02$, events with a very low predicted probability of originating from single top quark production are assigned to the corresponding CR. Such events mostly originate from QCD multijet production that have not been associated to the CR defined by $o_0 > 0.91$. Furthermore, the algorithm considers the node corresponding to $\mathrm{t\bar{t}}+\mathrm{jets}$ events last, which shows that in this node the signal distribution most closely resembles that of the targeted SM process. Therefore, the smallest gain in sensitivity is expected by placing a cut on its output distribution.

In the final statistical interpretation of the results, the SR and each of the CRs is again divided in a boosted and a resolved category, based on the presence of a t-tagged AK8 jet. In both of them, the reconstructed $\mathrm{t\bar{t}}$ system is required to have $\chi^2 < 30$. The distributions of $M_{\mathrm{tt}}^{\mathrm{rec}}$ in the SR and the five CRs is shown in figure 8.16 for the resolved category and in figure 8.17 for the boosted regime. The high purity of each CR is clearly visible. If all twelve distributions would be used as an input to the final statistical analysis, the overwhelmingly large number of QCD multijet events, and the very high purity of the CRs defined by cuts on the nodes 0 and 4, would prevent the ML fit from converging. Therefore, the two CRs in each regime that are dominated by QCD multijet events are discarded. Since only a small fraction of signal events across all values of $M_{\mathrm{g_{KK}}}$ fall into the CRs defined by nodes 0 and 4, the impact on the overall sensitivity is negligible.

In the absence of signal, expected upper limits on the product of the $\mathrm{g_{KK}}$ production cross section and the branching fraction for the decay $\mathrm{g_{KK}} \to \mathrm{t\bar{t}}$ are placed as a function of $M_{\mathrm{g_{KK}}}$ for a branching fraction of unity. The ML fit and the computation of the expected limits follow the procedure described in section 8.3. The post-fit nuisance parameters as returned by the ML fit to pseudo-data are shown in figure 8.18. Good agreement between the pre- and post-fit nuisance parameter values is found. Compared to the post-fit parameters shown in figure 8.10, which have been obtained without using background-enriched CRs, the systematic uncertainties have been constrained significantly in this fit. The use of the CRs defined by the DNN output allows to constrain dominant uncertainties such as the uncertainty in the choice of μ_{r} and μ_{f} for the dominant background processes or in the SM production cross sections. Notably, also the uncertainty in the QCD multijet production cross section is constrained, despite excluding the dedicated QCD CR from the fit.

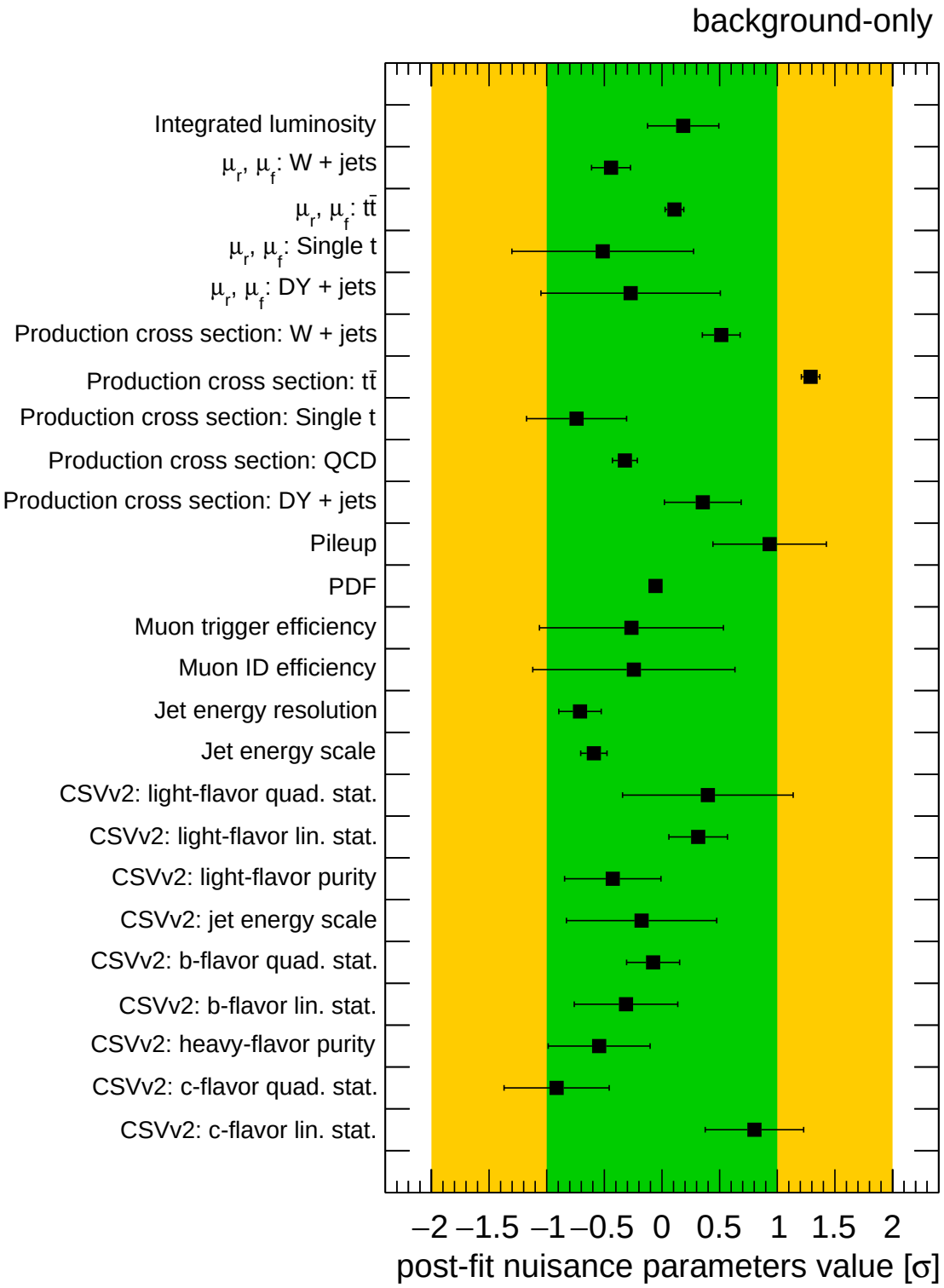

Figure 8.18: Values of the nuisance parameters after the background-only fit to pseudo-data including the CRs defined by the model-independent DNN trained with five event classes. The values are given in units of their prior uncertainty.

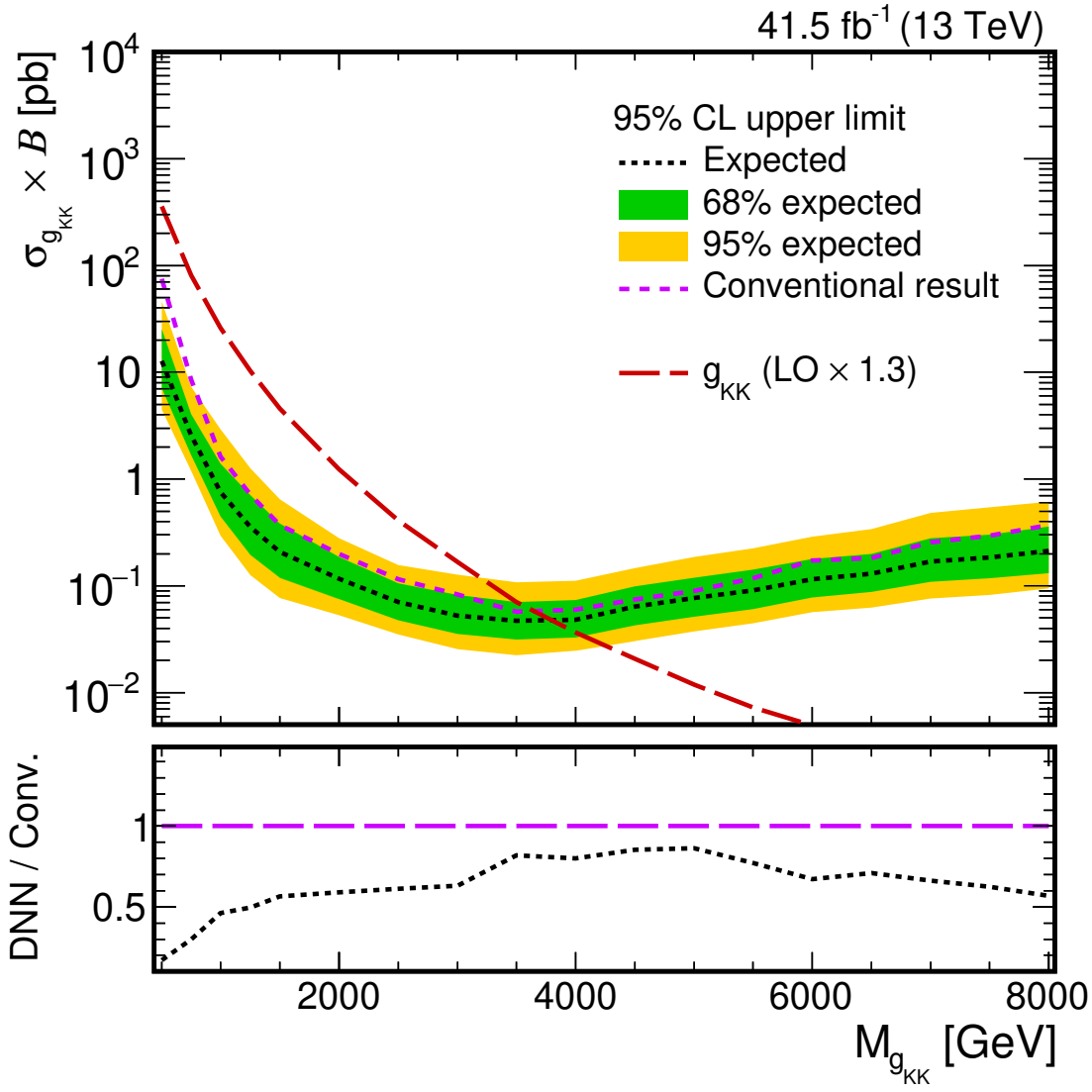

Figure 8.19: Expected upper limits on the product of the g_{KK} production cross section and $\mathcal{B}$ at the 95% CL as a function of the g_{KK} mass. The limits are obtained using the model-independent DNN event classifier trained with five SM background event classes. Unit branching fraction for the decay $g_{KK} \to t\bar{t}$ is assumed. The red dashed line depicts the prediction for the g_{KK} production cross section [205] corrected with an NLO K factor of 1.3 [206]. The dashed violet line corresponds to the expected upper limit obtained with the conventional search strategy not using the DNN event classifier. The lower panel shows the ratio of expected limits obtained with the DNN-based and the conventional strategy.

The expected upper limits on the g_{KK} production cross section obtained with these post-fit uncertainties are shown in figure 8.19. It is expected to exclude g_{KK} bosons below masses of 3.84 TeV with this selection approach, improving the exclusion limit by 200 GeV compared to the result obtained with the conventional event selection. The expected limits obtained with the DNN trained with five event classes are systematically stronger at all values of $M_{g_{KK}}$ than those of the analysis following a conventional selection strategy. At low resonance masses, the expected limit improves by more than a factor of 5. This improvement was achieved only by efficiently classifying the different SM background contributions to form CRs that constrain the systematic uncertainties in the limit setting procedure. No signal events have been used in the training of the DNN classifier. The use of CRs that are included in the final fit instead of one-dimensional selection requirements discarding a large fraction of signal events also enhances the signal selection efficiency. Especially the CR based on node 4, which contains mostly SM $t\bar{t}$ + jets and single t events, recovers many signal events of low $M_{g_{KK}}$, which would otherwise have been lost.

8.4.4 Model-Dependent DNN Training

In addition to the model-independent classification described previously, a new class of events is defined containing signal events of resonant $t\bar{t}$ production. The maximum gain in sensitivity to a potential signal can be reached by including simulated $g_{KK} \to t\bar{t}$ events in the training. On the other hand, a model dependence is introduced, potentially necessitating the training of new DNNs for each new signal model to be studied. Furthermore, considering the DNN output distributions shown in figure 8.14, it is natural to merge the two minor backgrounds with the corresponding major backgrounds. Instead, now a combined *heavy boson* class (W+jets and DY + jets events) and a *top quark* class, which targets SM single and pair production of top quarks, is defined. In this way, events are classified in broader classes containing processes of similar final states.

This new classification scheme requires the training of a new DNN with four instead of five nodes in the output layer. It is trained to predict a value close to 1 for QCD events in node 0, for events in the top quark class in node 1, for events in the heavy boson class in node 2, and for signal events in node 3. The signal sample used for training the DNN is composed of simulated events of all values of $M_{g_{KK}}$. The signal events of each sample passing the pre-selection are reweighted to a production cross section of 1 pb. The sum of all samples is then passed to the DNN as input.

The hyperparameters used for this new DNN are the same as for the background-

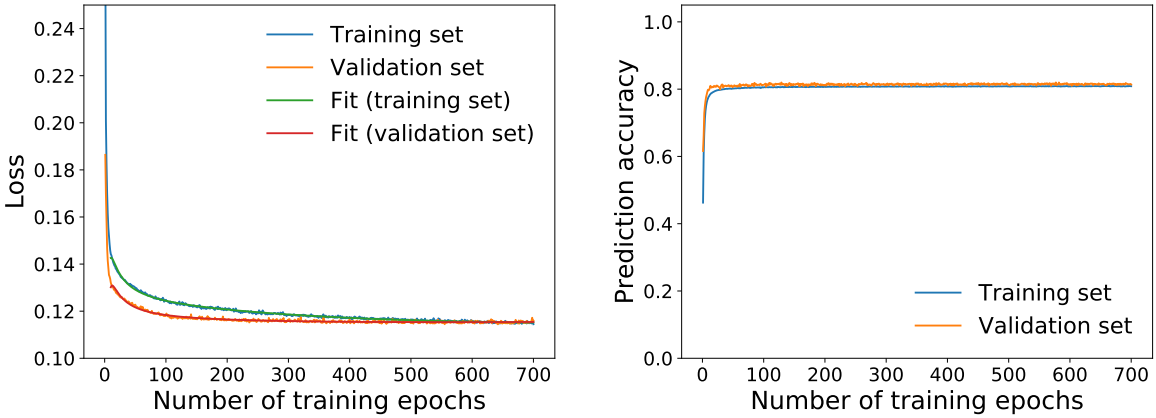

Figure 8.20: Left: Loss evaluated on the training and the validation set and the corresponding fitted functions as a function of the number of training epochs for the model-dependent DNN trained with three SM background and one signal event class. Right: Prediction accuracy in the training and the validation set as a function of the number of training epochs for the model-dependent DNN trained with four classes.

only DNN. It has been verified that only negligible improvements in the classification performance are achieved by varying the hyperparameters. The loss and the classification accuracy of this new DNN are shown as a function of the number of training epochs in figure 8.20. The optimal DNN is obtained after training for 641 epochs. It results in a loss of 0.115 in both the training and validation set. This value is smaller compared to that obtained with the DNN trained on five different classes due to the reduced number of classes entering the computation of the loss. Very similar behavior compared to the DNN trained with five classes of events is observed. Similarly, the classification accuracy reaches a slightly higher value of about 81% at its plateau.

The distributions of the value of each of the three output nodes are shown in figure 8.21. Again, excellent discrimination between individual event classes is found. Furthermore, the distributions of the DNN output values is very similar to the ones obtained with the DNN trained with five categories of SM background. In this DNN, all SM classes show the expected behavior and no systematic misclassification is visible. The shape of the signal of a heavy $t\bar{t}$ resonance can be well distinguished from the SM background processes using the distribution of node 3 (figure 8.21 lower right). While low-mass signal processes resemble SM $t\bar{t}+$jets production most closely as expected, very boosted topologies from heavy g_{KK} decays are identified correctly, which allows for the efficient selection of a pure SR.

The ROC curve and the purity as a function of the selection efficiency are shown in figure 8.22 (left and right, respectively) for all four classes of events. The classification

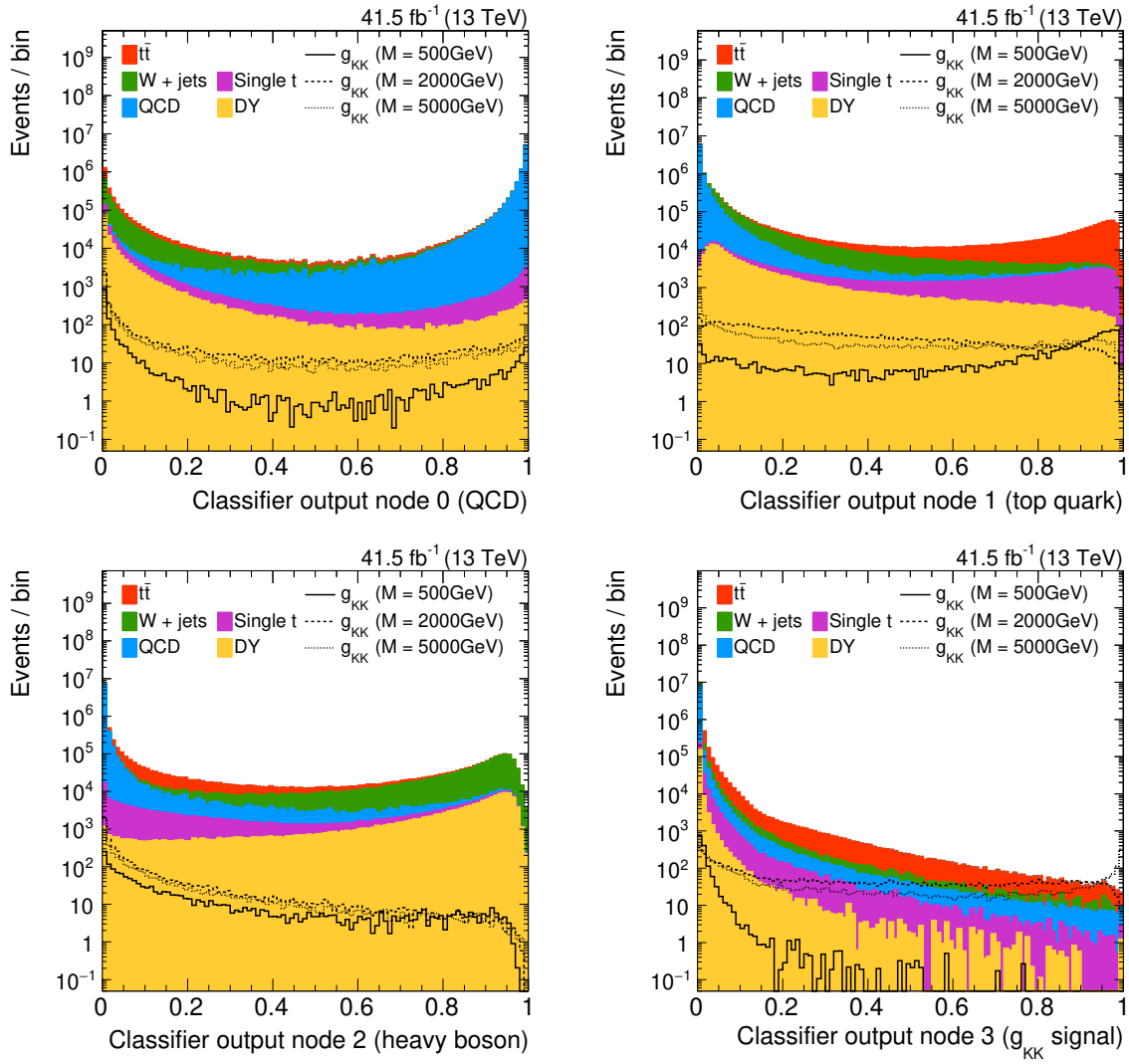

Figure 8.21: Distributions of the model-dependent DNN output for each of the four output nodes.

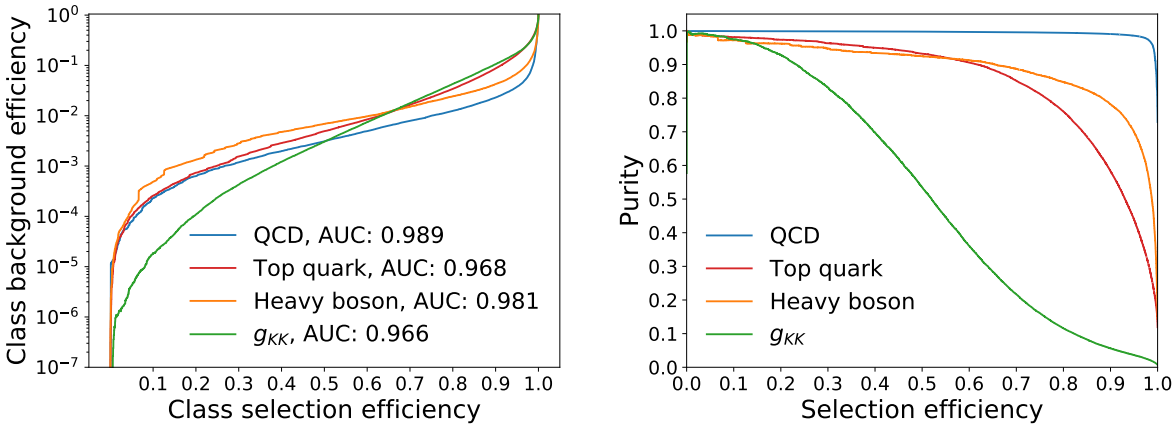

Figure 8.22: Left: ROC curves showing the misclassification rate as a function of the selection efficiency for a given process for the model-dependent DNN trained with four event classes. The AUC for each class is given in the legend. Right: Purity of the selected sample as a function of the selection efficiency of a given process for the model-dependent DNN trained with four event classes.

performance obtained with this DNN trained with three event classes is very similar to that obtained with five event classes. The background efficiency as a function of the selection efficiency for QCD multijet events closely follows the previous result and yields the same AUC of about 0.99. The classification performance of events in the top quark and heavy boson categories is driven by events of SM $\mathrm{t\bar{t}}+$jets and W+jets production, respectively. However, adding the corresponding minor backgrounds to the respective classes improves the AUC for both cases. By grouping events based on their underlying physical processes, the need to distinguish kinematically very similar events is eliminated. This results in improved classification performance for classes containing events that would otherwise receive similar predicted probabilities for two classes and hence would be easily confused by the DNN. In addition, a large fraction of signal events of $\mathrm{g_{KK}} \to \mathrm{t\bar{t}}$ decays is classified correctly again the SM background processes. In figure 8.22 right it is visible that it is possible to select signal events with an efficiency of about 50% and obtain a sample of events consisting to about 50% of $\mathrm{g_{KK}} \to \mathrm{t\bar{t}}$ events, promising improved sensitivity to new resonant $\mathrm{t\bar{t}}$ production mechanisms.

The SR and multiple CRs are defined using the distributions shown in figure 8.21. With the new signal event class, it is possible to design a dedicated SR as opposed to only classifying SM background events. Naturally, the most sensitive region can be obtained by defining a lower threshold applied to the distribution of the output of node 3. Considering all events passing the pre-selection and have $\chi^2 < 30$, the

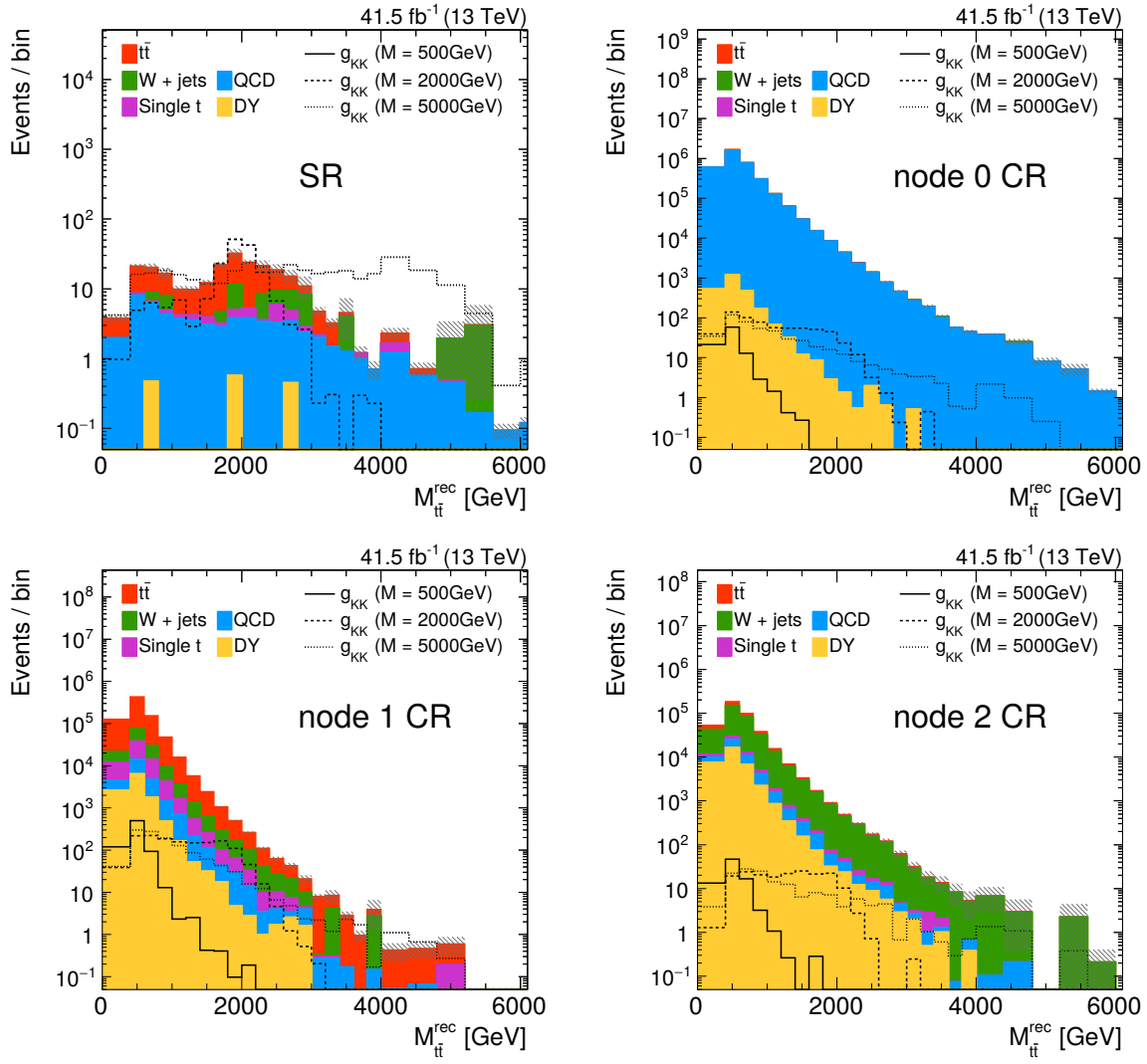

Figure 8.23: Distributions of $M_{\mathrm{tt}}^{\mathrm{rec}}$ in the resolved category in the SR and the three CRs defined by applying successive one-dimensional selections on the DNN output distributions. The model-dependent DNN trained with four event classes is used.

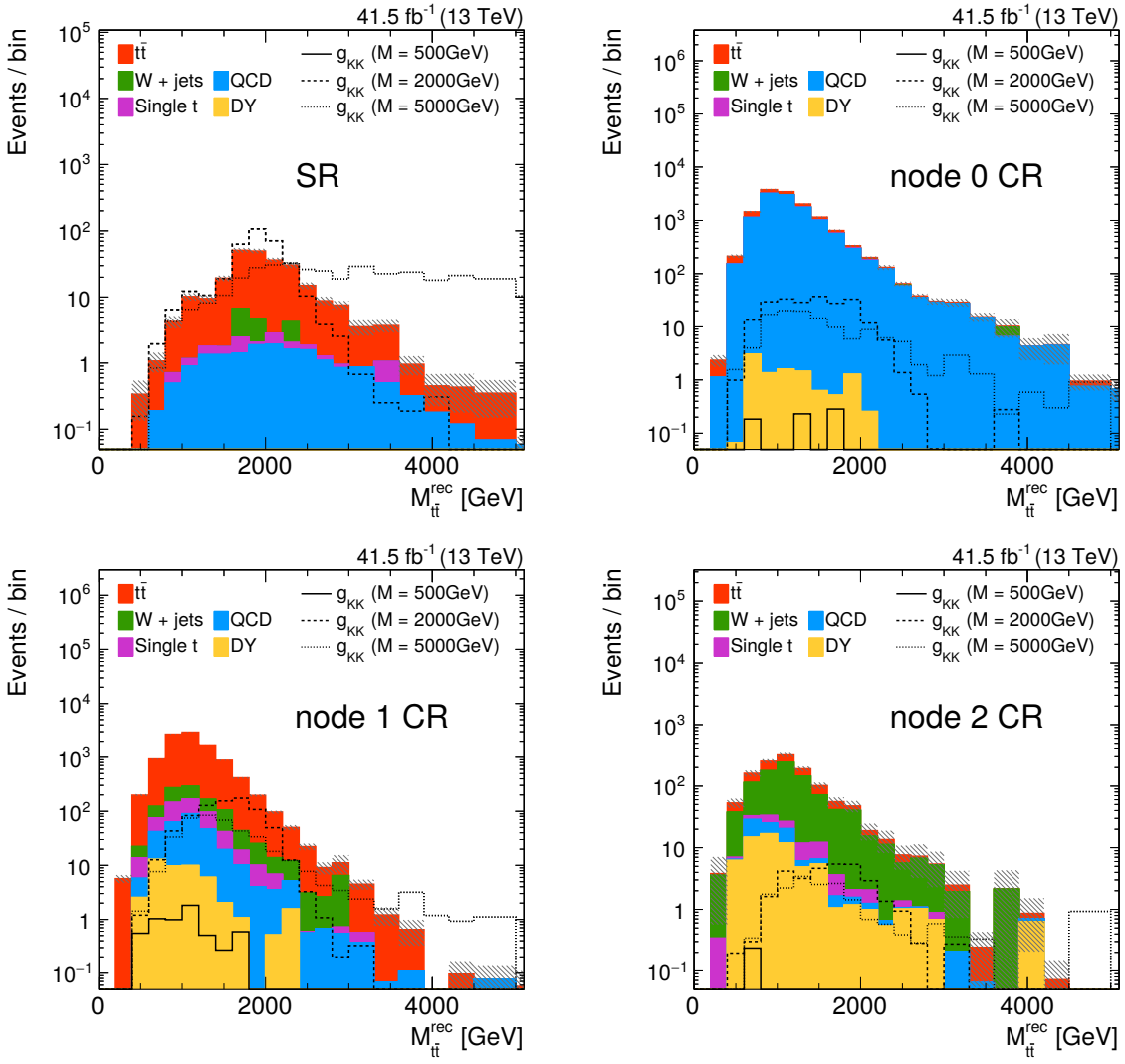

Figure 8.24: Distributions of $M_{\mathrm{t\bar{t}}}^{\mathrm{rec}}$ in the boosted category in the SR and the three CRs defined by applying successive one-dimensional selections on the DNN output distributions. The model-dependent DNN trained with four event classes is used.

threshold maximizing the sensitivity to a signal of $M_{g_{KK}} = 4\,\text{TeV}$ is given by $o_3 > 0.83$. The background-enriched CRs contain all remaining events that do not pass this requirement. Here, the highest output value of the three nodes targeting SM background processes is used to assign each event to one out of three corresponding CRs.

For the final statistical analysis, the resulting four event categories are split into resolved and boosted regions based on the presence of a t-tagged AK8 jet. The distributions of $M_{t\bar{t}}^{\text{rec}}$ in the SR and the three CRs are shown in figures 8.23 and 8.24 for the resolved and boosted regions, respectively. As for the DNN trained with five event classes, the CR enriched in QCD events is discarded in the final evaluation in order to avoid numerical instability of the fit.

The values of the nuisance parameters after the ML fit to pseudo-data (as described in section 8.3) are shown in figure 8.25. As for the previous fit, good agreement between the pre- and post-fit nuisance parameter values is found. Compared to the uncertainties shown in figure 8.18, similarly strongly constrained systematic uncertainties are obtained using the DNN trained with four event classes, including hypothetical signal. Reducing the number of event classes that aim at SM processes, by grouping processes of similar origin or signature, does not impair the potential to constrain systematic uncertainties in such processes in a combined fit.

Expected upper limits on the product of the g_{KK} production cross section and the branching fraction of the g_{KK} decay are placed. The computation of the expected limits follows the procedure described in section 8.3. The expected limits obtained under the assumption of exclusive $g_{KK} \to t\bar{t}$ decays are shown as a function of $M_{g_{KK}}$ in figure 8.26. Masses below $M_{g_{KK}} = 4.30\,\text{TeV}$ are expected to be excluded under the assumption of exclusive decays of the g_{KK} to a pair of top quarks. The expected limit on the g_{KK} production cross section is improved significantly over the entire signal mass range under consideration. In comparison to the result obtained with the conventional analysis strategy, an improvement by a factor of almost 2 in the expected upper limits across the whole mass range is achieved with this new DNN-based approach. For $M_{g_{KK}} > 2\,\text{TeV}$, the improvement is even larger.

This result is based on two main advantages of the DNN-based approach over the conventional strategy. A very pure region enriched in signal events can be defined. This SR efficiently selects events of high-mass-g_{KK} decays. Due to its kinematic similarity to SM $t\bar{t}+\text{jets}$ production, however, the low-mass signal is assigned to the corresponding CR almost exclusively. The pure SR selection is complemented by CRs enriched in the corresponding SM backgrounds. Since background events are assigned to these CRs

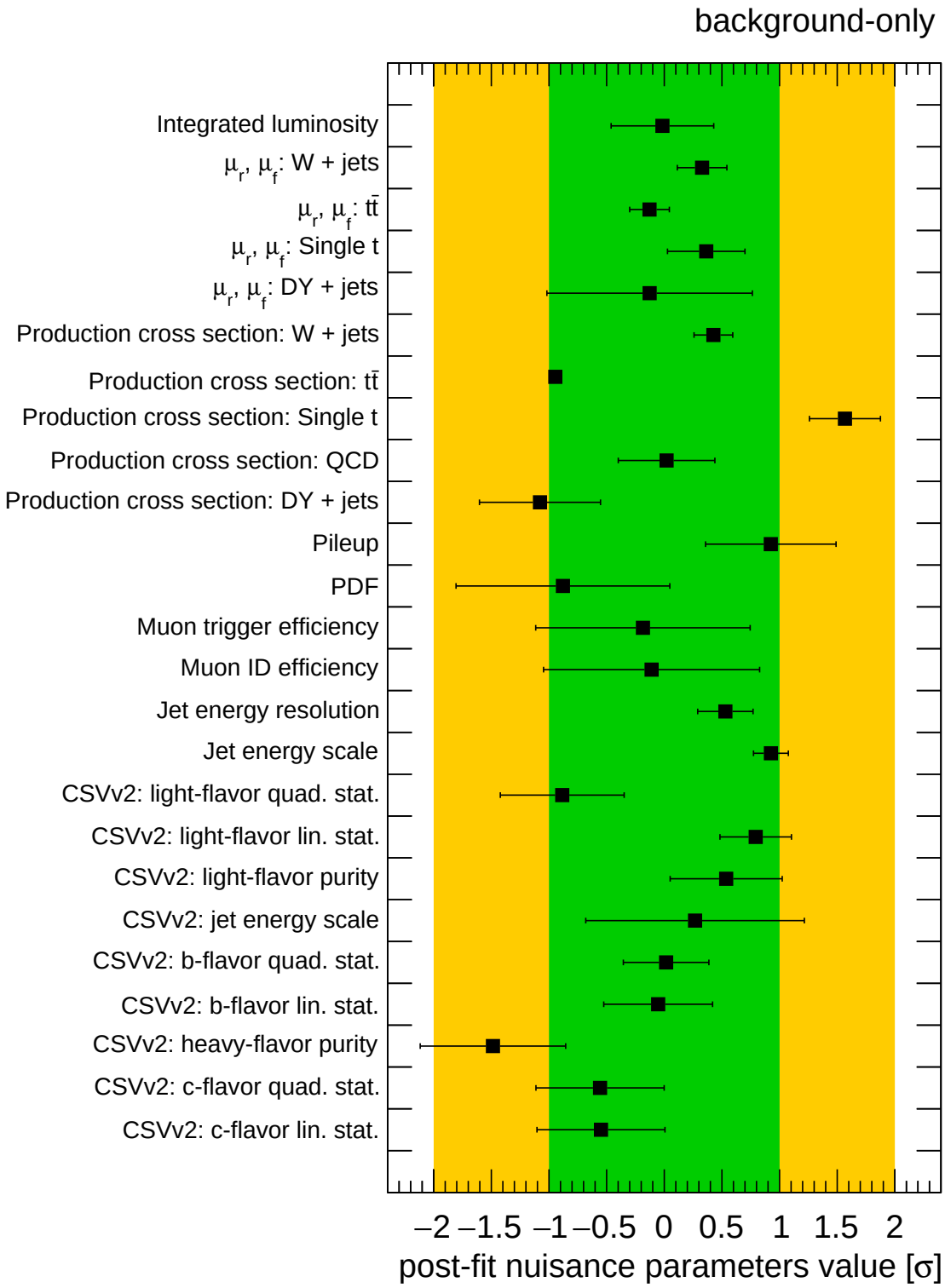

Figure 8.25: Values of the nuisance parameters after the background-only fit to pseudo-data including the CRs defined by the model-dependent DNN trained with four event classes. The values are given in units of their prior uncertainty.

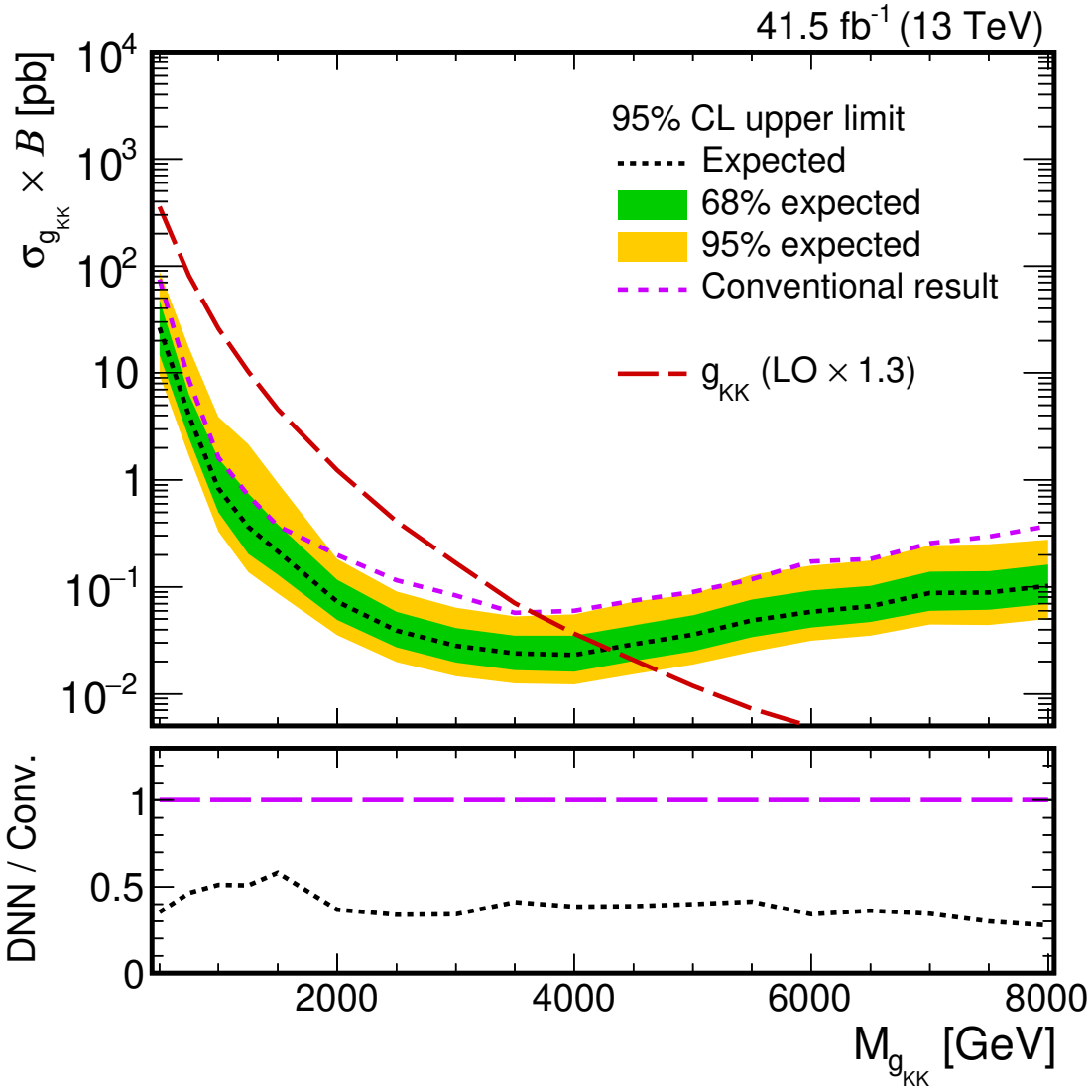

Figure 8.26: Expected upper limits on the product of the g_{KK} production cross section and $\mathcal{B}$ at the 95% CL as a function of the g_{KK} mass. The limits are obtained using the model-dependent DNN event classifier trained with three SM background and one signal event class. Unit branching fraction for the decay $g_{KK} \to t\bar{t}$ is assumed. The red dashed line depicts the prediction for the g_{KK} production cross section [205] corrected with an NLO K factor of 1.3 [206]. The dashed violet line corresponds to the expected upper limit obtained with the conventional search strategy not using the DNN event classifier. The lower panel shows the ratio of expected limits obtained with the DNN-based and the conventional strategy.

with high efficiency and a low misclassification rate, excellent purity of the process of interest is achieved throughout all regions. Largely constrained systematic uncertainties in combination with a highly sensitive SR result in the expected limit improved by a factor of almost 2 over the whole signal mass range. The improvement is even larger for $M_{\mathrm{g_{KK}}} > 2\,\mathrm{TeV}$. As for the model-dependent DNN, the SR event selection is optimized for a signal of $M_{\mathrm{g_{KK}}} = 4\,\mathrm{TeV}$. As a result, the expected mass exclusion limit is improved by more than 600 GeV from 3.68 TeV to 4.30 TeV with respect to the conventional analysis strategy, assuming unit branching fraction for the $\mathrm{g_{KK}} \to \mathrm{t\bar{t}}$ decay.

8.5 Summary and Outlook

A simulation-based study for the search for resonant top quark pair production in the μ+jets final state assuming an integrated luminosity of $41.5\,\mathrm{fb}^{-1}$, corresponding to the dataset collected by the CMS detector in the year 2017, was presented. Using the analysis strategy of the public analysis of the 2016 dataset, similar sensitivity could be achieved in the decay channel under study. KK excitations of the gluon are expected to be excluded up to masses of 3.68 TeV with the conventional analysis approach. In the presented analysis, the PUPPI PU mitigation technique was employed. Its impact on the number of reconstructed jets and their p_{T} was studied. A smaller number of reconstructed jets more likely to reflect the true number of expected jets was observed.

Considerable improvements to the analysis sensitivity were found when employing a novel DNN-based multiclass event classifier. Two complementary approaches have been studied. First, a signal-model independent classifier was trained. Only SM background processes were used for this purpose, making the algorithm independent of the modelling of the resonant signal. Its output distributions were used to define SM background-enriched CRs, resulting in constrained systematic uncertainties in the final statistical evaluation. The expected upper limit on the $\mathrm{g_{KK}}$ production cross section was improved by more than a factor of 5 for low values of $M_{\mathrm{g_{KK}}}$. In the second approach, signal events of resonant $\mathrm{t\bar{t}}$ production were included in the DNN training. At the disadvantage of introducing a model-dependent classifier response, the signal selection efficiency was largely increased. Consequently, the expected limits on the $\mathrm{g_{KK}}$ production cross section in the $\mathrm{g_{KK}} \to \mathrm{t\bar{t}}$ decay channel were improved by more than 50% with respect to the conventional analysis strategy. The expected mass exclusion limit on $\mathrm{g_{KK}}$ was found to be $M_{\mathrm{g_{KK}}} < 4.30\,\mathrm{TeV}$ in the μ+jets final state, which is comparable to the expected exclusion limit of $M_{\mathrm{g_{KK}}} < 4.45\,\mathrm{TeV}$ [204] obtained in the

combined analysis of all possible $t\bar{t}$ decay modes for the 2016 dataset.

Despite the demonstrated success of the DNN event classifier, further studies are required before employing the algorithm introduced in this chapter. First, the event selection based on the DNN output distributions as described in the previous section clearly does not make use of the full information provided by the DNN. It does not take into account any potential correlation between the individual output values and hence might not constitute the optimal selection. Furthermore, optimizing the selection based on the expected signal significance should only be used as a first approach. It does not take into account the shape of the SM backgrounds and the signal in the final variable used in the statistical analysis, $M_{\mathrm{tt}}^{\mathrm{rec}}$. The optimal event selection hence can only be found when optimizing for the target variable, the sensitivity to a signal as obtained by the full statistical shape analysis of the $M_{\mathrm{tt}}^{\mathrm{rec}}$ distribution. However, given the large number of possible combinations of one-dimensional thresholds, this would require significant computational work. In order to optimally reduce the dimensionality of the DNN output variables and facilitate one-dimensional selection strategies, secondary DNNs or BDTs could be trained with individual target quantities, such as the signal selection efficiency, or optimal CR purity.

For a DNN trained in a model-dependent way using simulated signal events, the distribution of $M_{\mathrm{tt}}^{\mathrm{rec}}$ might not be the optimal choice for maximizing the sensitivity to a potential signal. Instead, the output distribution of the signal node could be used, which was optimized to distinguish the SM backgrounds from a potential signal most efficienctly. Considering the DNN output in the signal node in bins of $M_{\mathrm{tt}}^{\mathrm{rec}}$ could further increase the sensitivity of the analysis, especially for signal expected to peak at high values of $M_{\mathrm{tt}}^{\mathrm{rec}}$, where the SM backgrounds are expected to have only a small contribution.

For applying the presented technique not only to simulated events but also to data, it is of crucial importance to study and validate the behavior of the DNN on data directly. It needs to be verified that the DNN, trained exclusively with simulated events, performs similarly on data. For this, the agreement between data and simulation in the input variables can be an indicator of potential mismodelling in simulated events. With the approach presented in this thesis, the performance of the DNN could be monitored in the background-enriched CRs. Classification efficiencies for the different event classes must be measured in data and simulation and potentially corrected if they do not agree.

While the DNN multi-class classifier is a powerful tool and expected to push the analysis sensitivity to values previously unprobed, also other aspects of the analysis

need to be refined in order to maximize its potential. The most inhibiting aspect at the current stage is the shape of the $M_{\mathrm{tt}}^{\mathrm{rec}}$ distribution for signal hypotheses with masses beyond about $M_{\mathrm{g_{KK}}} = 4\,\mathrm{TeV}$. In this regime, off-shell production dominates the overall production cross section, resulting in a non-resonant structure of the signal. The expected value of M_{tt} is shifted towards lower masses significantly and exhibits an increasingly background-like shape. Addressing this issue will be crucial for continued improvement of the analysis reach to higher signal masses. While the distribution of $M_{\mathrm{tt}}^{\mathrm{rec}}$ constitutes an optimized discriminator for resonant signal, employing a dedicated, model-specific DNN trained to identify such signal processes, and using its output distribution instead of $M_{\mathrm{tt}}^{\mathrm{rec}}$ could result in significant gain at very large masses and help to maximize the potential sensitivity to BSM $\mathrm{t\bar{t}}$ production at the LHC.

Chapter 9

Conclusions

The standard model of particle physics has been tested in a multitude of measurements to great precision and is one of the most successful theories to date. However, it is incomplete as it cannot explain a number of physical observations and theoretical shortcomings. Many theories extending the standard model and predicting the existence of new particles have therefore been proposed. Among the newly predicted particles are leptoquarks, which could be realized via extended symmetry groups embedding the standard model. Leptoquarks could contribute to the explanation of the recent results of precision measurements of the B meson decay modes, which hint at the violation of lepton flavor universality in nature. Masses at the TeV scale and predominant couplings to third-generation quarks are essential for leptoquarks in order to explain the experimental data and avoid the tight constraints from electroweak precision data.

Direct searches for leptoquarks have a long history in experimental particle physics and have been conducted at a multitude of particle colliders. No evidence for the existence of leptoquarks has been found to date. Analyses performed in electron-positron and electron-proton collisions studied electroweak pair-production and s-channel production of leptoquarks coupled to first-generation fermions. Single leptoquark production and cross-generational couplings have also been analyzed. In proton-(anti)proton collisions, leptoquark pairs could be produced copiously via the strong interaction. With the increased center-of-mass energies at the Tevatron and LHC colliders, pairs of leptoquarks coupled to top quarks became accessible kinematically for the first time.

In this thesis, the first search for pair-produced leptoquarks decaying to top quarks and muons has been presented. It is based on the dataset collected by the CMS detector at a center-of-mass energy of 13 TeV in the year 2016, which corresponds to an integrated luminosity of $35.9\,\mathrm{fb}^{-1}$. The existence of this leptoquark could explain the deviation measured not only in $R_{\mathrm{K}^{(\star)}}$ but also the anomalous magnetic moment of the

muon. It can also be essential in a combined explanation of $R_{\mathrm{K}^{(\star)}}$ and $R_{\mathrm{D}^{(\star)}}$. However, theoretical models predict leptoquarks to exhibit multiple simultaneous Yukawa couplings to different quarks and leptons. With increasingly many leptoquark decay modes being studied by the LHC collaborations, it is crucial to interpret the multitude of results with a more global perspective. Considering multiple couplings allows to place lower limits on the leptoquark mass as a function of the branching fraction of their decays and place constraints on the leptoquark coupling space favored by BSM models. In this thesis, three leptoquark decay modes are studied, $\mathrm{LQ} \to \mathrm{t}\mu$, $\mathrm{LQ} \to \mathrm{t}\tau$, and $\mathrm{LQ} \to \mathrm{b}\nu$. With these results, all decay modes of leptoquarks of charge -1/3e and couplings to top quarks relevant for explaining the hints for lepton flavor universality violation are examined for the first time. The results of this thesis are reinterpretable in different models, which is a key property eventually allowing for conclusive statements on the viability of models predicting the existence of leptoquarks.

Many theories extending the standard model also predict the existence of other new, heavy particles. They also appear in models proposing vector leptoquarks. The CMS Collaboration has conducted a search for new resonant production of top quark pairs with the dataset recorded in the year 2016. Lower limits of the mass of such resonances had been placed for several different model assumptions, ranging from 3.80 to 6.65 TeV. The reach of the limits placed, combining results from all three $\mathrm{t\bar{t}}$ decay modes, is limited by systematic uncertainties in the description of the SM backgrounds. Therefore, significant gains in later analyses of the full dataset recorded in the years 2016–2018 can only be achieved by changing the analysis strategy. Developing an event selection with an increased signal efficiency is the most promising improvement to be realized in a new analysis, together with better control of the SM backgrounds and the associated systematic uncertainties. The DNN-based multi-class event categorization presented in this thesis unifies both aspects and constitutes an approach that is independent of the model specifics of the potential signal. A large number of analyses could therefore profit from this strategy. It was demonstrated that a gain in sensitivity by up to a factor of 5 is expected from employing this technique. An additional challenge is the large width of the signal for very heavy new particles. As non-resonant signals will become increasingly important at the LHC, new analysis strategies must be developed to maintain sensitivity in this kinematic regime. In this thesis, a model-dependent DNN-based approach was presented, which was shown to improve the expected sensitivity across the full range of resonance masses by a factor of about 2 or more. The general approach could be tailored even more towards non-resonant signals, further increasing the expected gain.

Focusing on novel decay modes and analysis techniques, the results of this thesis pave the way for drawing conclusions on the nature of the flavor anomalies and possible explanations. Considering several relevant final states, previously unexplored regions of the leptoquark parameter space could be constrained for the first time.

Appendices

Appendix A

Distributions of Input Variables for the Deep Neural Network Event Classifiers

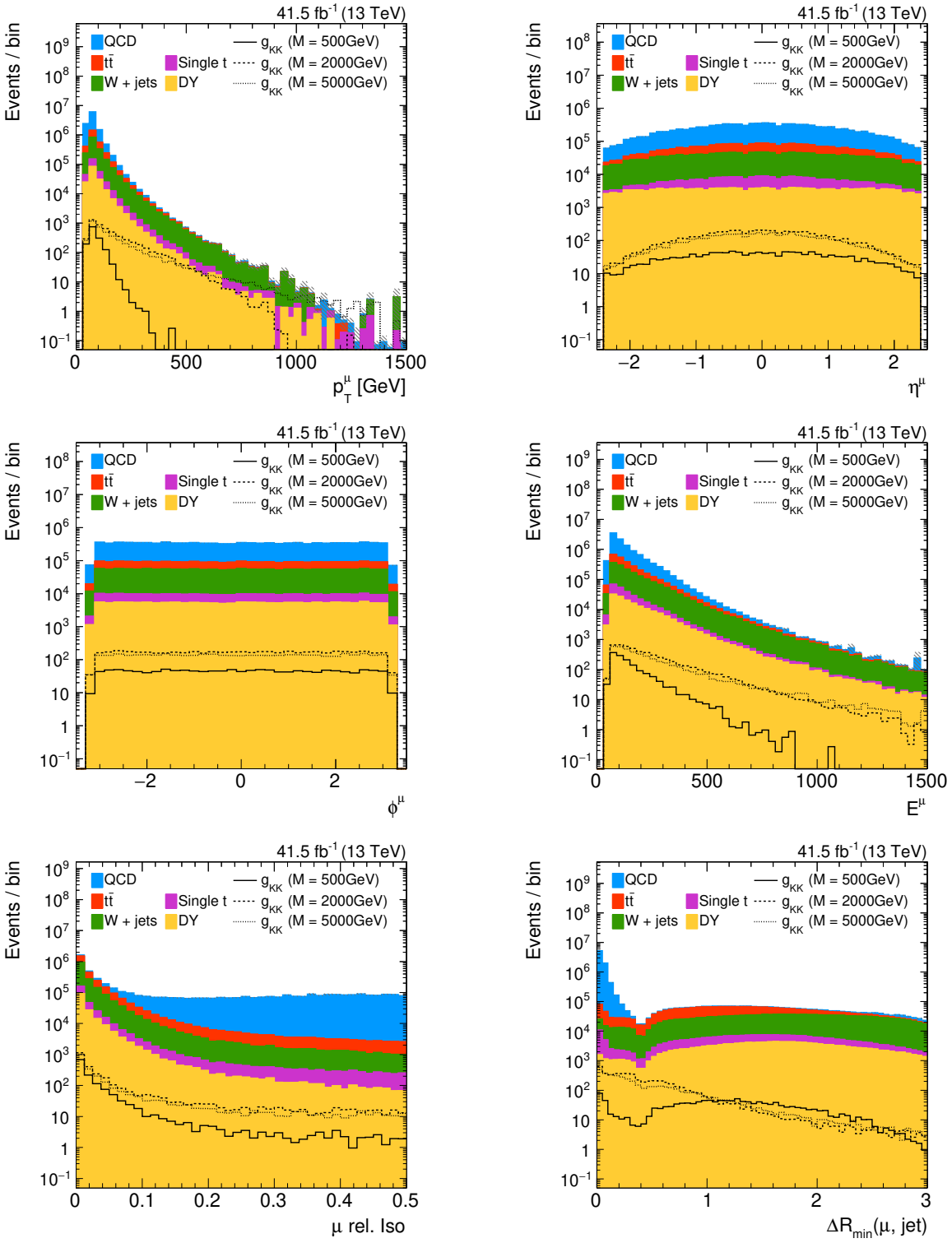

Figure A.1: Distributions of p_{T} (upper left), η (upper right), ϕ (middle left), E (middle right), I_{rel} (lower left), and $\Delta R_{\mathrm{min}}(\ell,\mathrm{j})$ (lower right) of the muon for events that pass the pre-selection and are used as input to the DNN event classifiers presented in section 8.4.

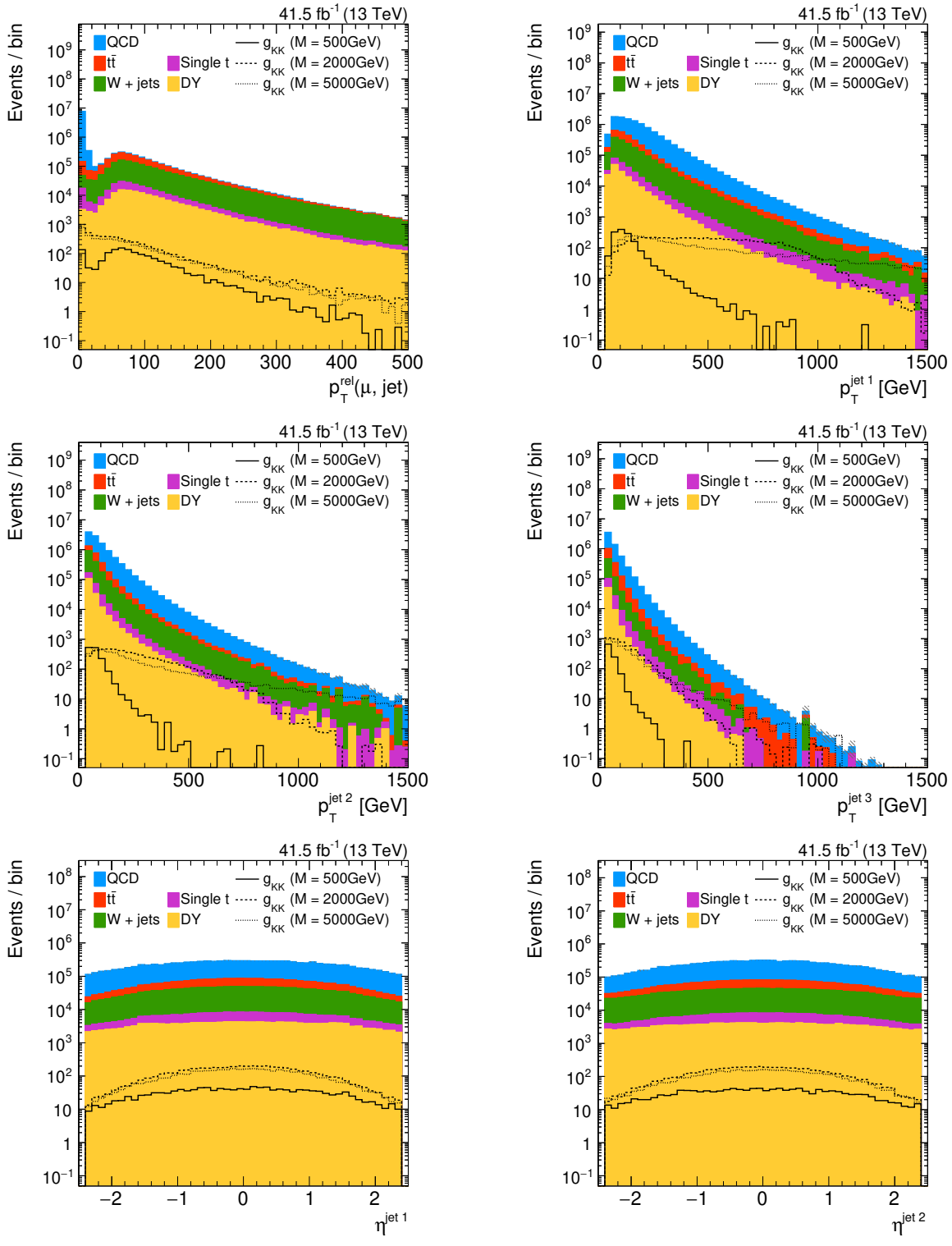

Figure A.2: Distributions of $p_{\mathrm{T,\,rel}}(\ell,\mathrm{j})$ of the muon (upper left), p_{T} of the leading (upper right), sub-leading (middle left), and sub-sub-leading (middle right) AK4 jet, and η of the leading (lower left), and sub-leading (lower right) AK4 jet for events that pass the pre-selection and are used as input to the DNN event classifiers presented in section 8.4.

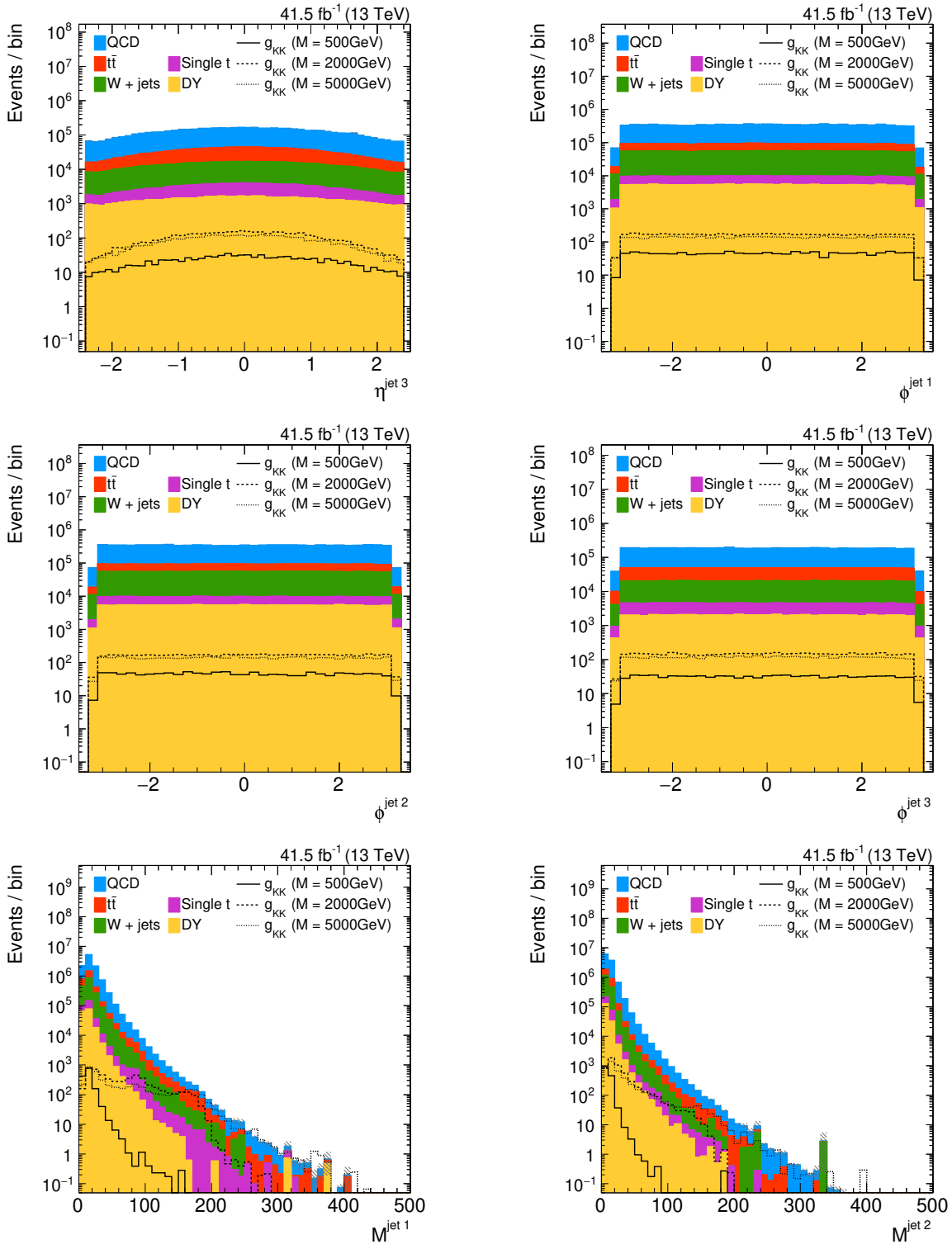

Figure A.3: Distributions of η of the sub-sub-leading AK4 jet (upper left), ϕ of the leading (upper right), sub-leading (middle left), and sub-sub-leading (middle right) AK4 jet, and the mass of the leading (lower left), and sub-leading (lower right) AK4 jet for events that pass the pre-selection and are used as input to the DNN event classifiers presented in section 8.4.

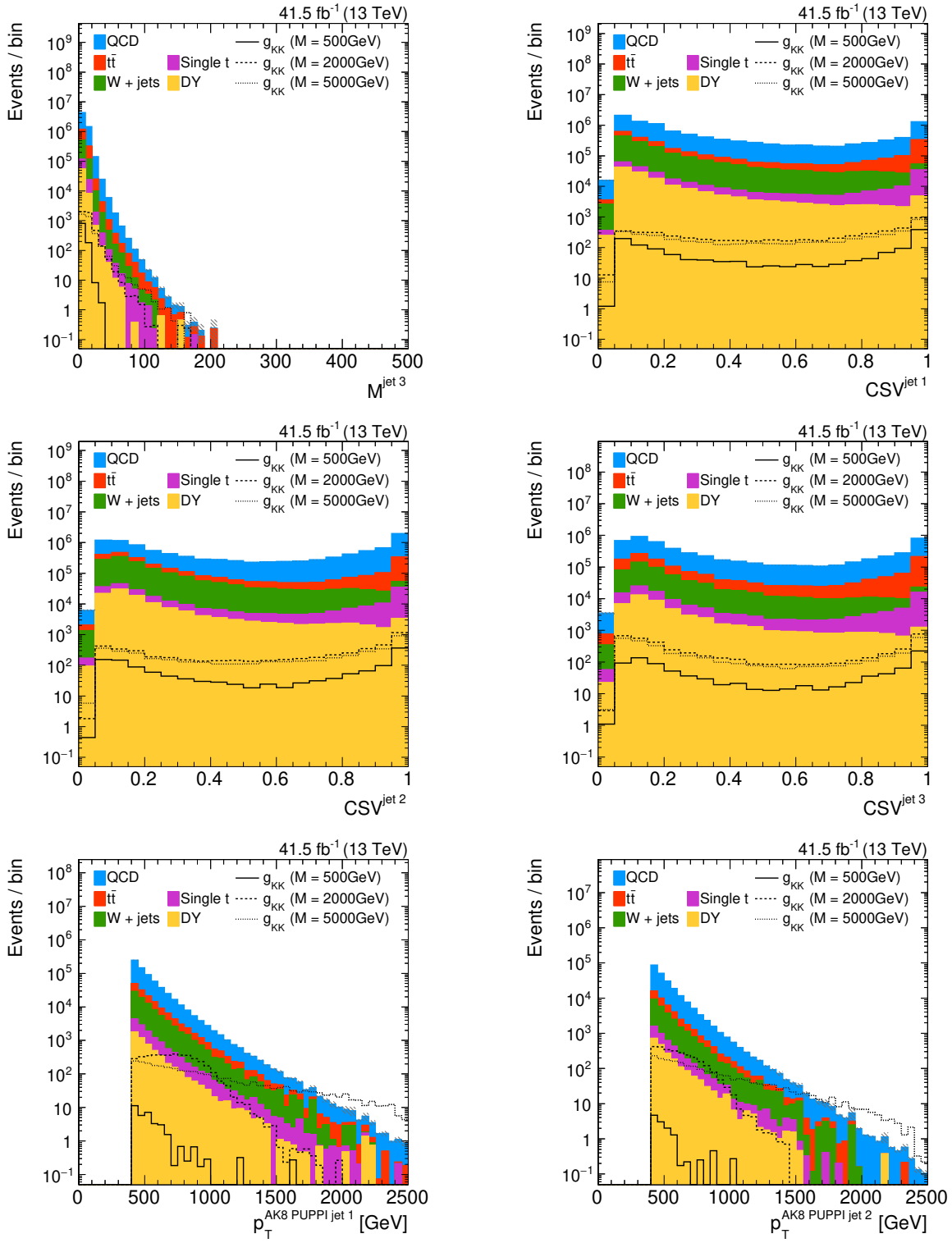

Figure A.4: Distributions of the mass of the sub-sub-leading AK4 jet (upper left), the CSVv2 discriminator of the leading (upper right), sub-leading (middle left), and sub-sub-leading (middle right) AK4 jet, and p_T of the leading (lower left), and sub-leading (lower right) AK8 jet for events that pass the pre-selection and are used as input to the DNN event classifiers presented in section 8.4.

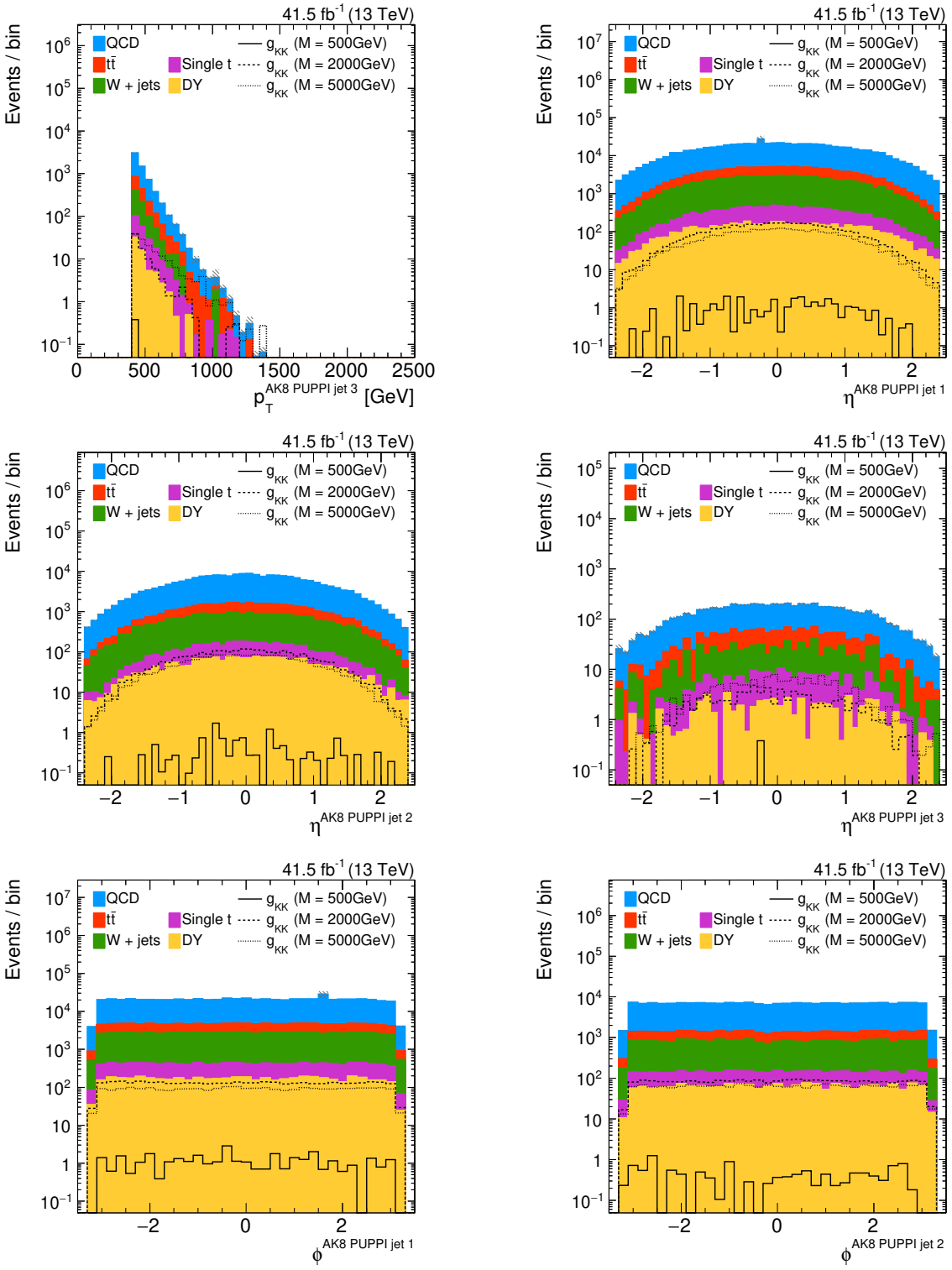

Figure A.5: Distributions of p_{T} of the sub-sub-leading AK8 jet (upper left), η of the leading (upper right), sub-leading (middle left), and sub-sub-leading (middle right) AK8 jet, and ϕ of the leading (lower left), and sub-leading (lower right) AK8 jet for events that pass the pre-selection and are used as input to the DNN event classifiers presented in section 8.4.

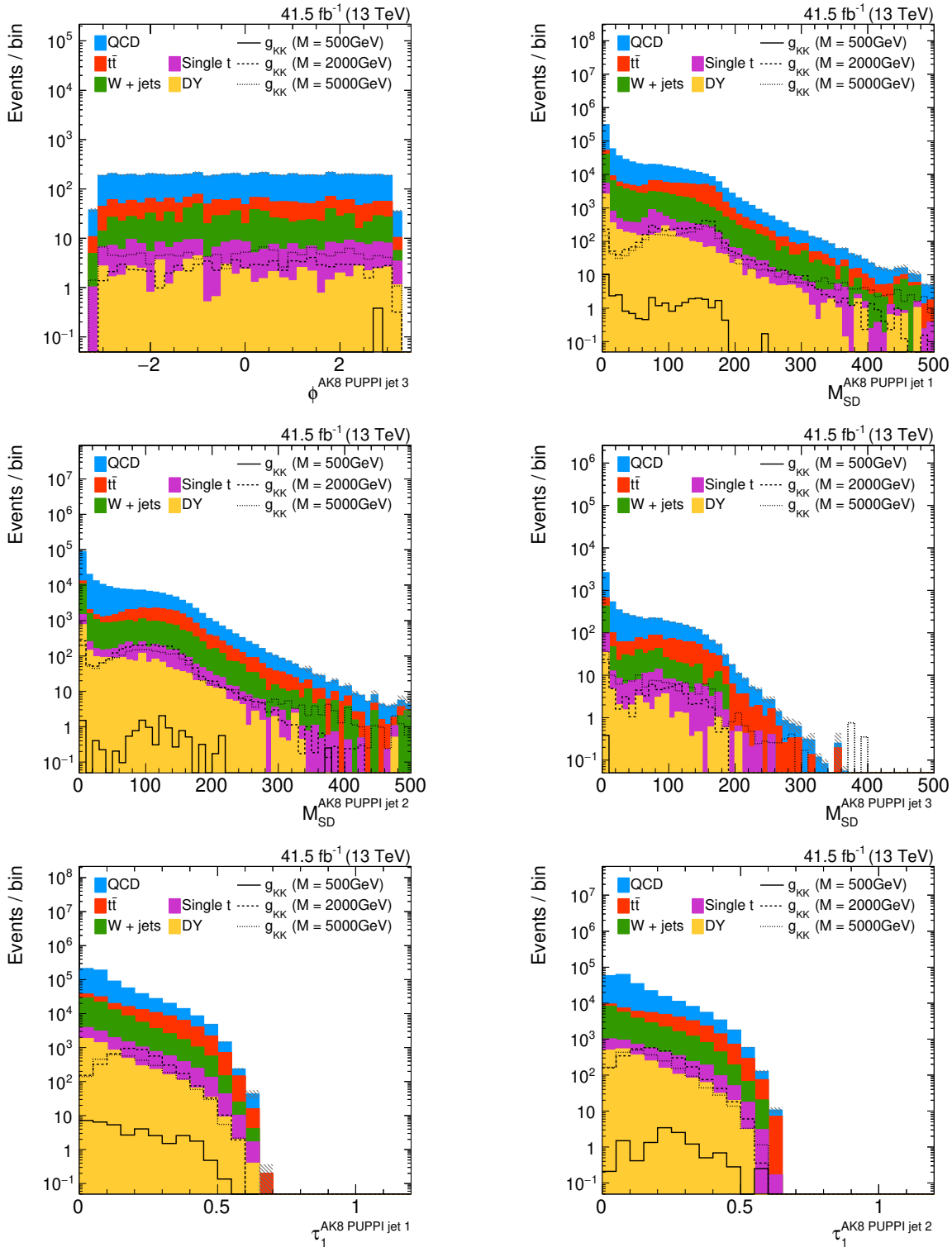

Figure A.6: Distributions of ϕ of the sub-sub-leading AK8 jet (upper left), M_{SD} of the leading (upper right), sub-leading (middle left), and sub-sub-leading (middle right) AK8 jet, and τ_1 of the leading (lower left), and sub-leading (lower right) AK8 jet for events that pass the pre-selection and are used as input to the DNN event classifiers presented in section 8.4.

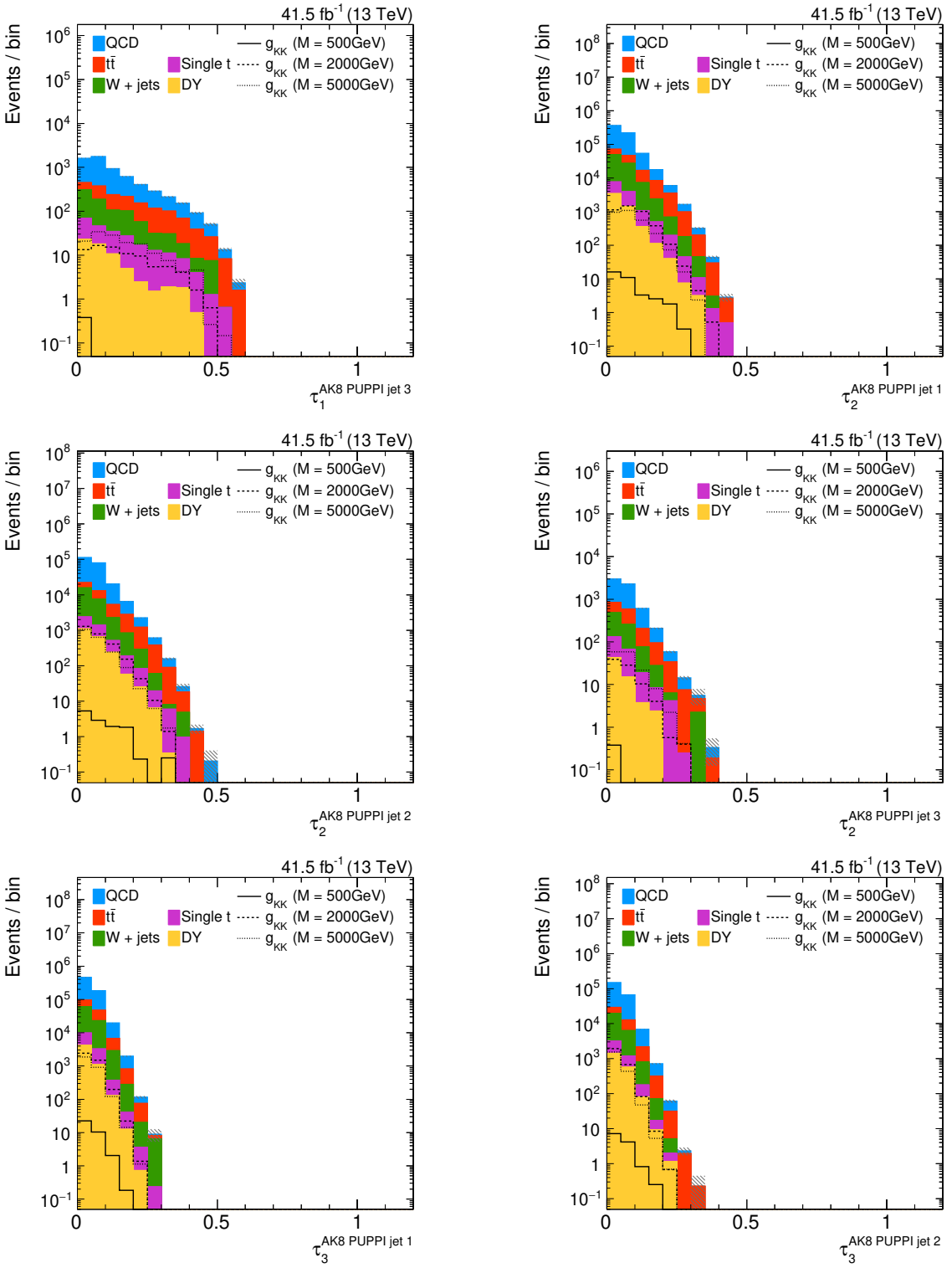

Figure A.7: Distributions of τ_1 of the sub-sub-leading AK8 jet (upper left), τ_2 of the leading (upper right), sub-leading (middle left), and sub-sub-leading (middle right) AK8 jet, and τ_3 of the leading (lower left), and sub-leading (lower right) AK8 jet for events that pass the pre-selection and are used as input to the DNN event classifiers presented in section 8.4.

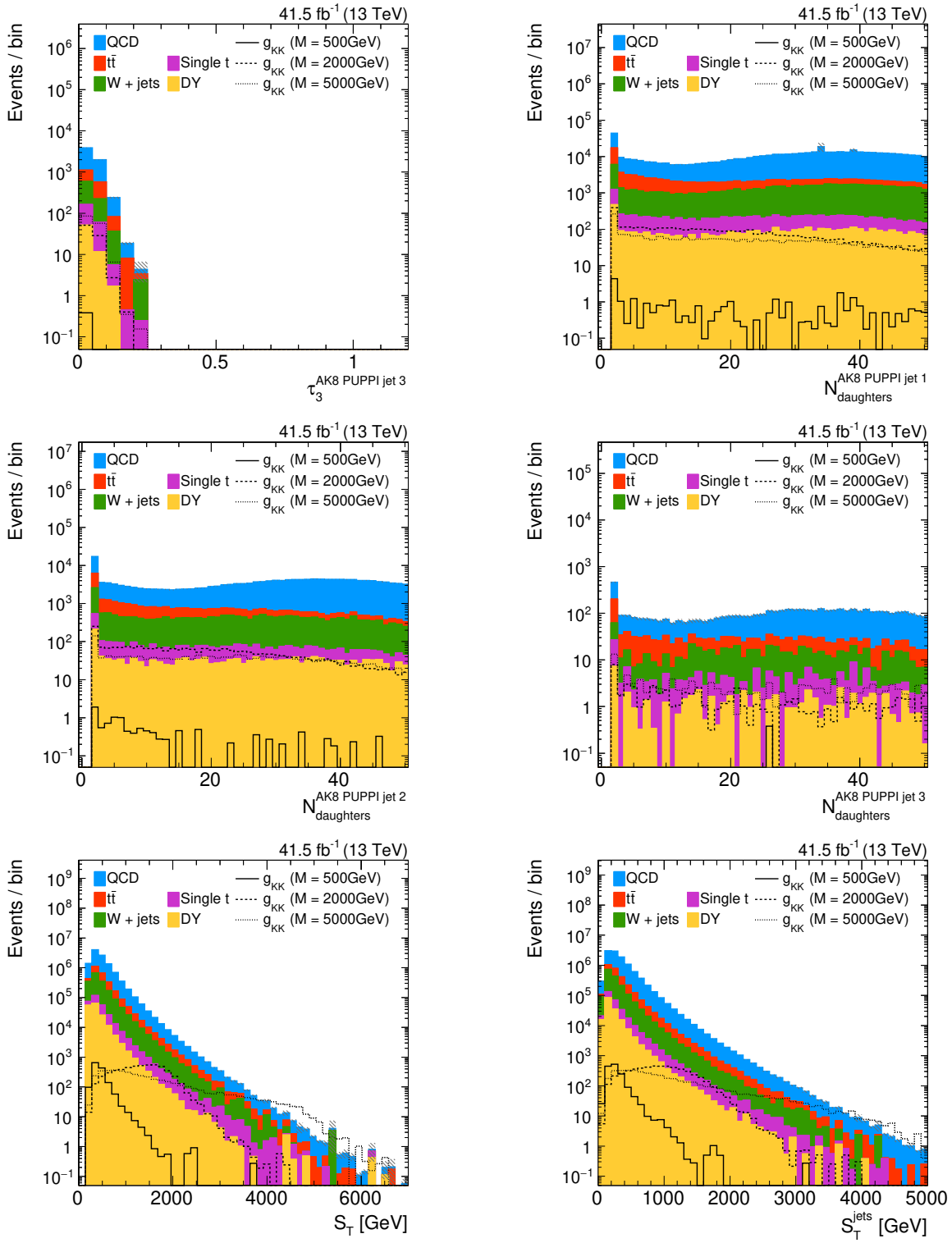

Figure A.8: Distributions of τ_3 of the sub-sub-leading AK8 jet (upper left), the number of constituents of the leading (upper right), sub-leading (middle left), and sub-sub-leading (middle right) AK8 jet, S_{T} (lower left), and $S_{\mathrm{T}}^{\mathrm{had}}$ (lower right) for events that pass the pre-selection and are used as input to the DNN event classifiers presented in section 8.4.

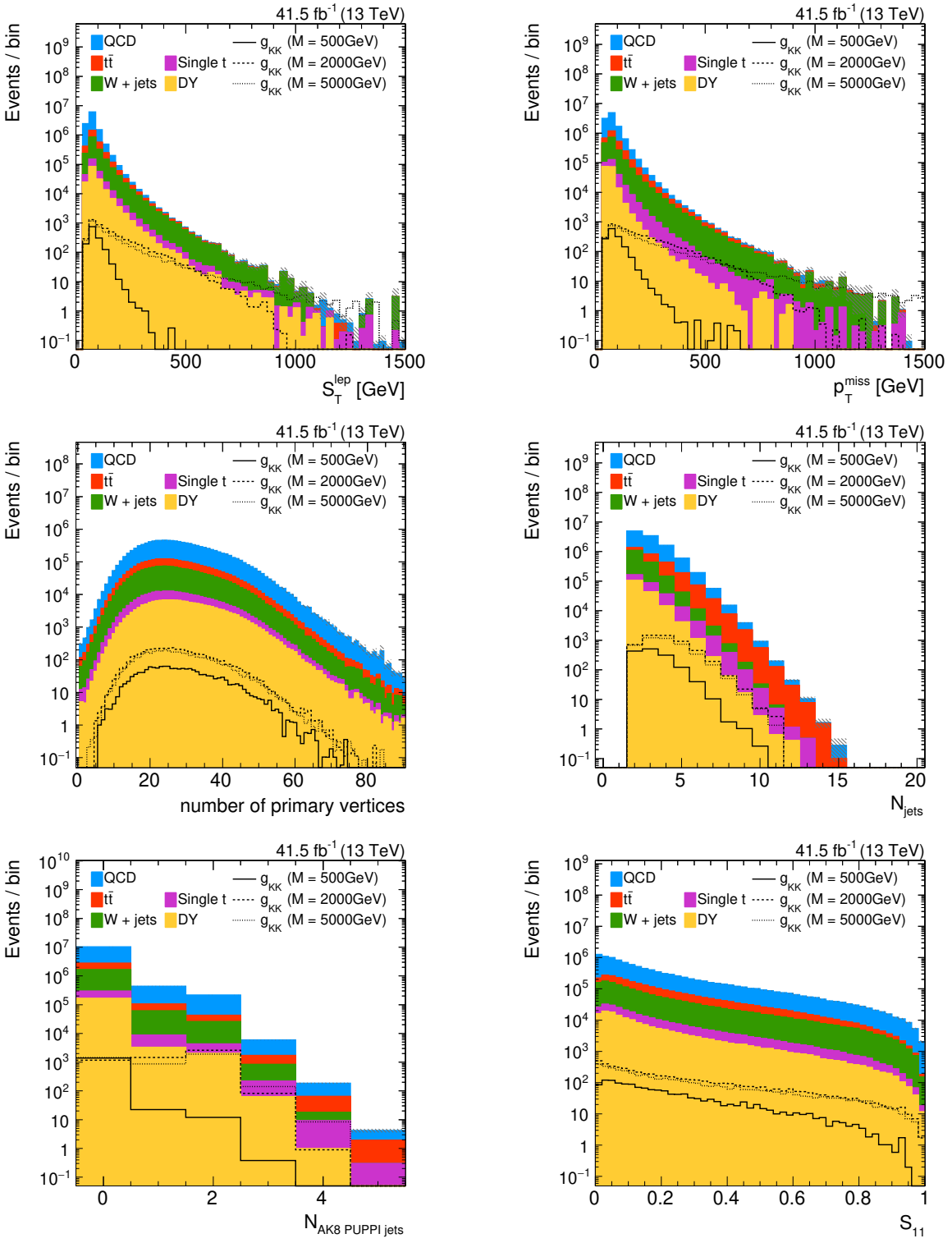

Figure A.9: Distributions of $S_{\mathrm{T}}^{\mathrm{lep}}$ (upper left), $p_{\mathrm{T}}^{\mathrm{miss}}$ (upper right), the number of reconstructed PVs (middle left), AK4 jets (middle right), and AK8 jets (lower left), and S_{11} (lower right) for events that pass the pre-selection and are used as input to the DNN event classifiers presented in section 8.4.

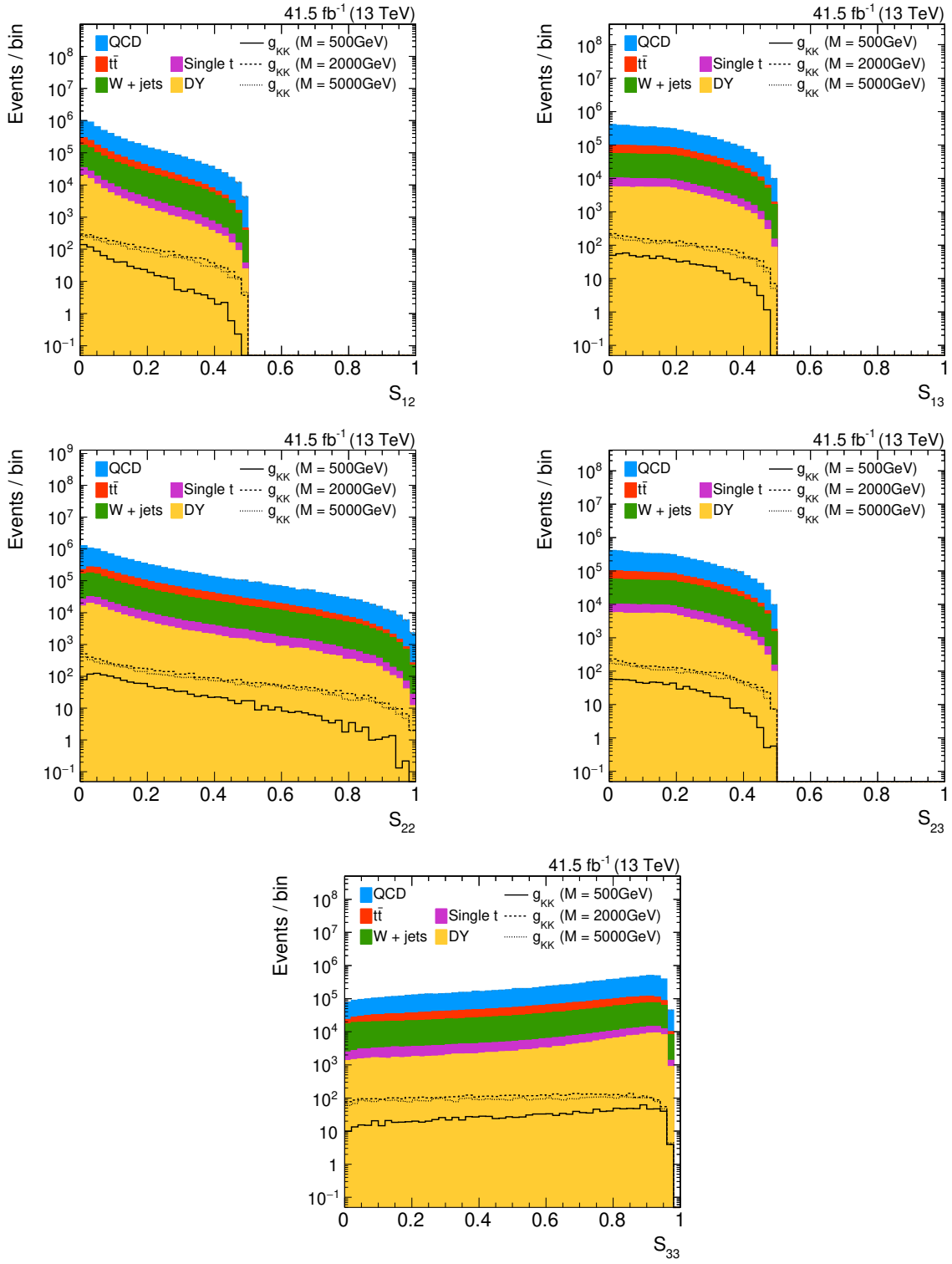

Figure A.10: Distributions of S_{12} (upper left), S_{13} (upper right), S_{22} (middle left), S_{23} (middle right), and S_{33} (lower) for events that pass the pre-selection and are used as input to the DNN event classifiers presented in section 8.4.

Bibliography

[1] M. Thomson, "Modern Particle Physics". Cambridge University Press, 2013.

[2] D. J. Griffiths, "Introduction to Elementary Particles". WILEY-VCH, 1987.

[3] M. E. Peskin and D. V. Schroeder, "An Introduction to quantum field theory". Westview Press, 1995.

[4] Particle Data Group Collaboration, "Review of Particle Physics", *Phys. Rev. D* **98** (2018) p. 030001.

[5] C. S. Wu, E. Ambler, R. W. Hayward et al., "Experimental Test of Parity Conservation in Beta Decay", *Phys. Rev.* **105** (1957) p. 1413.

[6] S. L. Glashow, "Partial Symmetries of Weak Interactions", *Nucl. Phys.* **22** (1961) p. 579.

[7] A. Salam and J. C. Ward, "Electromagnetic and weak interactions", *Phys. Lett.* **13** (1964) p. 168.

[8] S. Weinberg, "A Model of Leptons", *Phys. Rev. Lett.* **19** (1967) p. 1264.

[9] P. W. Higgs, "Broken symmetries, massless particles and gauge fields", *Phys. Lett.* **12** (1964) p. 132.

[10] P. W. Higgs, "Broken Symmetries and the Masses of Gauge Bosons", *Phys. Rev. Lett.* **13** (1964) p. 508.

[11] F. Englert and R. Brout, "Broken Symmetry and the Mass of Gauge Vector Mesons", *Phys. Rev. Lett.* **13** (1964) p. 321.

[12] L. Evans and P. Bryant, "LHC Machine", *JINST* **3** (2008) p. S08001.

[13] G. Altarelli and G. Parisi, "Asymptotic Freedom in Parton Language", *Nucl. Phys. B* **126** (1977) p. 298.

[14] Y. L. Dokshitzer, "Calculation of the Structure Functions for Deep Inelastic Scattering and e+ e- Annihilation by Perturbation Theory in Quantum Chromodynamics.", *Sov. Phys. JETP* **46** (1977) p. 641. [Zh. Eksp. Teor. Fiz. 73, 1216 (1977)].

[15] V. N. Gribov and L. N. Lipatov, "Deep inelastic e p scattering in perturbation theory", *Sov. J. Nucl. Phys.* **15** (1972) p. 438. [Yad. Fiz. 15, 781 (1972)].

[16] NNPDF Collaboration, "Parton distributions for the LHC Run II", *JHEP* **04** (2015) p. 040, arXiv:1410.8849.

[17] J. C. Collins and D. E. Soper, "The Theorems of Perturbative QCD", *Ann. Rev. Nucl. Part. Sci.* **37** (1987) p. 383.

[18] J. C. Collins, D. E. Soper, and G. F. Sterman, "Factorization of Hard Processes in QCD", *Adv. Ser. Direct. High Energy Phys.* **5** (1989) p. 1, arXiv:hep-ph/0409313.

[19] UA1 Collaboration, "Experimental Observation of Isolated Large Transverse Energy Electrons with Associated Missing Energy at $\sqrt{s} = 540\,\text{GeV}$", *Phys. Lett. B* **122** (1983) p. 103.

[20] UA2 Collaboration, "Observation of Single Isolated Electrons of High Transverse Momentum in Events with Missing Transverse Energy at the CERN anti-p p Collider", *Phys. Lett. B* **122** (1983) p. 476.

[21] UA2 Collaboration, "Evidence for $Z^0 \to e^+e^-$ at the CERN anti-p p Collider", *Phys. Lett. B* **129** (1983) p. 130.

[22] UA1 Collaboration, "Experimental Observation of Lepton Pairs of Invariant Mass Around $95\,\text{GeV/c}^2$ at the CERN SPS Collider", *Phys. Lett. B* **126** (1983) p. 398.

[23] CDF Collaboration, "Observation of top quark production in $\bar{p}p$ collisions", *Phys. Rev. Lett.* **74** (1995) p. 2626, arXiv:hep-ex/9503002.

[24] D0 Collaboration, "Observation of the top quark", *Phys. Rev. Lett.* **74** (1995) p. 2632, arXiv:hep-ex/9503003.

[25] ATLAS Collaboration, "Observation of a new particle in the search for the Standard Model Higgs boson with the ATLAS detector at the LHC", *Phys. Lett. B* **716** (2012) p. 1, arXiv:1207.7214.

[26] CMS Collaboration, "Observation of a new boson at a mass of 125 GeV with the CMS experiment at the LHC", *Phys. Lett. B* **716** (2012) p. 30, arXiv:1207.7235.

[27] CMS Collaboration, "Standard Model production cross sections measured by the CMS Collaboration". https://twiki.cern.ch/twiki/bin/view/CMSPublic/PhysicsResultsCombined, last accessed: 21.06.2019.

[28] P. Nason, "A New method for combining NLO QCD with shower Monte Carlo algorithms", *JHEP* **11** (2004) p. 040, arXiv:hep-ph/0409146.

[29] S. Frixione, P. Nason, and C. Oleari, "Matching NLO QCD computations with Parton Shower simulations: the POWHEG method", *JHEP* **11** (2007) p. 070, arXiv:0709.2092.

[30] S. Alioli, P. Nason, C. Oleari et al., "A general framework for implementing NLO calculations in shower Monte Carlo programs: the POWHEG BOX", *JHEP* **06** (2010) p. 043, arXiv:1002.2581.

[31] J. Alwall, R. Frederix, S. Frixione et al., "The automated computation of tree-level and next-to-leading order differential cross sections, and their matching to parton shower simulations", *JHEP* **07** (2014) p. 079, arXiv:1405.0301.

[32] M. Bahr et al., "Herwig++ Physics and Manual", *Eur. Phys. J. C* **58** (2008) p. 639, arXiv:0803.0883.

[33] T. Sjöstrand, S. Mrenna, and P. Z. Skands, "PYTHIA 6.4 Physics and Manual", *JHEP* **05** (2006) p. 026, arXiv:hep-ph/0603175.

[34] T. Sjöstrand, S. Ask, J. R. Christiansen et al., "An Introduction to PYTHIA 8.2", *Comput. Phys. Commun.* **191** (2015) p. 159, arXiv:1410.3012.

[35] R. Frederix and S. Frixione, "Merging meets matching in MC@NLO", *JHEP* **12** (2012) p. 061, arXiv:1209.6215.

[36] J. Alwall et al., "Comparative study of various algorithms for the merging of parton showers and matrix elements in hadronic collisions", *Eur. Phys. J. C* **53** (2008) p. 473, arXiv:0706.2569.

[37] GEANT4 Collaboration, "GEANT4—A simulation toolkit", *Nucl. Instrum. Meth. A* **506** (2003) p. 250.

[38] J. Allison et al., "GEANT4 developments and applications", *IEEE Trans. Nucl. Sci.* **53** (2006) p. 270.

[39] Muon g-2 Collaboration, "Final Report of the Muon E821 Anomalous Magnetic Moment Measurement at BNL", *Phys. Rev. D* **73** (2006) p. 072003, arXiv:hep-ex/0602035.

[40] M. Davier, A. Hoecker, B. Malaescu et al., "Reevaluation of the hadronic vacuum polarisation contributions to the Standard Model predictions of the muon $g-2$ and $\alpha(m_Z^2)$ using newest hadronic cross-section data", *Eur. Phys. J. C* **77** (2017) p. 827, arXiv:1706.09436.

[41] S. P. Martin, "A Supersymmetry primer", arXiv:hep-ph/9709356. [Adv. Ser. Direct. High Energy Phys.18, 1 (1998)].

[42] H. Harari, "A Schematic Model of Quarks and Leptons", *Phys. Lett. B* **86** (1979) p. 83.

[43] B. Schrempp and F. Schrempp, "Light Leptoquarks", *Phys. Lett. B* **153** (1985) p. 101.

[44] B. Gripaios, "Composite Leptoquarks at the LHC", *JHEP* **02** (2010) p. 045, arXiv:0910.1789.

[45] S. Dimopoulos and J. Preskill, "Massless Composites With Massive Constituents", *Nucl. Phys. B* **199** (1982) p. 206.

[46] M. J. Dugan, H. Georgi, and D. B. Kaplan, "Anatomy of a Composite Higgs Model", *Nucl. Phys. B* **254** (1985) p. 299.

[47] D. B. Kaplan, H. Georgi, and S. Dimopoulos, "Composite Higgs Scalars", *Phys. Lett. B* **136** (1984) p. 187.

[48] T. Banks, "Constraints on SU(2) x U(1) breaking by vacuum misalignment", *Nucl. Phys. B* **243** (1984) p. 125.

[49] J. C. Pati and A. Salam, "Lepton Number as the Fourth Color", *Phys. Rev. D* **10** (1974) p. 275. [Erratum: Phys. Rev. D 11, 703 (1975)].

[50] H. Georgi and S. L. Glashow, "Unity of All Elementary Particle Forces", *Phys. Rev. Lett.* **32** (1974) p. 438.

[51] H. Fritzsch and P. Minkowski, "Unified Interactions of Leptons and Hadrons", *Annals Phys.* **93** (1975) p. 193.

[52] CMS Collaboration, "Overview of CMS B2G results". `https://twiki.cern.ch/twiki/bin/view/CMSPublic/PhysicsResultsB2G`, last accessed: 02.12.2019.

[53] D. Dicus, A. Stange, and S. Willenbrock, "Higgs decay to top quarks at hadron colliders", *Phys. Lett. B* **333** (1994) p. 126, `arXiv:hep-ph/9404359`.

[54] P. H. Frampton and S. L. Glashow, "Chiral Color: An Alternative to the Standard Model", *Phys. Lett. B* **190** (1987) p. 157.

[55] D. Choudhury, R. M. Godbole, R. K. Singh et al., "Top production at the Tevatron/LHC and nonstandard, strongly interacting spin one particles", *Phys. Lett. B* **657** (2007) p. 69, `arXiv:0705.1499`.

[56] R. M. Godbole and D. Choudhury, "Nonstandard, strongly interacting spin one $t\bar{t}$ resonances", in *Proceedings, 34th International Conference on High Energy Physics (ICHEP 2008): Philadelphia, Pennsylvania, July 30-August 5, 2008.* 2008. `arXiv:0810.3635`.

[57] J. L. Rosner, "Prominent decay modes of a leptophobic Z'", *Phys. Lett. B* **387** (1996) p. 113, `arXiv:hep-ph/9607207`.

[58] K. R. Lynch, E. H. Simmons, M. Narain et al., "Finding Z' bosons coupled preferentially to the third family at LEP and the Tevatron", *Phys. Rev. D* **63** (2001) p. 035006, `arXiv:hep-ph/0007286`.

[59] M. Carena, A. Daleo, B. A. Dobrescu et al., "Z' gauge bosons at the Tevatron", *Phys. Rev. D* **70** (2004) p. 093009, `arXiv:hep-ph/0408098`.

[60] C. T. Hill, "Topcolor: Top quark condensation in a gauge extension of the standard model", *Phys. Lett. B* **266** (1991) p. 419.

[61] C. T. Hill and S. J. Parke, "Top production: Sensitivity to new physics", *Phys. Rev. D* **49** (1994) p. 4454, `arXiv:hep-ph/9312324`.

[62] C. T. Hill, "Topcolor assisted technicolor", *Phys. Lett. B* **345** (1995) p. 483, arXiv:hep-ph/9411426.

[63] R. M. Harris, C. T. Hill, and S. J. Parke, "Cross-Section for Topcolor Z'_t Decaying to $t\bar{t}$", arXiv:hep-ph/9911288.

[64] L. Randall and R. Sundrum, "A Large mass hierarchy from a small extra dimension", *Phys. Rev. Lett.* **83** (1999) p. 3370, arXiv:hep-ph/9905221.

[65] L. Randall and R. Sundrum, "An Alternative to compactification", *Phys. Rev. Lett.* **83** (1999) p. 4690, arXiv:hep-th/9906064.

[66] K. Agashe, A. Belyaev, T. Krupovnickas et al., "LHC Signals from Warped Extra Dimensions", *Phys. Rev. D* **77** (2008) p. 015003, arXiv:hep-ph/0612015.

[67] M. J. Baker, J. Fuentes-Martín, G. Isidori et al., "High- p_T signatures in vector–leptoquark models", *Eur. Phys. J. C* **79** (2019) p. 334, arXiv:1901.10480.

[68] W. Buchmüller, R. Rückl, and D. Wyler, "Leptoquarks in Lepton - Quark Collisions", *Phys. Lett. B* **191** (1987) p. 442. [Erratum: Phys. Lett. B 448, 320 (1999)].

[69] I. Doršner, S. Fajfer, A. Greljo et al., "Physics of leptoquarks in precision experiments and at particle colliders", *Phys. Rept.* **641** (2016) p. 1, arXiv:1603.04993.

[70] MEG Collaboration, "Search for the lepton flavour violating decay $\mu^+ \to \mathrm{e}^+\gamma$ with the full dataset of the MEG experiment", *Eur. Phys. J. C* **76** (2016) p. 434, arXiv:1605.05081.

[71] BaBar Collaboration, "Searches for Lepton Flavor Violation in the Decays $\tau^\pm \to e^\pm\gamma$ and $\tau^\pm \to \mu^\pm\gamma$", *Phys. Rev. Lett.* **104** (2010) p. 021802, arXiv:0908.2381.

[72] SINDRUM Collaboration, "Search for the Decay $\mu^+ \to e^+e^+e^-$", *Nucl. Phys. B* **260** (1985) p. 1.

[73] E. Gabrielli, "Model independent constraints on leptoquarks from rare muon and tau lepton processes", *Phys. Rev. D* **62** (2000) p. 055009, arXiv:hep-ph/9911539.

[74] E. Coluccio Leskow, G. DAmbrosio, A. Crivellin et al., "$(g-2)_\mu$, lepton flavor violation, and Z decays with leptoquarks: Correlations and future prospects", *Phys. Rev. D* **95** (2017) p. 055018, arXiv:1612.06858.

[75] B. Diaz, M. Schmaltz, and Y.-M. Zhong, "The leptoquark Hunter's guide: Pair production", *JHEP* **10** (2017) p. 097, arXiv:1706.05033.

[76] D. E. Acosta and S. K. Blessing, "Leptoquark searches at HERA and the Tevatron", *Annual Review of Nuclear and Particle Science* **49** (1999) p. 389, arXiv:https://doi.org/10.1146/annurev.nucl.49.1.389.

[77] M. Krämer, T. Plehn, M. Spira et al., "Pair production of scalar leptoquarks at the CERN LHC", *Phys. Rev. D* **71** (2005) p. 057503, arXiv:hep-ph/0411038.

[78] I. Doršner and A. Greljo, "Leptoquark toolbox for precision collider studies", *JHEP* **05** (2018) p. 126, arXiv:1801.07641.

[79] ATLAS Collaboration, "Searches for scalar leptoquarks and differential cross-section measurements in dilepton-dijet events in proton-proton collisions at a centre-of-mass energy of $\sqrt{s} = 13$ TeV with the ATLAS experiment", *Eur. Phys. J. C* **79** (2019) p. 733, arXiv:1902.00377.

[80] CMS Collaboration, "Search for pair production of first-generation scalar leptoquarks at $\sqrt{s} = 13$ TeV", *Phys. Rev. D* **99** (2019) p. 052002, arXiv:1811.01197.

[81] CMS Collaboration, "Search for pair production of second-generation leptoquarks at $\sqrt{s} = 13$ TeV", *Phys. Rev. D* **99** (2019) p. 032014, arXiv:1808.05082.

[82] CMS Collaboration, "Constraints on models of scalar and vector leptoquarks decaying to a quark and a neutrino at $\sqrt{s} = 13$ TeV", *Phys. Rev. D* **98** (2018) p. 032005, arXiv:1805.10228.

[83] CMS Collaboration, "Search for leptoquarks coupled to third-generation quarks in proton-proton collisions at $\sqrt{s} = 13$ TeV", *Phys. Rev. Lett.* **121** (2018) p. 241802, arXiv:1809.05558.

[84] ATLAS Collaboration, "Searches for third-generation scalar leptoquarks in $\sqrt{s}$ = 13 TeV pp collisions with the ATLAS detector", *JHEP* **06** (2019) p. 144, arXiv:1902.08103.

[85] CMS Collaboration, "Search for third-generation scalar leptoquarks decaying to a top quark and a τ lepton at $\sqrt{s} = 13$ TeV", *Eur. Phys. J. C* **78** (2018) p. 707, arXiv:1803.02864.

[86] CMS Collaboration, "Search for heavy neutrinos and third-generation leptoquarks in hadronic states of two τ leptons and two jets in proton-proton collisions at $\sqrt{s} = 13$ TeV", *JHEP* **03** (2019) p. 170, arXiv:1811.00806.

[87] CMS Collaboration, "Search for a singly produced third-generation scalar leptoquark decaying to a τ lepton and a bottom quark in proton-proton collisions at $\sqrt{s} = 13$ TeV", *JHEP* **07** (2018) p. 115, arXiv:1806.03472.

[88] HFLAV Collaboration, "Average of $R(\mathrm{D})$ and $R(\mathrm{D}^\star)$ for Spring 2019". https://hflav-eos.web.cern.ch/hflav-eos/semi/spring19/html/RDsDsstar/RDRDs.html, accessed: 25.06.2019.

[89] BaBar Collaboration, "Evidence for an excess of $\bar{B} \to D^{(*)}\tau^-\bar{\nu}_\tau$ decays", *Phys. Rev. Lett.* **109** (2012) p. 101802, arXiv:1205.5442.

[90] BaBar Collaboration, "Measurement of an Excess of $\bar{B} \to D^{(*)}\tau^-\bar{\nu}_\tau$ Decays and Implications for Charged Higgs Bosons", *Phys. Rev. D* **88** (2013) p. 072012, arXiv:1303.0571.

[91] Belle Collaboration, "Measurement of the branching ratio of $\bar{B} \to D^{(*)}\tau^-\bar{\nu}_\tau$ relative to $\bar{B} \to D^{(*)}\ell^-\bar{\nu}_\ell$ decays with hadronic tagging at Belle", *Phys. Rev. D* **92** (2015) p. 072014, arXiv:1507.03233.

[92] Belle Collaboration, "Measurement of the τ lepton polarization and $R(D^*)$ in the decay $\bar{B} \to D^*\tau^-\bar{\nu}_\tau$", *Phys. Rev. Lett.* **118** (2017) p. 211801, arXiv:1612.00529.

[93] Belle Collaboration, "Measurement of the τ lepton polarization and $R(D^*)$ in the decay $\bar{B} \to D^*\tau^-\bar{\nu}_\tau$ with one-prong hadronic τ decays at Belle", *Phys. Rev. D* **97** (2018) p. 012004, arXiv:1709.00129.

[94] Belle Collaboration, "Measurement of $\mathcal{R}(D)$ and $\mathcal{R}(D^*)$ with a semileptonic tagging method", *Phys. Rev. Lett.* **124** (2020) p. 161803, arXiv:1910.05864.

[95] LHCb Collaboration, "Measurement of the ratio of branching fractions $\mathcal{B}(\bar{B}^0 \to D^{*+}\tau^-\bar{\nu}_\tau)/\mathcal{B}(\bar{B}^0 \to D^{*+}\mu^-\bar{\nu}_\mu)$", *Phys. Rev. Lett.* **115** (2015) p. 111803, arXiv:1506.08614. [Erratum: Phys. Rev. Lett. 115, 159901 (2015)].

[96] LHCb Collaboration, "Measurement of the ratio of the $B^0 \to D^{*-}\tau^+\nu_\tau$ and $B^0 \to D^{*-}\mu^+\nu_\mu$ branching fractions using three-prong τ-lepton decays", *Phys. Rev. Lett.* **120** (2018) p. 171802, arXiv:1708.08856.

[97] LHCb Collaboration, "Test of Lepton Flavor Universality by the measurement of the $B^0 \to D^{*-}\tau^+\nu_\tau$ branching fraction using three-prong τ decays", *Phys. Rev. D* **97** (2018) p. 072013, arXiv:1711.02505.

[98] HFLAV Collaboration, "Averages of b-hadron, c-hadron, and τ-lepton properties as of summer 2016", *Eur. Phys. J. C* **77** (2017) p. 895, arXiv:1612.07233.

[99] M. Bordone, G. Isidori, and A. Pattori, "On the Standard Model predictions for R_K and R_{K^*}", *Eur. Phys. J. C* **76** (2016) p. 440, arXiv:1605.07633.

[100] LHCb Collaboration, "Search for lepton-universality violation in $B^+ \to K^+\ell^+\ell^-$ decays", *Phys. Rev. Lett.* **122** (2019) p. 191801, arXiv:1903.09252.

[101] LHCb Collaboration, "Test of lepton universality with $B^0 \to K^{*0}\ell^+\ell^-$ decays", *JHEP* **08** (2017) p. 055, arXiv:1705.05802.

[102] Belle Collaboration, "Test of lepton flavor universality in $B \to K^*\ell^+\ell^-$ decays at Belle", arXiv:1904.02440.

[103] Belle Collaboration, "Test of lepton flavor universality in $B \to K\ell^+\ell^-$ decays", arXiv:1908.01848.

[104] M. Tanaka and R. Watanabe, "New physics in the weak interaction of $\bar{B} \to D^{(*)}\tau\bar{\nu}$", *Phys. Rev. D* **87** (2013) p. 034028, arXiv:1212.1878.

[105] Y. Sakaki, M. Tanaka, A. Tayduganov et al., "Testing leptoquark models in $\bar{B} \to D^{(*)}\tau\bar{\nu}$", *Phys. Rev. D* **88** (2013) p. 094012, arXiv:1309.0301.

[106] I. Doršner, S. Fajfer, N. Košnik et al., "Minimally flavored colored scalar in $\bar{B} \to D^{(*)}\tau\bar{\nu}$ and the mass matrices constraints", *JHEP* **11** (2013) p. 084, arXiv:1306.6493.

[107] B. Dumont, K. Nishiwaki, and R. Watanabe, "LHC constraints and prospects for S_1 scalar leptoquark explaining the $\bar{B} \to D^{(*)}\tau\bar{\nu}$ anomaly", *Phys. Rev. D* **94** (2016) p. 034001, arXiv:1603.05248.

[108] I. Doršner, S. Fajfer, D. A. Faroughy et al., "The role of the S_3 GUT leptoquark in flavor universality and collider searches", *JHEP* **10** (2017) p. 188, arXiv:1706.07779.

[109] D. Bečirević, I. Doršner, S. Fajfer et al., "Scalar leptoquarks from grand unified theories to accommodate the B-physics anomalies", *Phys. Rev. D* **98** (2018) p. 055003, arXiv:1806.05689.

[110] A. Crivellin, D. Müller, and T. Ota, "Simultaneous explanation of $R(D^{(*)})$ and $b \to s\mu^+\mu^-$: the last scalar leptoquarks standing", *JHEP* **09** (2017) p. 040, arXiv:1703.09226.

[111] B. Gripaios, M. Nardecchia, and S. A. Renner, "Composite leptoquarks and anomalies in B-meson decays", *JHEP* **05** (2015) p. 006, arXiv:1412.1791.

[112] M. Bauer and M. Neubert, "Minimal Leptoquark Explanation for the $R_{D^{(*)}}$, R_K , and $(g-2)_\mu$ Anomalies", *Phys. Rev. Lett.* **116** (2016) p. 141802, arXiv:1511.01900.

[113] D. Bečirević and O. Sumensari, "A leptoquark model to accommodate $R_K^{\rm exp} < R_K^{\rm SM}$ and $R_{K^*}^{\rm exp} < R_{K^*}^{\rm SM}$", *JHEP* **08** (2017) p. 104, arXiv:1704.05835.

[114] G. Hiller and I. Nišandžić, "R_K and R_{K^*} beyond the standard model", *Phys. Rev. D* **96** (2017) p. 035003, arXiv:1704.05444.

[115] G. Hiller, D. Loose, and I. Nišandžić, "Flavorful leptoquarks at hadron colliders", *Phys. Rev. D* **97** (2018) p. 075004, arXiv:1801.09399.

[116] L. Di Luzio, A. Greljo, and M. Nardecchia, "Gauge leptoquark as the origin of B-physics anomalies", *Phys. Rev. D* **96** (2017) p. 115011, arXiv:1708.08450.

[117] L. Di Luzio, J. Fuentes-Martin, A. Greljo et al., "Maximal Flavour Violation: a Cabibbo mechanism for leptoquarks", *JHEP* **11** (2018) p. 081, arXiv:1808.00942.

[118] L. Calibbi, A. Crivellin, and T. Li, "Model of vector leptoquarks in view of the B-physics anomalies", *Phys. Rev. D* **98** (2018) p. 115002, arXiv:1709.00692.

[119] M. Bordone, C. Cornella, J. Fuentes-Martin et al., "A three-site gauge model for flavor hierarchies and flavor anomalies", *Phys. Lett. B* **779** (2018) p. 317, arXiv:1712.01368.

[120] R. Barbieri and A. Tesi, "B-decay anomalies in Pati-Salam SU(4)", *Eur. Phys. J. C* **78** (2018) p. 193, arXiv:1712.06844.

[121] D. Buttazzo, A. Greljo, G. Isidori et al., "B-physics anomalies: a guide to combined explanations", *JHEP* **11** (2017) p. 044, arXiv:1706.07808.

[122] D. Marzocca, "Addressing the B-physics anomalies in a fundamental Composite Higgs Model", *JHEP* **07** (2018) p. 121, arXiv:1803.10972.

[123] A. Angelescu, D. Becirevic, D. A. Faroughy et al., "Closing the window on single leptoquark solutions to the B-physics anomalies", *JHEP* **10** (2018) p. 183, arXiv:1808.08179.

[124] O. S. Brüing, P. Collier, P. Lebrun et al., "LHC Design Report". CERN Yellow Reports: Monographs. CERN, Geneva, 2004.

[125] E. Mobs, "The CERN accelerator complex. Complexe des accélérateurs du CERN",. General Photo.

[126] CMS Collaboration, "CMS luminosity – public results". https://twiki.cern.ch/twiki/bin/view/CMSPublic/LumiPublicResults#Multi_year_plots, last accessed: 26.09.2019.

[127] CMS Collaboration, "CMS Physics: Technical Design Report Volume 1: Detector Performance and Software". Technical Design Report CMS. CERN, Geneva, 2006.

[128] CMS Collaboration, "The CMS Experiment at the CERN LHC", *JINST* **3** (2008) p. S08004.

[129] A. Dominguez, D. Abbaneo, K. Arndt et al., "CMS Technical Design Report for the Pixel Detector Upgrade", Technical Report CERN-LHCC-2012-016, CMS-TDR-11, 2012.

[130] CMS Collaboration, "Particle-flow reconstruction and global event description with the CMS detector", *JINST* **12** (2017) p. P10003, arXiv:1706.04965.

[131] W. Adam, B. Mangano, T. Speer et al., "Track Reconstruction in the CMS tracker", Technical Report CMS-NOTE-2006-041, CERN, Geneva, 2006.

[132] K. Rose, "Deterministic annealing for clustering, compression, classification, regression, and related optimization problems", *Proceedings of the IEEE* **86** (1998) p. 2210.

[133] R. Frühwirth, W. Waltenberger, and P. Vanlaer, "Adaptive Vertex Fitting", Technical Report CMS-NOTE-2007-008, CERN, Geneva, 2007.

[134] M. Cacciari, G. P. Salam, and G. Soyez, "The anti-k_{t} jet clustering algorithm", *JHEP* **04** (2008) p. 063, arXiv:0802.1189.

[135] M. Cacciari, G. P. Salam, and G. Soyez, "FastJet User Manual", *Eur. Phys. J. C* **72** (2012) p. 1896, arXiv:1111.6097.

[136] CMS Collaboration, "Pileup mitigation at CMS in 13 TeV data", Technical Report CMS-PAS-JME-18-001, CERN, Geneva, 2019.

[137] M. Cacciari and G. P. Salam, "Pileup subtraction using jet areas", *Phys. Lett. B* **659** (2008) p. 119, arXiv:0707.1378.

[138] M. Cacciari, G. P. Salam, and G. Soyez, "The Catchment Area of Jets", *JHEP* **04** (2008) p. 005, arXiv:0802.1188.

[139] CMS Collaboration, "Jet energy scale and resolution in the CMS experiment in pp collisions at 8 TeV", *JINST* **12** (2017) p. P02014, arXiv:1607.03663.

[140] CMS Collaboration, "Jet algorithms performance in 13 TeV data", Technical Report CMS-PAS-JME-16-003, CERN, Geneva, 2017.

[141] D. Bertolini, P. Harris, M. Low et al., "Pileup Per Particle Identification", *JHEP* **10** (2014) p. 059, arXiv:1407.6013.

[142] CMS Collaboration, "Performance of Electron Reconstruction and Selection with the CMS Detector in Proton-Proton Collisions at $\sqrt{s} = 8$ TeV", *JINST* **10** (2015) p. P06005, arXiv:1502.02701.

[143] W. Adam, R. Frühwirth, A. Strandlie et al., "Reconstruction of Electrons with the Gaussian-Sum Filter in the CMS Tracker at the LHC", Technical Report CMS-NOTE-2005-001, CERN, Geneva, 2005.

[144] CMS Collaboration, "Performance of the CMS muon detector and muon reconstruction with proton-proton collisions at $\sqrt{s} = 13$ TeV", *JINST* **13** (2018) p. P06015, arXiv:1804.04528.

[145] S. Catani, Y. L. Dokshitzer, M. H. Seymour et al., "Longitudinally invariant K_t clustering algorithms for hadron hadron collisions", *Nucl. Phys. B* **406** (1993) p. 187.

[146] S. D. Ellis and D. E. Soper, "Successive combination jet algorithm for hadron collisions", *Phys. Rev. D* **48** (1993) p. 3160, arXiv:hep-ph/9305266.

[147] Y. L. Dokshitzer, G. D. Leder, S. Moretti et al., "Better jet clustering algorithms", *JHEP* **08** (1997) p. 001, arXiv:hep-ph/9707323.

[148] CMS Collaboration, "Identification of heavy-flavour jets with the CMS detector in pp collisions at 13 TeV", *JINST* **13** (2018) p. P05011, arXiv:1712.07158.

[149] M. Dasgupta, A. Fregoso, S. Marzani et al., "Towards an understanding of jet substructure", *JHEP* **09** (2013) p. 029, arXiv:1307.0007.

[150] A. J. Larkoski, S. Marzani, G. Soyez et al., "Soft Drop", *JHEP* **05** (2014) p. 146, arXiv:1402.2657.

[151] CMS Collaboration, "Machine learning-based identification of highly Lorentz-boosted hadronically decaying particles at the CMS experiment", Technical Report CMS-PAS-JME-18-002, CERN, Geneva, 2019.

[152] J. Thaler and K. Van Tilburg, "Identifying Boosted Objects with N-subjettiness", *JHEP* **03** (2011) p. 015, arXiv:1011.2268.

[153] CMS Collaboration, "Determination of Jet Energy Calibration and Transverse Momentum Resolution in CMS", *JINST* **6** (2011) p. P11002, arXiv:1107.4277.

[154] CMS Collaboration, "Jet energy scale and resolution performance with 13 TeV data collected by CMS in 2016", Technical Report CMS-DP-2018-028, 2018.

[155] CMS Collaboration, "Projection of searches for pair production of scalar leptoquarks decaying to a top quark and a charged lepton at the HL-LHC", Technical Report CMS-PAS-FTR-18-008, CERN, Geneva, 2018.

[156] X. Cid Vidal et al., "Report from Working Group 3", *CERN Yellow Rep. Monogr.* **7** (2019) p. 585, arXiv:1812.07831.

[157] A. Cerri et al., "Report from Working Group 4", *CERN Yellow Rep. Monogr.* **7** (2019) p. 867, arXiv:1812.07638.

[158] S. Frixione, P. Nason, and G. Ridolfi, "A Positive-weight next-to-leading-order Monte Carlo for heavy flavour hadroproduction", *JHEP* **09** (2007) p. 126, arXiv:0707.3088.

[159] S. Alioli, P. Nason, C. Oleari et al., "NLO single-top production matched with shower in POWHEG: s- and t-channel contributions", *JHEP* **09** (2009) p. 111, arXiv:0907.4076. [Erratum: JHEP 02, 011 (2010)].

[160] E. Re, "Single-top Wt-channel production matched with parton showers using the POWHEG method", *Eur. Phys. J. C* **71** (2011) p. 1547, arXiv:1009.2450.

[161] T. Melia, P. Nason, R. Rontsch et al., "W^+W^-, WZ and ZZ production in the POWHEG BOX", *JHEP* **11** (2011) p. 078, arXiv:1107.5051.

[162] P. Nason and G. Zanderighi, "W^+W^- , WZ and ZZ production in the POWHEG-BOX-V2", *Eur. Phys. J. C* **74** (2014) p. 2702, arXiv:1311.1365.

[163] P. Skands, S. Carrazza, and J. Rojo, "Tuning PYTHIA 8.1: the Monash 2013 Tune", *Eur. Phys. J. C* **74** (2014) p. 3024, arXiv:1404.5630.

[164] CMS Collaboration, "Event generator tunes obtained from underlying event and multiparton scattering measurements", *Eur. Phys. J. C* **76** (2016) p. 155, arXiv:1512.00815.

[165] CMS Collaboration, "Investigations of the impact of the parton shower tuning in Pythia 8 in the modelling of $t\bar{t}$ at $\sqrt{s} = 8$ and 13 TeV", Technical Report CMS-PAS-TOP-16-021, CERN, Geneva, 2016.

[166] CMS Collaboration, "Measurement of the inelastic proton-proton cross section at $\sqrt{s} = 13$ TeV", *JHEP* **07** (2018) p. 161, arXiv:1802.02613.

[167] J. Ott, "Theta—A framework for template-based modeling and inference", 2010.

[168] CMS Collaboration, "CMS Luminosity Measurements for the 2016 Data Taking Period", Technical Report CMS-PAS-LUM-17-001, CERN, Geneva, 2017.

[169] CMS Collaboration, "Measurement of the $t\bar{t}$ production cross section using events in the eμ final state in pp collisions at $\sqrt{s} = 13$ TeV", *Eur. Phys. J. C* **77** (2017) p. 172, arXiv:1611.04040.

[170] CMS Collaboration, "Measurement of inclusive W and Z boson production cross sections in pp collisions at $\sqrt{s} = 8$ TeV", *Phys. Rev. Lett.* **112** (2014) p. 191802, arXiv:1402.0923.

[171] CMS Collaboration, "Cross section measurement of t-channel single top quark production in pp collisions at $\sqrt{s} = 13$ TeV", *Phys. Lett. B* **772** (2017) p. 752, arXiv:1610.00678.

[172] N. Kidonakis, "NNLL threshold resummation for top-pair and single-top production", *Phys. Part. Nucl.* **45** (2014) p. 714, arXiv:1210.7813.

[173] CMS Collaboration, "Observation of the associated production of a single top quark and a W boson in pp collisions at $\sqrt{s}$ =8 TeV", *Phys. Rev. Lett.* **112** (2014) p. 231802, arXiv:1401.2942.

[174] T. Gehrmann, M. Grazzini, S. Kallweit et al., "W^+W^- Production at Hadron Colliders in Next to Next to Leading Order QCD", *Phys. Rev. Lett.* **113** (2014) p. 212001, arXiv:1408.5243.

[175] J. M. Campbell, R. K. Ellis, and C. Williams, "Vector boson pair production at the LHC", *JHEP* **07** (2011) p. 018, arXiv:1105.0020.

[176] CMS Collaboration, "Measurement of the WZ production cross section in pp collisions at $\sqrt{(s)} = 13$ TeV", *Phys. Lett. B* **766** (2017) p. 268, arXiv:1607.06943.

[177] CMS Collaboration, "Measurement of the cross section for top quark pair production in association with a W or Z boson in proton-proton collisions at $\sqrt{s} = 13$ TeV", *JHEP* **08** (2018) p. 011, arXiv:1711.02547.

[178] J. Butterworth et al., "PDF4LHC recommendations for LHC Run II", *J. Phys. G* **43** (2016) p. 023001, arXiv:1510.03865.

[179] "HEPData entry for 'Search for leptoquarks coupled to third-generation quarks in proton-proton collisions at $\sqrt{s} = 13$ TeV'". https://www.hepdata.net/record/ins1694381, last accessed: 03.12.2019.

[180] A. O'Hagan and J. J. Forster, "Kendall's advanced theory of statistics. Vol. 2B: Bayesian Inference". Arnold, London, 2004.

[181] G. Cowan, "Statistics", Ch. 39 in Particle Data Group, "Review of particle physics", *Chin. Phys. C* **40** (2016) p. 100001.

[182] CMS Collaboration, "Search for supersymmetry in events with at least three electrons or muons, jets, and missing transverse momentum in proton-proton collisions at $\sqrt{s} = 13$ TeV", *JHEP* **02** (2018) p. 067, arXiv:1710.09154.

[183] G. Apollinari, I. Béjar Alonso, O. Brüning et al., "High-Luminosity Large Hadron Collider (HL-LHC): Preliminary Design Report". CERN Yellow Reports: Monographs. CERN, Geneva, 2015.

[184] D. Contardo, M. Klute, J. Mans et al., "Technical Proposal for the Phase-II Upgrade of the CMS Detector", Technical Report CERN-LHCC-2015-010, CMS-TDR-15-02, 2015.

[185] CMS Collaboration, "The Phase-2 Upgrade of the CMS Tracker", Technical Report CERN-LHCC-2017-009. CMS-TDR-014, CERN, Geneva, 2017.

[186] CMS Collaboration, "The Phase-2 Upgrade of the CMS Barrel Calorimeters Technical Design Report", Technical Report CERN-LHCC-2017-011. CMS-TDR-015, 2017.

[187] CMS Collaboration, "The Phase-2 Upgrade of the CMS Endcap Calorimeter", Technical Report CERN-LHCC-2017-023. CMS-TDR-019, 2017.

[188] CMS Collaboration, "The Phase-2 Upgrade of the CMS Muon Detectors", Technical Report CERN-LHCC-2017-012. CMS-TDR-016, 2017.

[189] CMS Collaboration, "Expected performance of the physics objects with the upgraded CMS detector at the HL-LHC", Technical Report CMS-NOTE-2018-006, CERN, Geneva, 2018.

[190] CDF Collaboration, "Limits on the production of narrow $t\bar{t}$ resonances in $p\bar{p}$ collisions at $\sqrt{s} = 1.96$-TeV", *Phys. Rev. D* **77** (2008) p. 051102, arXiv:0710.5335.

[191] CDF Collaboration, "Search for resonant $t\bar{t}$ production in $p\bar{p}$ collisions at $\sqrt{s} =$ 1.96-TeV", *Phys. Rev. Lett.* **100** (2008) p. 231801, arXiv:0709.0705.

[192] CDF Collaboration, "A Search for resonant production of $t\bar{t}$ pairs in 4.8 fb^{-1} of integrated luminosity of $p\bar{p}$ collisions at $\sqrt{s} = 1.96$ TeV", *Phys. Rev. D* **84** (2011) p. 072004, arXiv:1107.5063.

[193] D0 Collaboration, "Search for a Narrow $t\bar{t}$ Resonance in $p\bar{p}$ Collisions at $\sqrt{s} = 1.96$ TeV", *Phys. Rev. D* **85** (2012) p. 051101, arXiv:1111.1271.

[194] CDF Collaboration, "Search for resonant production of $t\bar{t}$ decaying to jets in $p\bar{p}$ collisions at $\sqrt{s} = 1.96$ TeV", *Phys. Rev. D* **84** (2011) p. 072003, arXiv:1108.4755.

[195] D0 Collaboration, "Search for $t\bar{t}$ resonances in the lepton plus jets final state in $p\bar{p}$ collisions at $\sqrt{s} = 1.96$ TeV", *Phys. Lett. B* **668** (2008) p. 98, arXiv:0804.3664.

[196] CMS Collaboration, "Search for Anomalous $t\bar{t}$ Production in the Highly-Boosted All-Hadronic Final State", *JHEP* **09** (2012) p. 029, arXiv:1204.2488. [Erratum: JHEP 03, 132 (2014)].

[197] ATLAS Collaboration, "A search for $t\bar{t}$ resonances in lepton+jets events with highly boosted top quarks collected in pp collisions at $\sqrt{s} = 7$ TeV with the ATLAS detector", *JHEP* **09** (2012) p. 041, arXiv:1207.2409.

[198] ATLAS Collaboration, "Search for $t\bar{t}$ resonances in the lepton plus jets final state with ATLAS using 4.7 fb^{-1} of pp collisions at $\sqrt{s} = 7$ TeV", *Phys. Rev. D* **88** (2013) p. 012004, arXiv:1305.2756.

[199] CMS Collaboration, "Search for Z ' Resonances Decaying to $t\bar{t}$ in Dilepton + Jets Final States in pp Collisions at $\sqrt{s} = 7$ TeV", *Phys. Rev. D* **87** (2013) p. 072002, arXiv:1211.3338.

[200] CMS Collaboration, "Searches for new physics using the $t\bar{t}$ invariant mass distribution in pp collisions at $\sqrt{s}$=8 TeV", *Phys. Rev. Lett.* **111** (2013) p. 211804, arXiv:1309.2030. [Erratum: Phys. Rev. Lett. 112, 119903 (2014)].

[201] CMS Collaboration, "Search for $t\bar{t}$ resonances in highly boosted lepton+jets and fully hadronic final states in proton-proton collisions at $\sqrt{s} = 13$ TeV", *JHEP* **07** (2017) p. 001, arXiv:1704.03366.

[202] ATLAS Collaboration, "Search for heavy particles decaying into top-quark pairs using lepton-plus-jets events in proton–proton collisions at $\sqrt{s} = 13$ TeV with the ATLAS detector", *Eur. Phys. J. C* **78** (2018) p. 565, arXiv:1804.10823.

[203] ATLAS Collaboration, "Search for heavy particles decaying into a top-quark pair in the fully hadronic final state in pp collisions at $\sqrt{s} = 13$ TeV with the ATLAS detector", *Phys. Rev. D* **99** (2019) p. 092004, arXiv:1902.10077.

[204] CMS Collaboration, "Search for resonant $t\bar{t}$ production in proton-proton collisions at $\sqrt{s} = 13$ TeV", *JHEP* **04** (2019) p. 031, arXiv:1810.05905.

[205] S. Ask, J. H. Collins, J. R. Forshaw et al., "Identifying the colour of TeV-scale resonances", *JHEP* **01** (2012) p. 018, arXiv:1108.2396.

[206] R. Bonciani, T. Jezo, M. Klasen et al., "Electroweak top-quark pair production at the LHC with Z' bosons to NLO QCD in POWHEG", *JHEP* **02** (2016) p. 141, arXiv:1511.08185.

[207] NNPDF Collaboration, "Parton distributions from high-precision collider data", *Eur. Phys. J. C* **77** (2017) p. 663, arXiv:1706.00428.

[208] CMS Collaboration, "Extraction and validation of a new set of CMS PYTHIA8 tunes from underlying-event measurements", *Eur. Phys. J. C* **80** (2020) p. 4, arXiv:1903.12179.

[209] CMS Collaboration, "CMS luminosity measurement for the 2017 data-taking period at $\sqrt{s} = 13$ TeV", Technical Report CMS-PAS-LUM-17-004, CERN, Geneva, 2018.

[210] I. Goodfellow, Y. Bengio, and A. Courville, "Deep Learning". MIT Press, 2016. http://www.deeplearningbook.org.

[211] J. D. Bjorken and S. J. Brodsky, "Statistical Model for electron-Positron Annihilation Into Hadrons", *Phys. Rev. D* **1** (1970) p. 1416.

[212] G. Hanson et al., "Evidence for Jet Structure in Hadron Production by e+ e- Annihilation", *Phys. Rev. Lett.* **35** (1975) p. 1609.

[213] D. P. Kingma and J. Ba, "Adam: A Method for Stochastic Optimization", in *3rd International Conference on Learning Representations, ICLR 2015, San Diego, CA, USA, May 7-9, 2015, Conference Track Proceedings*, Y. Bengio and Y. LeCun, eds. 2015. arXiv:1412.6980.

[214] N. Srivastava, G. Hinton, A. Krizhevsky et al., "Dropout: A Simple Way to Prevent Neural Networks from Overfitting", *Journal of Machine Learning Research* **15** (2014) p. 1929.

Danksagung

Hier möchte ich mich bei allen bedanken, die mich in den letzten Jahren begleitet und bei meiner Promotion unterstützt haben.

Zuerst danke ich meinem Doktorvater Johannes Haller dafür, dass er es mir ermöglicht hat, meine Promotion in seiner Gruppe durchzuführen. Er hat meine Begeisterung für die Teilchenphysik geweckt und im Laufe der Jahre maßgeblich dazu beigetragen, mich zu dem Physiker zu machen, der ich bin. Ich bin sehr dankbar für die vielen Möglichkeiten, die Du mir eröffnet hast!

Ich danke Elisabetta Gallo für die Übernahme des Zweitgutachtens und außerdem Günter Sigl, Peter Schleper und Christian Schwanenberger für die Mitgliedschaft in meiner Prüfungskommission.

Ich bedanke mich auch bei Roman Kogler, auf dessen umfassende Hilfe und Ratschläge ich mich jederzeit und zu jedem Thema verlassen konnte. Seit meiner ersten Stunde in dieser Gruppe hast Du mich begleitet und ich hätte mir keinen Besseren dafür wünschen können!

Anastasia Karavdina has certainly had major influence on my expertise in jet energy calibration. It was a demanding time, thank you for always staying calm and keeping me from drowning in code and mails!

My thanks go to Robin Aggleton for his CCLE-skills, which he still has not claimed his reward for!

Natürlich wurde die Arbeit auch deutlich durch die gute Atmosphäre im Büro und außerhalb unterstützt. Hier danke ich zuerst meinen schon lange entschwundenen Bürokollegen Marc Stöver und Tobias Lapsien. Marc, auch Du hast mich seit meinem ersten Tag hier begleitet und bist glücklicherweise auch darüber hinaus ein guter Freund geworden!

I thank Irene Zoi, Alexander Fröhlich, Dennis Schwarz, Anna Benecke, Karla Peña Rodriguez, Andrea Malara, who have been around most of my time in this group, for lots of funny noises, lots of coffee on the sofa, lots of selfmade cake, many many fun evenings, much cheeeeeese, and an amazing time in and outside the office! Of course

that includes Jan Skottke and especially Nino Ehlers and Henrik Jabusch, who were part of the leptoquark-team! I had a lot of fun!

A dedicated, great Thank You goes to Andrea Malara, whose support exceeds everything I could ask for. At any time or wherever you are, there is nothing I cannot ask you, there is nothing you would not do. Grazie!

Meiner Familie, ganz besonders meinen Eltern, und allen anderen Freunden danke ich für ihre unbedingte Unterstützung in jeder Situation. Ich konnte mich immer auf Euch verlassen und auf euch zählen!

Eidesstattliche Versicherung / Declaration on oath

Hiermit versichere ich an Eides statt, die vorliegende Dissertationsschrift selbst verfasst und keine anderen als die angegebenen Hilfsmittel und Quellen benutzt zu haben. Die eingereichte schriftliche Fassung entspricht der auf dem elektronischen Speichermedium. Die Dissertation wurde in der vorgelegten oder einer ähnlichen Form nicht schon einmal in einem früheren Promotionsverfahren angenommen oder als ungenügend beurteilt.

Ort, Datum	Arne Christoph Reimers